



HAL
open science

VUV photoionisation of astrophysical molecules : fundamental and quantitative aspects

Oliver Harper

► **To cite this version:**

Oliver Harper. VUV photoionisation of astrophysical molecules : fundamental and quantitative aspects. Chemical Physics [physics.chem-ph]. Université Paris-Saclay, 2020. English. NNT : 2020UP-ASS102 . tel-02926158

HAL Id: tel-02926158

<https://theses.hal.science/tel-02926158>

Submitted on 31 Aug 2020

HAL is a multi-disciplinary open access archive for the deposit and dissemination of scientific research documents, whether they are published or not. The documents may come from teaching and research institutions in France or abroad, or from public or private research centers.

L'archive ouverte pluridisciplinaire **HAL**, est destinée au dépôt et à la diffusion de documents scientifiques de niveau recherche, publiés ou non, émanant des établissements d'enseignement et de recherche français ou étrangers, des laboratoires publics ou privés.

VUV photoionisation of astrophysical molecules: fundamental and quantitative aspects

Thèse de doctorat de l'Université Paris-Saclay

École Doctorale n° 572, Ondes et Matière (EDOM)

Spécialité de doctorat : Physique

Unité de recherche : Institut des Sciences Moléculaires d'Orsay (ISMO), Université
Paris-Saclay, CNRS, Institut des Sciences Moléculaires d'Orsay, 91405, Orsay,
France

Réfèrent : Faculté des sciences d'Orsay

Thèse présentée et soutenue à Orsay, le 03/07/2020, par

Oliver J. HARPER

Composition du jury :

Laurent Nahon Directeur de recherche assimilé, Synchrotron SOLEIL (St-Aubin)	Président du jury
Amanda Ross Directrice de recherche, Institut Lumière Matière (Lyon)	Rapporteuse
Ian Sims Professeur des Universités, Institut de Physique de Rennes (Rennes)	Rapporteur
Christian Alcaraz Directeur de recherche, Institut de Chimie Physique (Orsay)	Examineur
Astrid Bergeat Maître de conférences, Institut des Sciences Moléculaires (Bordeaux)	Examinatrice
Séverine Boyé-Péronne Professeure des Universités, Institut des Sciences Moléculaires d'Orsay (Orsay)	Directrice de thèse
Bérenger Gans Chargé de recherche, Institut des Sciences Moléculaires d'Orsay (Orsay)	Co-encadrant

Résumé

L'évolution de la matière diluée dans les milieux astrophysiques tels que le milieu inter-stellaire, les atmosphères planétaires ou la coma des comètes, résulte d'une photochimie très complexe faisant intervenir en particulier un grand nombre d'espèces stables et réactives en phase gazeuse. Cette photochimie est induite par le rayonnement galactique ou par le rayonnement solaire dans le domaine spectral de l'ultra-violet du vide (VUV, longueur d'onde < 200 nm). Une bonne compréhension de cette évolution nécessite une modélisation précise de la photochimie de ces milieux, en prenant en compte l'ensemble des réactions chimiques et des processus photo-induits. Dans ce contexte, le travail principal de cette thèse porte sur le processus de photoionisation ($M + h\nu \rightarrow M^+ + e^-$).

Un des buts de cette thèse était de déterminer des paramètres quantitatifs, souvent jamais mesurés, pour décrire le processus de photoionisation de composés d'intérêt astrophysique, en particulier d'espèces réactives. Pour ce faire, le montage moyenne – haute résolution (SAPHIRS) de la ligne DESIRS du synchrotron SOLEIL et le nouveau montage laser VUV haute résolution (VULCAIM) de l'ISMO basé sur un spectromètre de photoélectrons à énergie cinétique nulle (ZEKE) ont été utilisés pour mener diverses études expérimentales. Cette thèse présente aussi le développement de cette nouvelle expérience, unique en France, et la caractérisation de ses principales performances. Les deux expériences employées dans cette thèse sont comparées et leur complémentarité est soulignée.

Un paramètre quantitatif important est la section efficace de photoionisation, reliant le nombre d'ions produits au nombre initial d'espèces neutres. Pour les espèces réactives, ce paramètre est rarement connu à cause des difficultés inhérentes à ce type de mesure. Ce travail présente deux mesures de sections efficaces de photoionisation (pour les radicaux NH_2 et OH). D'autres résultats préliminaires sur des sections efficaces de radicaux dérivés du méthanol sont également présentés et discutés. D'un point de vue pratique et en plus de leur intérêt astrophysique, ces sections efficaces permettent indirectement de quantifier la présence d'espèces neutres. Dans le cadre de cette thèse, cela a été utile lors de l'étude d'autres processus de relaxation (*i.e.* la photodissociation d'espèces neutres et stables) à travers des expériences pompe VUV – sonde VUV, qui sont aussi décrites dans le manuscrit.

En plus de l'importance de ces expériences pour les applications, ces études permettent d'obtenir des informations fondamentales et détaillées sur le processus de photoionisation, surtout via la spectroscopie de photoélectrons. Au synchrotron SOLEIL, les structures vibroniques de différentes molécules astrophysiques (C_2 et CH_3NCO) ont été étudiées au voisinage de leurs premiers potentiels d'ionisation adiabatiques. Au laboratoire, le nouveau laser VUV s'est montré très performant pour des expériences de spectroscopie VUV à des résolutions rarement atteintes dans ce domaine spectral (jusqu'à 0.06 cm^{-1}). Ce nouveau montage a été validée par spectroscopie PFI-ZEKE en étudiant la transition $\text{CO}_2^+ X^+ \ ^2\Pi_g \leftarrow \text{CO}_2 X \ ^1\Sigma_g^+$. L'état électronique fondamental du cation est particulièrement intéressant d'un point de vue spectroscopique puisqu'il présente des couplages spin-orbite et Renner-Teller et également une résonance de Fermi. Les structures rotationnelles d'un grand nombre de niveaux vibroniques de cet état ont été étudiées et comprises grâce à des simulations qui s'appuient sur des hamiltoniens effectifs. En plus de ce travail spectroscopique, l'utilisation de ce laser VUV pour la spectroscopie de photoélectron couplée à une technique d'analyse d'images révèle la possibilité d'entreprendre des études de photoionisation à haute résolution avec un meilleur rapport signal sur bruit par rapport aux méthodes traditionnelles, ce qui permettra la détermination de nouvelles informations spectroscopiques concernant la structure rovibronique d'un grand nombre de cations, et en particulier d'espèces radicalaires.

Acknowledgements

The majority of the work undertaken during this PhD was at the Institut des Sciences Moléculaires d'Orsay. I would therefore like to start by thanking the successive directors **Bernard BOURGUIGNON** and **Thomas PINO** for hosting me at the institute.

I would also like to thank the two referees **Amanda ROSS** and **Ian SIMS** for accepting to scrutinise this manuscript along with **Astrid BERGEAT**, **Christian ALCARAZ**, and **Laurent NAHON** who accepted to form my PhD jury. I am all the more grateful given the circumstances in which this PhD ended, with the Covid 19 pandemic, which made all of our lives more difficult. I also thank **Christian ALCARAZ** for his lending of the ZEKE spectrometer.

I cannot put into words how grateful I am for the unwavering support of my supervisors **Séverine BOYE-PERONNE** and **Bérenger GANS**. As I look back over the last three years, I am surprised at how much I have learnt and how much I have grown as both a scientist and a human being. Your availability and trust were invaluable throughout. You had big parts to play in this adventure and I cannot thank you enough. Even during the lockdown, you were always at my side... at least electronically speaking.

Séverine, je te remercie pour les gâteaux, les conseils, les questions, les réponses, les discussions sur l'enseignement et sur la physique moléculaire ou encore l'optique. Ton recul sur la science associé à ta gentillesse m'ont toujours permis de tirer quelque chose de nos discussions.

Bérenger, coach sportif, expérimentateur / bricoleur hors-pair, expert en spectroscopie et R, je te remercie pour ta patience et ta pédagogie qui m'ont accompagnées en salle de manip et au-delà ! J'ai appris énormément de choses à manipuler à côté de toi et à discuter de tout à tout moment avec toi.

I would like to thank all the people who assisted us during the synchrotron SOLEIL campaigns and in particular the DESIRS beamline scientists **Gustavo GARCIA** and **Nelson de OLIVEIRA** who were always available to help and answer any queries, both on and off the beamline. During these campaigns, I enjoyed fruitful exchanges with exterior collaborators. I thank **Jean-Claude GUILLEMIN** for synthesising molecular samples of study: CH_3NC and CH_3NCO . I thank **Jean-Christophe LOISON** for his passion and enthusiasm concerning flow tube reactions and his theoretical background concerning the observed phenomena. Likewise, I thank **Stephen PRATT** for the interesting discussions on free radical photoionisation cross sections and his theoretical view point.

During my time at ISMO, I also appreciated conversations I had with members of the SYSTEMAE team. I thank **Stéphane DOUIN** for his interest and encouragement in my work and experimental top-tips, **Karine BEROFF** for the discussions on breakdown curves, and **Laurent COUDERT** for his seemingly bottomless well of theoretical knowledge, that helped us understand a great deal about CH_3NCO , and his \LaTeX know-how. On top of this, I am very grateful to the whole team for the good atmosphere, which meant I was always happy to come to the lab, and which made the whole experience even more beneficial. Outside the team, I thank **Michel BROQUIER** and **Satchin SOORKIA** for their always-useful input, support and multiple lendings of equipment.

This brings me to the PhD students of ISMO who, on the whole, do not have the best singing voices or the most honed skills at escaping rooms, but whose infallible and friendly support were precious on a daily basis. En particulier je remercie la *dreamteam* avec qui j'ai eu l'honneur de partager un bureau et dont la folie m'a permis de rester sain !

A l'ISMO, j'ai bénéficié d'un excellent soutien de la part des équipes techniques. Neuf fois sur dix, je pense que vous avez pu m'aider le jour-même. Purement pour raisons de fréquence de visite, je voudrais remercier tout particulièrement **Christophe CHARRIERE**, **Thierry**

CHAMAILLE, Sébastien DEBEST, Catherine LEBRIS, Christophe LEFUMEUX, Julien VINCENT et tout l'atelier de mécanique et l'administration mais j'en oublie très certainement.

Last but not least, I would like to thank my family, especially my parents who have selflessly always put me first in every undertaking. Je voudrais remercier mes amis qui me soutiennent dans tous mes projets d'année en année. **Eloi**, binôme de confiance, compère de brasserie, compagnon de voyage, musicien talentueux et grand physicien, un grand et tendre merci d'avoir toujours été là.

Contents

Résumé	i
Acknowledgements	iii
Introduction	1
1 Experimental tools	7
1.1 Synchrotron SOLEIL	7
1.1.1 The SOLEIL synchrotron facility	7
1.1.2 The DESIRS beamline	8
1.1.3 SAPHIRS	9
The DELICIOUS 3 spectrometer	10
Molecular samples	15
1.2 VUV laser setup	17
1.2.1 VUV laser production	18
1.2.2 Implementation of VUV laser production	19
1.2.3 High resolution tunable UV laser chain	21
1.2.4 High resolution dye laser	25
1.2.5 VUV spectral range	26
1.2.6 VUV photon flux monitoring	27
1.2.7 Vacuum experimental setup	28
Gas-phase sample and molecular beam generation	28
Time Of Flight mass spectrometer	29
Temporal synchronisation of the setup	30
1.2.8 First VUV laser experiment with Icare on N ₂	31
1.2.9 From Icare to VULCAIM	32
Theoretical reminders on Rydberg states	32
Probing Rydberg states using Pulsed-Field-Ionisation spectroscopy	34
Probing rare gas Rydberg states using Pulsed-Field-Ionisation (PFI) spectroscopy with Icare	35
The birth of VULCAIM	36
Probing rare gas Rydberg states using Pulsed-Field-Ionisation (PFI) spectroscopy with VULCAIM	38
Detecting electrons using VULCAIM	41
1.3 Complementary VUV light sources on the Saclay Plateau	42
2 Ion yields and absolute photoionisation cross section measurements	43
Motivations	43
2.1 Absolute photoionisation cross section determination: general method	46
2.1.1 Absolute photoionisation cross section measurement	46

2.1.2	Uncertainty determination	47
2.1.3	Ion yields	49
2.1.4	Choosing the photon energy for the absolute measurement	49
2.1.5	Specificities to our experimental setup	50
2.2	The absolute photoionisation cross section of the hydroxyl (OH) free radical . . .	52
2.2.1	The OH free radical: current state-of-the-art	52
2.2.2	The OH ⁺ photoion yield	53
2.2.3	The fixed energy measurement of the OH photoionisation cross section .	53
2.2.4	The OH photoionisation cross section from threshold up to 15 eV.	55
2.2.5	A follow-up study	57
2.3	The absolute photoionisation cross section of the amino (NH ₂) free radical	60
2.3.1	The NH ₂ free radical: current state-of-the-art	60
2.3.2	The NH ₂ ⁺ ion yields	60
2.3.3	Fixed energy absolute measurements	62
2.3.4	NH ₂ photoionisation cross section determination	64
2.4	Preliminary study on the carbonated fragments of methanol	68
2.4.1	Context and motivation	68
2.4.2	Specific experimental details	69
2.4.3	Ion yields	70
	Precursor ion yields (CH ₃ OH ⁺)	70
	Single H-abstraction product ion yields	71
	Double H-abstraction product ion yields	73
	Triple H-abstraction product ion yields	74
	Methanol isotopologue summary	75
2.5	Photoionisation cross section and ion yield conclusions	75
3	Photoelectron spectroscopy, from medium to high resolution	79
3.1	Photoelectron spectroscopy with synchrotron radiation	80
3.1.1	Threshold photoelectron spectroscopy of CH ₃ NCO	80
	Astrophysical context	80
	Spectroscopic context	80
	Specific experimental details	81
	Theoretical model	82
	Results and discussion	82
	Conclusion	84
3.1.2	First single-photon ionisation study of C ₂	85
	Astrophysical context	85
	Spectroscopic context	85
	Specific experimental details	85
	<i>Ab initio</i> calculations	87
	Assignment of the Threshold-Photoelectron spectrum of C ₂	88
	Ion yield	92
	Conclusion on the C ₂ study	93
3.2	High-resolution photoelectron spectroscopy	94
3.2.1	Pulsed Field Ionisation - ZERo Kinetic Energy (PFI-ZEKE) spectroscopy .	94
	Introduction	94
	Ionisation rates of Rydberg states	95
	Experimental implementation	96

3.2.2	CO ₂ PFI-ZEKE spectroscopy	97
	Motivations	97
	Overview of the X ⁺ ² Π _g CO ₂ ⁺ ground state	98
	Spin-orbit components of X ⁺ ² Π _g (<i>v</i> ₁ = 0, <i>v</i> ₂ = 0, <i>v</i> ₃ = 0)	100
	Rotational energy levels of a linear triatomic molecule in a ² Π electronic state - simulations	102
	Stark-shift corrections	103
	The CO ₂ ⁺ X ⁺ ² Π _{3/2} vibronic state	104
	The CO ₂ ⁺ X ⁺ ² Π _{1/2} vibronic state	106
	Vibronic states of the (<i>v</i> ₁ = 0, <i>v</i> ₂ = 1, <i>v</i> ₃ = 0) band.	107
	Vibronic states of the (<i>v</i> ₁ = 0, <i>v</i> ₂ = 2, <i>v</i> ₃ = 0) and (<i>v</i> ₁ = 1, <i>v</i> ₂ = 0, <i>v</i> ₃ = 0) bands.	109
	CO ₂ photoionisation summary	111
3.2.3	Pulsed-Ramped-Field-Ionisation ZERo-Kinetic-Energy	111
	Technique description	111
	Image treatment	112
	Discussion	113
	Conclusions & perspectives	116
A	Exploratory studies of the photodissociation process	121
A.1	Experimental setup	122
	A.1.1 General principle of the measurement: pump-probe scheme	122
	A.1.2 Modified Icare setup	123
	A.1.3 VUV production <i>via</i> four-wave mixing in a rare gas cell	123
A.2	NH ₃ photodissociation at 213 nm	125
	A.2.1 Context and motivations	125
	Astrophysical interest	125
	NH ₃ photodissociation, state-of-the-art	125
	Choice of photodissociation photon energy	126
	A.2.2 Experimental specificities	128
	A.2.3 Results	128
	A.2.4 Conclusions and perspectives	131
	Towards free radical photoionisation cross section measurements	131
	Summary	132
A.3	CH ₃ OH photodissociation studies	132
	A.3.1 Context and motivations	132
	Astrophysical interest	132
	CH ₃ OH photodissociation, state-of-the-art	132
	Choice of photodissociation photon energy	134
	A.3.2 Experimental specificities	134
	A.3.3 CH ₄ photodissociation	136
	A.3.4 CH ₃ OH photodissociation at 118.2 nm: results	137
	A.3.5 CH ₃ OH photodissociation summary	139

B	Dissociative ionisation of CH₃NCO	141
B.1	Experimental details	141
B.2	Context	141
B.3	Ion yields and assignments of the products of CH ₃ NCO dissociative ionisation .	142
B.4	TPES of dissociative states	146
B.5	CH ₃ NCO dissociative ionisation summary	147
C	List of publications as co-author	149
	Bibliography	151

List of Figures

1	Main relaxation pathways for the amino free radical (NH_2) after absorbing a VUV photon.	1
1.1	Schematic layout of the Synchrotron SOLEIL [19] along with its various components.	8
1.2	Left: layout of the DESIRS beamline displaying its various components and branches, adapted from ref. [19]. Right: simplified layout of the DESIRS beamline as seen from above;	8
1.3	Left: photo of the SAPHIRS molecular beam chamber. Right: Technical layout of the SAPHIRS molecular beam chamber containing the flow-tube reactor and the DELICIOUS 3 spectrometer adapted from ref. [23]	10
1.4	Illustration of the DELICIOUS 3 spectrometer. Added are example images of electrons (bottom) and ions (top).	10
1.5	Example of ion image treatment. a) Ion image on detector with red rectangle showing region of interest with ions originating from the molecular beam. b) Raw mass spectrum constructed using all ions in ion image a). c) Same mass spectrum with ion contributions reduced to region of interest in ion image c). . .	11
1.6	Example of electron image treatment for N_2 photoionisation adapted from ref. [25]. a) Mass-selected (from N_2) raw electron image on detector for a photon energy of 19.5 eV and a repeller voltage set to 750 V. b) Inverted electron image. c) Corresponding mass-selected PES with blue arrows linking spectral features to areas in the image b).	11
1.7	Photo-Ion Yield and Threshold Photoelectron Spectrum principle demonstrated on $\text{R} + h\nu \rightarrow \text{R}^+ + \text{e}^-$ reaction. If the photon energy $h\nu$ is equal or greater than the energy of the cationic vibronic state, photoelectrons can be issued from that state along with photo-ions. As $h\nu$ increases, higher energy cationic states are reached producing yet more electrons and ions. This access to states manifests itself by the appearance of steps in the photo-ion yield. Photoelectrons whose kinetic energies are vanishing are recorded in the Threshold Photoelectron Spectrum for photon energies close to those of cationic states.	12
1.8	a) Raw PES matrix of CH_3NCO between 10.4 and 12 eV with a 300 V repeller voltage. b) Rotated PES matrix to make diagonal lines vertical. c) Zoom on non-rotated PES matrix to visualise slow electrons. d) Zoom on rotated PES matrix to visualise slow electrons. e) TPES: Integration of electron counts in non-rotated PES matrix for electrons slower than 0.01 eV represented by a thin dashed box in c) and \int symbol. f) SPES: Integration of electron counts in rotated PES matrix for electrons slower than 0.01 eV represented by a thin dashed box in d) and \int symbol. Comparing e) and f), using the same electrons, the rotation in the SPES treatment offers the better compromise between signal-to-noise and resolution compared to TPES.	14

1.9	Photo-Ion Yield and Threshold PhotoElectron Spectroscopy principle demonstrated on $R + h\nu \rightarrow R^+ + e^-$ as in Fig. 1.7, but with autoionisation. R^* and R^{**} are neutral states situated above the first IP and are respectively resonant and non-resonant with cationic states. Autoionisation leads to resonances in the ion yield and enhances peaks in the TPES if resonant.	15
1.10	Schematic of the flowtube reactor where H-abstraction of CH_4 by F atoms produces CH_3 , CH_2 , <i>etc.</i> The injector distance is noted d ; d can be tuned to adjust conditions within the reactor.	16
1.11	Typical mass spectrum obtained by summing all mass spectra recorded between 12.4 and 13.6 eV when using CH_4 as a precursor during the experiments on C_2 (see section 3.1.2).	17
1.12	Rough general layout of the laboratory-based high-resolution VUV laser setup at ISMO.	18
1.13	Four-wave mixing resonant scheme combining UV and visible radiation in rare gas. Dashed lines represent virtual states in the rare gas; full lines represent actual states in the rare gas that are exploited as resonances.	18
1.14	Implementation of four-wave mixing scheme in a freely expanded rare gas used to generated tunable VUV radiation. Reflective VUV grating selects the intended wavelength for the study to pass through the 1 to 2 mm in diameter iris. Only 0 th and 1 st order components from the grating are presented.	20
1.15	Top: Photo of the high-resolution UV laser chain at ISMO. Bottom: Illustration of the high-resolution UV laser chain at ISMO with main characteristics.	21
1.16	Optical layout of the Sirah Matisse ring dye-laser from ref. [32]	22
1.17	Optical layout of the Sirah Pulsed Amplifier from ref. [32]	23
1.18	Schematic spectra of overlap between UV laser bandwidth and two-photon transition width in a rare gas. a) Spectrum displaying a narrow UV laser bandwidth with all spectral components within the rare-gas transition that all contribute in VUV production ($\Delta\nu_{UV} < \Delta\nu_{RG}$). b) Spectrum displaying a wide UV laser bandwidth with spectral components outside the rare-gas transition ($\Delta\nu_{UV} > \Delta\nu_{RG}$). As more laser spectral components in the a) spectrum overlap with the rare gas transition as compared to the b) spectrum, VUV production will have a higher efficiency in a).	24
1.19	Normalised VUV intensity as a function of UV wavenumber. Lorentzian curves fit the data sets whose average UV laser energy are 0.06 mJ/pulse (green line) and 1 mJ/pulse (red line).	24
1.20	Top: Photo of the Cobra-Stretch double grating dye-laser pumped by a Spectra-Physics Quanta Ray Nd:YAG laser. Bottom: Optical layout of the Sirah Cobra Stretch double grating dye-laser from ref. [32]	25
1.21	I_2 laser-induced-fluorescence spectrum resulting from the excitation of I_2 with a Cobra Stretch dye laser (black) compared to FT absorption spectrum (blue) from ref. [35]	26
1.22	VUV laser spectral range for each rare gas resonance (same notations as Tables 1.4 and 1.7). Green (blue) zones represent spectral regions using ν_{vis} produced by the Cobra-Stretch pumped at 532 nm (355 nm).	27
1.23	Schematic drawing of a gas expanding through a nozzle followed by a skimmer which selects the innermost part of the jet. A reduction of the velocity distribution (black arrows) leads to lower translational temperatures after the skimmer.	29
1.24	Temporal synchronisation of the various elements of the experimental setup.	30

1.25	Left: Two-photon, two-colour ionisation scheme to probe at rotational resolution the $c'_4 \ ^1\Sigma_u^+$ ($v = 3$) state of N_2 . Right: Rotationally resolved spectra of the $c'_4 \ ^1\Sigma_u^+$ ($v = 3$) \leftarrow $X \ ^1\Sigma_g^+$ transition in N_2 with a 1 mm (top) and 2 mm (bottom) in diameter skimmers. These experimental spectra (black) are simulated using PGOPHER software (blue).	31
1.26	Simplified 2D schemes of an electron (green dot) in a potential well (V) representing the bound nature of an electron within the atom. a) Arrival of a VUV laser pulse to excite the atom and promote an electron to a highly excited Rydberg state. b) The laser pulse has passed, the Rydberg atom has been formed. c) PFI: Application of electric field F which deforms the potential well allowing the electron to escape.	34
1.27	Icare PFI spectra of Rydberg series of Ar (top) and Kr (bottom) converging to their first IPs , the ground states of their respective ions (noted in pink). Rydberg states are resolved and visible for up to $n \approx 55$ in both Ar and Kr.	36
1.28	Degeneracy lifting of $n = 40$ Rydberg state with electric field F . Observation of blue and red shifted states. Black arrow at $F \approx 1.5 \text{ V.cm}^{-1}$ represents the 0.3 cm^{-1} experimental resolution	37
1.29	Top left: Photo of the VULCAIM setup with the various laser sources in the background. Top right: Close-up photo of the VULCAIM vacuum chambers. Bottom: Schematic layout within VULCAIM.	38
1.30	VULCAIM PFI spectra of Rydberg series of Ar (top) and Kr (bottom) converging to their first IPs , the ground states of their respective ions (noted in pink). Rydberg states are resolved and visible for up to $n \approx 80$ in Ar and $n \approx 130$ in Kr.	39
1.31	Comparative PFI spectra of Rydberg series of ^{84}Kr (top) and ^{40}Ar (bottom) recorded using Icare (blue) and VULCAIM (black). In the case of the Icare experiment, higher extraction fields were used which explains why Rydberg states of lower n are observed.	40
1.32	Maximum resolution measurement of photon resolution of VULCAIM using the $39d[3/2](J=1)$ Rydberg state in ^{82}Kr . A red dashed gaussian line whose FWHM= 0.06 cm^{-1} is superimposed on the experimental spectrum.	41
1.33	Simulated degeneracy lifting of a $n = 40$ Rydberg state with electric field F . Observation of blue and red shifted states. Black arrow at $F \approx 0.2 \text{ V.cm}^{-1}$ represents the upper limit for parasitic electric fields in the experiment.	41
2.1	Illustration of mass spectra recorded in two experimental conditions. a) Only the precursor P is present in situation 1. b) Free radical species R are produced from the precursor in situation 2. c) The lowest spectrum is the difference spectrum b) - a).	46
2.2	Block diagram of the Monte Carlo uncertainty propagation procedure generating the R photoionisation cross section distribution, whose mean value is taken as the final cross section value and two standard (2σ) deviations constitute the error bars	48
2.3	Effect of experimental resolution on measured resonance (schematic illustration). A simulated pair of resonances (black line) corresponding to the energy difference between energy states is measured using apparatus whose resolution is 0.5 (green), 2 (blue) and 5 (red) times the natural width of the resonance.	50
2.4	Typical astrophysical water regeneration cycle featuring the photoionisation of OH (pink arrow)	52

2.5	OH ⁺ ion yields from Cutler <i>et al.</i> (top) [73], Dehmer (middle) [72] and this work (bottom) taken from ref. [46, 47].	53
2.6	Mass spectra recorded at 13.800 eV with the F-atom-producing discharge off (top) and on (middle) and the difference spectrum (bottom). The same arbitrary unit is used in all spectra.	55
2.7	Measured H ₂ O ⁺ (top) and O ⁺ (bottom) set to an absolute photoionisation cross section scale respectively using data from Fillion <i>et al.</i> (blue line) [81] and Angel and Samson (orange dots) [82]. Note the vertical scale of the lower panel is cut truncating the atomic oxygen resonances around 14.1 eV. The red dashed vertical line marks the photon energy (13.800 eV) of the absolute measurements of this work.	56
2.8	Absolute photoionisation cross section of OH from this work [46, 47] (black curve) as a function of photon energy; the blue area represents the error bars presented with a 2σ confidence level. They take into account both the error bar on the cross section value, and the uncertainty on the photon energy value (absolute measurement as well as scaling of the photoion yield). The red cross at 13.800 eV constitutes the absolute fixed energy measurement and associated uncertainty. The green points represent the absolute measurements from Dodson <i>et al.</i> [45] performed at 13.346 and 14.193 eV.	56
2.9	Mass spectra recorded at 14.505 eV (left-hand panels) and 13.250 eV (right-hand panels) with the F-atom-producing discharge off (top) and on (middle) and the difference spectrum (bottom). For each energy, the same arbitrary unit is used in three corresponding panels.	58
2.10	Absolute photoionisation cross section of OH from this work (black curve) as a function of photon energy from ref. [46, 47]; the blue area represents the error bars presented with a 2σ confidence level. The red cross at 13.800 eV constitutes the absolute fixed energy measurement and associated uncertainties on both <i>x</i> - and <i>y</i> -values from ref. [46, 47]. The green points represent the absolute measurements from Dodson <i>et al.</i> [45]. Red triangles represent cross section values determined in this follow-up study at 13.250 and 14.505 eV.	59
2.11	a) NH ₂ ⁺ ion yield from Gibson <i>et al.</i> [90]. b) Ion yield measured during this PhD for <i>m/q</i> = 16 a.m.u. attributed mainly to NH ₂ ⁺ . Sharp and imposing resonances at 14.1 eV are attributed to atomic oxygen autoionisation resonances. Purple asterisks mark Ar absorption lines from the beamline gas filter used to calibrate the photon energy. Both panels feature dot-dashed blue lines pinpointing the three lowest electronic states of NH ₂ ⁺ [92]. Panel b) contains dashed red vertical lines pinpointing the energies of the absolute measurements at 12.700, 13.200, and 14.000 eV.	61
2.12	Left-hand panels a) to c): mass spectra recorded at 13.200 eV in NH ₂ study. Spectra recorded with F-atom-producing discharge off (panel a)), on (panel b)) and difference spectrum (panel c)). Right-hand panels d) to f): mass spectra recorded at 17.500 eV in NH ₂ study without injecting any NH ₃ . Spectra recorded with F-atom-producing discharge off (panel d)), on (panel e)) and difference spectrum (panel f)). Mass peaks are assigned to various ionic fragments as indicated in the middle panel. The bottom panel shows which species are consumed (negative peaks) and which are formed by switching the F producing discharge on.	62

2.13	Top: ion yield of $m/q = 30$ a.m.u. of our study (black line) compared to the NO^+ ion yield of Watanabe <i>et al.</i> [44] (green line). Bottom: ion yield of $m/q = 32$ a.m.u. of our study (black line) compared to the O_2^+ ion yield of Holland <i>et al.</i> [84] (green line)	63
2.14	NH_2 photoionisation cross section as a function of photon energy. Panels a) and b) display our ion yield and the ion yield of Gibson <i>et al.</i> [90]), respectively, set to an absolute scale using our fixed-energy values at 12.700 and 13.200 eV, noted in red along with their respective error bars (see Table 2.6). An orange cross marks a fixed-energy cross section value at 14.000 eV, corrected for O^+ contributions, but not used in the scaling of the ion yield. The blue area denotes error bars extended over the whole range. A grey area in the top panel around 14.1 eV masks the O^+ resonance that could not be corrected, cross section values could not be determined in this narrow area. Drops in the spectrum due to gas filter absorption lines also constitute points where cross section values cannot be determined (purple asterisks).	66
2.15	NH_2 photoionisation cross section as a function of photon energy. All values and notations are the same as in Fig. 2.14 a) with in addition a green line representing NH_2 cross section values from the Leiden database [8].	67
2.16	Typical mass spectrum obtained by summing all mass spectra recorded between 7.4 and 11.4 eV when using CD_3OH as a precursor.	69
2.17	Typical mass spectrum at 11.4 eV when using CD_3OH as a precursor and the microwave discharge turned off.	71
2.18	Ion yields resulting from the direct ionisation of CH_3OH (black line) and CD_3OH (red line). A TPES of CH_3OH is also presented in grey. A purple dashed line at 10.846 eV locates the $IP(\text{CH}_3\text{OH})$ [105].	71
2.19	Single H-abstraction product ion yields. a) The $m/q = 33$ a.m.u. ion yield from the CD_3OH study assigned to CD_2OH^+ with a dashed vertical line at 7.55 eV locating the IP of CH_2OH [106]. b) The $m/q = 34$ a.m.u. ion yield from the CD_3OH study assigned to CD_3O^+ with a dashed vertical line at 10.72 eV locating the IP of CH_3O [106]. c) The $m/q = 31$ a.m.u. ion yield (black line) from the CH_3OH study is compared to a linear combination (red dashed line) of panels a) and b) with a 60/40 ratio. The same y -axis arbitrary unit is used in all panels. Purple asterisks locate Kr absorption lines caused by the beamline gas filter used to calibrate the photon energy for all non-deuterated scans of this section.	72
2.20	Double H-abstraction product ion yields. a) The $m/q = 32$ a.m.u. ion yield from the CD_3OH study assigned to CD_2O^+ . b) The $m/q = 31$ a.m.u. ion yield from the CD_3OH study assigned to CDOH^+ . c) The $m/q = 30$ a.m.u. ion yield (black line) from the CH_3OH study is compared to a linear combination (red dashed line) of panels a) and b) with a 95/5 ratio. This panel also features a H_2CO^+ ion yield from Dodson <i>et al.</i> [50] in green. Vertical purple dashed lines at 8.86 and 10.72 eV locate the ionisation potentials of CHOH [108] and CH_2O [107], respectively. The same y -axis arbitrary unit is used in all panels.	73
2.21	Triple H-abstraction product ion yields. The $m/q = 29$ a.m.u. ion yield (black line) from the CH_3OH study is compared to the $m/q = 30$ a.m.u. ion yield (red line) from the CD_3OH study. A vertical purple dashed line at 8.14 eV locates the $IP(\text{HCO})$ [109].	74

2.22	Schematic representation of a photoionisation cross section as a function of incident photon energy. The plateau value is reached at photon energies above vibrational levels of the cationic electronic ground state with non-vanishing FCF, but below the first excited state.	76
3.1	Scheme illustrating the difference between vertical and adiabatic <i>IPs</i> (pink arrows). Projections of the neutral (X) and cationic (X^+) potential energy surfaces along an internal coordinate are drawn along with vibrational energy levels. The internal coordinate can be a bond length, an angle, or a function of several geometric parameters.	79
3.2	Sketch of the CH_3NCO molecule (geometry adopted in the neutral ground electronic state \tilde{X}^1A'). White, grey, blue, and red spheres represent hydrogen, carbon, nitrogen, and oxygen atoms, respectively. The coordinates of the two large amplitude motions are marked (angles τ and ρ).	81
3.3	Experimental TPES (black) of CH_3NCO with the peak labelling referring to Table 3.3 compared to a calculated spectrum (blue) using a vibrational temperature of 300 K. The <i>ab initio</i> calculated spectrum is shifted -0.133 eV to fit the experimental spectrum. Assignments in the calculated spectrum refer to vibrational bands of the $\tilde{X}^+ 2A'' \leftarrow \tilde{X}^1A'$ photoionising transition. The labels correspond to vibrational mode numbers (see Table 3.3) followed by cationic (superscript) and neutral (subscript) vibrational quantum numbers.	83
3.4	Typical mass spectrum obtained by summing all mass spectra recorded between 12.4 and 13.6 eV using CH_4 as a precursor.	86
3.5	Experimental TPES (red line) and PIY (black) of C_2 . Purple asterisks locate Ar absorption lines visible in the PIY and used to calibrate the energy scale of the spectrum.	87
3.6	Theoretical potential energy curves of C_2 and C_2^+ from ref. [147]	88
3.7	Experimental TPE spectrum of C_2 (upper panel) compared to FCF simulations of vibronic transitions (other panels) from ref. [147]. The same colour code as in Fig. 3.6 is used for the final state of the transition. Full line spectra correspond to transitions from the neutral metastable $a^3\Pi_u$ state and those with dashed lines correspond to transitions from the neutral ground state $X^1\Sigma_g^+$. Black stick spectra in the simulated spectra correspond to FCF, the resulting spectra result from convoluting the FCF by a gaussian function whose <i>FWHM</i> = 25 meV.	90
3.8	Experimental TPE spectrum of C_2 (upper black trace) compared to a simulated spectrum (lower red trace) which combines the simulated $a^+ 2\Pi_u \leftarrow X^1\Sigma_g^+$, $X^+ 4\Sigma_g^- \leftarrow a^3\Pi_u$, and $a^+ 2\Pi_u \leftarrow a^3\Pi_u$ vibronic transitions from ref. [147]. The red stick spectrum represents FCF values and the red trace, their convolution by a gaussian function whose <i>FWHM</i> is 25 meV.	91
3.9	C_2^+ ion yield adapted from ref. [147]. The vertical lines mark the transition energies ($E_{I,\text{calc.},\text{corr.},\text{ZPE}}$) from the $a^3\Pi_u$ state (full line) or $X^1\Sigma_g^+$ state (dashed line). Triangles locate the position of autoionising features. The grey area represents the statistical error on the C_2^+ ion signal. A purple line represents the integrated experimental TPES.	92

3.10	Illustration of PFI-ZEKE scheme. Left: Rydberg states, reached using a VUV photon (pink), converging to IP . Right: voltage scheme applied to electrons in interaction zone after laser excitation; an electron signal on the MCP is detected for each voltage step after a time-of-flight. Each section of Rydberg states (colour code) is ionised at each successive voltage step (same colour code).	94
3.11	Simulated degeneracy lifting of a $n = 180$ ($m = 0$) Rydberg state with electric field F , only states with n_2 a multiple of 10 are represented for clarity (except for $n_2 = 179$) adapted from ref. [18]. Black dots locate field thresholds for which the ionisation rate is high enough for detection. States represented by light pink lines are ionised under a 65 V.m^{-1} field. States represented by green lines are ionised under a -65 V.m^{-1} field. In grey are states ionised by neither voltage.	95
3.12	PFI-ZEKE spectrum (points) around the first IP of Kr. Superimposed on this experimental spectrum is a red-dashed gaussian line shape whose $FWHM$ is 0.14 cm^{-1}	97
3.13	Raw PFI-ZEKE spectrum of the lowest vibrational levels of the $\text{CO}_2^+ X^+ {}^2\Pi_g$ ground state.	99
3.14	Energy diagram of the lowest vibrational levels of the $\text{CO}_2^+ X^+ {}^2\Pi_g$ ground state accounting for the Renner-Teller and spin-orbit effects adapted from ref. [157].	100
3.15	PFI-ZEKE spectrum of both spin-orbit components of the $\text{CO}_2^+ X^+ {}^2\Pi_g$ ($v_1 = 0, v_2 = 0, v_3 = 0$).	101
3.16	Illustration of an autoionisation process from a Rydberg state converging to the ${}^2\Pi_{1/2}$ to the ${}^2\Pi_{3/2}$ ground state in $\text{CO}_2^+ (X^+)$. This process yields an electron with non-zero kinetic energy ($E_K > 0$).	101
3.17	Zoom on PFI-ZEKE experimental spectra of the vibrationless $X^+ {}^2\Pi_{3/2} \leftarrow X^+ {}^1\Sigma_g^+$ transition recorded at different voltage steps. Using colour coding, the spectrum for each voltage step is represented, shifted vertically for clarity. Red dots locate maxima for a given transition which move to lower energies, the lower the voltage.	104
3.18	PFI-ZEKE experimental (black) and simulated (blue) spectra of the vibrationless $X^+ {}^2\Pi_{3/2} \leftarrow X^+ {}^1\Sigma_g^+$ transition. Note the simulated spectrum used $T = 10 \text{ K}$ and is inverted with respect to the experimental spectrum to facilitate comparisons. Assignments to ΔJ branches are noted with the ground state rotational quantum J underneath.	105
3.19	PFI-ZEKE experimental (black) and simulated (blue) spectra of the vibrationless $X^+ {}^2\Pi_{1/2} \leftarrow X^+ {}^1\Sigma_g^+$ transition. Note the simulated spectrum uses $T = 10 \text{ K}$ and is inverted with respect to the experimental spectrum to facilitate comparisons. Assignments to ΔJ branches are noted with the ground state rotational quantum J underneath.	106
3.20	Raw PFI-ZEKE experimental (black) and simulated (blue) spectra of the $X^+ {}^2\Pi(0, 1, 0) \leftarrow X^+ {}^1\Sigma_g^+$ transition. Note the simulated spectrum uses $T = 10 \text{ K}$ and is inverted with respect to the experimental spectrum to facilitate comparisons. Assignments to vibronic states are noted.	107
3.21	Raw PFI-ZEKE experimental (black) and simulated (blue) spectra of the $X^+ {}^2\Pi(0, 2, 0) \leftarrow X^+ {}^1\Sigma_g^+$ and $X^+ {}^2\Pi(1, 0, 0) \leftarrow X^+ {}^1\Sigma_g^+$ transitions. Note the simulated spectrum uses $T = 10 \text{ K}$ and is inverted with respect to the experimental spectrum to facilitate comparisons. Assignments to vibronic states are noted. The positions of the ${}^2\Phi$ states are noted with green vertical lines according to the model, but are not observed experimentally.	109

3.22	Illustration of the PRFI-ZEKE spectroscopy technique. a) Fixed photon energy ramped voltage scheme analogous to the step voltage scheme of Fig. 3.10. b) Zero-field stick spectrum. c) PRFI-ZEKE matrix gathering electron signals from ramped voltage schemes (a) for every photon energy step of the scan, note the shift of spectral maxima (b) with voltage follows a quadratic law (orange curves).	112
3.23	PRFI-ZEKE ramped voltage scheme (black line). A traditional PFI-ZEKE scheme (red dashed line) is used to relate electron arrival times to voltage values.	113
3.24	PRFI-ZEKE image treatment on the $X^+ \ ^2\Pi_{1/2} \leftarrow X \ ^1\Sigma_g^+$ photoionising transition in CO_2 . a) Raw PRFI-ZEKE matrix. b) Linearised PRFI-ZEKE matrix. c) Linearised and rotated PRFI-ZEKE matrix. d) PRFI-ZEKE spectrum (black) obtained by summing all electron signals in dashed box in c), compared to a simulated spectrum.	114
A.1	NH_3 photodissociation scheme. Following photoexcitation, excited NH_3 can relax <i>via</i> a number of different photodissociation channels. Branching ratios (<i>BR</i>) are noted for each.	121
A.2	General pump-probe scheme dissociating a generic molecule <i>M</i> producing neutral fragments (F_1, F_2, \dots). The neutral fragments are then ionised to form cations which are detected after a time-of-flight (TOF) and recorded in a mass spectrum. Note that if $h\nu_{\text{probe}} > IP(M)$, M^+ also appears in the mass spectrum.	122
A.3	Icare adaptation scheme for pump-probe setup. Each UV laser can be used directly or frequency tripled (<i>via</i> four-wave mixing) to provide VUV radiation if needed.	124
A.4	Implementation of four-wave mixing to generate VUV laser radiation in a rare gas cell.	124
A.5	Illustration of the role of the MgF_2 prism to disperse the radiation exiting the rare gas cell. An iris selects the VUV radiation for the experiment.	125
A.6	a) Typical VUV solar flux taken from ref. [191]. b) NH_3 VUV photodissociation cross section [8]. c) Product of the solar flux with the photodissociation cross section (c) = a) \times b)), a blue vertical line at 213 nm (5.82 eV) locates the photodissociation energy of this work.	126
A.7	Pump-probe scheme of Fig. A.2 adapted to this specific NH_3 study.	128
A.8	Mass spectra obtained during the NH_3 photodissociation study using a photodissociating pump at 5.82 eV (213 nm) and a photoionising probe at 13.6 eV (91 nm) in different laser configurations: a) Pump + probe (see e) for zoom) b) Pump only (see f) for zoom) c) Probe only (see g) for zoom) d) difference spectrum (= a) - b) - c)) (see h) = e) - f) - g) for zoom)	129
A.9	The NH_2^+ signal as a function of incident UV laser intensity on a log-log scale. Circles represent experimental points, the linear fit, whose slope is 1.03 ± 0.04 , is represented as a red line.	130
A.10	a) Typical VUV solar flux taken from [191]. b) CH_3OH VUV photodissociation cross section [8]. c) Product of the solar flux with the photodissociation cross section (c) = a) \times b)), a dashed blue vertical line at 118.2 nm (10.49 eV) locates the photodissociation energy of this work. A dashed purple vertical line at 121.6 nm (10.20 eV) locates the relevant wavelength for astrophysical applications.	135
A.11	Pump-probe scheme of Fig. A.2 adapted to this specific CH_3OH study.	136
A.12	Mass spectra obtained during the CH_4 photodissociation at 10.49 eV (118.2 nm) probed at the same energy.	137

A.13	Mass spectra obtained during the CH ₃ OH photodissociation at 10.49 eV (118.2 nm) probed at 10.78 eV (115 nm) in different laser configurations: a) Pump + probe b) Pump only c) Probe only d) difference spectrum (= a) - b) - c))	138
B.1	Summed mass spectrum over the whole scan (10.3 to 15.7 eV). CH ₃ NCO dissociative ionisation products are identified.	142
B.2	Ion yields of the products of CH ₃ NCO dissociative ionisation. Blue- and red-dashed lines correspond to the thermodynamic thresholds (E_T) and theoretical thresholds (E_{th}) of Table B.1, respectively. Black arrows pinpoint appearance energies (E_a) of the corresponding fragments, also summarised in Table B.1. Purple asterisks locate Ar absorption lines from the beamline gas filter used to calibrate the energy scale.	143
B.3	a) TPES of $m/q = 55$ (red) and 57 a.m.u. (blue) spectra from this work, assigned to CHCNO ⁺ and CH ₃ NCO ⁺ , respectively; $m/q = 55$ a.m.u. has a $\times 20$ zoom. b) TPES combining the two spectra from panel a). c) Digitalised He I PES of CH ₃ NCO from ref. [130].	146

List of Tables

1	Molecules observed in the Interstellar Space Medium and in circumstellar shells, from the CDMS website [3]. Around 30 % of the species are free radicals or their corresponding ions, noted in bold. Species studied in this thesis are highlighted in red. Questions marks label species whose observation is ambiguous.	2
1.1	<i>IPs</i> of rare gases used in the DESIRS beamline gas filter	9
1.2	Free radical production techniques: advantages and disadvantages	16
1.3	Typical settings for the flow tube reactor	16
1.4	Two-photon rare gas transitions used in VUV laser generation <i>via</i> four-wave mixing.	19
1.5	Horiba TGM300 VUV grating characteristics.	20
1.6	Equipment characteristics on the high-resolution UV laser chain.	22
1.7	Two-photon rare gas transitions and corresponding UV generation processes. . .	23
1.8	Quantum defects of Ar Rydberg series from ref. [34]	35
1.9	Quantum defects of Kr Rydberg series from ref. [34]	36
1.10	Characteristics of VUV light sources on the Saclay Plateau	42
2.1	Summary of all known experimental photoionisation cross section measurements for free radicals	45
2.2	Summary of the photoionisation cross section determination method	51
2.3	Ionisation Potentials (<i>IP</i>) of species implicated in the OH photoionisation cross section determination of this work.	54
2.4	OH photoionisation cross section values.	58
2.5	Ionisation potentials of species implicated in the NH ₂ photoionisation cross section determination of this work.	61
2.6	NH ₂ absolute photoionisation cross section values	64
2.7	<i>m/q</i> values and <i>IPs</i> of methanol isotopomers and their flow-tube products . . .	69
2.8	Photoionisation cross section evaluation using a simple model.	77
3.1	Summary of internal coordinates of CH ₃ NCO in the three electronic states of interest extracted from the <i>ab initio</i> calculations.	81
3.2	Summary of physical properties of CH ₃ NCO	82
3.3	Peak energies ^a and assignments.	84
3.4	C ₂ and C ₂ ⁺ electronic state energies extrapolated to the CBS limit (see text) as presented in ref. [147].	89
3.5	Adiabatic ionization energies of C ₂	91
3.6	Energy differences between C ₂ and C ₂ ⁺ states.	92
3.7	Vibrational modes of CO ₂ (X) and CO ₂ ⁺ (X ⁺)	98
3.8	ΔJ branch weightings for the vibrationless X ⁺ ² $\Pi_{3/2} \leftarrow X$ ¹ Σ_g^+ transition	105
3.9	Adiabatic <i>IP</i> of CO ₂	106
3.10	ΔJ branch weightings for the vibrationless X ⁺ ² $\Pi_{1/2} \leftarrow X$ ¹ Σ_g^+ transition	106

3.11	Spin-orbit parameter of CO_2^+	107
3.12	Fit parameters for $^2\Sigma$ states of (0, 1, 0) states of CO_2^+ from ref. [159].	108
3.13	Effective parameters (in cm^{-1}) for $^2\Pi$ states of (0, 2, 0) and (1, 0, 0) states of CO_2^+ from ref. [161].	110
A.1	$\text{NH}_3(\tilde{X}^1A_1)$ photodissociation relaxation channels and their calculated thermodynamic thresholds (assuming there is no potential energy barrier) at 0 K [118]. Accessible channels whose thresholds are below 5.82 eV are separated from the others with a dashed line.	127
A.2	Ionisation Potentials of species implicated in the NH_3 photodissociation study of this work.	128
A.3	$\text{CH}_3\text{OH}(\tilde{X}^1A')$ photodissociation relaxation channels (forming fragments in their ground electronic states) and their calculated thermodynamic thresholds (assuming there is no potential energy barrier) at 0 K [118]. All products are thermodynamically accessible at 121.6 nm (10.20 eV).	133
A.4	CH_3OH branching ratios at different photolysis wavelengths (photon energies) from the literature.	134
A.5	Ionisation potentials of species implicated in the CH_3OH photodissociation study of this work.	136
B.1	Observed cationic fragments following the dissociative ionisation of CH_3NCO and corresponding measured appearance energies (E_a). These energies are compared to the thermodynamic (E_T) and theoretical thresholds (E_{th}) that sometimes account for transition states (TS).	144

List of Abbreviations

a. m. u.	atomic mass units
arb. u.	arbitrary units
CASSCF	Complete Active Space Self-Consistent Field
CBS	Complete Basis Set
COM	Complex Organic Molecule
DELICIOUS	Dichroism and ELeCtron / Ion Coincidence in IOnization Using Synchrotron
DESIRS	Dichroïsme Et Spectroscopie par Interaction avec le Rayonnement Synchrotron
FC(F)	Franck-Condon (Factor)
FT(S)	Fourier-Transform (Spectroscopy)
FWHM	Full Width at Half Maximum
IP	Ionisation Potential
IR	InfraRed
ISM	Interstellar Space Medium
ISMO	Institut des Sciences Moléculaires d'Orsay
MATI	Mass-Analysed Threshold Ionisation
MCP	Micro-Channel Plates
MRCI (+Q)	Multi-Reference Configuration Interaction (Davidson correction)
PEPICO	PhotoElectron PhotoIon COincidence
PES	PhotoElectron Spectroscopy / Spectrum
PFI	Pulsed-Field Ionisation
PIY	PhotoIon Yield
PRFI	Pulsed-Ramped-Field Ionisation
REMPI	Resonance-Enhanced MultiPhoton Ionisation
RT	Renner-Teller
SAPHIRS	Spectroscopie d'Agrégats PhotoIonisés par le Rayonnement Synchrotron
SO	Spin-Orbit
SOLEIL	Source Optimisée de Lumière d'Énergie Intermédiaire du Laboratoire pour l'utilisation du rayonnement électromagnétique
SPES	Slow PhotoElectron Spectroscopy
TOF	Time-Of-Flight
TPEPICO	Threshold PhotoElectron PhotoIon COincidence
TPES	Threshold PhotoElectron Spectroscopy / Spectrum
UV	UltraViolet
VUV	Vacuum UltraViolet
XPS	X-ray Photoelectron Spectroscopy
ZEKE	ZErO Kinetic Energy

"If I have seen further, it is by standing on the shoulders of giants"
I. Newton

To all those giants...

Introduction

It has been known since the 1920s that light-induced processes can control the abundances of molecules in Space [1]. In practically all astrophysical media, high UV and VUV (Vacuum UltraViolet) fluxes, defined by wavelengths situated between 60 and 200 nm (20 - 6 eV), irradiate molecules found therein, which cause them to fragment. In the vicinity of stars for example, there are solar fluxes whose wavelength-dependency resembles that of a 4000 K black body along with absorption and emission features due to elements in the heliosphere. In particular the Lyman- α hydrogen emission line at 121.6 nm is a dominant spectral feature in the VUV, several orders of magnitude more intense than the background black body radiation. Far away from stars and even in dark regions, there are still intense UV and VUV fluxes, in particular the Draine flux [2], also called the interstellar radiation field. This type of radiation is produced by the photoelectric emission of interstellar grains following heating by cosmic rays and other sources.

Following irradiation and absorption of a VUV photon, a number of relaxation channels are possible for the molecule, namely fragmentation, ionisation, or dissociative ionisation. These are illustrated on NH_2 in Fig. 1.

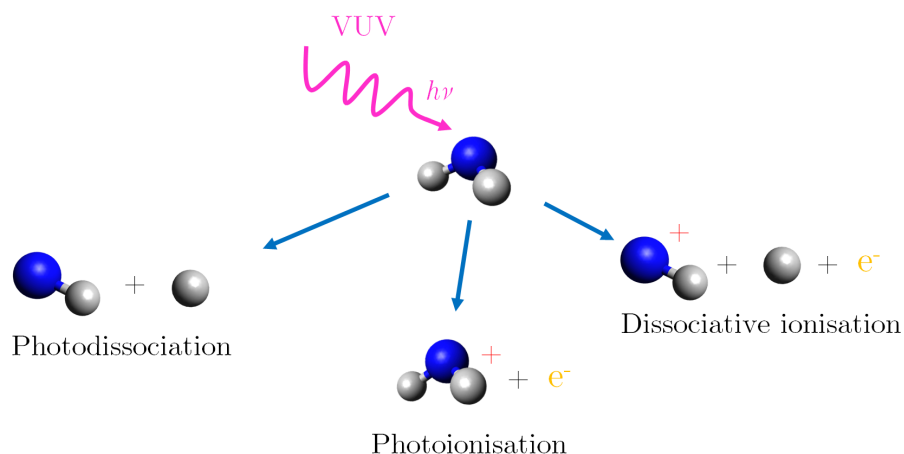


FIGURE 1: Main relaxation pathways for the amino free radical (NH_2) after absorbing a VUV photon.

As of April 2020 [3], over 200 molecules have been detected in the Interstellar Space Medium and in circumstellar shells. Even more have been found in cometary or planetary atmospheres of our solar system. The recent instrumental developments have allowed the detailed analysis of the composition of cometary environments, both of the coma and even of the surface, notably using the COSAC experiment of the Philae lander on comet 67P/Churyumov-Gerasimenko [4]. On top of identifying species and quantifying their abundance, chemical reactivities are also explored. In these cold environments, many chemical networks require the implication of photons to initiate reactivity [5].

TABLE 1: Molecules observed in the Interstellar Space Medium and in circumstellar shells, from the CDMS website [3]. Around 30 % of the species are free radicals or their corresponding ions, noted in bold. Species studied in this thesis are highlighted in red. Questions marks label species whose observation is ambiguous.

2 atoms	3 atoms	4 atoms	5 atoms	6 atoms	7 atoms
H ₂	C₃	c-C₃H	C₅	C₅H	C₆H
AlF	C₂H	l-C₃H	C₄H	l-H ₂ C ₄	CH ₂ CHCN
AlCl	C ₂ O	C ₃ N	C ₄ Si	C ₂ H ₄	CH ₃ C ₂ H
C₂	C ₂ S	C ₃ O	l-C₃H₂	CH ₃ CN	HC ₅ N
CH	CH₂	C₃S	c-C₃H₂	CH ₃ NC	CH ₃ CHO
CH⁺	HCN	C ₂ H ₂	H₂CCN	CH₃OH	CH ₃ NH ₂
CN	HCO	NH₃	CH ₄	CH ₃ SH	c-C ₂ H ₄ O
CO	HCO⁺	HCCN	HC ₃ N	HC ₃ NH ⁺	H ₂ CCHOH (?)
CO⁺	HCS⁺	HCNH ⁺	HC ₂ NC	HC ₂ CHO	C₆H⁻
CP	HOC⁺	HNCO	HCOOH	NH ₂ CHO	CH₃NCO
SiC	H ₂ O	HNCS	H ₂ CNH	C₅N	HC ₅ O
HCl	H ₂ S	HOCO ⁺	H ₂ C ₂ O	l-HC ₄ H	HOCH ₂ CN
KCl	HNC	H₂CO	H ₂ NCN	l-HC ₄ N	
NH	HNO	H ₂ CN	HNC ₃	c-H ₂ C ₃ O	
NO	MgCN	H ₂ CS	SiH ₄	H ₂ CCNH (?)	
NS	MgNC	H₃O⁺	H ₂ COH ⁺	C₅N⁻	
NaCl	N₂H⁺	c-SiC ₃	C₄H⁻	HNCHCN	
OH	N ₂ O	CH₃	HC(O)CN	SiH ₃ CN	
PN	NaCN	C₃N⁻	HNCNH	C ₅ S (?)	
SO	OCS	PH ₃	CH₃O	MgC ₄ H	
SO⁺	SO ₂	HCNO	NH ₄ ⁺		
SiN	c-SiC ₂	HOCN	H ₂ NCO ⁺		
SiO	CO₂	HSCN	NCCNH ⁺		
SiS	NH₂	H ₂ O ₂	CH ₃ Cl		
CS	H₃⁺	C₃H⁺	MgC ₃ N		
HF	SiCN	HMgNC			
HD	AlNC	HCCO			
FeO?	SiNC	CNCN			
O₂	HCP	HONO			
CF⁺	CCP	MgC ₂ H			
SiH?	AlOH				
PO	H ₂ O ⁺				
AlO	H ₂ Cl ⁺				
OH⁺	KCN				
CN⁻	FeCN				
SH⁺	HO ₂				
SH	TiO ₂				
HCl ⁺	C₂N				
TiO	Si ₂ C				
ArH ⁺	HS ₂				
N ₂	HCS				
NO⁺?	HSC				
NS⁺	NCO				
HeH ⁺	CaNC				

Table 1 continued

8 atoms	9 atoms	10 atoms	11 atoms	12 atoms	> 12 atoms
CH ₃ C ₃ N	CH ₃ C ₄ H	CH ₃ C ₅ N	HC ₉ N	c-C ₆ H ₆	C ₆₀
HC(O)OCH ₃	CH ₃ CH ₂ CN	(CH ₃) ₂ CO	CH ₃ C ₆ H	n ⁻ C ₃ H ₇ CN	C ₇₀
CH ₃ COOH	(CH ₃) ₂ O	(CH ₂ OH) ₂	C ₂ H ₅ OCHO	i-C ₃ H ₇ CN	C ₆₀ ⁺
C₇H	CH ₃ CH ₂ OH	CH ₃ CH ₂ CHO	CH ₃ OC(O)CH ₃	C ₂ H ₅ OCH ₃	c-C ₆ H ₅ CN
C ₆ H ₂	HC ₇ N	CH ₃ CHCH ₂ O			
CH ₂ OHCHO	C₈H	CH ₃ OCH ₂ OH			
l-HC ₆ H	CH ₃ C(O)NH ₂				
CH ₂ CHCHO(?)	C₈H⁻				
CH ₂ CCHCN	C ₃ H ₆				
H ₂ NCH ₂ CN	CH ₃ CH ₂ SH(?)				
CH ₃ CHNH	CH ₃ NHCHO				
CH ₃ SiH ₃	HC ₇ O				
H ₂ NC(O)NH ₂					

The 200 plus molecules detected are summarised in Table 1. As this table shows, a wide variety of species have been observed: small and large (complex molecules), neutral and charged, reactive (free radicals) and stable species. Many contain carbon so can be called organic. The nature of the molecule tells the story of the environment where it was observed and its past evolution. In a similar fashion to the molecules of Table 1, these can be very diverse ranging from cold and icy grains or dust to giant molecular clouds containing young stellar objects and hot cores.

These observations guide the laboratory experiments [6], which, in turn, yield information on the photophysics and photochemistry that can be incorporated into models to better describe the astrophysical media. Dozens of databases (*e.g.* KIDA [7], LAMBDA [8],...) collect quantitative information to be used in models. Observations, models, and laboratory-based experiments therefore form a powerful trio of tools for understanding astrophysical environments and the molecules found therein.

In the context of this PhD, the relaxation channels of astrophysically relevant molecules have been studied *via* laboratory-based experiments. The process at the heart of this work is photoionisation, which can be defined as the process by which a molecule emits an electron as a means of relaxation following the absorption of a photon. The importance of photon-induced processes for astrophysical molecules has already been noted. Photoionisation, in particular, is a means for a neutral stable molecule to become a charged ion, which is often more reactive. Even neutral but reactive species (*e.g.* free radicals) can gain in reactivity once ionised in some cases.

One of the aims of this work is to provide unprecedented quantitative data for describing photoionisation. This involves the determination of photoionisation cross sections, which relate the produced quantity of photoions to the initial quantity of neutral species. They are essential quantitative parameters to be included in models, but seldom available due to experimental difficulties. Indeed, free radicals are species that are difficult to produce in quantity and in a reliable fashion. The production of VUV radiation is non-trivial as the corresponding light sources are not commercially available. Finally, detection methods must be sensitive enough to probe the low quantities of radicals amongst much more abundant species (*e.g.* precursor molecules).

Quantitative measurements are never easy in any case and they often rely on references

or data from the literature. In addition to providing quantitative results, carefully evaluated error bars are also needed. They are essential for models using the quantitative data in order to constrain the predictions.

Other aspects of this work, in particular the use of spectroscopy, give access to other information on photoionisation processes. For example, ionisation energies are measured, which are important for determining thresholds for photoionisation; they also lead to the determination of key thermodynamic quantities such as enthalpies of formation or even bond dissociation energies when combined with other thermodynamic data. All of these quantitative parameters are essential for adequately modelling or simulating the relevant environments.

Spectroscopy also offers more qualitative information. In the VUV range, highly excited electronic neutral states, even above the ionisation threshold, and cationic states can be studied including their (ro)vibrational structure; all of which are of great fundamental interest in addition to their application value. Photoionisation also offers the means of directly producing and studying simultaneously reactive cations from a stable neutral species without having to first produce and then conduct studies in the cation.

Fundamental interest and applications in photoionisation have motivated experimental works to pursue higher and higher resolution for over 50 years. One of the first pioneers in high-resolution photoelectron spectroscopy was Nobel laureate Kai Siegbahn who used X-ray sources in the 1950s to analyse the chemical composition of the surfaces of solids (X-ray Photoelectron Spectroscopy: XPS). He then applied this technique to atomic vapours in order to determine binding energies by photoionising core electrons with accuracies of around 1 eV. Higher resolution was achieved by the use of UV or VUV sources rather than X-rays. Notably, David Turner developed the use of He lamps in the 1960s, exploiting the 21.3 eV resonance [9], giving access to sub-eV resolution when probing valence electron ionisation. Other elements in lamps were also used to exploit different resonance energies. Turner studied, for example, the first ionisation potential (*IP*) of Ar at a resolution of 0.015 eV (121 cm^{-1}) in 1967 [10]. This sort of resolution is quite sufficient to resolve the vibrational structures.

In this first method of PhotoElectron Spectroscopy (PES), the photon energy of the source is fixed. The kinetic energy of the emitted photoelectrons is analysed in order to retrieve information on the cation. In parallel to the development of this fixed-energy technique, another technique was developed in the 1960s by the group of Mark Inghram with Tomas Baer [11, 12] that used a photon source whose energy is tunable thanks to a monochromator (Hopfield-continuum source & grating). Their experiments constrain the detection of photoelectrons to those with vanishing kinetic energy, *i.e.* threshold electrons. Hence, electrons are only detected if the incident photon energy corresponds to the transition energy towards a cationic state. This technique is thus called Threshold PhotoElectron Spectroscopy (TPES) [13]. Initial resolutions were typically 0.05 to 0.04 eV, but these were improved over time to become competitive with PES techniques. A major improvement in TPES was the use of velocity map imaging, which relies on stronger extraction fields. The result was higher resolution, but also the possibility of extracting the ions instead of electrons. The next step was to detect ions and electrons in coincidence: (Threshold) PhotoElectron PhotoIon COincidence ((T)PEPICO spectroscopy), which allows the production of mass-selective photoelectron spectra [14]. Nowadays, these techniques can produce mass-selective photoelectron spectra at sub-meV (0.8 meV , 6 cm^{-1}) resolutions [15]. This technique is used extensively in this thesis to produce medium-high-resolution spectra.

With the development of tunable lasers in the 1980s, these became popular photon sources for conducting high-resolution spectroscopy, especially as the laser line width was below the

resolution of traditional UV spectrometers. Much of this work was pioneered by Mueller-Dethlefs *et al.* who used REsonant MultiPhoton Ionisation (REMPI) and also Pulsed Field Ionisation (PFI) techniques to produce spectra of around 1 cm^{-1} [16]. In order to further improve the resolution, PFI setups were coupled to narrow-bandwidth tunable VUV lasers capable of producing monochromatic VUV radiation with a bandwidth down to 0.008 cm^{-1} (10^{-6} eV) [17]. These setups were developed in the groups of Timothy Softley and then Frédéric Merkt and represent a means of accessing the highest photoelectron resolution (0.06 cm^{-1} , 7.10^{-6} eV) today [18]. This is the sort of setup that I helped develop and characterise during my PhD and will be described in full in Chapter 1; some first results were also obtained with this setup and are presented in the manuscript.

All of these developments in photoelectron spectroscopy mean that the rotational structure can now be studied in detail *via* photoionisation. The spectroscopic constants that are deduced have great fundamental value, but are also of interest to scientific areas where these cations come into play. In astrophysics for example, most molecular detections are made in the Infrared or Millimetre domain based on the assignments of pure rotational transitions. The cationic spectroscopic constants determined in VUV photoelectron spectroscopy can therefore guide the observations and assist the assignments, when pure rotational data are not available.

Although photoionisation is the main focus of this work, other relaxation pathways are possible for a molecule following the absorption of a VUV photon (see Fig. 1), namely photodissociation (the formation of neutral fragments) and dissociative ionisation (the formation of a charged and neutral fragments or, in some cases, the production of an ion pair cation / anion). Again in an astrophysical context, these relaxation processes are ways of forming reactive species from stable species, which go on to react to form more complex molecules.

This manuscript is split into three chapters:

- Chapter 1 details the experimental setups used to study the VUV photoionisation of astrophysical molecules. Two setups are distinguished. The first is the DELICIOUS 3 spectrometer of the DESIRS beamline at synchrotron SOLEIL. The second is the new VULCAIM laboratory setup of ISMO featuring a new high-resolution VUV laser, which was developed during my PhD. The experimental development and characterisation of this new setup are described in this chapter. The experimental techniques used in both setups are explained. Finally, comparisons are drawn between both setups to highlight their complementarity.
- Chapter 2 focuses on the relative and absolute photoionisation cross sections of free radicals (OH, NH₂, and methanol-derived isotopologues) recorded at SOLEIL.
- Chapter 3 presents photoelectron spectroscopy results. The medium high-resolution photoelectron spectroscopy of CH₃NCO and C₂, obtained using the SOLEIL setup, are discussed first of all. The second part of this chapter is dedicated to the first high-resolution results of VULCAIM using PFI-ZEKE spectroscopy. Finally, this chapter describes a promising imaging technique that has the capability of recording high-resolution spectra with a high signal-to-noise ratio in a fraction of the time of that used in traditional PFI-ZEKE spectroscopy.

In order to ensure constant coherence throughout the three chapters of the manuscript, focusing on photoionisation, I chose to present in the appendices the work I performed on the other relaxation channels consecutive to a VUV photoexcitation:

- Appendix A describes exploratory works on the photodissociation of NH₃ and CH₃OH using the laboratory setup adapted for a pump-probe study.

- Appendix B extends the photoionisation study of CH_3NCO presented in chapter 3 to higher energies to study dissociative ionisation.

In addition, Appendix C lists my publication records as co-author. Conclusions and perspectives are given at the end of each main section. These are summarised and generalised in a final conclusion.

Chapter 1

Experimental tools

In this chapter, I will present the two main experimental setups of this work. Both use a VUV light source to probe molecules of astrophysical interest in the gas phase:

- The first is a synchrotron-based experiment and will be described in the first section.
- The second is a laboratory setup based around a high-resolution VUV laser as described in the second section of this chapter. It constitutes a unique laser setup to France and there are only two others in Europe, and to our knowledge the world, one at Vrije Universiteit Amsterdam in the team of Wim Ubachs and one at ETH Zurich in the team of Frédéric Merkt.

As the synchrotron setup has been outlined in previous works, only a brief overview will be given here with an emphasis on the specificities of its use in the context of this work. As the VUV laser setup is very recent and was developed during this PhD, a more in-depth presentation will describe its various elements and characteristics.

A final section will stress the importance and complementarity of these two experiments.

1.1 Synchrotron SOLEIL

1.1.1 The SOLEIL synchrotron facility

A synchrotron is a cyclic particle accelerator. Once accelerated and injected into the storage ring, particles are deviated by magnetic fields to maintain the cyclic trajectory. Associated to the University of Paris-Saclay is the French synchrotron facility SOLEIL (Source Optimisée de Lumière d'Énergie Intermédiaire du Laboratoire pour l'utilisation du rayonnement électromagnétique).

As pictured in Fig. 1.1, SOLEIL's ring, measuring 354 m in circumference, contains several packets of electrons travelling with an energy of 2.75 GeV at almost the speed of light [19]. It takes just 1.2 μs for an electron to complete a lap of the ring. Given the extremely high repetition rate, it is therefore a good approximation to consider this light source continuous.

A closer look at SOLEIL's ring reveals that it is not exactly a circle, but rather a 24-sided polygon made up of straight sections and small bends. In 1st and 2nd generation synchrotrons used bending magnets to accelerate electrons around the bends causing the emission of radiation known as *Bremsstrahlung* or synchrotron radiation. On 3rd generation rings, such as SOLEIL, insertion devices (undulatory or wigglers) are used instead of bending magnets, which produce a sinusoidal magnetic field. This field, *via* the Laplace force, puts the electron on a sinusoidal trajectory. Radiation is then emitted at each wiggle. The successive emissions interfere (enhanced coherence), leading to a discrete spectrum (fundamental plus harmonics). The resulting radiation is much more brilliant than bending magnet emission, by a factor N^2 where N is the

- ① : Electron accelerator
- ② : Booster
- ③ : Storage ring
- ④ : Undulator
- ⑤ : Radiofrequency cavity
- ⑥ : Storage ring
- ⑦ : Beamline

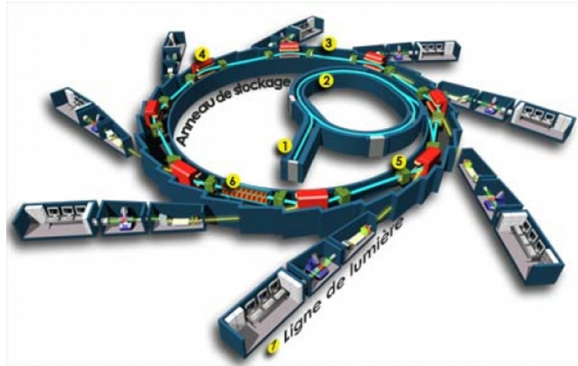


FIGURE 1.1: Schematic layout of the Synchrotron SOLEIL [19] along with its various components.

number of periods of the undulator. The position of the resonant emission wavelength can be tuned by varying the magnetic fields seen by the electron beam, controlled by the intensity of electric current fed through the electromagnetic undulator. Even on a given beamline, the undulator is tuned to produce photons at various energies. In the context of this work, we used the DESIRS beamline whose undulator produces synchrotron radiation in the VUV range (6 to 40 eV). The spectral width for the produced radiation is around 7%. If need be, this radiation can then be monochromatised using a VUV grating.

1.1.2 The DESIRS beamline

The DESIRS beamline (Dichroïsme Et Spectroscopie par Interaction avec le Rayonnement Synchrotron) is easily tuned over the VUV range at medium high resolution (down to 1 meV) [20]. It is well adapted for photoionisation studies and medium high resolution spectroscopy studies presented in this work.

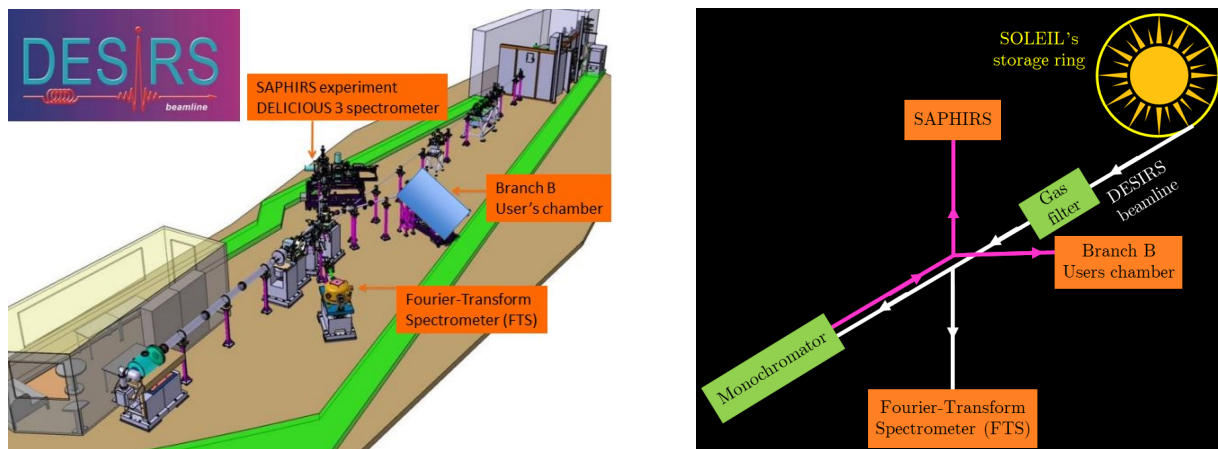


FIGURE 1.2: Left: layout of the DESIRS beamline displaying its various components and branches, adapted from ref. [19]. Right: simplified layout of the DESIRS beamline as seen from above;

A common white-light (spectral width: ≈ 1.5 eV) branch leads the synchrotron radiation towards the three branches of the beamline (see Fig. 1.2). A gas filter is placed on this common branch in order to cut high harmonics generated by the undulator (see Fig. 1.2). The principle behind this filter is to use rare gases (Kr, Ar,...) which will absorb any photons whose energy is above their first ionisation potentials (*IPs*), see Table 1.1. Below their *IPs*, rare gases can also

TABLE 1.1: *IPs* of rare gases used in the DESIRS beamline gas filter

Rare Gas	Xe	Kr	Ar	Ne
<i>IP</i> ^a / eV	12.12987	13.99961	15.759	21.56454

^a Data from NIST [21]

absorb at discrete energies corresponding to atomic transitions thus producing absorption lines in the final spectra. These lines can be used to calibrate the photon energy scale to within around 2 meV.

Downstream from the gas filter, the beam is fed into one of three branches as pictured in Fig. 1.2:

- a monochromatised branch containing the SAPHIRS (Spectroscopie d’Agrégats PhotoIonisés par le Rayonnement Synchrotron) molecular beam chamber where most studies conducted in this work were carried out (see following paragraphs),
- a second monochromatised branch where users can attach their own chambers, not used in this work, and
- a non-monochromatised branch leading to the VUV Fourier-Transform Spectrometer (FTS) [22].

Before entering the interaction chamber on the SAPHIRS branch, a calibrated photodiode (AXUV100, IRD) can be inserted in the path of the beam which allows the measurement of photon flux. Whilst accounting for the calibrated photodiode response function, the produced electric current from this device is proportionate to the incident photon flux. Dividing signals by the photodiode signal enables photon flux fluctuation corrections. VUV generation by the undulator is wavelength-dependent and the flux can also be modified by beamline optics (grating, mirrors, *etc.*) so this correction is important in order to guarantee reliable relative intensities over the whole scan range.

1.1.3 SAPHIRS

In the context of the synchrotron experiments conducted in this thesis, most work was carried out on the monochromatised branch containing the SAPHIRS molecular beam chamber pictured in Fig. 1.3. It is basically made up of two chambers: the first contains the molecular jet and potentially the flow tube reactor described later (see paragraph 1.1.3). The molecular beam is generally twice skimmed before arriving in the interaction chamber containing the DELICIOUS 3 (Dichroism and ELection/Ion Coincidence in IONization Using Synchrotron) spectrometer. Between the two skimmers is a differential pumping stage allowing the pressure to go from ≈ 1 mbar in the reactor to $\approx 5 \times 10^{-8}$ mbar in the interaction chamber with a typical intermediary pressure of $\approx 3 \times 10^{-4}$ mbar. In the interaction chamber, the molecular beam is irradiated by the synchrotron radiation thus inducing photoionisation or even dissociative ionisation at yet higher photon energies.

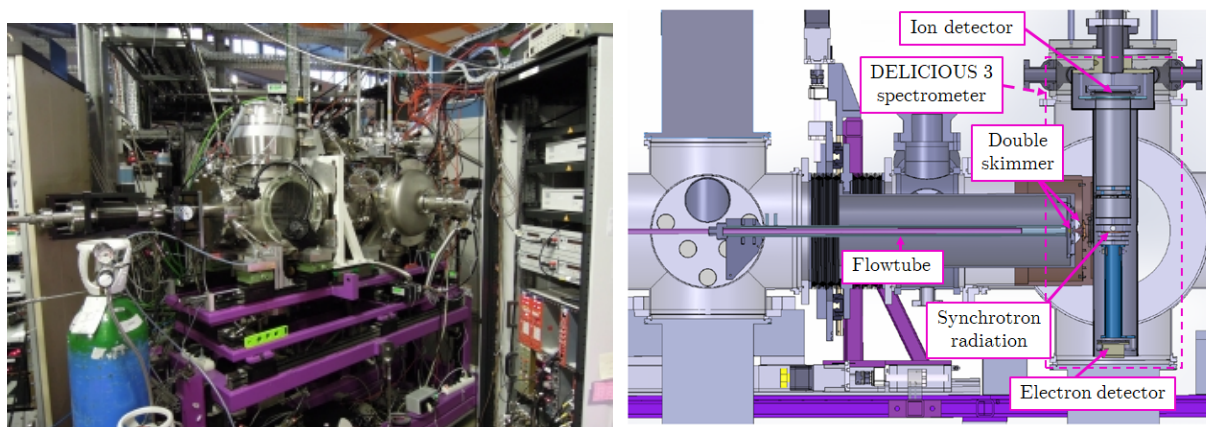


FIGURE 1.3: Left: photo of the SAPHIRS molecular beam chamber. Right: Technical layout of the SAPHIRS molecular beam chamber containing the flow-tube reactor and the DELICIOUS 3 spectrometer adapted from ref. [23]

The DELICIOUS 3 spectrometer

In the interaction chamber, the application of extraction voltages to electrodes in the interaction zone sends produced ions and electrons to their relevant detectors. All produced charged particles are simultaneously detected by the double imaging electron/ion coincidence spectrometer as illustrated in Figs. 1.3 and 1.4. This versatile experimental setup can be used in various manners in order to use different data analysis techniques, each yielding a different type of spectrum. The spectrometer, along with its various modes, are presented in full by Garcia *et al.* [24] and Tang *et al.* [25].

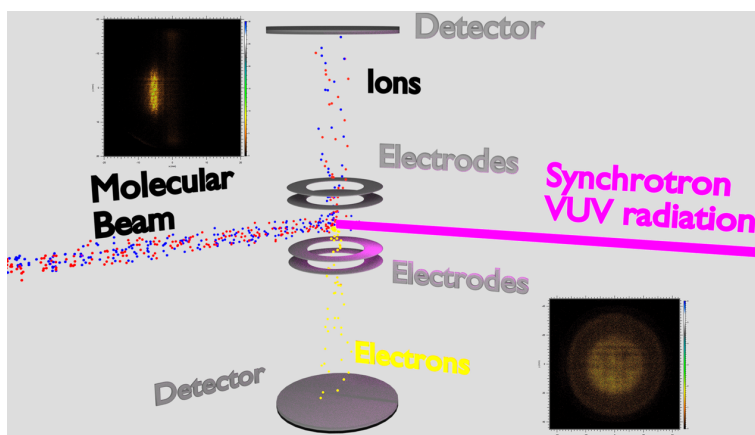


FIGURE 1.4: Illustration of the DELICIOUS 3 spectrometer. Added are example images of electrons (bottom) and ions (top).

Coupling a Velocity-Map-Imaging spectrometer (VMI) used to picture electron kinetic energy to a Wiley-McLaren Time Of Flight 3D momentum imaging ion spectrometer, both electrons and ions are detected in coincidence which enables ion mass selectivity. As each electron hits the detector, this starts a clock against which can be recorded the arrival time of ions. Statistically, unless the incident ion originates from the same neutral molecule as the electron, the time at which it hits the detector is random. This hit is accounted for, but only contributes to

random noise in the mass spectra. However, if the ion and the electron originate from the same initial molecule, the time between the arrival of the electron and ion will consistently recur for all fragments of that mass over charge (m/q) thus producing a signal in the mass spectrum.

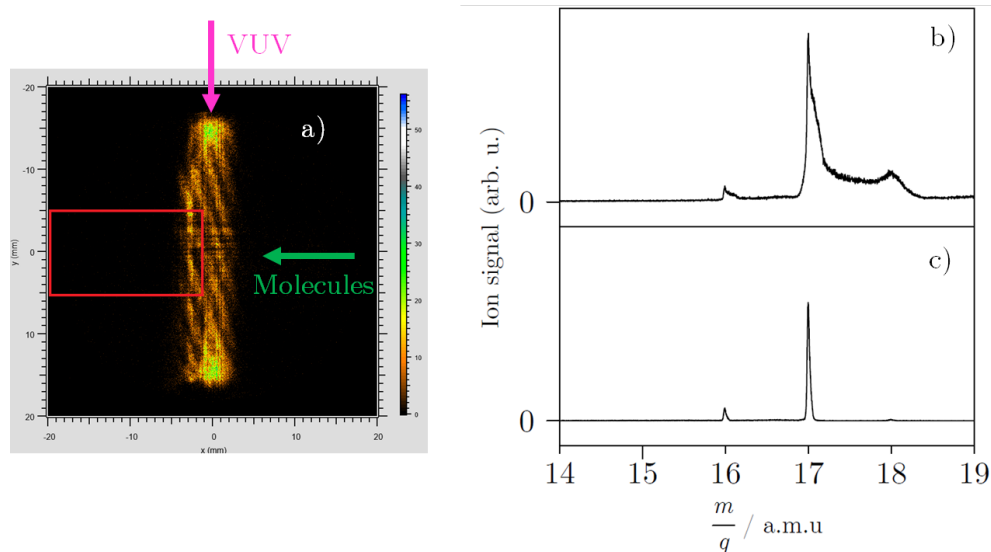


FIGURE 1.5: Example of ion image treatment. a) Ion image on detector with red rectangle showing region of interest with ions originating from the molecular beam. b) Raw mass spectrum constructed using all ions in ion image a). c) Same mass spectrum with ion contributions reduced to region of interest in ion image c).

In order to improve the mass spectrum resolution, ion images can also be reduced to regions of interest only containing ions from the molecular beam (see Fig. 1.5). This eliminates, in particular, contributions from thermal species present in the experiment and whose velocity distributions are much larger than those contained in the beam and thus widen the mass peaks in the spectra (see Fig. 1.5 b) and c)).

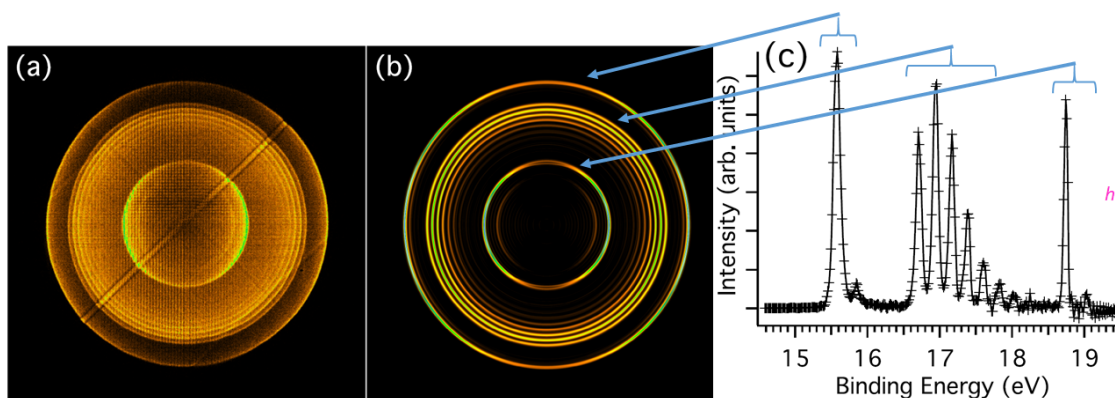


FIGURE 1.6: Example of electron image treatment for N_2 photoionisation adapted from ref. [25]. a) Mass-selected (from N_2) raw electron image on detector for a photon energy of 19.5 eV and a repeller voltage set to 750 V. b) Inverted electron image. c) Corresponding mass-selected PES with blue arrows linking spectral features to areas in the image b).

On top of the ion image treatments, the electron images can be treated in various ways to gain access to different information. Thanks to the ion mass selectivity and the electron-ion coincidence detection, electron images can be reduced to electron contributions from a given neutral parent mass. It is then possible to construct **mass-selective photoelectron spectra**, unlike the case of conventional photoelectron spectroscopy (PES). An example of electron image is given in Fig. 1.6 for a fixed photon energy of 19.5 eV, the electrons are extracted using a 750 V repeller voltage.

Extraction fields project the 3D-emitted electrons onto the 2D surface of the detector. As described in ref. [25], an Abel inversion algorithm is performed on the raw electron image to make sense of the 3D nature of photoionisation from the 2D image on the detector. The inverted image presents concentric circles; each circle is made up of electrons carrying the same kinetic energy. The greater the circle's radius, the higher the corresponding kinetic energy of those electrons. This means that these electrons are issued from lower energy states compared to the photon energy and make up the energy difference by carrying more kinetic energy. From the inverted image, it is possible to produce a PhotoElectron Spectrum (PES). As shown in Fig. 1.6, spectral features in the PES can be related to the concentric circles of the inverted image.

By scanning the photon energy and producing electron images at each step in the scan, photoelectron matrices can be produced. These 3D representations show electron kinetic energy as a function of photon energy with the number of electron counts as the third dimension. For a photoelectron stemming from a cationic state at energy E_0 , produced at photon energy $h\nu$ and whose kinetic energy is noted E_K , the three characteristic energies are linked in equation (1.1):

$$E_K = h\nu - E_0 \quad (1.1)$$

Note in this equation that photoelectrons whose kinetic energy is vanishing are produced by photons whose energy is close to that of a cationic state.

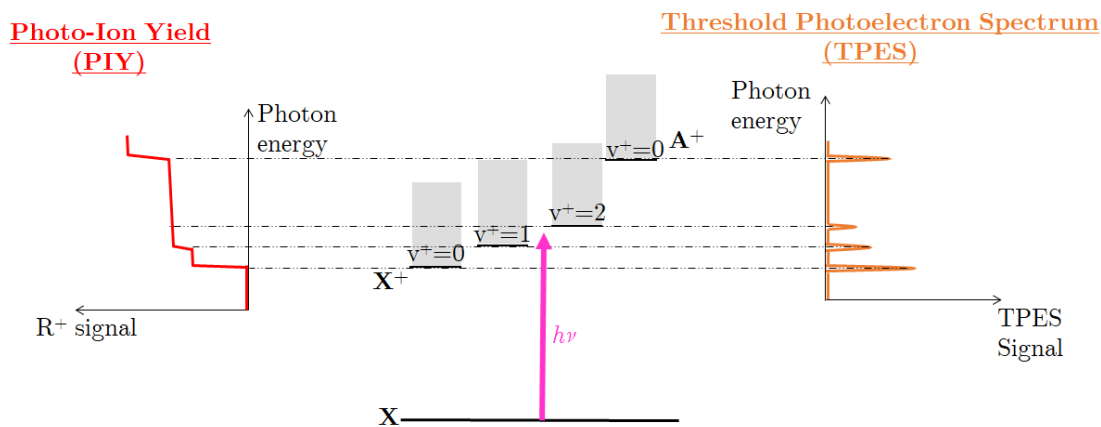


FIGURE 1.7: Photo-Ion Yield and Threshold Photoelectron Spectrum principle demonstrated on $R + h\nu \rightarrow R^+ + e^-$ reaction. If the photon energy $h\nu$ is equal or greater than the energy of the cationic vibronic state, photoelectrons can be issued from that state along with photo-ions. As $h\nu$ increases, higher energy cationic states are reached producing yet more electrons and ions. This access to states manifests itself by the appearance of steps in the photo-ion yield. Photoelectrons whose kinetic energies are vanishing are recorded in the Threshold Photoelectron Spectrum for photon energies close to those of cationic states.

In the context of photoionisation cross section measurements (see chapter 2), a relative photo-ion yield must first be recorded (see Fig. 1.7). An ion yield is the recording on a relative scale of the signal of a given ion as a function of the incident photon energy. At this end, the DELICIOUS 3 spectrometer is used in PEPICO (PhotoElectron PhotoIon COincidence) mode where contributions from all electrons across the whole scan range are recorded. This means applying high repeller voltages to the electrodes to not miss any electrons. The issue is with fast electrons which are ionised from states well below the photon energy and which carry the excess energy as kinetic energy. These hot electrons require greater repeller voltages to direct them towards the detector. For photoion yields, the resulting resolution is that of the photons only.

All spectroscopic information on cationic states is contained in threshold electrons, *i.e.* electrons whose kinetic energy is near-zero. This is why the TPEPICO (Threshold PhotoElectron PhotoIon COincidence) mode is used for spectroscopy studies, which only uses threshold electrons for which much lower repeller voltages are used (see Fig. 1.7); the result is a Threshold PhotoElectron Spectrum (TPES) for which the spectral resolution depends on both that of the photons and the photoelectrons. Generally, lower signals are achieved in this threshold technique owing to fewer electrons hitting the detector. In order to improve the signal-to-noise ratio, slow electrons can also be taken into account in the spectroscopy studies, at increasing loss in photoelectron resolution as faster and faster electrons are used. This deterioration is caused by the fact that faster electrons from a given state are shifted according to equation (1.1) and visualised in the diagonals of Fig. 1.8 a); their consideration therefore widens, even shifts, peaks in the spectra.

The answer is to right the diagonals by rotating the raw PES matrix and then integrate faster electron signals. This method is called Slow PhotoElectron Spectroscopy (SPES) [26] (see Fig. 1.8 b), d) and f)). The diagonal shift in energy is no longer a limiting factor for resolution loss, but only the loss due to spherical aberrations in the electrostatic lens. Such lenses are a common feature in VMI and are used to focus ions onto the detector. Spherical aberrations in these lenses, larger for off-axis particles (*i.e.* faster particles) are known to introduce resolution losses [27].

Both methods are described in Fig. 1.8 for the case of CH_3NCO , which was investigated during this PhD. Both display tradeoffs between noise and resolution, but SPES ultimately does generally offer better signal-to-noise ratios for a given resolution.

A phenomenon called autoionisation can present itself in such photoionisation studies. Such a process denotes the promotion of an electron to a highly excited neutral state, often a Rydberg state situated above the first IP ($E_{\text{Ryd.}} > IP$), which then ionises towards a cationic state at equal or lower energy ($E_{\text{cat.}} \leq E_{\text{Ryd.}}$), as illustrated in Fig. 1.9. If the neutral and cationic states have different energies ($E_{\text{cat.}} < E_{\text{Ryd.}}$), the energy difference is carried in the electron as kinetic energy; this process is called non-resonant autoionisation. If the highly excited neutral state is at the same energy as a cationic state to which it relaxes ($E_{\text{cat.}} = E_{\text{Ryd.}}$), the process is called resonant autoionisation; the ensuing photoelectron does not carry any kinetic energy.

Both types of autoionisation lead to resonances in the ion yield, but only resonant autoionisation appears in a TPES as the produced electron does have vanishing kinetic energy. In this case, threshold electrons from highly excited neutral states add to those from cationic states which enhances line intensities in the spectra. This is illustrated by the enlargement of the $\text{X}^+(v^+ = 2)$ resonance in the TPES of Fig. 1.9 in the presence of autoionisation compared with that of Fig. 1.7. The rotation of PES matrices is not advised if autoionisation is dominant as the autoionisation vertical lines, once rotated, are simply moved by an unmeaningful quantity and their x -axis projections therefore do not correspond to any relevant photon energies.

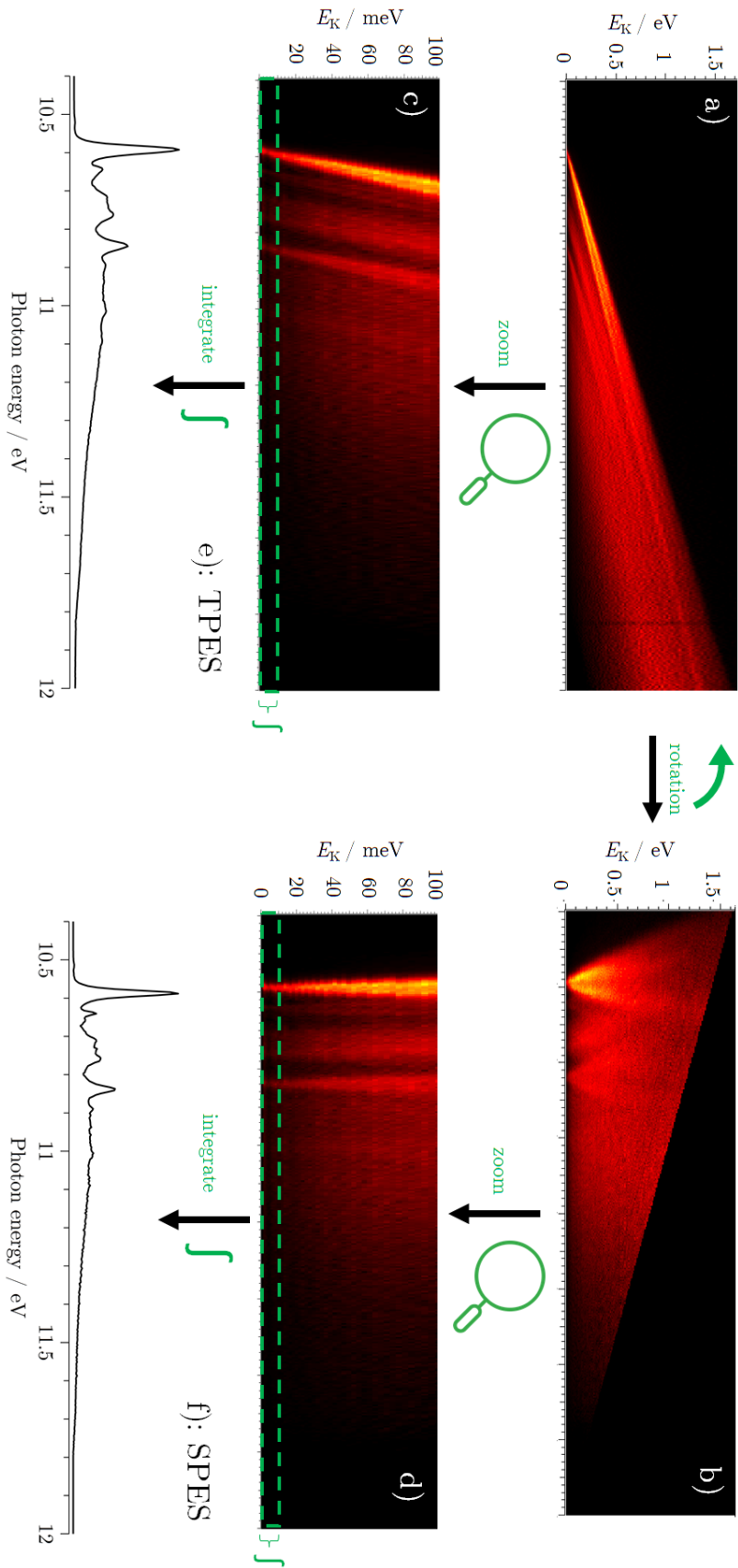


FIGURE 1.8: a) Raw PES matrix of CH_3NCO between 10.4 and 12 eV with a 300 V repeller voltage. b) Rotated PES matrix to make diagonal lines vertical. c) Zoom on non-rotated PES matrix to visualise slow electrons. d) Zoom on rotated PES matrix to visualise slow electrons. e) TPES: Integration of electron counts in non-rotated PES matrix for electrons slower than 0.01 eV represented by a thin dashed box in c) and \int symbol. f) SPES: Integration of electron counts in rotated PES matrix for electrons slower than 0.01 eV represented by a thin dashed box in d) and \int symbol. Comparing e) and f), using the same electrons, the rotation in the SPES treatment offers the better compromise between signal-to-noise and resolution compared to TPES.

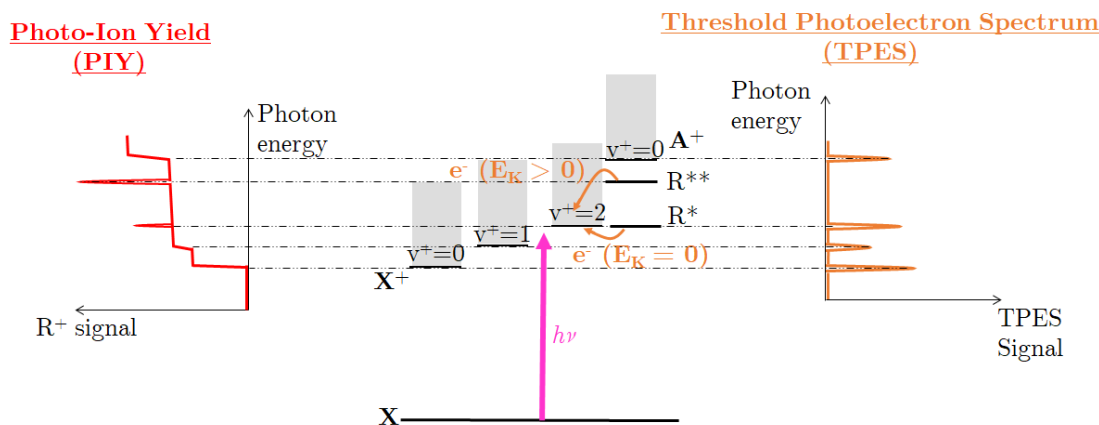


FIGURE 1.9: Photo-Ion Yield and Threshold PhotoElectron Spectroscopy principle demonstrated on $R + h\nu \rightarrow R^+ + e^-$ as in Fig. 1.7, but with autoionisation. R^* and R^{**} are neutral states situated above the first IP and are respectively resonant and non-resonant with cationic states. Autoionisation leads to resonances in the ion yield and enhances peaks in the TPES if resonant.

Molecular samples

The molecular sample can be constituted of a supersonic or effusive jet, the advantage of a supersonic jet being that it cools molecules down to lower rotational temperatures. An effusive jet does not cool down the molecules as much, but consumes less of the sample which is useful when working with small quantities. It is preferable to work with smaller samples if they are dangerous or are hard to synthesize in vast quantities. The use of an effusive jet modifies the setup presented in Fig. 1.3 as the sample is injected *via* a needle close to the interaction area, but from the other side of the vacuum chamber.

When working with gaseous stable species, a gas cylinder can be connected to the setup. On entering the setup, the sample is seeded in a rare gas using a mass-flow controller before entering the experiment. In the case of a stable liquid, a vial can be connected to the setup and used in the same way as with a gas sample if the vapour pressure is high enough. Alternatively, a rare gas can be bubbled through the sample to increase the amount arriving in the experiment. To a certain degree, we are able to control the vapour pressure by controlling the sample temperature using a chiller, the vapour pressure increasing with temperature. All samples used in this PhD work were commercially available except for CH_3NCO which was synthesized by Jean-Claude Guillemin of Rennes University.

In an astrophysical context, but also from a fundamental point of view, more work is needed on unstable species, notably free radicals. In order to further our understanding of such species, free radicals feature as the object of study at various points in this work. As they cannot be stored, they must be produced *in situ*, within the experiment. This can be achieved using a number of techniques, each presenting advantages and disadvantages as shown in Table 1.2.

During this thesis, this was achieved by using a flow tube reactor (see Fig. 1.10) designed by Jean-Christophe Loison from Bordeaux University and the DESIRS beamline scientists in the framework of the SYNCHROKIN ANR contract. The reactor, based on F-reactivity, is used as it offers the optimal compromise between selectivity and free-radical productivity. It is made up of two concentric tubes, the outer is fixed containing the reactor and the inner, referred to as injector, is mobile through which is fed the precursor. A third tube feeds F atoms into the

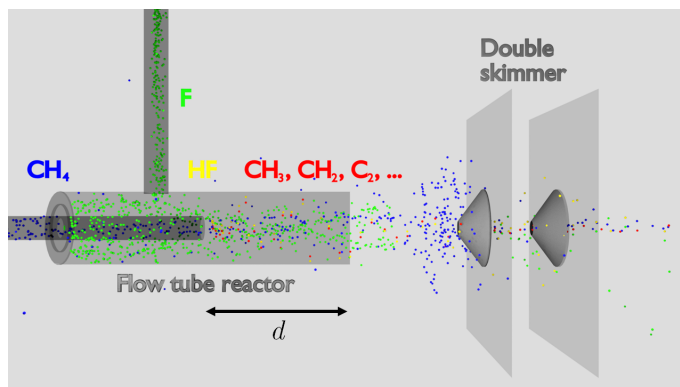


FIGURE 1.10: Schematic of the flowtube reactor where H-abstraction of CH_4 by F atoms produces CH_3 , CH_2 , etc. The injector distance is noted d ; d can be tuned to adjust conditions within the reactor.

TABLE 1.2: Free radical production techniques: advantages and disadvantages

Technique	Advantages	Disadvantages
Pyrolysis	High productivity	High production temperature Bond specificity
Photolysis	Internal energy selectivity	Low productivity Need for a laser
Discharge	High productivity	Lack of selectivity
F-reactivity	High productivity High selectivity (tunability)	Reactivity limitations

reactor. The principle behind the flow tube is to inject a hydrogen-bearing stable species (seeded in He) which will encounter F atoms issued from F_2 (seeded in He) dissociated upstream in a microwave discharge. F atoms react with the stable species along an H-abstraction reaction producing free radicals. The products of the reactor are probed by mass spectrometry after ionisation by synchrotron radiation, the means of conducting this spectrometry are detailed in the following section. The example given in Fig. 1.10 uses CH_4 which acted as a precursor to produce CH_3 , CH_2 , etc.

TABLE 1.3: Typical settings for the flow tube reactor

d distance range	10 - 60 mm
typical microwave discharge power	100 - 150 W
typical flow rate	1000 sccm
typical reactor pressure	1.6 mbar
typical free radical density	$10^{11} - 10^{13}$ molecules. cm^{-3}

A typical mass spectrum shows in Fig. 1.11 the wide variety of produced free radicals. It is obtained by summing all mass spectra recorded between 12.4 and 13.6 eV and by using CH_4 as a precursor. The large number of species in the mass spectrum is the result of complex chemical

reactions taking place in the reactor. Given the low energy range of the mass spectra, the signals most probably result from direct ionisation rather than dissociative ionisation.

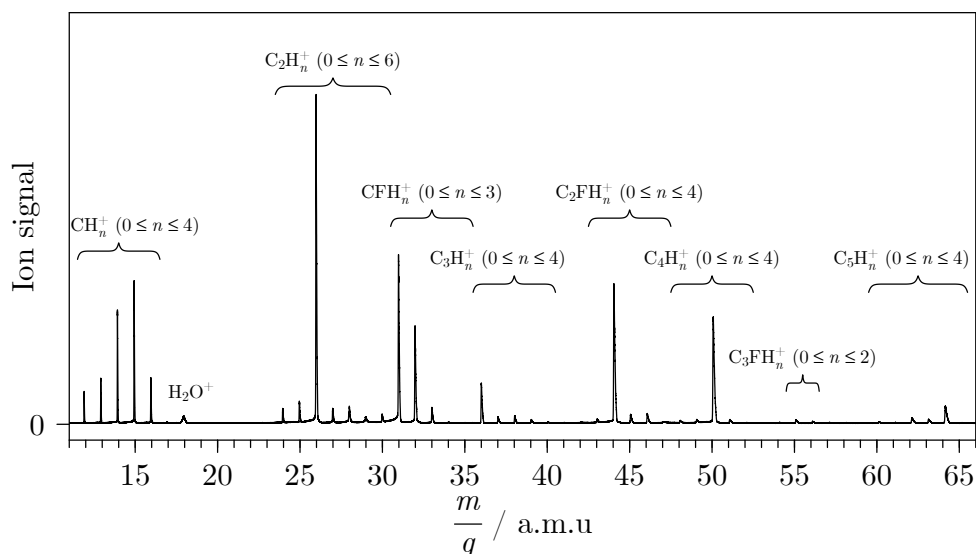


FIGURE 1.11: Typical mass spectrum obtained by summing all mass spectra recorded between 12.4 and 13.6 eV when using CH_4 as a precursor during the experiments on C_2 (see section 3.1.2).

The adjustment of experimental conditions such as gas flows or injector distance d can prioritise a given reaction while reducing or even eliminating other potentially parasitic reactions (double H-abstraction, radical-radical reactions,...) if only one reaction is intended or if the production of a large number of species is the aim. The basic idea is the increase of the F_2 flow increases the initial radical production and the longer the injector distance, the more time there is for radicals to react with each other. Increasing radical production would be desired, but there has to be a balance as increasing radical production can favour radical-radical reactions and F-addition for high F_2 flows, all of which are undesirable if only one reaction is intended. Table 1.3 summarises typical settings for the flow tube parameters.

1.2 VUV laser setup

Accelerating electrons around bends is not the only way of producing VUV radiation. A complementary VUV light source to the DESIRS beamline is the new high-resolution VUV laser setup at ISMO which uses non-linear optical processes to generate VUV radiation. This laser setup was developed and installed in 2018 and its coupling to a new vacuum experiment was finalised in 2019 as presented in Fig. 1.12. After having recalled the means of generating VUV laser radiation through four-wave mixing, I will present the various elements of this setup: the UV light sources (including the high-resolution UV laser chain), visible sources, the vacuum experimental setup containing VUV generation and spectral-purification stages, and ways the VUV laser radiation can probe relaxation processes in molecules, mainly photoionisation. Special care was taken to characterise the novel VUV laser radiation during my PhD.

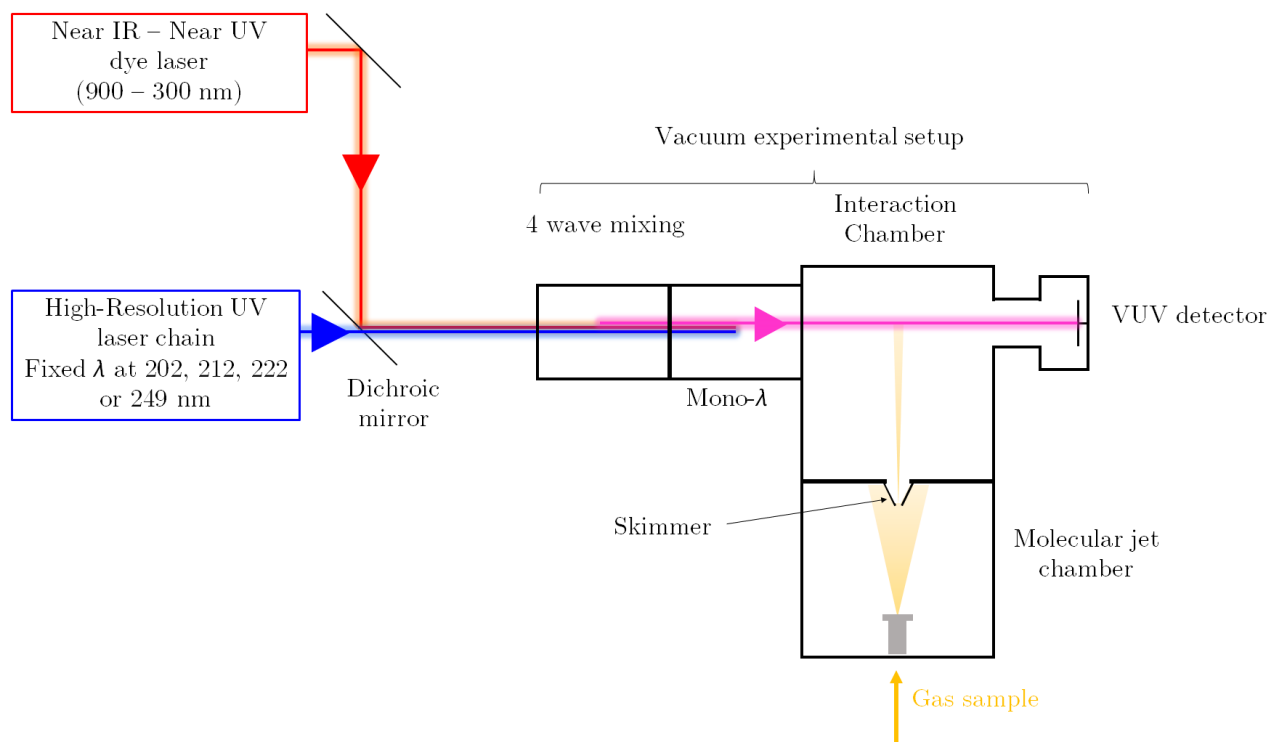


FIGURE 1.12: Rough general layout of the laboratory-based high-resolution VUV laser setup at ISMO.

1.2.1 VUV laser production

VUV lasers are not commercially available, they have to be built using commercially-available visible lasers and the VUV range can be reached *via* non-linear optical processes in rare gases (Kr or Xe), namely four-wave mixing, as pictured in Fig. 1.13.

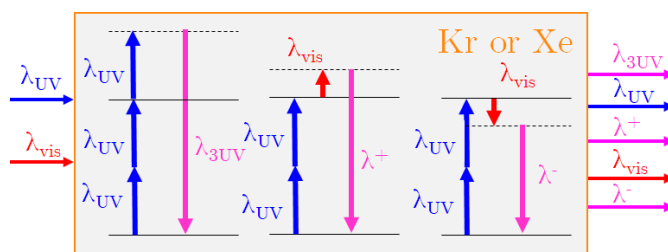


FIGURE 1.13: Four-wave mixing resonant scheme combining UV and visible radiation in rare gas. Dashed lines represent virtual states in the rare gas; full lines represent actual states in the rare gas that are exploited as resonances.

Such non-linear processes can be enhanced by using atomic resonances in the aim of improving efficiencies. In the case of non-resonant VUV generation *via* four-wave mixing, typical production efficiencies are of the order of 10^{-6} , but these can be improved to reach around 10^{-4} with the help of atomic resonances [28]. In our case, the UV photon energy (corresponding to a wavelength λ_{UV} in Fig. 1.13) is tuned to be in a two-photon resonance with an excited state from the ground state of a rare gas (Kr or Xe); the forbidden single-photon transition prevents this excited state fluorescing back to the ground state. Once in the excited state, a 3rd photon

is used to reach a virtual state before relaxing to the ground state by emission of a VUV photon. This 3rd photon could be the same UV photon as used previously to reach the excited state (case of third-harmonic generation). In this case, to be at resonance, the UV photon energy is determined by half the energy of the two-photon transition.

Alternatively, a different colour photon can be used, in particular a photon whose energy is tunable (from a dye laser in our case, corresponding to λ_{vis}). This enables tunability in the VUV spectral domain (λ^+ or λ^- of Fig. 1.13). This can be done by selecting various two-photon resonances in rare gases (see Table 1.4) by adjusting the photon energy of the UV photon. Once a resonance has been selected, the tuning of λ_{vis} allows the continuous tuning of λ^+ or λ^- over a certain range (limited by the dye curve of λ_{vis} in our case)

TABLE 1.4: Two-photon rare gas transitions used in VUV laser generation *via* four-wave mixing.

Resonance*	Rare Gas	Two-photon transition	Wavenumber ($2\tilde{\nu}_{\text{UV}}$) / cm^{-1}
Kr(1)	Kr [29]	$(4p)^6\ ^1S_0 \rightarrow (4p)^55p[1/2]_0$	94 092.86
Kr(2)	Kr [29]	$(4p)^6\ ^1S_0 \rightarrow (4p)^55p'[1/2]_0$	98 855.06
Xe(1)	Xe [30]	$(5p)^6\ ^1S_0 \rightarrow (5p)^56p[1/2]_0$	80 118.96
Xe(2)	Xe [30]	$(5p)^6\ ^1S_0 \rightarrow (5p)^56p'[1/2]_0$	89 860.02

* Referred to in Fig. 1.22.

In order to improve VUV efficiencies, Ar can be mixed with Kr or Xe to improve the phase-matching. Total and relative pressures can be adjusted to optimise the final VUV intensity. From one wavelength to another, optimal pressure conditions can substantially vary especially for non-resonant four-wave mixing. This significantly reduces the scan range in the non-resonant case.

1.2.2 Implementation of VUV laser production

In practice and due to the need for tunability in order to undertake photon energy studies by scanning the laser wavelength, the resonant four-wave mixing scheme was mostly implemented in the context of this work. Non-resonant fixed-energy four-wave mixing was only used in pump-probe studies (see appendix A).

The four-wave mixing scheme of Fig. 1.13 can be realised in a rare gas cell (see appendix A) or in a free jet. Most of the time a free jet was used during this PhD as it does not impose spectral limitations present in the case of gas cells due to the transmission range of cell windows. As illustrated in Fig. 1.14, the rare gas acting as a medium for the non-linear processes is firstly freely expanded through a gas nozzle (either General Valve or Amsterdam Piezo Valve). The gas nozzles are pulsed and synchronised with the laser pulses which limits the consumption of rare (and expensive) gases. The General Valve has a pulse time of about 100 - 200 μs whereas the Amsterdam Piezo Valve has a pulse time of just a few tens of μs . Both are backed by a pressure of a few bar. The pressure conditions in the rare-gas jet are varied by changing the release time of the gas; the VUV radiation is therefore generated at different points in the jet and therefore in different pressure and density conditions. The release time is tuned to optimise the VUV signal on the detector.

Using the notations for optics as defined in Fig. 1.12, the incident UV and visible lasers are superimposed using a dichroic mirror, both laser beams are then focused just beneath the gas

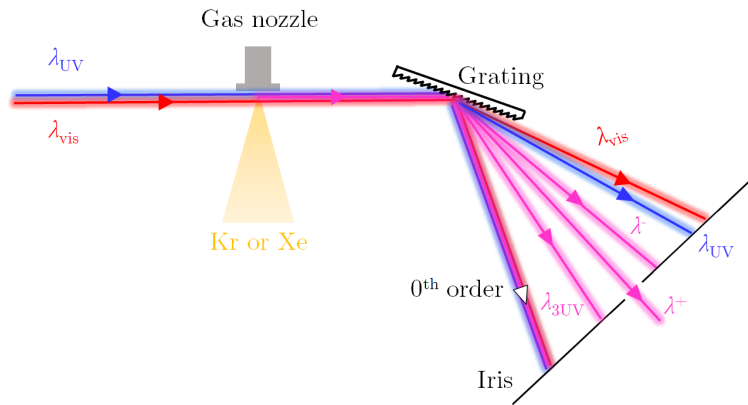


FIGURE 1.14: Implementation of four-wave mixing scheme in a freely expanded rare gas used to generate tunable VUV radiation. Reflective VUV grating selects the intended wavelength for the study to pass through the 1 to 2 mm in diameter iris. Only 0th and 1st order components from the grating are presented.

nozzle using lens L_3 . In order to compensate the longer focal distance of the visible radiation compared to that of the UV, a telescope is inserted on the path of the visible radiation. This telescope is composed of one divergent (L_1) and one convergent (L_2) lens, the distance between the two being adjusted to ensure both the visible and UV lasers focus on the same point just below the gas nozzle. Following the gas nozzle, all VUV wavelengths of Fig. 1.13 and the initial UV and visible wavelengths propagate. In order to select one unique VUV wavelength intended for the experiment, a monochromator is needed.

TABLE 1.5: Horiba TGM300 VUV grating characteristics.

deviation angle	142°
spectral domain	50 - 300 nm
grooves / mm	275 gr/mm
focal distance	319.9 mm

Except for pump-probe studies (see appendix A), the monochromator consists of a VUV grating coupled to a small iris. In our case, a TGM300 VUV reflective diffraction grating by Horiba is used to disperse the polychromatic light [31], its main characteristics are summarised in Table 1.5. Master VUV gratings are generally made out of Pt- or Au-coated glass, but in our case a replica (Pt coated epoxy resin) was used. Replicas are not able to handle high photon fluxes, but in the case of VUV laser radiation are sufficient and are much cheaper! The toroidal grating possesses 275 gr/mm, its curvature makes all wavelengths converge to the grating's focal point ($f = 319.9$ mm) where a $\varnothing = 1$ mm iris is placed. Rotating the grating allows the selection of only one monochromatic component to pass through the iris which is intended for interacting with the molecules in the extraction chamber (see Fig. 1.14). In some cases, the non-dispersive 0th order is selected, the grating then just acts as mirror not separating the various components.

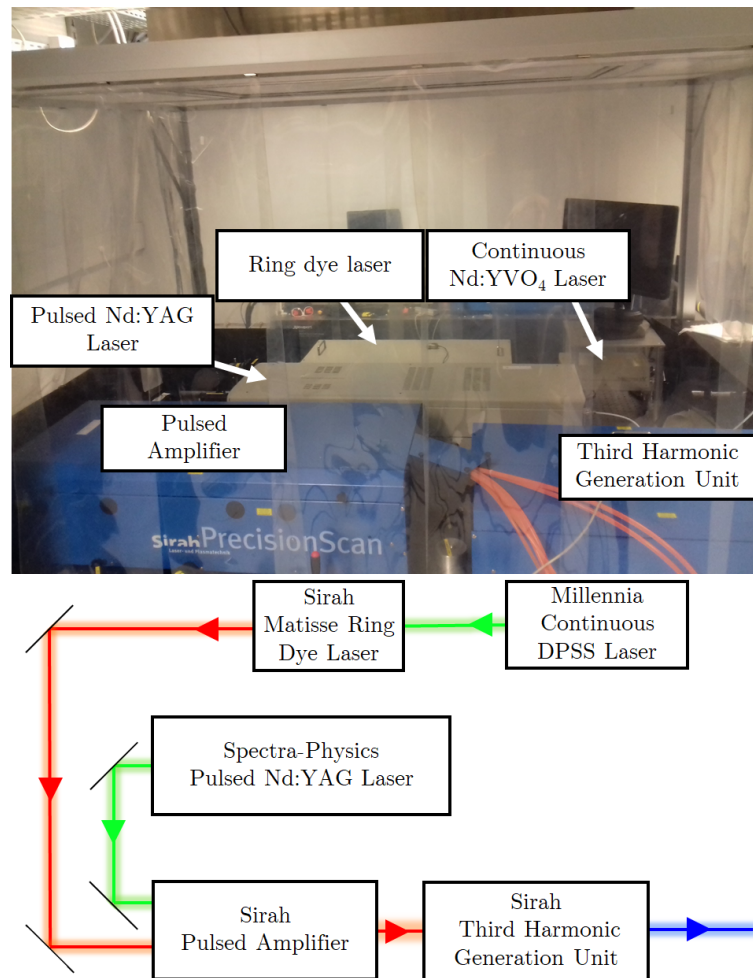


FIGURE 1.15: Top: Photo of the high-resolution UV laser chain at ISMO. Bottom: Illustration of the high-resolution UV laser chain at ISMO with main characteristics.

1.2.3 High resolution tunable UV laser chain

The UV radiation used in the four-wave mixing scheme is produced by a high-resolution UV laser chain depicted in Fig. 1.15 and whose elements are summarised in Table 1.6. This chain starts with a continuous-wave, narrow-linewidth tunable ring dye-laser. More specifically, it is a Sirah Matisse 2 DR series laser pumped at 532 nm and 4 W by a Millennia continuous-wave diode-pumped solid-state (DPSS) frequency-doubled laser containing a neodymium-doped yttrium orthovanadate (Nd:YVO₄) crystal. The wavelength of the dye laser can be tuned between 550 and 750 nm (using different dyes) depending on the desired two-photon resonance in the rare gas. The resulting radiation has a typical power of 0.4 W and an extremely narrow bandwidth of typically $7 \cdot 10^{-4} \text{ cm}^{-1}$. See Fig. 1.16 for an optical layout of this laser.

In order to efficiently produce UV radiation from the visible range *via* doubling and tripling processes in BBO crystals and also due to the nature of the intended experiments, pulsed radiation is required [17]. To achieve this, the continuous-wave laser is used as a seed source for a Sirah Pulsed Amplifier pumped by an injected Spectra-Physics Quanta-Ray Lab-190 pulsed Nd:YAG laser at 20 Hz, at typically 300 mJ per pulse. The laser injector is used to offer greater

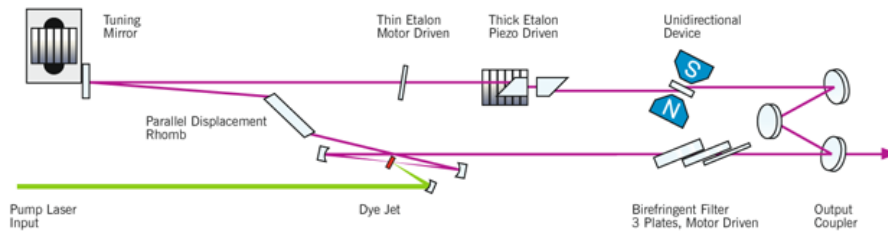


FIGURE 1.16: Optical layout of the Sirah Matisse ring dye-laser from ref. [32]

time and frequency stability.

TABLE 1.6: Equipment characteristics on the high-resolution UV laser chain.

Equipment	Pulse duration /ns	Exit wavelength / nm	Maximum power or energy-per-pulse	Typical power or energy-per-pulse	Bandwidth / cm^{-1}
Millenia	continuous	532	10 W	4 W	$< 2.10^{-4}$
Matisse	continuous	550 - 750	1.8 W	0.4 W	7.10^{-4}
Quanta-Ray Lab-190 Pulsed Amplifier	6 - 7	532	500 mJ / pulse	300 mJ / pulse	5.10^{-3}
THU-205	6 - 7	200 - 250	>3 mJ / pulse	1 mJ / pulse	$\approx 5.10^{-3}$

After the pulsed amplification-stage, the resulting radiation is at approximately the same wavelength as the incident continuous radiation, but now pulsed at 20 Hz. Each pulse is 6 to 7 ns long and contains around 30 mJ of energy. Because of the pulsing, the radiation is now FT-limited which amounts to a wider bandwidth of approximately $5.10^{-3} \text{ cm}^{-1}$. The role of the SBS cell, within the pulsed amplifier (see Fig. 1.17), is to filter out Brillouin light scattering or spontaneous emission from the laser radiation. It induces a slight shift in wavelength which is checked using a HighFinesse WS7-60 Wavemeter [33] placed after the pulsed amplification-stage.

Following the pulsed amplifier, the pulsed visible laser is then mixed using two BaB_2O_4 (BBO) crystals in a Sirah THU-205 third-harmonic unit. The first crystal acts as a doubler and the second a mixer, combining the doubled frequency with the fundamental in order to produce a tripled frequency at one third of the fundamental visible wavelength. The Nd:YAG fundamental ($\lambda_{\text{Nd:YAG}} = 1064 \text{ nm}$) can also be mixed with the doubled radiation in the second crystal (see Table 1.7) if required. The final UV radiation has a wavelength of between 200 and 250 nm, a spectral resolution of $\approx 5.10^{-3} \text{ cm}^{-1}$, a repetition rate of 20 Hz, a temporal pulse length of 6 to 7 ns and an energy-per-pulse of between 1 and 3 mJ.

As the previous paragraphs show, a complex setup is required in order to produce the high-resolution UV laser radiation. This effort is however justified: firstly, in order to generate a high-resolution VUV laser, there can be no loss in resolution at any point in the radiation production process, so the UV must have a high resolution. Secondly, as can be seen in Fig. 1.13, the VUV production process uses a two-photon resonant transition in a rare gas. Given this, it follows that the more energy that can be put into this transition, the greater the VUV efficiency. Mathematically, this can be understood using equation (1.2)

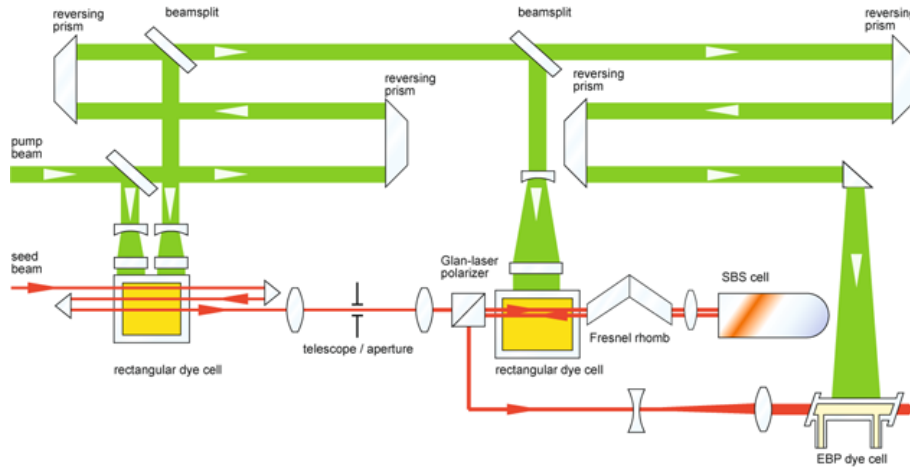


FIGURE 1.17: Optical layout of the Sirah Pulsed Amplifier from ref. [32]

TABLE 1.7: Two-photon rare gas transitions and corresponding UV generation processes.

Resonance*	Rare Gas	Wavenumber ($2\tilde{\nu}_{UV}$) / cm^{-1}	UV generation process	ν_{UV}
Kr(1)	Kr [29]	94 092.86	third harmonic	$3\nu_{\text{fun}}^{**}$
Kr(2)	Kr [29]	98 855.06	third harmonic	$3\nu_{\text{fun}}^{**}$
Xe(1)	Xe [30]	80 118.96	mixing after doubling	$2\nu_{\text{fun}}^{**} + \nu_{\text{Nd:YAG}}$
Xe(2)	Xe [30]	89 860.02	third harmonic	$3\nu_{\text{fun}}^{**}$

* Referred to in Fig. 1.22

** Fundamental frequency corresponding to the delivered radiation of the Matisse ring dye-laser before any mixing processes.

$$I_{VUV}(\nu) \propto I_{UV}(\nu - \nu'_0)^2 \times g(\nu - \nu_0), \quad (1.2)$$

that relates the produced VUV intensity $I_{VUV}(\nu)$ to the incident UV intensity $I_{UV}(\nu - \nu'_0)$ characterised by its own bandwidth $\Delta\nu_{UV}$, and spectral profile of the two-photon transition in rare gas $g(\nu - \nu_0)$ characterised by its width $\Delta\nu_{RG}$. The width of the rare-gas transition contains the natural width and potentially other causes of broadening (pressure or power). Of course the VUV intensity also depends on the third photon intensity, rare-gas density, *etc.*, but for motivating the use of a high-resolution UV laser, the proportionality law of equation (1.2) suffices [34]. In order to efficiently produce VUV radiation, the UV laser has to be centered around the rare gas transition: $\nu'_0 = \nu_0$.

This implies that the narrower the bandwidth of this radiation, the more energy can be channelled into this transition (see Fig. 1.18). Furthermore, as it is a two-photon transition, the VUV radiation intensity scales as the square of the incident UV intensity so any increase in UV intensity has an even larger impact on VUV intensity.

In trying to increase VUV laser intensity, it is apparent in equation (1.2) that this can be achieved by increasing the UV laser intensity. Increasing laser intensity however causes the rare gas transition to widen, an effect called power broadening. If the spectral shape of the

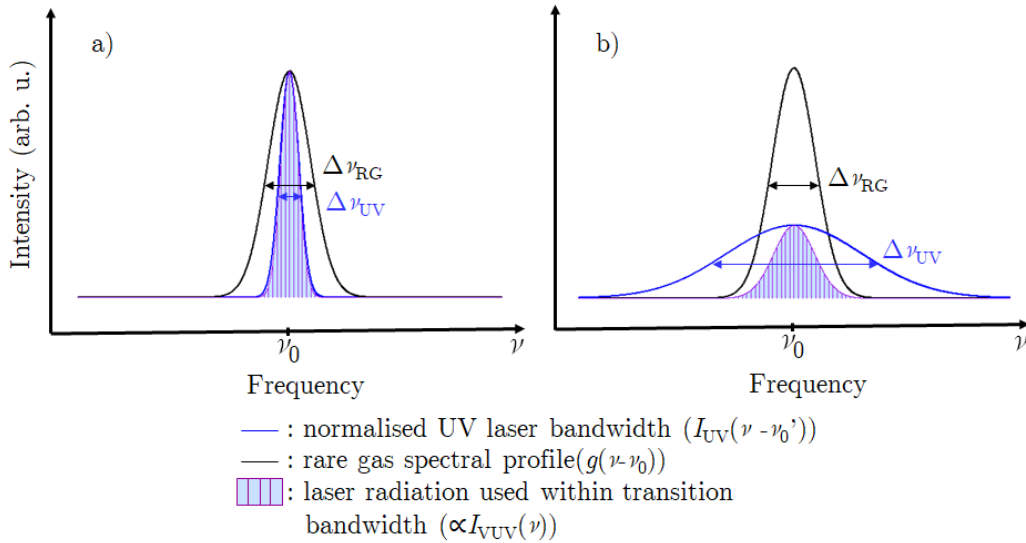


FIGURE 1.18: Schematic spectra of overlap between UV laser bandwidth and two-photon transition width in a rare gas. a) Spectrum displaying a narrow UV laser bandwidth with all spectral components within the rare-gas transition that all contribute in VUV production ($\Delta\nu_{UV} < \Delta\nu_{RG}$). b) Spectrum displaying a wide UV laser bandwidth with spectral components outside the rare-gas transition ($\Delta\nu_{UV} > \Delta\nu_{RG}$). As more laser spectral components in the a) spectrum overlap with the rare gas transition as compared to the b) spectrum, VUV production will have a higher efficiency in a).

transition is broadened by the laser intensity, VUV production remains resonant, but over a wider spectral range. As long as the UV laser is of narrow bandwidth, the produced VUV is still also of narrow bandwidth (Fig. 1.18 b))

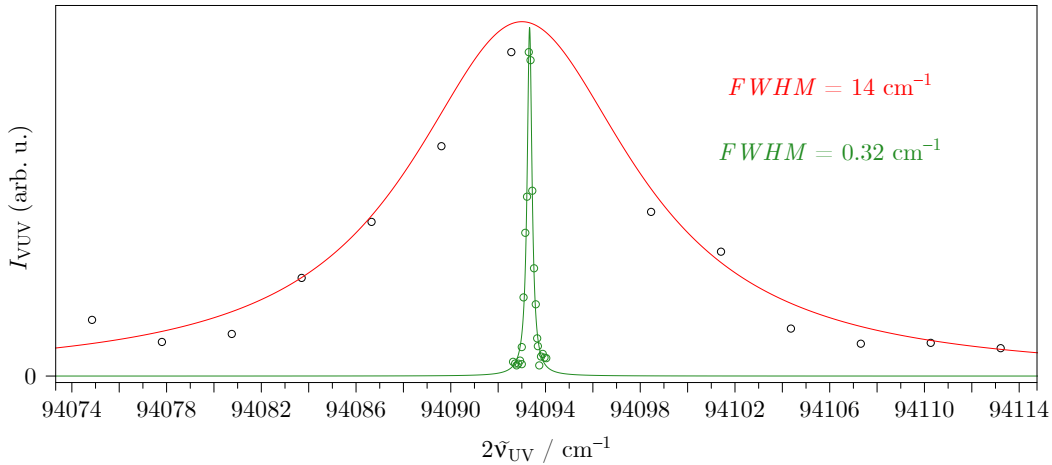


FIGURE 1.19: Normalised VUV intensity as a function of UV wavenumber. Lorentzian curves fit the data sets whose average UV laser energy are 0.06 mJ/pulse (green line) and 1 mJ/pulse (red line).

In order to probe the effect of UV laser intensity on the width of the rare gas transition, the produced VUV intensity was recorded as a function of UV wavenumber for two laser pulse

energies: 1 mJ/pulse and 0.06 mJ/pulse. This study was performed on the 94 092.86 cm^{-1} Kr resonance, UV laser power can be adjusted by optimising or deoptimising the phase matching in the BBO crystals of the THU-205 or by opening and closing an entrance iris. The corresponding data sets, presented in Fig. 1.19, can be modelled by lorentzian functions whose *FWHM* are 14 and 0.32 cm^{-1} respectively. If power broadening was completely absent, the width of the transition would be Doppler limited, *i.e.* at worst 0.12 cm^{-1} at 300 K.

Note that even for a narrow bandwidth laser, too intense a UV laser can generate a plasma in the rare gas. This is detrimental for VUV production as the plasma can reabsorb the produced VUV radiation.

1.2.4 High resolution dye laser

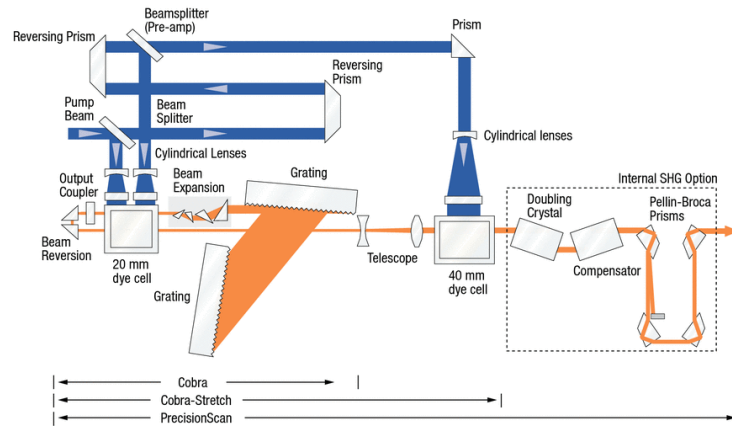


FIGURE 1.20: Top: Photo of the Cobra-Stretch double grating dye-laser pumped by a Spectra-Physics Quanta Ray Nd:YAG laser. Bottom: Optical layout of the Sirah Cobra Stretch double grating dye-laser from ref. [32]

One of the advantages of using the 4-wave mixing process, depicted in Fig. 1.13, is the tunability of the produced VUV radiation. The tunable visible laser delivering the last photon producing λ^+ or λ^- must offer high spectral resolution if high-resolution VUV radiation is desired in the end. In our experimental setup, this visible laser is a Sirah Cobra-Stretch dye laser pumped by a Spectra-Physics Quanta-Ray pulsed Nd:YAG laser (see Fig. 1.20) at 355 or 532 nm. The Cobra-Stretch functions as any dye laser, but is equipped with a double grating

(1800 & 1800 or 1800 & 3000 gr/mm). It is tunable across from the near-IR to the near-UV (from 900 to 300 nm). The UV range is reached by the means of a BBO crystal acting as a frequency doubler of visible radiation. Visible radiation wavelength is measured using a High Finesse WS6-600 series wavemeter [33] placed after the laser or, in the case of frequency doubling, just before the BBO crystal.

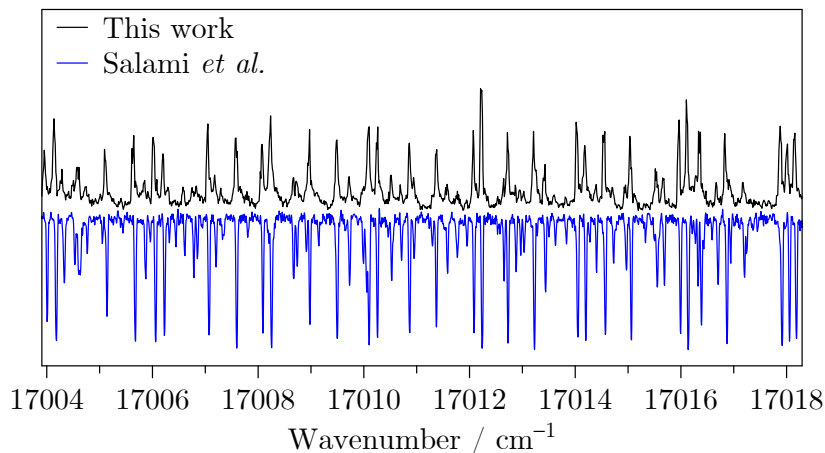


FIGURE 1.21: I_2 laser-induced-fluorescence spectrum resulting from the excitation of I_2 with a Cobra Stretch dye laser (black) compared to FT absorption spectrum (blue) from ref. [35]

The photon resolution and the wavelength calibration of this visible radiation are checked by recording a laser-induced-fluorescence emission spectrum of I_2 using an I_2 -cell and comparing it to an I_2 absorption spectrum obtained by FT spectroscopy, see Fig. 1.21 [35]. The I_2 cell is irradiated by the tunable visible laser and its fluorescence is collected at a right angle with a photomultiplier. The spectra are obtained by plotting the fluorescence signal as a function of the excitation-laser wavelength. A typical linewidth was found to be around 0.05 cm^{-1} . Relative line intensities cannot be compared as the spectra were recorded using different methods, but the line positions are in very good agreement after calibration with the wavemeter. This study therefore confirms that the visible wavelength is correctly calibrated and has a very narrow bandwidth.

In the four-wave mixing scheme (see Fig. 1.13), the linewidth of the produced VUV radiation is given in rough terms by that of the implicated photon whose linewidth is the largest. In our setup, the linewidth in question is that of the photon produced by the Cobra-Stretch laser. We would therefore expect a VUV linewidth of around 0.05 cm^{-1} .

1.2.5 VUV spectral range

Having shed light on the high-resolution UV laser chain and the high-resolution dye-laser in the previous sections, it is now possible to give the spectral range of the tunable VUV laser (see Fig. 1.22). For each resonance, there are two accessible spectral ranges. The lower range is reached using difference-frequency mixing (λ^-). The upper is reached used sum-frequency mixing (λ^+), see Fig. 1.13. Depending on the desired dye laser wavelength, the Cobra-Stretch can be pumped at 355 or 532 nm.

As Fig. 1.22 shows, the VUV laser can be tuned continuously to any photon energy between 6 and 16 eV except for a narrow hole around 11 eV. Introducing an IR pulsed-laser (able to reach

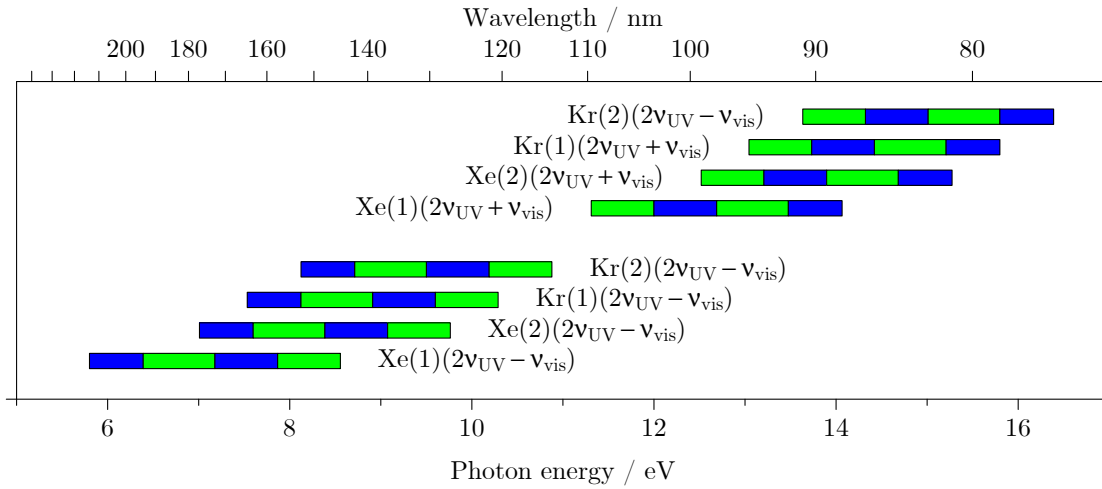


FIGURE 1.22: VUV laser spectral range for each rare gas resonance (same notations as Tables 1.4 and 1.7). Green (blue) zones represent spectral regions using ν_{vis} produced by the Cobra-Stretch pumped at 532 nm (355 nm).

5000 nm) instead of the Cobra-Stretch would bridge this gap. Alternatively, a metallic vapour could also be used with the current setup as a medium to generate VUV radiation around 11 eV.

1.2.6 VUV photon flux monitoring

At any photon energy, after interacting with the molecules, the laser beam continues to a VUV detector (see Fig. 1.12). More specifically the detector is a R5150-10 electron multiplier tube from Hamamatsu [36]. Relative VUV intensity must be measured for various reasons.

Before being able to record any scan, the great number of elements involved in VUV production described in previous paragraphs must be optimised. This can be done by monitoring the VUV signal in real time and adjusting parameters to increase the signal.

Once the VUV signal is sufficient, a study can begin and will last for between a few minutes and several hours. During this time, the VUV signal can vary; the mass-spectra intensities, being proportional to the VUV photon flux, vary accordingly. Variations can be corrected by renormalising spectra by the VUV detector signal.

There are several sources of VUV intensity variations. Firstly, and in the case of a photon energy scan, the four-wave mixing process pictured in Fig. 1.13, is very wavelength (λ_{vis}) dependent. At some wavelengths, VUV production is very difficult. Even at fixed wavelength, the VUV signal can vary slowly due to the deoptimisation of the experimental settings. Amongst many things, a common cause is the BBO crystal phase-matching loss over time as the crystal expands through the heating by the laser, this requires adjusting the position of the crystal to reoptimise the phase matching every so often.

On a much shorter time scale are laser fluctuations. In non-linear optical processes, the intensity I_1 of a beam made up of photons generated using p lower energy photons whose beam intensity is noted I_0 is ruled by the proportionality relationship (1.3):

$$I_1 \propto I_0^p. \quad (1.3)$$

This power law dictates that any fluctuation in the first photon's intensity is then amplified in the final intensity I_1 . In the laser setup described in this chapter, 3 visible photons are used to produce the high-resolution UV photons and 2 UV photons are used in the VUV generation process to produce 1 VUV photon (see section 1.2.3). In total, 6 visible photons are used to reach the excited state in the rare gas. On top of these 6, and once in the excited state, one more photon is implicated in the final step to produce a VUV photon which brings even more fluctuations. These non-linear processes therefore make the produced VUV radiation very sensitive to fluctuations in the initial laser sources.

This shows that VUV intensity fluctuations do exist, but they are accounted for and corrected accordingly, by renormalising the recorded signals by the VUV photon flux.

1.2.7 Vacuum experimental setup

As its name suggests and due to O_2 absorption below approximately 200 nm, VUV radiation does not travel through air. This means that the experiment, from the VUV production onwards, must be under vacuum as shown in Fig. 1.12. A primary pumping system relying on rotary vane pumps brings the pressure down from atmospheric pressure to around 10^{-2} mbar. A secondary pumping system further lowers the pressure to around 10^{-7} mbar using turbo or diffusion pumps, which is the usual operating pressure. Each chamber is equipped with a secondary pump; those containing gas nozzles are connected to higher capacity systems.

The various forms of the VUV laser, as described previously, were used in order to probe relaxation processes of molecules in the gas phase. Initially coupled to the Time-Of-Flight (TOF) mass spectrometer Icare, the experimental setup underwent substantial changes throughout my PhD leading to the final version renamed VULCAIM. I took part in the experimental developments. The coupling of a VUV laser to the experimental setup is detailed in the following sections along with the motivations behind the setup modifications.

Gas-phase sample and molecular beam generation

Roughly speaking, in all setup versions, molecules expand supersonically through a pulsed gas nozzle at 20 Hz, into the vacuum chamber before being skimmed and encountering monochromatic VUV radiation in an interaction chamber (see Fig. 1.12). The gas nozzle is mounted on the end of a rod whose position is adjustable in three directions. Initially, a General Valve pulsed plunger valve was used, equipped with a handle allowing the tightening of the plunger whilst under vacuum. A typical opening time for such a valve is around 100 μ s. This valve was replaced by an Amsterdam Piezo Valve whose opening time is of the order of a few tens of μ s [37]. The new valve does not require a handle for tightening as the opening of the valve is completely controlled electronically, notably by changing the voltage applied to the piezoelectric crystal which is responsible for the release mechanism.

When studying stable species, the initial gas sample can be seeded in a rare gas (Ar or Ne) or in the case of liquid samples, the rare gas can be bubbled through the liquid or simply over the liquid to induce the sample flow towards the experiment.

After entering the first vacuum chamber by expanding through a gas nozzle, the molecules pass through a skimmer which selects the coolest, most central part of the expanding gas, thus generating a molecular beam. This selectivity can be understood in terms of relative velocities

in the center-of-momentum frame and by referring to Fig. 1.23: after the skimmer, the velocity distribution is reduced which leads to a lowering of temperature. The hole diameter of the skimmer varies from a few mm to a few hundred μm . The larger the skimmer hole, the larger the probed sample size and resulting ion signal, but this comes at an increase in temperature. The temperature is not solely controlled by the skimmer diameter, but also the gas nozzle characteristics (*e.g.* plunger tightness), backing pressure (typically a few bar) or even the molecular beam alignment (if it is slightly off-axis with the skimmer, a warmer part of the jet will be selected).

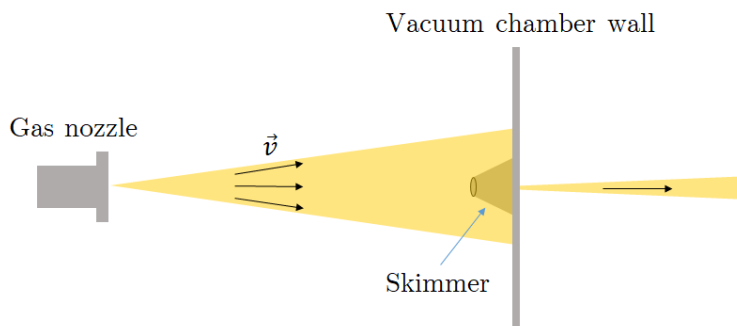


FIGURE 1.23: Schematic drawing of a gas expanding through a nozzle followed by a skimmer which selects the innermost part of the jet. A reduction of the velocity distribution (black arrows) leads to lower translational temperatures after the skimmer.

In supersonic jets, it is known that translational and rotational degrees of freedom are generally at equilibrium, whereas the vibrational degrees of freedom are much more difficult to cool. Vibrational cooling was not studied, but the rotational temperature was measured down to ≈ 5 K (see N_2 study of section 1.2.8), but this does depend on the sample and carrier gas.

Time Of Flight mass spectrometer

The molecular beam enters the interaction chamber where it is irradiated at a right angle by laser radiation. The various methods employed to probe the molecules are detailed in the following chapters of this thesis, but the final step must be ionising as only charged particles can be detected. The detection stage relies on micro-channel plates (MCP) supplying a voltage signal as a function of time to the oscilloscope and the data-acquisition interface.

In a similar way to the synchrotron experiment, the application of voltages to electrodes sends the produced charged particles towards a detector, which they hit after a Time-Of-Flight (TOF). Unlike the synchrotron however, this setup only allows the separate detection of electrons or ions and is pulsed, not continuous. This means that the extraction voltages can be applied after the laser pulse, the irradiation of molecules therefore happens in the absence of an applied electric field which should prevent Stark broadening and any field-induced shift of *IPs* (see Fig. 1.24).

After irradiation, the application of voltages (typically 500 – 1000 V) to electrodes constitutes the start time for the synchronisation clock of the experiment. It is well known in classical mechanics that an initially immobile particle, characterised by its mass m and charge q , makes an energy gain of qU when accelerated by a voltage U . On exiting the vicinity of the electrodes, the gained potential energy translates into kinetic energy following the classical equation

$$\frac{1}{2}mv^2 = qU. \quad (1.4)$$

If the ensuing TOF is free from any interactions, the velocity is maintained until the particle hits the detector at time t , typically a few microseconds, after having travelled over a distance noted d_{TOF} . From equation (1.4) and given all produced particles are accelerated by the same voltage, it is possible to derive the quadratic relationship between time and mass over charge:

$$t = d_{\text{TOF}} \sqrt{\frac{m}{2qU}}. \quad (1.5)$$

In all cases in this work, $q = e$ as only singly charged species are produced; this means that mass over charge quantities will often be referred to as simply masses, the charge implicitly equal to one positive elementary charge. Equation (1.5) means that heavier fragments arrive after lighter ones which is quite intuitive. For different m/q values, ions arrive at discrete intervals on the detector. This enables ion signal mass-selectivity in the time domain. Furthermore, the assignment of ion signals to known fragments (usually precursors, carrier gas or impurities) allows the determination of constants in equation (1.5) and the transformation of the arrival time distribution into a mass spectrum.

Temporal synchronisation of the setup

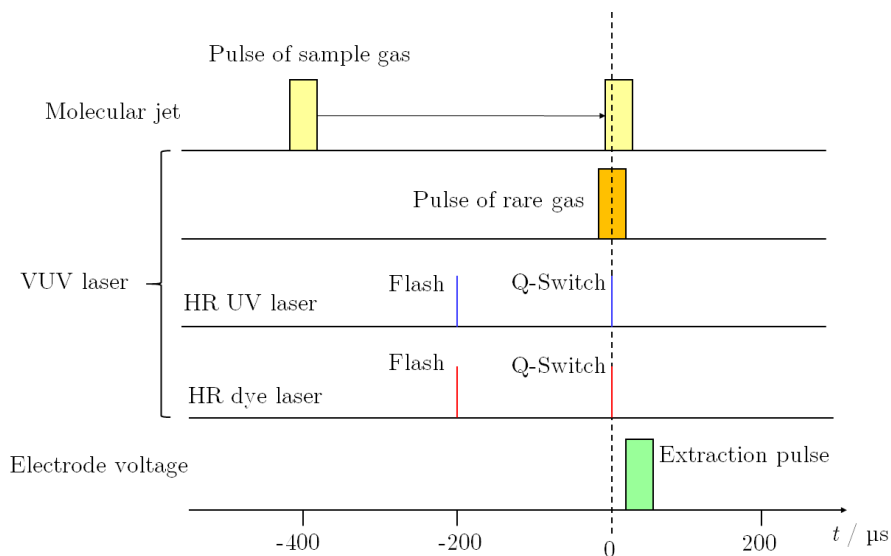


FIGURE 1.24: Temporal synchronisation of the various elements of the experimental setup.

It is worth noting that, given the number of lasers and molecular beams implicated in the experiment, there is not only a complex spatial optimisation of the various elements to provide a spatial overlap, but is also complexity in the time domain as all laser beams and all the molecular beams must be synchronised. This is achieved using an electronic interface which controls all the trigger times of the various elements (see Fig. 1.24).

As a molecular jet travels at around 1000 m/s, a lot slower than the speed of light, the gas sample must be released well before the laser firing time (Q-switch). This is especially true for

the gas sample whose nozzle is around 50 cm from the interaction zone; the rare gas for the four-wave mixing scheme is not released as early as the UV and visible lasers focus just below the corresponding gas nozzle. Furthermore, the laser flash-lamps must be turned on at the correct time to allow sufficient population inversion in the laser gain-medium by the time the laser fires. Finally, extraction voltages must be applied after the laser has irradiated the sample, not before as the presence of electric fields in the interaction zone generates Stark shifts.

Laser times can be checked by the means of photodiodes and the gas nozzle release times are set directly by optimising the ion signals on the MCP detector

1.2.8 First VUV laser experiment with Icare on N₂

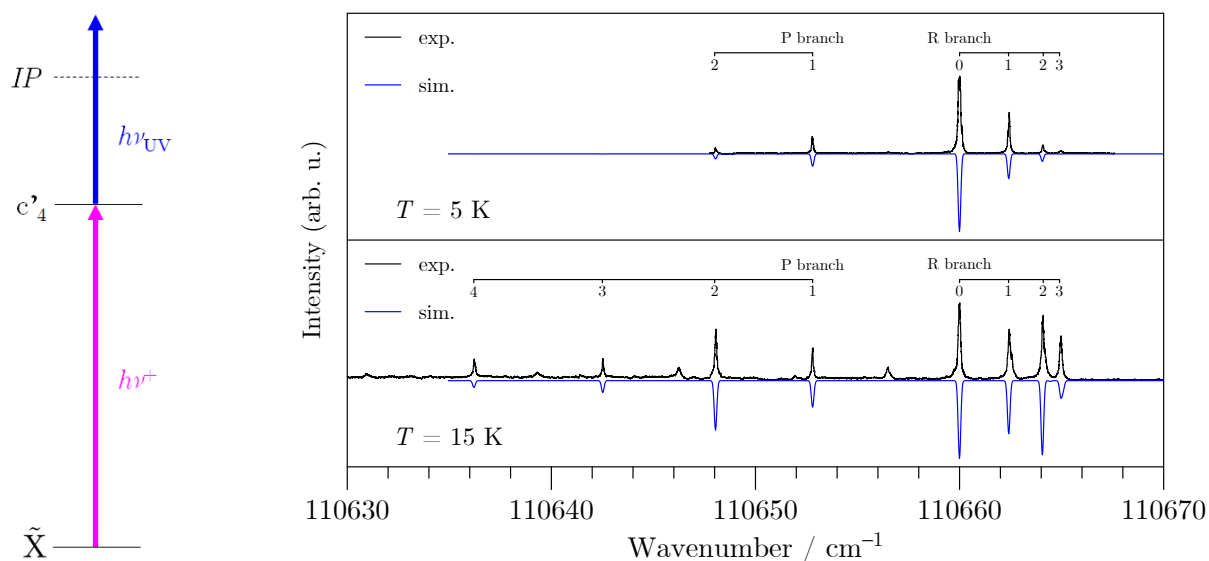


FIGURE 1.25: Left: Two-photon, two-colour ionisation scheme to probe at rotational resolution the $c'_4 \ ^1\Sigma_u^+$ ($v = 3$) state of N₂. Right: Rotationally resolved spectra of the $c'_4 \ ^1\Sigma_u^+$ ($v = 3$) \leftarrow $X \ ^1\Sigma_g^+$ transition in N₂ with a 1 mm (top) and 2 mm (bottom) in diameter skimmers. These experimental spectra (black) are simulated using PGOPHER software (blue).

Following the installation of the VUV laser chain in 2018, N₂ was selected as a suitable test-species in a preliminary study. Experimentally, N₂ molecules are excited from their ground state along the $c'_4 \ ^1\Sigma_u^+$ ($v = 3$) \leftarrow $X \ ^1\Sigma_g^+$ transition using $h\nu^+$ photons, which is not expected to be Doppler-limited. Once in the excited state, N₂ is then ionised by a UV photon ($\lambda_{UV} = 212$ nm). The ensuing cation is collected by mass spectrometry. In this study, the grating of the VUV laser was turned to allow the 0th order into the extraction zone; this has the effect of using the grating as a mirror. Using the notations of Fig. 1.13, the polychromatic radiation contains in particular the tunable VUV radiation at photon energy $h\nu^+$ and the initial UV radiation used to produce it.

Fig 1.25 displays an almost textbook example of a rovibronic transition. Following conventional notations, noting J'' and J' the rotational quantum numbers for the ground and excited electronic states respectively, and $\Delta J = J' - J''$. One can identify the transitions within the P branch ($\Delta J = -1$) at lower energies and the R branch ($\Delta J = +1$) at higher energies. Because both electronic states in the $c'_4 \ ^1\Sigma_u^+$ ($v = 3$) \leftarrow $X \ ^1\Sigma_g^+$ transition have a vanishing orbital angular

momentum projection along the internuclear axis ($\Lambda = 0$), no Q branch ($\Delta J = 0$) is present in the spectra.

In blue are represented simulations of these experimental spectra. Using the PGOPHER software, assigning the various experimental lines to given rovibronic transitions provides inputs used in order to fit the model parameters, namely the rotational constants of both states ($B_{v=0}(X)$ and $B_{v=3}(c'_4)$) and the origin energy (E_0) between the two. Not all experimental lines are reproduced by the simulations, these unassigned lines could be attributed to sequence bands, but their assignment was not pursued any further.

The relative line-intensities of the simulations account mainly for the rotational temperature of N_2 in its ground state, which governs the population of the various rotational levels according to Boltzman's law. The choice of temperature in the simulation that best reproduces the experimental spectrum gives the value of the experimental rotational temperature. As Fig. 1.25 shows, the 5 K spectrum, recorded using a $\varnothing = 1$ mm skimmer, is cooler than the 15 K spectrum, recorded using a $\varnothing = 2$ mm skimmer. This can be understood as the smaller the skimmer hole, the more restrictive the skimmer is in selecting only the central part of the molecular jet. The distance between the gas nozzle and the skimmer (adjustable between 1–15 cm) also has an influence on the temperature, but was kept constant (≈ 10 cm) for both spectra.

Independent of the Boltzman factor, there is an alternating intensity between even and odd J values. This is due to spin statistics owing to the ^{14}N nuclear spin being 1. One can show that the spin statistics yield a 2:1 intensity ratio in favour of rovibronic transitions from even J as compared to those from odd J [38]. Concerning the line shape, the width of the lines is adjusted manually (to 0.3 cm^{-1}) to reproduce the experimental linewidth. It is worth noting here that the N_2 Doppler widening due to a 15 K translational temperature is around 0.05 cm^{-1} and thus does not constitute the main contribution to linewidths.

As the resolution is given in this study by the linewidth of the first photon enabling the $c'_4 \ ^1\Sigma_u^+(v=3) \leftarrow X \ ^1\Sigma_g^+$ transition, this study already points towards a spectral-resolution problem when coupling the VUV laser to the Icare setup.

1.2.9 From Icare to VULCAIM

The larger-than-expected resolution, observed in the previously described N_2 study (see paragraph 1.2.8), was a clue indicating an intrinsic resolution loss in the experiment. If Doppler broadening is not limiting, the spectral resolution should be given by the VUV linewidth. In the case of sum- or difference-frequency mixing, that should be more or less the tunable dye laser bandwidth, *i.e.* 0.05 cm^{-1} (the UV laser being much narrower). In the aim of measuring the bandwidth of the new VUV laser setup, Rydberg series of rare gases were studied as described in the following paragraphs.

Theoretical reminders on Rydberg states

Rydberg states are highly excited electronic states. A Rydberg series is a collection of Rydberg states converging towards an ionic state. For higher and higher energy states, an electron ventures out onto wider and wider orbits, the ionic core increasingly resembling the ionic state to which the Rydberg series converges.

Using conventional notations when describing a polyelectronic atom: n and l respectively the principal and orbital quantum number describing the excited electron, IP the ionisation potential and δ_{nl} the quantum defect, the energy of a given Rydberg state E_{nl} can be expressed

as

$$E_{nl} = IP - \frac{R_y}{(n - \delta_{nl})^2} \quad (1.6)$$

in which R_y represents the Rydberg constant of an atom of mass M , a quantity that can be written as a combination of fundamental constants and the reduced mass μ :

$$R_y = \frac{\mu e^4}{8\epsilon_0 h^3 c} \quad (1.7)$$

$$\text{with } \mu = \frac{m_e M}{m_e + M}.$$

In polyelectronic atoms, as the Rydberg electron penetrates the ionic core, the screening of the highly positively charged nucleus weakens as fewer core electrons are between it and the core. In simple terms, the quantum defect δ_{nl} accounts for this penetration and loss of screening. The defect is therefore greatly l -dependent as the shape of the Rydberg electron's orbital affects the way the electron interacts with the ionic core. At the first order, the defect does not depend on n ; this approximation will be used throughout this work. The defect will thus be noted δ_l . Note that as n is an integer, the quantum defect can be defined plus or minus any integer as this just causes a shift in the origin of the Rydberg series.

Throughout this manuscript, Rydberg series notations will follow Racah notation: $nl[K](J)$, with

- J , the total angular momentum for the whole atom combining orbital momentum and spin ($J = L + S$), and
- $K = J_1 + l$, with J_1 the total angular momentum for the unexcited part of the atom. So $J = K + s$, with $s = 1/2$ the electron spin.

So far, the above results are applicable to isolated Rydberg atoms in the absence of electric fields. In the presence of electric fields, a degeneracy is lifted within the Rydberg states which implicates new quantum numbers. Using perturbation theory to the fourth order on the field-atom interaction Hamiltonian, the effect of a field F on Rydberg states can be seen as follows in equation (1.8) [39], valid for weak fields:

$$E(n, m, n_1, n_2, F) = -\frac{1}{2n^2} + \frac{3}{2}n(n_1 - n_2)F - \frac{1}{16}n^4[17n^2 - 3(n_1 - n_2)^2 - 9m^2 + 19]F^2$$

$$+ \frac{3}{32}n^7(n_1 - n_2)[23n^2 - (n_1 - n_2)^2 + 11m^2 + 39]F^3 - \frac{1}{1024}n^{10}[5487n^4 + 35182n^2$$

$$- 1134m^2(n_1 - n_2)^2 + 1806n^2(n_1 - n_2)^2 - 3402n^2m^2 + 147(n_1 - n_2)^4 - 549m^4$$

$$+ 5754(n_1 - n_2)^2 - 8622m^2 + 16211]F^4 \quad (1.8)$$

with:

- n , the principal quantum number,
- m , the magnetic quantum number,

- n_1 and n_2 , parabolic quantum numbers, positive integers obeying $n_1 + n_2 + |m| + 1 = n$; given this relationship, it is numerically easier to work with one quantum parabolic number $p = n_1 - n_2$ obeying $-(n - 1 - |m|) \leq p \leq n - 1 - |m|$ in steps of 2,
- F , the electric field, and
- $E(n, m, n_1, n_2, F)$, energy values for the the degeneracy-lifted Rydberg states.

Probing Rydberg states using Pulsed-Field-Ionisation spectroscopy

Using a VUV laser, atoms can be excited from their ground state to Rydberg states very close to the IP . Once excited, the atoms can be ionised, this can be done employing pulsed electric fields using the Stark shift of the IP . As a function of applied electric field F (in V/cm), the shift in IP as compared to the absence of electric field, ΔIP (in cm^{-1}), follows the quadratic relationship

$$\Delta IP = IP(F > 0) - IP(F = 0) = -A\sqrt{|F|} \quad (1.9)$$

where A is a constant ranging between 2 and 6 $\text{V}^{-1/2} \cdot \text{cm}^{-1/2}$ depending on the character of the given Rydberg state and the characteristics of the applied field [18]. Importantly, equation (1.9) shows that the drop in IP due to the Stark effect is proportionate to the square root of the applied electric field. This Stark shift is used in the context of Pulsed-Field-Ionisation (PFI) spectroscopy as demonstrated in Fig. 1.26.

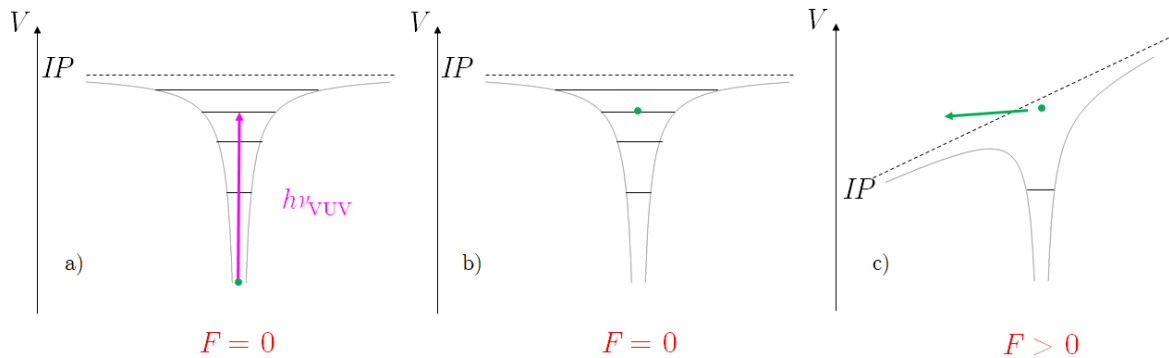


FIGURE 1.26: Simplified 2D schemes of an electron (green dot) in a potential well (V) representing the bound nature of an electron within the atom. a) Arrival of a VUV laser pulse to excite the atom and promote an electron to a highly excited Rydberg state. b) The laser pulse has passed, the Rydberg atom has been formed. c) PFI: Application of electric field F which deforms the potential well allowing the electron to escape.

Experimentally, the scheme of Fig. 1.26 uses the tunable high-resolution VUV laser described previously within the experimental setup Icare. Static electric-fields can be applied to electrodes within the interaction zone to ionise atoms and then send ions towards the detector which they hit after a time-of-flight. Typical voltages are of the order of 1kV which translate into electric fields of a few hundred V/cm.

Probing rare gas Rydberg states using Pulsed-Field-Ionisation (PFI) spectroscopy with Icare

PFI spectroscopy was used to characterise the new VUV laser chain coupled to the TOF mass spectrometer Icare mainly *via* the study of Rydberg series of Ar and Kr. Experimentally, the VUV laser was scanned just below the *IP* exciting the rare gas from the ground state to highly excited Rydberg states. Voltages of the order of several hundred volts were applied to electrodes to ionise the Rydberg states. The corresponding ions were collected after a time-of-flight using mass spectrometry. The integration of the corresponding mass peaks constitutes the ion signal which is plotted against VUV photon energy in Fig. 1.27. In the case of Ar, one main isotope was detectable and identified as ^{40}Ar , whereas the five most naturally abundant isotopes of Kr were detected (^{80}Kr , ^{82}Kr , ^{83}Kr , ^{84}Kr , and ^{86}Kr). The mass resolution of the TOF spectra was greater than 1 a.m.u. meaning that all isotope signals were distinguishable and separable in the integration. Kr spectra in this section use the ^{84}Kr isotope.

These sort of experiments are similar to those conducted at ETH Zurich in the group of Frédéric Merkt. Differences in their setup with ours explain that they can achieve higher resolution (down to 0.008 cm^{-1} [17]), but their results still provide excellent benchmarks against which we can compare our own results.

The resulting Ar spectrum of Fig. 1.27 shows a dominant, apparently single series along with a second much weaker one both converging to the first *IP* of Ar: the $^2\text{P}_{3/2}$ ground state of Ar^+ . According to Merkt *et al.* [40], who conducted a similar experiment, this dominant series is actually made up of two practically degenerate series ($nd[3/2](J = 1)$ and $ns[3/2](J = 1)$) which are not distinguishable in our spectrum.

In the same work, Merkt *et al.* assigned the secondary peaks to a $nd[1/2](J = 1)$ series. Their work on DC fields showed that the relative intensity of this weaker series compared to the dominant series was increased in the case of greater DC fields. Ar quantum defects from Merkt *et al.* were used to assign Rydberg states using equation 1.6 and are summarised in Table 1.8. In our Ar spectrum, Rydberg states are visible up to $n \approx 55$ and exhibit a typical linewidth of 0.3 cm^{-1} . Merkt *et al.* observed states with $n > 100$ and measured a record resolution for the VUV of 0.008 cm^{-1} [17].

TABLE 1.8: Quantum defects of Ar Rydberg series from ref. [34]

Series	Quantum defect δ_l
$nd[3/2](J = 1), ns[3/2](J = 1)^*$	2.1258
$nd[1/2](J = 1)$	0.512

* As these Rydberg series overlap, their quantum defects are the same to within one or two units.

The Kr spectrum displays three Rydberg series also converging to the first Kr *IP* ($\text{Kr}^+(^2\text{P}_{3/2})$). Comparing our results to those of ref. [41] and using quantum defects from ref. [34] (summarised in Table 1.9), the Rydberg series in Fig. 1.27 could be assigned. Again, the observation of Rydberg states is limited to $n \approx 55$ and the resolution is the same as with Ar whereas Merkt *et al.* observed states above $n = 200$, again under 10^{-2} cm^{-1} in resolution.

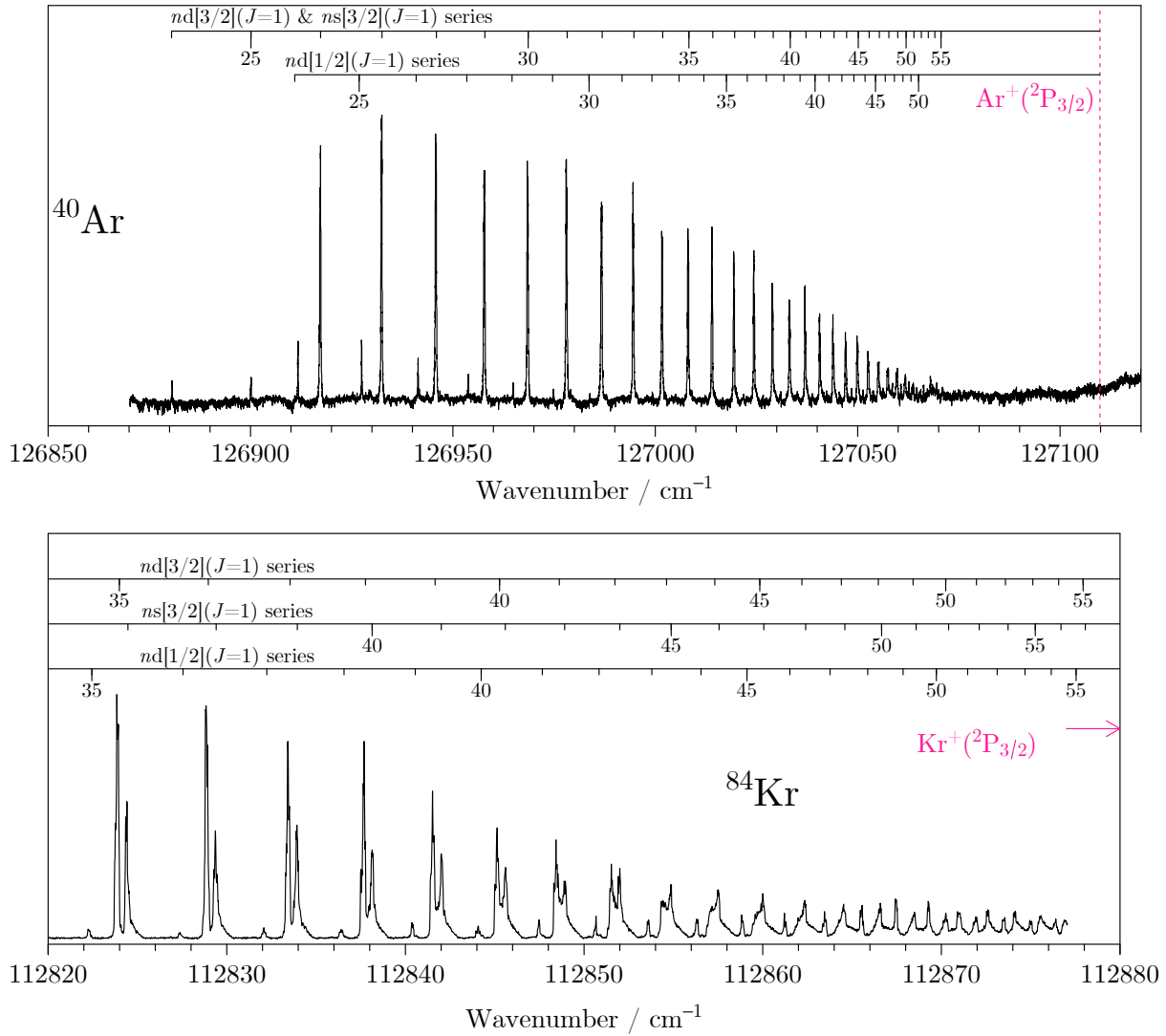


FIGURE 1.27: Icare PFI spectra of Rydberg series of Ar (top) and Kr (bottom) converging to their first IPs, the ground states of their respective ions (noted in pink). Rydberg states are resolved and visible for up to $n \approx 55$ in both Ar and Kr.

TABLE 1.9: Quantum defects of Kr Rydberg series from ref. [34]

Series	Quantum defect δ_l
$nd[3/2](J = 1)$	1.16787
$ns[3/2](J = 1)$	3.07523
$nd[1/2](J = 1)$	1.46047

The birth of VULCAIM

These results, achieved with the Icare setup, were very encouraging. They display high resolution spectroscopy capabilities in the VUV range. Although satisfactory, a higher resolution was

expected. Ar and Kr are even heavier than N_2 so the spectra should not be Doppler-limited. Typically, a resolution of the same order as the least resolved photon used in the VUV generation scheme was expected, *i.e.* the Cobra Stretch visible photon at around $5.10^{-2} \text{ cm}^{-1}$. It was also hoped that higher- n Rydberg states could have been observed, but the limitation to just $n \approx 55$ points towards the presence of stray electric fields. With the scheme of Fig. 1.26 in mind, if an additional electric field is present, the atom's *IP* is always lowered and it therefore directly ionises on the irradiation by the VUV laser. In some cases, the resulting ions can be collected, but will hit the detector at different times compared to the ions produced by PFI and the application of voltages to electrodes after irradiation.

The presence of stray fields also causes a loss in resolution due to Stark broadening, which is quantifiable. The effect of electric fields on Rydberg states was explained in paragraph 1.2.9, mainly *via* equation (1.8). Fig. 1.28 shows the degeneracy lifting within a $n = 40$ Rydberg state as a function of electric field F (arbitrarily $m = 0$). The emerging states can be described by p ranging from $-(n-1)$ to $n-1$. Compared to the single state at $F = 0$, some states are shifted to lower energies (red shifted), some are shifted to higher energies (blue shifted). Experimentally, it is not possible to resolve each component, but rather the resulting envelope of all of these states combined, convoluted by the experimental resolution. If the envelope of states is the main factor determining resolution, it is possible to extrapolate the field intensity given the width of the envelope. In Fig. 1.28, the 0.3 cm^{-1} bandwidth measured on Icare is reached for a 1.5 V.cm^{-1} electric field.

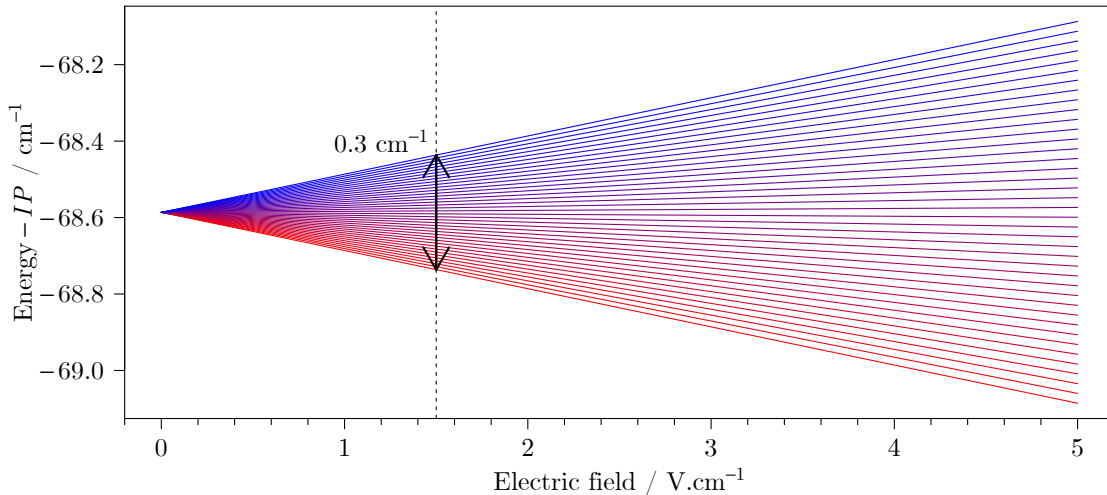


FIGURE 1.28: Degeneracy lifting of $n = 40$ Rydberg state with electric field F . Observation of blue and red shifted states. Black arrow at $F \approx 1.5 \text{ V.cm}^{-1}$ represents the 0.3 cm^{-1} experimental resolution

Various sources of stray fields are experimentally possible. Firstly, the use of a diffusion pump on the jet source chamber of Icare risks the contamination of the vacuum chambers with oil. This oil can encapsulate ions which in turn produce stray electric fields. In addition, pressure gauges containing permanent magnetic moments were used on some vacuum chambers and no precautions were taken as to shield the experiment from external magnetic fields. There are therefore a number of possible sources of stray electric and magnetic fields present within the experiment that could have been responsible for a loss in resolution.

In 2019, new vacuum chambers to replace the existing jet source and interaction chambers were designed. All diffusion and oil pumps were replaced by dry pumps (scroll or turbo

pumps). Pressure gauges were replaced by gauges without permanent magnetic moments. The interaction area at the intersection of the VUV laser and the molecular beam containing the extraction electrodes was placed within two concentric μ -metal cylinders with small holes to allow the laser and the molecules in and out. μ -metal is a nickel–iron ferromagnetic alloy with very high permeability that is able to channel magnetic field lines around the interaction area. It therefore acts as shielding for the electrons from Earth’s magnetic field and any other magnetic field present. This piece of equipment is lent to us from the team of Christian ALCARAZ (Institut de Chimie Physique, Orsay) and was developed within the context of the PhD of Barbara K. CUNHA DE MIRANDA [42, 43].

On the coupling of this new setup to the recent high-resolution VUV laser, the experiment was baptised VULCAIM (VUV Laser for Considering Astrophysical and Isolated Molecules) and is shown in Fig. 1.29.

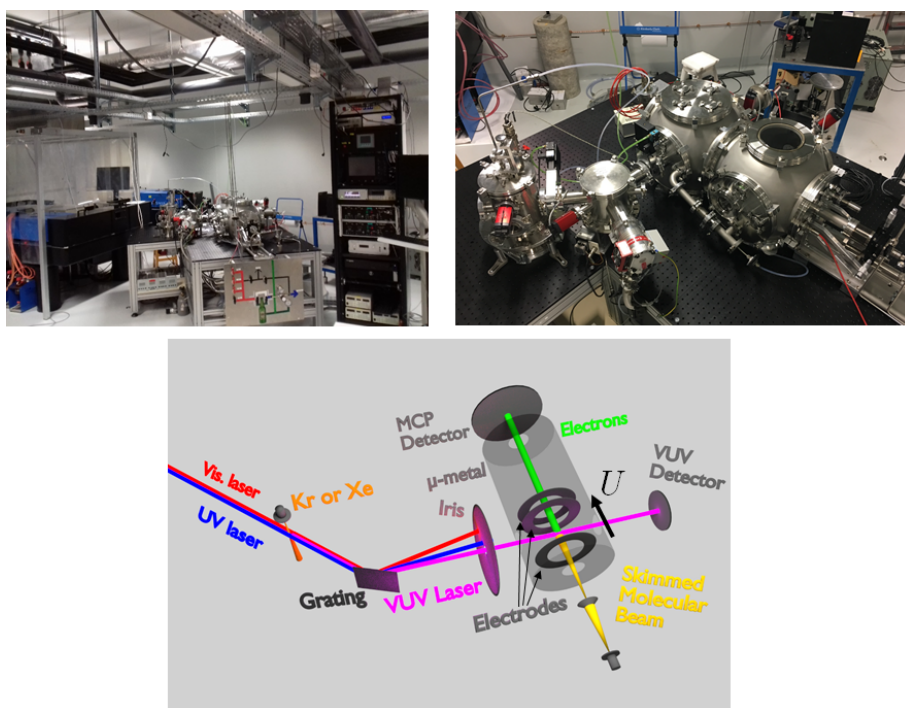


FIGURE 1.29: Top left: Photo of the VULCAIM setup with the various laser sources in the background. Top right: Close-up photo of the VULCAIM vacuum chambers. Bottom: Schematic layout within VULCAIM.

Probing rare gas Rydberg states using Pulsed-Field-Ionisation (PFI) spectroscopy with VULCAIM

The previous Rydberg study was repeated using the same laser setup, this time on VULCAIM. The corresponding spectra are presented in Fig. 1.30.

Compared to the same study on ICARE (see Fig. 1.31), much higher energy states can be observed with VULCAIM (up to $n = 80$ in Ar and $n = 130$ in Kr) and the typical resolution is now around a few 10^{-2} cm^{-1} . The secondary peaks in the spectra are also a lot less visible than before. All of these observations point towards the reduction of stray fields in VULCAIM compared to Icare. As the resolution (see Fig. 1.32) is close to the resolution of the Cobra-Stretch

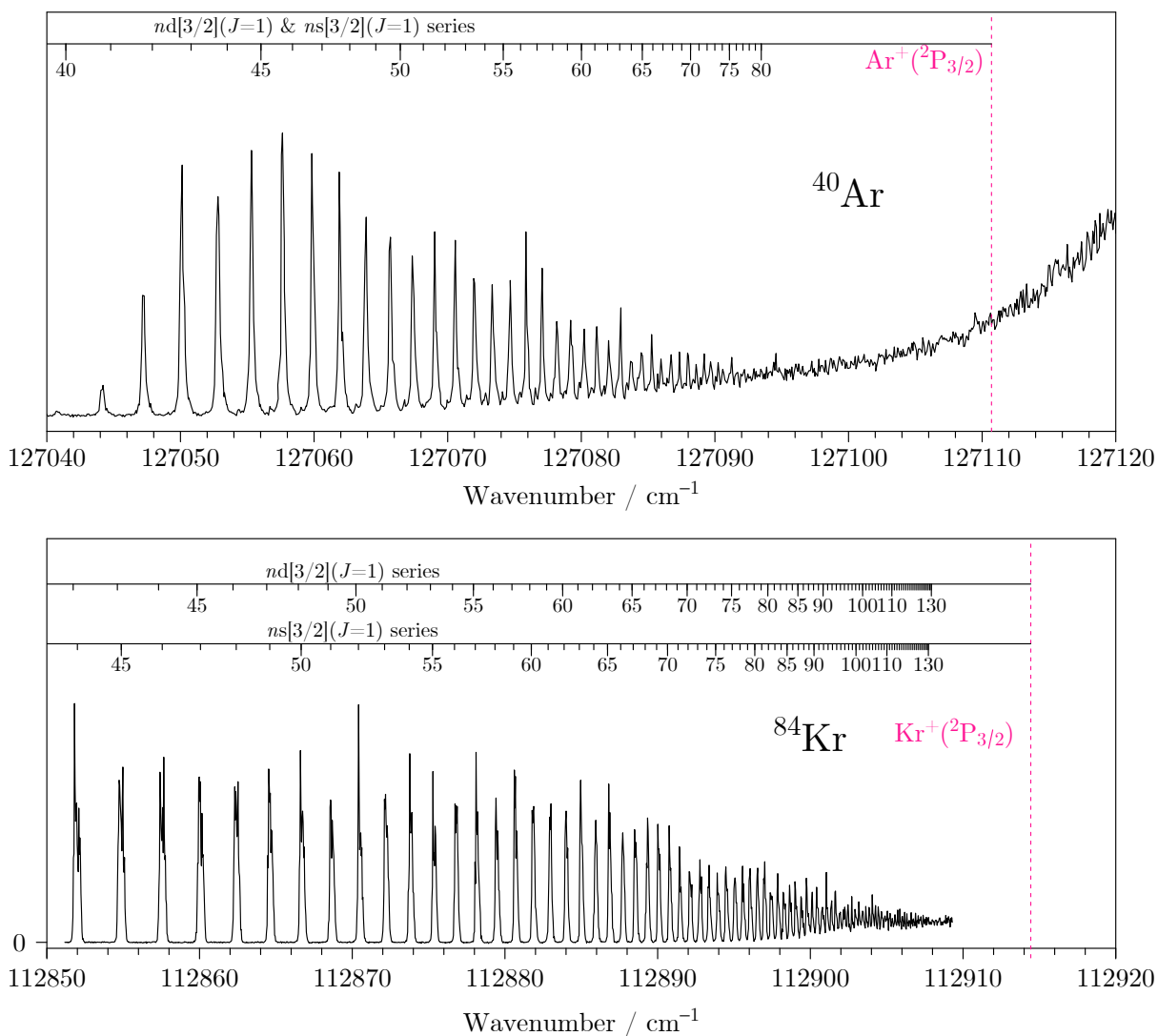


FIGURE 1.30: VULCAIM PFI spectra of Rydberg series of Ar (top) and Kr (bottom) converging to their first *IP*s, the ground states of their respective ions (noted in pink). Rydberg states are resolved and visible for up to $n \approx 80$ in Ar and $n \approx 130$ in Kr.

visible dye laser (see Fig. 1.21), the *ultimate* resolution would appear to be reached for this laser setup. Stray fields no longer appear to be limiting the resolution.

The highest resolution recorded on VULCAIM is 0.06 cm^{-1} and was measured using the $39d[3/2](J=1)$ Rydberg State of ^{82}Kr (see Fig. 1.32). The resolution was measured by placing a gaussian line over an experimental peak in the spectrum and adjusting the Full Width at Half Maximum (FWHM) to fit the experimental width. As previously stated, the spectrum is not Doppler-limited and as Rydberg states have very long life times, meaning that their natural bandwidths are very narrow and no other sources are responsible for resolution, the width of the total experimental spectral resolution is given by the photon resolution. Finally, given this maximum resolution, it is possible to deduce the maximum resolving power of VULCAIM which is greater than 4.10^6 , very impressive in any spectral domain, but especially so in the

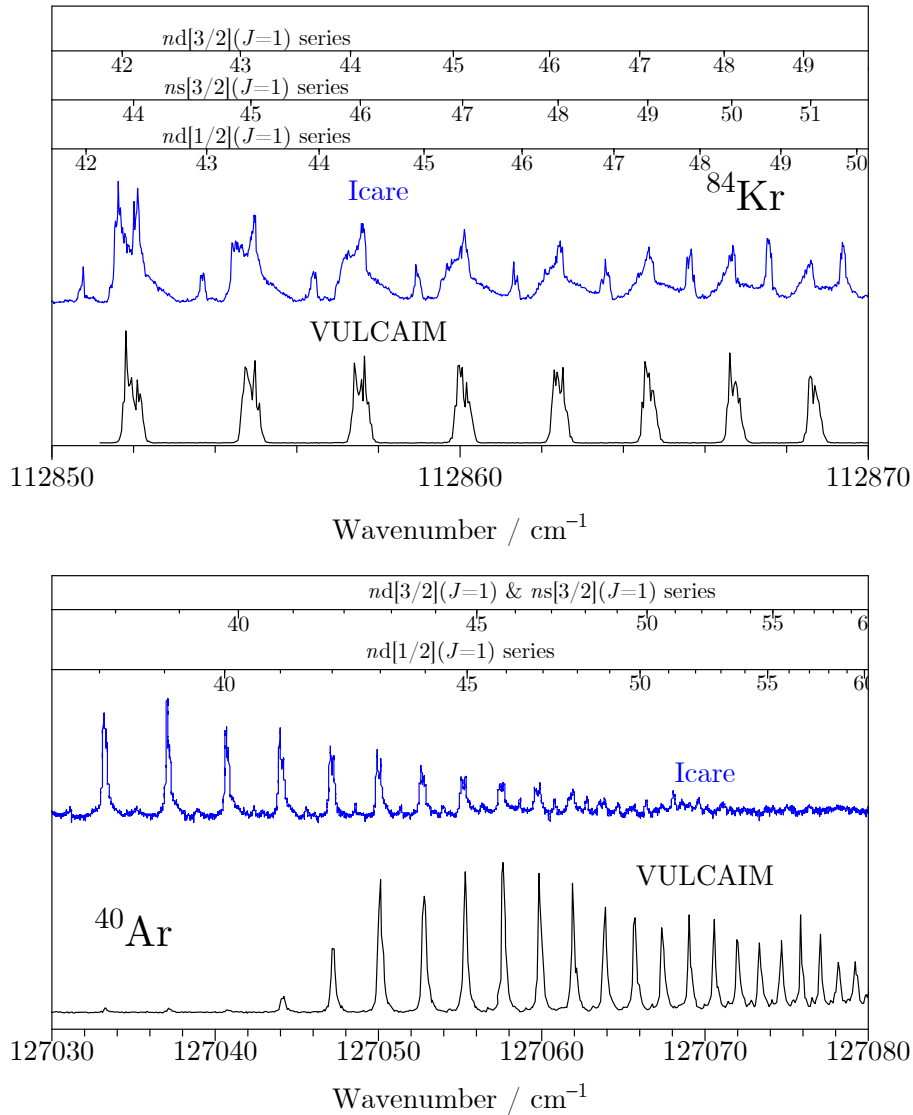


FIGURE 1.31: Comparative PFI spectra of Rydberg series of ^{84}Kr (top) and ^{40}Ar (bottom) recorded using Icare (blue) and VULCAIM (black). In the case of the Icare experiment, higher extraction fields were used which explains why Rydberg states of lower n are observed.

VUV.

This *ultimate* VUV resolution is strongly linked to the bandwidth of the visible laser used in the four-wave mixing scheme (see Fig. 1.13). Any deterioration in this laser has a direct and detrimental effect on the final resolution of the VULCAIM setup.

In a similar way to as presented previously using Icare in Fig. 1.28, it is possible to explore the effects of parasitic electric fields in VULCAIM. With Icare, the Stark broadening was taken as the main factor responsible for the experimental resolution. In the case of VULCAIM, the field does not appear to produce a loss in resolution as the resolution is close to that of the Cobra-Stretch. It is therefore only possible to set an upper limit for the electric field which is the electric field responsible for causing a Stark broadened envelope of Rydberg states at the

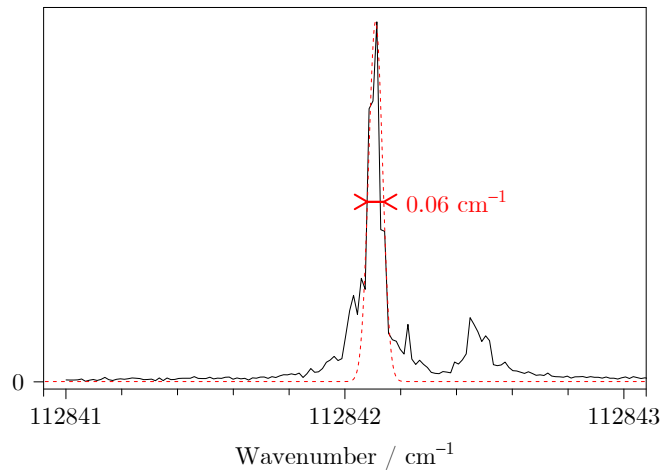


FIGURE 1.32: Maximum resolution measurement of photon resolution of VULCAIM using the $39d[3/2](J=1)$ Rydberg state in ^{82}Kr . A red dashed gaussian line whose FWHM= 0.06 cm^{-1} is superimposed on the experimental spectrum.

experimental spectral resolution. As shown by the black arrow in Fig. 1.33, the maximum field is around $0.2\text{ V}\cdot\text{cm}^{-1}$.

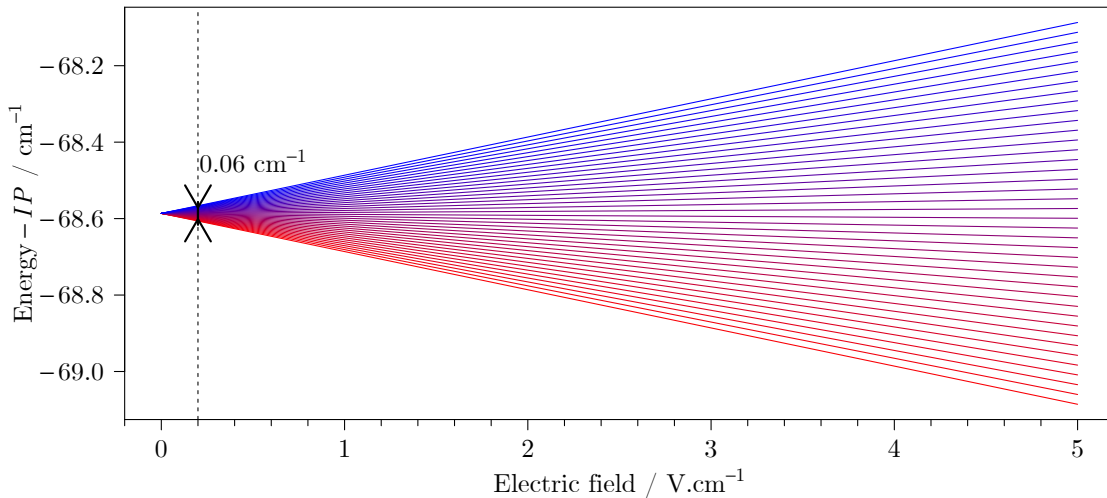


FIGURE 1.33: Simulated degeneracy lifting of a $n = 40$ Rydberg state with electric field F . Observation of blue and red shifted states. Black arrow at $F \approx 0.2\text{ V}\cdot\text{cm}^{-1}$ represents the upper limit for parasitic electric fields in the experiment.

Detecting electrons using VULCAIM

By simply inverting the polarity on the electrodes and the MCP detector, it is possible to detect electrons instead of ions. As electrons and ions cannot be collected simultaneously, the resulting photoelectron spectra are not mass-selective unlike with photoelectron spectra produced using the DELICIOUS 3 spectrometer at SOLEIL. This is not an issue as VULCAIM is only used in a reduced spectral range, to finely probe a transition whose energy is known, at least roughly; the

chance that a transition of another species occurs at the same energy is minimal. In any case, as the polarity can be switched back easily, it is always possible to record a mass spectrum to check which species are present in the setup.

Like the ions of the previous section, electrons are also collected using PFI, but these electric fields are applied in a manner so only electrons with ZERo Kinetic Energy (ZEKE) are recorded. The experimental techniques (PFI-ZEKE spectroscopy) involved in detecting electrons will be developed in chapter 3. The resulting spectral resolution will not only be given by the VUV photon linewidth, but also the photoelectron resolution; it remains, nevertheless, a high-resolution technique.

1.3 Complementary VUV light sources on the Saclay Plateau

In this chapter, two experimental setups have been presented, both in the VUV spectral domain and both able to probe similar molecular relaxation processes. They do however have very different characteristics which make them complementary as summarised in Table 1.10

TABLE 1.10: Characteristics of VUV light sources on the Saclay Plateau

	SAPHIRS branch of DESIRS (SOLEIL)	VULCAIM (ISMO)
Range / eV	6 - 40 , continuously	6 - 17, by ranges of $\approx 1000 \text{ cm}^{-1}$
Photon flux	$10^{10} - 10^{14}$ ph/s	$10^9 - 10^{10}$ ph/pulse*
Resolution / cm^{-1}	1	0.06
Resolving power	10^4	10^6
Typical acquisition time	1 h / 1 eV	1 h / 0.001 eV
Access time / yr	a few days	unlimited

*For ≈ 7 ns pulses at 20 Hz

The synchrotron setup presents itself as a medium high-resolution setup capable of scanning over a wide range quite quickly. It can therefore be used to study how observables continuously vary over a greater energy range. It can also be used to pinpoint much narrower spectral regions of interest that warrant a much higher resolution study which can be undertaken with VULCAIM. The exploration of large spectral ranges with VULCAIM is unrealistic due to the times involved. As it is a laboratory setup however, it offers unlimited access and time for instrumental developments, unlike the synchrotron whose access is granted for typically just a few days a year. Note also that the VULCAIM acquisition time does not take into account the time needed for changing spectral regions for the scan (laser dyes, different two-photon resonances in rare gases, reoptimisation from one sample to another, *etc.*).

Chapter 2

Ion yields and absolute photoionisation cross section measurements

In this chapter, I will present results concerning the measurement of ion yields on the DESIRS beamline (see chapter 1) and their absolute scaling to provide an important quantity: a photoionisation cross section. The photoionisation cross section of species A (σ_A^{ion}) quantifies photoionisation ($A + h\nu \rightarrow A^+ + e^-$) and can be defined using the ionisation probability per species per unit time (W_A^{ion}), such that

$$W_A^{\text{ion}} = \sigma_A^{\text{ion}} \times \phi, \quad (2.1)$$

with ϕ , the photon flux representing the number of photons irradiating the sample per unit area per unit time.

The definition stated in equation (2.1) implies that the cross section has the dimension of an area and can be interpreted as the ionisation probability per species per unit time, renormalised by a given photon flux. Another way of looking at it is: if N_A species are available,

$$\frac{dN_{A^+}}{dt} = W_A^{\text{ion}} \times N_A \quad (2.2)$$

$$= \sigma_A^{\text{ion}} \phi N_A, \quad (2.3)$$

which therefore represents the quantity of produced A^+ ions per unit time. Typical photoionisation cross section values are around 10^{-18} cm^2 , which is why the megabarn (Mb) unit is often used with $1 \text{ Mb} = 10^{-18} \text{ cm}^2$.

Motivations

From a fundamental perspective, photoionisation cross sections are of great interest. Measuring them against incident photon energy highlights fundamental information on the species of study.

In an astrophysical or atmospheric context, photoionisation can be a pathway through which a neutral stable species can produce a much more reactive charged species, which can in turn be implicated in complex photochemical networks. Photoionisation cross sections are important parameters that are used in astrophysical and atmospheric models to determine the initial quantity of reactive species. Despite their importance, they are not always well known due to measurement difficulties, especially when dealing with free radicals, which are the main focus of this chapter. When experimental data are not available, models rely on crude estimations, theoretical values, or even omit specific photoionisation processes.

Photoionisation cross sections are also of particular interest to the combustion chemistry and plasma physics communities. Quantitative measurements in these fields of research are often performed using photoionisation to probe quantities of neutral species in their experiment by mass spectrometry. Photoionisation cross sections are then required to relate the number of produced ions to the quantity of neutral species in the probed environment.

The lack of data mainly concerns free radicals, as they are difficult to produce and quantify; to date, only a handful of free radical photoionisation cross sections are known. As summarised in Table 2.1, the free radicals in photoionisation cross section studies are generally produced by chemical reactivity, pyrolysis or by photodissociation of a stable species using a UV laser. The ionising step relies often on VUV laser or synchrotron radiation [6].

During this PhD, in the context of cometary or planetary photophysics, such experiments involving mass spectrometry were performed in the aim of determining photodissociation branching ratios for NH_3 photolysis, (see Appendix A). To extract branching ratios for the fragmentation channels from mass spectra, VUV photoionisation cross sections for the pertinent radical fragments are essential and had to be measured first.

This chapter will deal with previously unknown photoionisation cross sections of free radicals. I will begin by describing the general method for determining cross sections, before presenting two case studies: OH and NH_2 (expected fragment of NH_3 photodissociation). The final section of this chapter will deal with relative ion yields that are not yet set to an absolute scale.

TABLE 2.1: Summary of all known experimental photoionisation cross section measurements for free radicals

Species	Radical production method	Ionising probe	Energy range for cross section value(s) / eV	Ref.
NO	Commercially available	HeI and H ₂ lamps	9.2 - 21.4	[44]
OH	O(¹ D) reactivity or F flow tube	synchrotron	10.8 - 15.0	[45–47]
SH	F flow tube	synchrotron	10.4 - 15.0	[48]
ClO	laser photodissociation	VUV laser	10.85 - 15.74	[49]
OCIO	laser photodissociation	VUV laser	10.35 - 13.33	[49]
HO ₂	CH ₃ OH oxidation	synchrotron	10.5 - 12.0	[50]
HCO	laser photodissociation	VUV laser	10.257, 10.304, and 10.379	[51]
	O + C ₃ H ₆ reactivity	synchrotron	8.0 - 12.5	[52]
NH ₂	F flow tube	synchrotron	10.8 - 15.7	^a
CH ₃	laser photodissociation, pyrolysis or NO ₂ reactivity	VUV laser or synchrotron	9.0 - 11.6	[53–55]
C ₂ H ₃	laser photodissociation	synchrotron	8.0 - 11.0	[56, 57]
C ₂ H ₅	laser photodissociation, pyrolysis or F flow tube	VUV laser or synchrotron	8.0 - 12.1	[58, 59]
c-C ₃ H ₂	pyrolysis	synchrotron	(8.8 - 9.8)	[60]
C ₃ H ₃	laser photodissociation	VUV laser or synchrotron	8.4 - 10.6	[56, 61, 62]
C ₃ H ₅	laser photodissociation	synchrotron	7.75 - 10.75	[63]
C ₄ H ₅	F flow tube	synchrotron	7.9 - 11	[64]
C ₆ H ₅	laser photodissociation	synchrotron	7.8 - 10.8	[65]
C ₆ H ₅ O	laser photodissociation	VUV laser	10.486	[66]
Cl ₂ S(CH ₃) ₂	Cl ₂ flow tube	HeI lamp	21.22	[67]

^a To be published (see section 2.3).

2.1 Absolute photoionisation cross section determination: general method

2.1.1 Absolute photoionisation cross section measurement

In this work, as in many others, free radical photoionisation cross sections are measured in reference to known photoionisation cross sections of other species. Typically, the reference species is a stable molecule, *i.e.* the precursor leading to the radical. In this paragraph, aimed at explaining the general principle for such measurements, a precursor species noted P will be used to produce a radical noted R. In order to extract the unknown photoionisation cross section, ionisation experiments are conducted following the injection of species in two experimental conditions:

- situation 1: radical species are not produced from the precursor, only the precursor cation appears in the mass spectrum after ionisation (Fig. 2.1 a)),
- situation 2: radical production is induced from the precursor. The radical cation appears alongside the precursor cation in the mass spectrum (Fig. 2.1 b)).

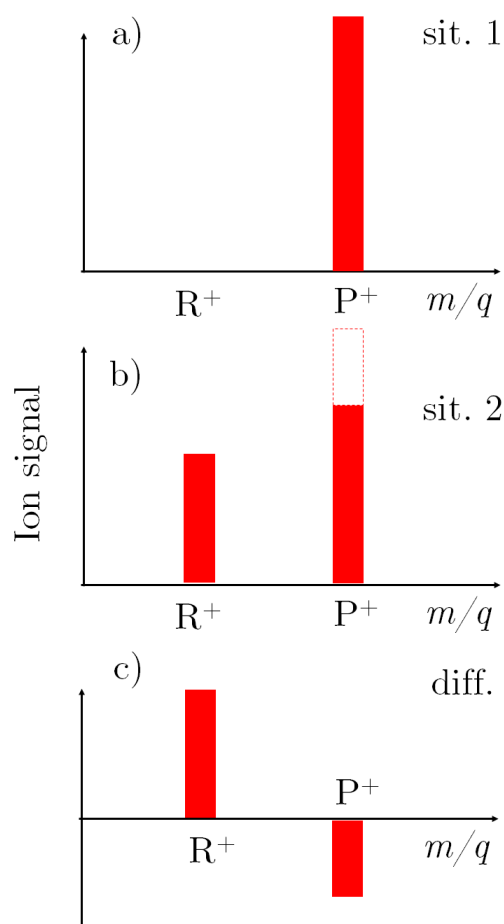


FIGURE 2.1: Illustration of mass spectra recorded in two experimental conditions. a) Only the precursor P is present in situation 1. b) Free radical species R are produced from the precursor in situation 2. c) The lowest spectrum is the difference spectrum b) - a).

The R photoionisation cross section determination lies in the analysis of the difference spectrum of Fig. 2.1 c).

Because of matter conservation and because only one reaction takes place, the quantity of formed radicals ΔN_R equals the quantity of consumed precursor molecules ΔN_P . This can be expressed mathematically as (2.4)

$$\Delta N_R = \Delta N_P. \quad (2.4)$$

After encountering the ionising radiation (with photon energy $h\nu_0$ above their *IP*), neutral species produce cations, which are subsequently detected. In mass spectrometry, the ion signal of a given species is taken as the temporal integration of the corresponding peak in the mass spectrum and is proportionate to the number of ion hits (see chapter 1). Relating the number of ionised species to the initial quantity of neutral species using the photoionisation cross section of equation (2.1), the ion signal (S_{R^+}) of the free radical cation in the mass spectrum is proportionate to the quantity of produced radicals

$$S_{R^+} = \sigma_R^{\text{ion}}(h\nu_0) \times N_R \times \phi(h\nu_0) \times f(m_R/q), \quad (2.5)$$

with:

- $\sigma_R^{\text{ion}}(h\nu_0)$, the R photoionisation cross section at photon energy $h\nu_0$,
- $\phi(h\nu_0)$, the photon flux,
- $f(m_R/q)$, the apparatus response function [68].

A similar relationship to equation (2.5) exists for any species detected in the mass spectrum. Using matter conservation (equation (2.4)), the equality governing ion signals (equation (2.5)) and by measuring spectral differences, it is possible to deduce the radical photoionisation cross section $\sigma_R^{\text{ion}}(h\nu_0)$ as a function of known or measurable quantities

$$\sigma_R^{\text{ion}}(h\nu_0) = \sigma_P^{\text{ion}}(h\nu_0) \times \frac{\Delta S_{R^+}}{\Delta S_{P^+}} \times \frac{f(m_P/q)}{f(m_R/q)}, \quad (2.6)$$

with:

- $\sigma_P^{\text{ion}}(h\nu_0)$, the known precursor photoionisation cross section,
- ΔS_{R^+} , the R^+ signal difference comparing spectra obtained in the two aforementioned conditions ($\Delta S_{R^+} = S_{R^+}^{\text{sit.2}} - S_{R^+}^{\text{sit.1}}$); Note that as no radical is produced in situation 1, $S_{R^+}^{\text{sit.1}} = 0$,
- ΔS_{P^+} , the P^+ signal difference comparing spectra obtained in the two aforementioned conditions ($\Delta S_{P^+} = S_{P^+}^{\text{sit.1}} - S_{P^+}^{\text{sit.2}}$). The order is inverted compared to ΔS_{R^+} as the precursor is consumed rather than produced; this is also reflected in the change of sign in the schematic difference mass spectrum of Fig. 2.1 c),
- the same photon flux irradiates precursor and radical species and therefore simplifies in the fixed energy measurements.

2.1.2 Uncertainty determination

After measuring the photoionisation cross section following the procedure described above, it is important to determine reliable error bars. This is an important step as the cross section will

be used in various atmospheric and/or astrophysical models, as well as in the determination of photodissociation branching ratios, that also require uncertainties on their input values in order to provide meaningful and reliable results.

Referring to equation (2.6), there are various possible sources of error. Firstly, the precursor photoionisation cross section values are often used from the literature along with their error bars. Conventionally, these are given at 2σ , *i.e.* a 95% confidence interval that the actual value is within the error bars.

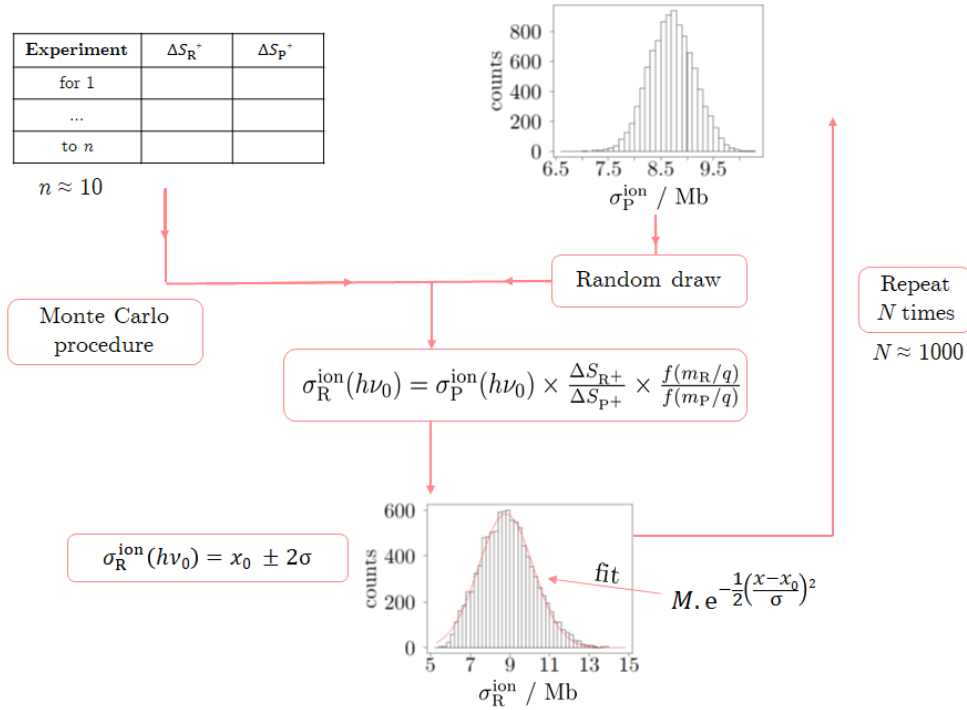


FIGURE 2.2: Block diagram of the Monte Carlo uncertainty propagation procedure generating the R photoionisation cross section distribution, whose mean value is taken as the final cross section value and two standard (2σ) deviations constitute the error bars

As for the uncertainties on experimentally measured values, multiple mass spectra are recorded in order to perform statistical analysis. The series of mass spectra can be recorded in varying experimental conditions. Typically around 10 values are recorded for one absolute measurement determination, this means recording 10 spectra in situation 1 (precursor alone) and 10 in situation 2 (with radical production) allowing the determination of 10 ΔS_{R^+} and ΔS_{P^+} values. The dispersion of experimental data is approximately equal to or less than the uncertainty on the precursor cross-section in order to maintain a gaussian distribution in the radical cross-section.

The radical photoionisation cross section error is achieved by using a Monte-Carlo uncertainty propagation procedure. It is true that equation (2.6) is simple enough to obtain error bars using the typical uncertainty calculations with partial derivatives, but the analysis is sometimes more complicated in some cases (parasitic reactions, apparatus function,...). The Monte-Carlo uncertainty propagation procedure is then convenient.

Firstly, a gaussian distribution of precursor cross section values is generated, whose central value is the reported cross section value from the literature and the standard deviation equates to half the reported uncertainty value (given supposedly at 2σ). The number of points in this

distribution is derived through trial and error: too few and the distribution is not evenly gaussian, too many and the computational time is too long. Around 1000 points is typical. A loop is then implemented, selecting one precursor value at random from the distribution and one experimental couple of ΔS_{R^+} and ΔS_{P^+} values from the table; this allows the determination of one radical photoionisation cross section value. This process is repeated during the 1000 loop cycles (again determined by trial and error) and all generated radical cross section values are re-grouped in a distribution, which can be modelled as a gaussian distribution. Taking the median value and the standard deviation yields a final cross section value and associated uncertainty taken as two standard deviations. This Monte-Carlo procedure is summarised in Fig. 2.2.

The energy uncertainty (of the absolute measurement and of the relative spectrum) is accounted for when scaling the cross section over the whole scan range. This procedure will be described at the end of paragraph 2.1.5.

2.1.3 Ion yields

Before measuring a photoionisation cross section value, an ion yield for the studied radical must be recorded. The means of recording an ion yield were explained in section 1.1.3 of chapter 1. An ion yield is the same curve as a photoionisation cross section except that the y -axis is completely arbitrary. This means that the intensity of each point of the spectrum is only known relatively to the others.

Ion yields are corrected for the incident photon flux which is energy-dependent. The uncertainty on this correction, mainly related to the beamline photodiode response function is neglected. This is justified as the statistical error on the photodiode is less than 2% even if the spectral response can vary over time, due to carbon pollution for example, in an unquantifiable manner.

Measuring a photoionisation cross section at one fixed photon energy ($h\nu_0$) within the range of the ion yield allows the absolute scaling of the ion yield, thus producing photoionisation cross section values over the whole range; fixing one point in the spectrum fixes all remaining points in the spectrum. After recording an ion yield, the next step is then choosing the photon energy ($h\nu_0$) for the absolute measurement. The photoionisation cross section can also be recorded at several photon energies to increase overall reliability.

2.1.4 Choosing the photon energy for the absolute measurement

In rough terms and referring to Fig. 1.7 of chapter 1, an ion yield can be represented as a step function or a series of step functions punctuated by resonances which appear as sharp and sometimes imposing peaks. When probing resonances, much care must be taken as the measured height and width of these resonances are extremely resolution-dependent as illustrated in Fig. 2.3. In this figure, a simulated pair of resonances is convoluted by a gaussian line shape whose $FWHM$ (Full Width at Half Maximum) is 0.5, 2 and 5 times the natural $FWHM$ of the resonance. This simulates the measurement of the resonance experimentally by gradually lower resolved setups. Note the changes in height, width, but the peak areas remain constant from curve to curve.

In order to correctly sample the doublet of resonances, the experimental spectral resolution must be less than the resonance's natural width. If the spectral resolution exceeds the width of the desired resonance, the width and height (*i.e.* intensity) are distorted. In extreme cases, this can result in structure loss; *e.g.* the transition of a pair of closely-spaced resonances to a wide single-resonance (red trace in Fig. 2.3). If the spectral resolution is negligible compared to each

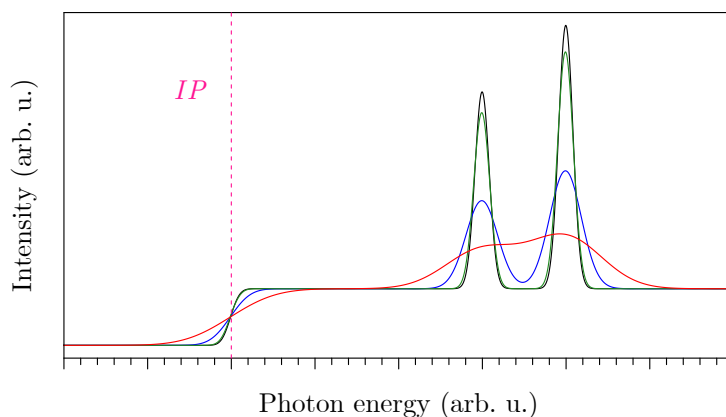


FIGURE 2.3: Effect of experimental resolution on measured resonance (schematic illustration). A simulated pair of resonances (black line) corresponding to the energy difference between energy states is measured using apparatus whose resolution is 0.5 (green), 2 (blue) and 5 (red) times the natural width of the resonance.

resonance's natural width, the real widths of the resonances can be measured (green trace in Fig. 2.3).

In order to measure intensities that are not resolution-dependent, it is important to identify regions in the ion yields that do not present resonances. It is in these regions that absolute measurements will be made. In addition and when possible, absolute measurements and ion yields will be recorded at the same resolution. This means that if absolute measurements are inadvertently conducted on a resonance, the recorded resonance is deformed, but in the same manner in both the ion yield and the absolute measurement, which renders both measurements compatible.

Furthermore, it is also important to conduct absolute measurements at energies away from electronic cationic state thresholds. In particular, the energy should be chosen outside regions presenting non-negligible FCF (Franck-Condon Factors) values in both the precursor and the radical. The main reason for this is the internal energy dependency of the ion yield in these regions.

In short, the photon energy for the absolute measurement should be chosen in a spectral region that is neither temperature-dependent nor resolution-dependent.

The main steps for recording photoionisation cross sections of free radicals are summarised in Table. 2.2:

2.1.5 Specificities to our experimental setup

In our setup, the precursor corresponds to a H-bearing molecule. Injected into the flow-tube reactor (see section 1.1.3), it undergoes F-induced H-abstraction reactions to produce radicals. The two situations described previously are realised by switching the microwave discharge producing F atoms on and off :

- situation 1: microwave discharge off, no F atoms are produced, which means no radical species are produced either; only the precursor cation appears in the mass spectrum after ionisation (Fig. 2.1 a)), and

- Ionise R and record R^+ ion yield,
- Measure absolute value for R photoionisation at a given energy $h\nu_0$,
- Set previously measured ion yield on absolute scale cross section.

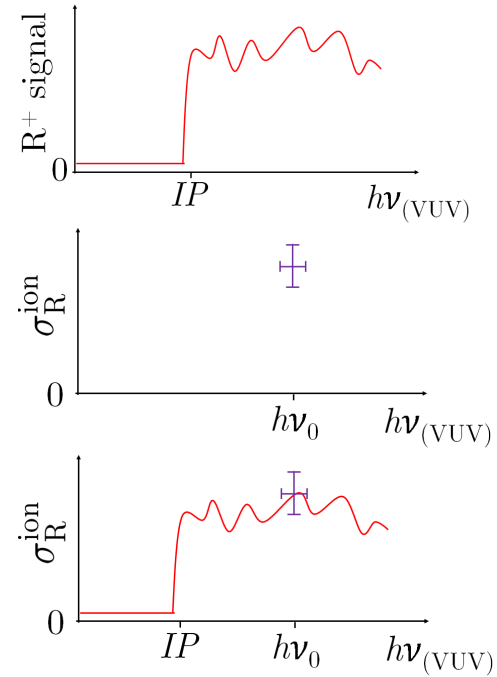


TABLE 2.2: Summary of the photoionisation cross section determination method

- situation 2: microwave discharge on, F atoms are produced, which induce radical production from the precursor. The radical cation appears alongside the precursor cation in the mass spectrum (Fig. 2.1 b)).

As the produced radicals only differ from the precursor by 1 or 2 atomic mass units, the apparatus response function, $f(m/q)$, can be assumed constant in this reduced m/q range. This particular radical source hence presents a great advantage for cross section measurements over other experiments (in which the precursor and radical have very different masses), since there is no need to perform measurements of $f(m/q)$.

The focus on the uncertainties so far has been on errors on the y -axis (cross sections, ion signals...), but there are also errors on the x -axis, related to energy, noted δE . Two sources of error can be identified:

- the error on the ion yield energy scale calibration, using absorption lines from the beam-line gas filter or known autoionisation features in the ion yield. This error is evaluated on a case-by-case basis, and
- the error on the delivered photon energy ($h\nu_0$) for the fixed-energy measurements. The position of the DESIRS beamline monochromator indicates the photon energy to within 10 meV.

These errors are accounted for when setting the relative ion yield using the absolute fixed-energy ($E_0 = h\nu_0$) measurement to a cross section scale. This is achieved once more using a Monte Carlo procedure. The scaling factor is determined a number of times, each time varying the point within an interval $E_0 \pm \delta E$ in the ion yield at which the scaling takes place. The dispersion of scaling factors yielded through this process transforms the error on the x -axis to an error on the y -axis. This error is combined with the previously discussed y -axis error obtained using the Monte-Carlo procedure of section 2.1.2.

2.2 The absolute photoionisation cross section of the hydroxyl (OH) free radical

An application of the above procedure led to the determination of the hydroxyl (OH) free radical absolute photoionisation cross section [46, 47].

2.2.1 The OH free radical: current state-of-the-art

In atmospheric chemistry, the OH radical, thanks to its strong oxidising properties, has been called "the Ajax of the atmosphere" for its role in cleansing the atmosphere as a sort of detergent [69]. In a wide variety of astrophysical media, OH is implicated in chemical cycles and in particular the water regeneration cycle [70, 71]. The $\text{OH} + \text{H}_2 \rightarrow \text{H}_2\text{O} + \text{H}$ reaction has a significant activation barrier, which means that OH mainly reacts with C-, N- and O-bearing compounds yielding CO, NO or O_2 for example rather than H_2O . However, the OH^+ cation readily reacts with H_2 producing H_2O^+ which in turn can react with H_2 generating H_3O^+ . The dissociative recombination of H_3O^+ can then form H_2O , see Fig. 2.4.

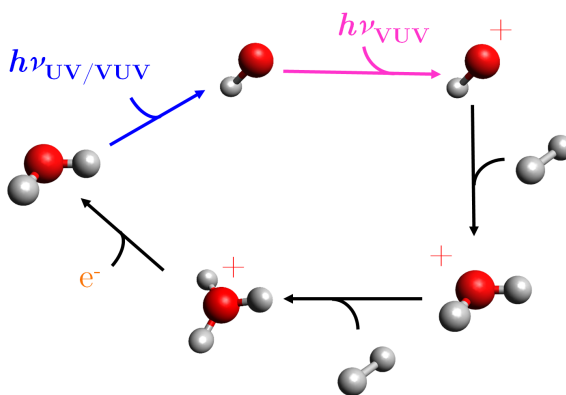


FIGURE 2.4: Typical astrophysical water regeneration cycle featuring the photoionisation of OH (pink arrow)

Before starting the experiments, there was no experimental value for the OH photoionisation cross section. Experimentally, only relative ion yields had been recorded from 13 to 18.2 eV at around 1 meV resolution. These were undertaken by Dehmer followed by Cutler *et al.* [72, 73] who assigned spectral features to autoionising Rydberg states converging to excited electronic states of the cation. Models relied on theoretical values [74, 75] or completely ignored OH photoionisation. For example, OH photoionisation does not feature in the Meudon PDR (Photon-Dominated-Region) code [76] or in the Leiden database [8].

Whilst analysing our data, the first experimental photoionisation cross section measurement was published by Dodson *et al.* [45]. Unlike our means of producing free radicals *via* F-induced H-abstraction, their OH radicals were produced through the $\text{O}(^1\text{D}) + \text{H}_2\text{O}$ reaction, the $\text{O}(^1\text{D})$ being itself produced from ozone flash-photolysis. The setting to an absolute scale was less obvious in their study because the OH production occurred in a complex chemical network involving 18 reactions (see Table II of ref. [45]). The comparison between their findings and ours will be discussed in paragraph 2.2.4.

2.2.2 The OH⁺ photoion yield

Implementing the procedure described in section 2.1, the OH radical was produced in the flow-tube reactor by H-abstraction initiated by F atoms on H₂O. An ion yield was recorded from 12.8 to 15 eV at 4 meV resolution (see Fig. 2.5) which compares well with those previously mentioned. Slight differences in resonance widths and intensities exist, but these can be attributed to differences in spectral resolution (see Fig. 2.3 for explanation). Known autoionisation resonances [72, 73] in the OH⁺ ion yield were used to calibrate the energy scale to within 3 meV.

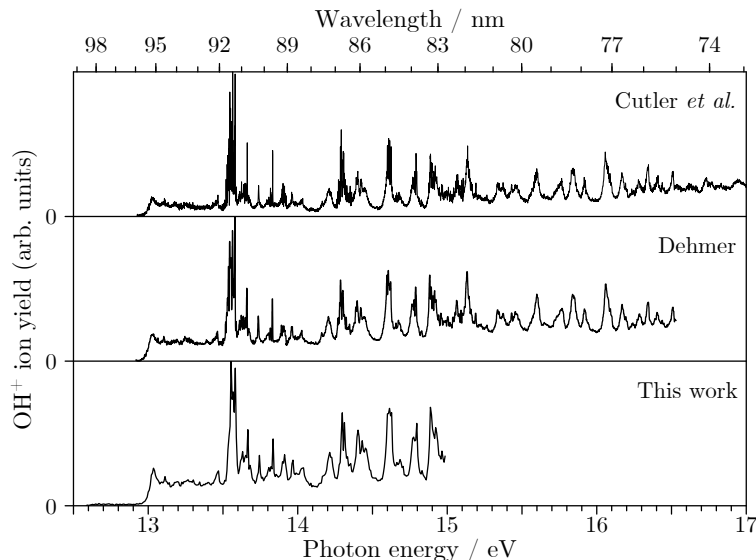


FIGURE 2.5: OH⁺ ion yields from Cutler *et al.* (top) [73], Dehmer (middle) [72] and this work (bottom) taken from ref. [46, 47].

From these ion yields, it is necessary to find an energy ($h\nu_0$) for the absolute measurement in a spectral region that is:

- free of OH resonances,
- located above all vibrational levels of the OH⁺ electronic ground state with non negligible FCF upon ionisation [77], and
- located between the transitions towards the two lowest electronic states of H₂O⁺.

The last two criteria guarantee that no internal energy in OH (and possibly H₂O) can affect the ion yield at the fixed-energy of the absolute measurement (see for instance the discussion in ref. [55] on CH₃). 13.800 eV was selected as a suitable photon energy for the fixed energy absolute measurements. At this photon energy, several O-bearing compounds pertinent for the flow-tube operating mode can be ionised, as shown in Table 2.3.

2.2.3 The fixed energy measurement of the OH photoionisation cross section

Mass spectra recorded at $h\nu_0 = 13.800$ eV are presented in Fig. 2.6 for discharge on and discharge off conditions. The production of OH is clear from the presence of mass 17 assigned to OH⁺, only visible when the F producing discharge is on. However, conditions could never be adjusted to eliminate mass 16, assigned to O⁺ produced by double H-abstraction of H₂O before

TABLE 2.3: Ionisation Potentials (IP) of species implicated in the OH photoionisation cross section determination of this work.

Species	IP / eV	m/q (a.m.u.)
O	13.61806 [78]	16
OH	13.0170 [79]	17
H ₂ O	12.62656 [80]	18

ionisation. The O⁺ signal is not caused by the dissociative ionisation of O₂; the threshold for this relaxation channel is reported to be above 17 eV in many works [21]. It is unlikely to stem from the dissociative ionisation of OH at photon energies within 2 eV of the IP , although the threshold for dissociative ionisation of OH is not known to our knowledge.

The production of O in addition to OH by H abstraction means that the matter conservation equation (2.4) must be modified as follows:

$$\Delta N_{\text{H}_2\text{O}} = \Delta N_{\text{OH}} + \Delta N_{\text{O}} \quad (2.7)$$

and then

$$\frac{\Delta S_{\text{H}_2\text{O}^+}}{\sigma_{\text{H}_2\text{O}}^{\text{ion}}(h\nu_0)} = \frac{\Delta S_{\text{OH}^+}}{\sigma_{\text{OH}}^{\text{ion}}(h\nu_0)} + \frac{\Delta S_{\text{O}^+}}{\sigma_{\text{O}}^{\text{ion}}(h\nu_0)}, \quad (2.8)$$

assuming the same $f(m/q)$ function for all three masses. This slightly complicates the radical cross section expression:

$$\sigma_{\text{OH}}^{\text{ion}}(h\nu_0) = \frac{\Delta S_{\text{OH}^+}}{\frac{\Delta S_{\text{H}_2\text{O}^+}}{\sigma_{\text{H}_2\text{O}}^{\text{ion}}(h\nu_0)} - \frac{\Delta S_{\text{O}^+}}{\sigma_{\text{O}}^{\text{ion}}(h\nu_0)}} \quad (2.9)$$

Despite the complication, equation (2.9) still only contains measurable quantities (signal differences) or parameters available in the literature (O and H₂O photoionisation cross sections at $h\nu_0$).

Concerning the atomic oxygen cross section, the corresponding curve (see Fig. 2.7, bottom) resembles a step function (≈ 3 Mb on the plateau) punctuated by very intense resonances at 14.1 eV as described by Angel and Samson [82]. These data were independently found to be the most reliable in an independent review [83]. The value at 13.800 eV can be extracted by interpolating data which plateau in this region: $\sigma_{\text{O}}^{\text{ion}}(13.8 \text{ eV}) = 3.08 \pm 0.25$ Mb. Noting this low photoionisation cross section value and bearing equation (2.5) in mind, despite a very small mass signal, a considerable quantity of atomic oxygen is produced and should not be neglected.

As for the H₂O photoionisation cross section, it was determined by Fillion *et al.* [81] by separately recording the absorption cross section and the ionisation quantum yield η^{ion} defined as the ratio between ionisation and absorption cross sections ($\sigma_{\text{R}}^{\text{ion}} = \eta^{\text{ion}} \times \sigma_{\text{R}}^{\text{abs}}$). The photoionisation cross section presents oscillations which originate from the photoabsorption cross section. Fillion *et al.* assigned these structures to vibrational progressions of Rydberg series converging to the two lowest excited states of H₂O⁺. As their spectra were recorded at 25 meV photon resolution and ours at 4 meV, these structures may not have the same widths and intensities if they depend on their spectral resolution. In order to test this dependency, we measured the H₂O photoabsorption cross section at the ion yield resolution of 4 meV. This was done on the VUV FT branch of the DESIRS beamline [22]. The ionisation quantum yield does not present any visible features so was not remeasured. The newly measured photoionisation cross section

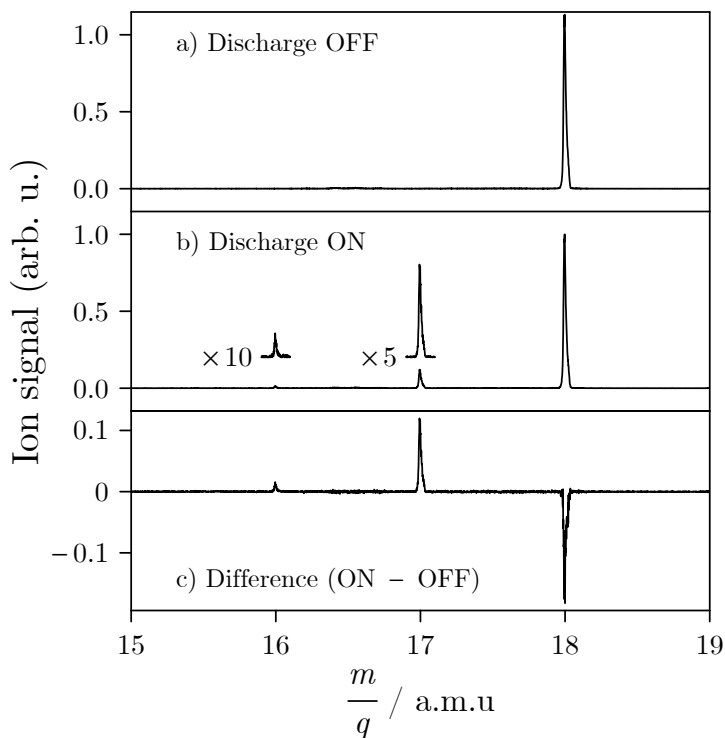


FIGURE 2.6: Mass spectra recorded at 13.800 eV with the F-atom-producing discharge off (top) and on (middle) and the difference spectrum (bottom). The same arbitrary unit is used in all spectra.

presents the same resonances as those reported by Fillion *et al.* (see Fig. 2.7, top), which confirms that Fillion *et al.*'s measurement was not limited by the spectral resolution. Their cross section values can be used in our data treatment despite resolution differences. In particular at 13.800 eV, $\sigma_{\text{H}_2\text{O}}^{\text{ion}} = 8.7 \pm 0.8$ Mb.

Alongside the OH^+ ion yield presented in the lower panel of Fig. 2.5, the integration of mass peaks at $m/q = 16$ and 18 a.m.u. over the scan range produces O^+ and H_2O^+ ion yields. These ion yields can be set to an absolute scale using the previously mentioned literature values yielding photoionisation cross section values over the whole scan range. All of these cross sections are summarised in Fig. 2.7.

20 experiments were performed yielding 10 mass spectra with the radical source on and 10 others with the radical source off (see Fig. 2.6). These were used in the Monte Carlo procedure of Fig. 2.2 to determine an OH photoionisation cross section value at 13.800 eV: $\sigma_{\text{OH}}^{\text{ion}} = 9.0 \pm 2.7$ Mb (with a 2σ confidence level). To justify the importance of the atomic oxygen correction, we can recalculate the cross section neglecting O. This leads to a cross section of only 7.1 Mb, over 20% lower than the corrected value. Although the O^+ signal is quite weak, its non-negligible impact is explained by the low photoionisation cross section of O at 13.800 eV.

2.2.4 The OH photoionisation cross section from threshold up to 15 eV.

Using the value at 13.800 eV, the OH^+ ion yield can be set to an absolute scale thus producing photoionisation cross section values from 12.8 to 15 eV (see Fig. 2.8). Error bars can also be carried over the whole range by maintaining the relative uncertainty constant (blue area in

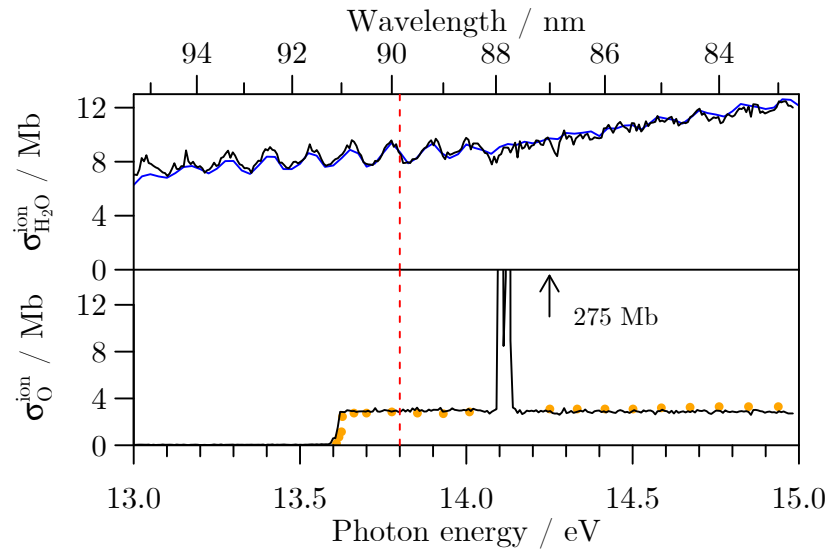


FIGURE 2.7: Measured H_2O^+ (top) and O^+ (bottom) set to an absolute photoionisation cross section scale respectively using data from Fillion *et al.* (blue line) [81] and Angel and Samson (orange dots) [82]. Note the vertical scale of the lower panel is cut truncating the atomic oxygen resonances around 14.1 eV. The red dashed vertical line marks the photon energy (13.800 eV) of the absolute measurements of this work.

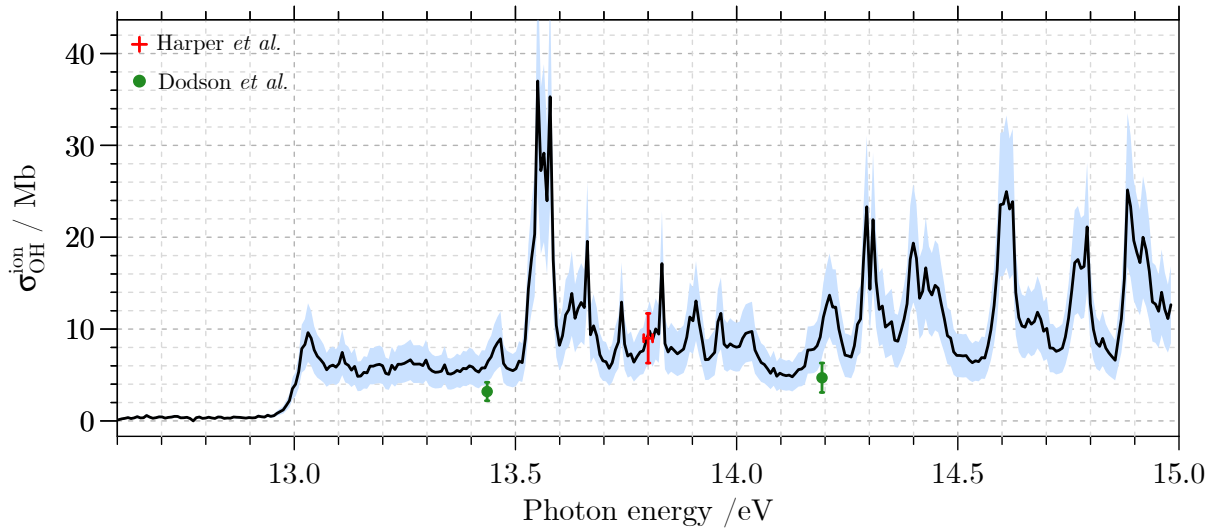


FIGURE 2.8: Absolute photoionisation cross section of OH from this work [46, 47] (black curve) as a function of photon energy; the blue area represents the error bars presented with a 2σ confidence level. They take into account both the error bar on the cross section value, and the uncertainty on the photon energy value (absolute measurement as well as scaling of the photoion yield). The red cross at 13.800 eV constitutes the absolute fixed energy measurement and associated uncertainty. The green points represent the absolute measurements from Dodson *et al.* [45] performed at 13.346 and 14.193 eV.

Fig. 2.8). During this scaling process, error bars on the x -axis (energy scale) are also accounted

for, following the procedure described in paragraph 2.1.5. There is a 10 meV uncertainty on the energy of the absolute measurement and 3 meV accuracy for the ion yield spectrum. There is no overlap between the values from this work and those of Dodson *et al.* [45] or the respective error bars (green dots in Fig. 2.8).

The discrepancy between both results is not understood. We investigated potential causes within our method and data as discussed in the supplementary material of ref. [46], but no sources of error could be found. In fact, in many cases, the possible sources of error (other parasitic reactions, wall effects, *etc.*) would actually increase our values, thus further distancing the two values rather than uniting them.

As for comparison to theoretical works, Stephens and McKoy [74] found non-resonant continuum values at around 4 Mb so in good agreement with Dodson *et al.* More advanced calculations employing many body perturbation theory yielded higher values (around 12 Mb at 14 eV) which are in better agreement with our findings [75].

Finally, this study shows that, because of both experimental and theoretical disagreements, more work is needed on the OH photoionisation cross section. It also highlights the challenge of such measurements and explains why they are so scarce in the literature.

2.2.5 A follow-up study

The OH photoionisation cross section results presented so far were achieved during experimental campaigns undertaken in 2018; the results were published in early 2019 [46] followed by an erratum in 2020 due to a slight correction on the calibrated photon energy scale [47]. The results of the previous section use the corrected energy scale.

In order to settle the disagreement with Dodson *et al.*, more absolute measurements were undertaken in the summer of 2019 during a second experimental campaign. Unlike the first injector used in 2018 (and in all other absolute measurements presented in this manuscript) presenting a single exit hole into the reactor, a different injector was employed in this follow-up study presenting multiple exit holes into the reactor similar to a shower head. This increases the mixing of species within the reactor. The downside to this injector is the increase of wall effects on the produced radicals. We observed these effects as a drop in free radical ion signals at greater injector distances. For this reason, we only use mass spectra recorded at minimum injector distances to minimise these parasitic effects. As only one injector distance is used, it is not easy to derive cross section uncertainties, which is why no error bars will be provided in the follow-up study measurements.

A photon energy of 14.505 eV was firstly selected for a first measurement as it corresponds to a zone free of resonances in the OH⁺ ion yield and is above the ionisation potential of atomic oxygen still present in the spectra. A second absolute measurement was carried out in the same experimental conditions at 13.250 eV, in a flat region in the OH⁺ ion yield, but below the atomic oxygen *IP*. In order to account for the formation of O atoms at this lower energy, the proportion of H₂O consumed to produce atomic oxygen was extrapolated from the 14.505 eV measurement.

Mass spectra, presented in Fig. 2.9 and recorded at both energies, are very similar, except for the presence of O⁺ only at 14.505 eV. Another feature in both sets of mass spectra is the O₂⁺ signal, present notably in the difference spectra of panels c) and f). This shows that O₂ is not only present in the experiment, but actually produced by the discharge. Molecular oxygen can be produced either by self-reaction of atomic oxygen (2O → O₂) or with the OH radical (O + OH → O₂ + H). In any case, its production must be accounted for in the matter conservation

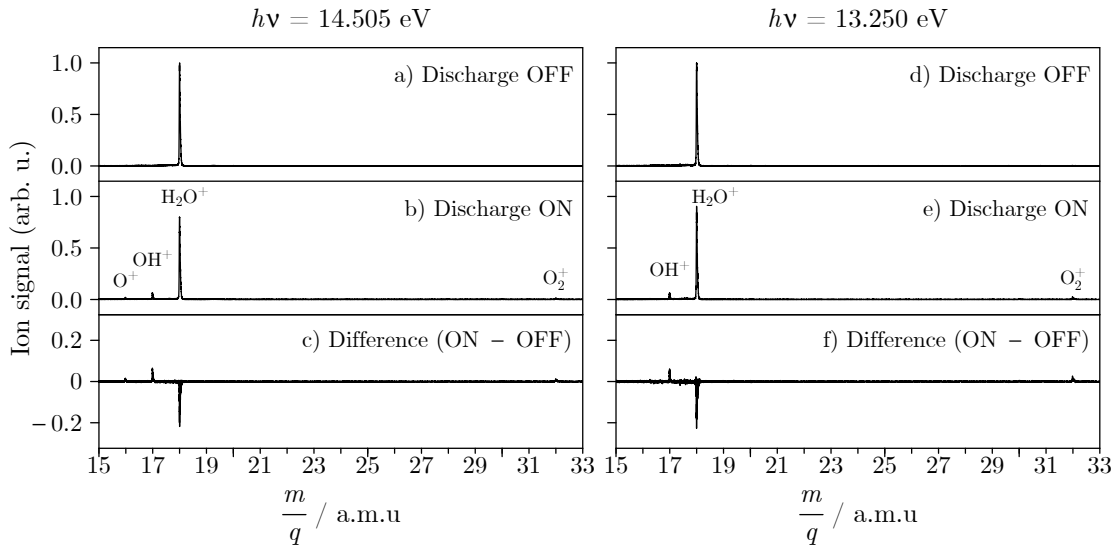


FIGURE 2.9: Mass spectra recorded at 14.505 eV (left-hand panels) and 13.250 eV (right-hand panels) with the F-atom-producing discharge off (top) and on (middle) and the difference spectrum (bottom). For each energy, the same arbitrary unit is used in three corresponding panels.

equation:

$$\Delta N_{H_2O} = \Delta N_{OH} + \Delta N_O + 2 \times \Delta N_{O_2}. \quad (2.10)$$

The O_2^+ signal is related to the produced quantity of neutral O_2 via the known photoionisation cross section [84]. Apart from this correction and the O production extrapolation at 13.250 eV, the OH photoionisation cross section is determined as in the original study. Cross section values are deduced at 14.505 and 13.250 eV and compared to values obtained using our previous work and also the work of Dodson *et al.* [45], as summarised in Table 2.4.

TABLE 2.4: OH photoionisation cross section values.

Measurement	σ_{OH}^{ion} (13.250 eV) / Mb	σ_{OH}^{ion} (13.800 eV) / Mb	σ_{OH}^{ion} (14.505 eV) / Mb
Harper <i>et al.</i> [46, 47]	5.9 ± 1.8	9.0 ± 2.7	6.7 ± 2.0
Follow-up study	5.9	-	8.6
Dodson <i>et al.</i> [45]	3.0 ± 0.8 *	4.6 ± 1.2 *	3.4 ± 0.9 *

* value achieved by setting our OH^+ ion yield to an absolute scale using both data points and error bars of Dodson *et al.*

These new values (see Table 2.4) are compared with our previous results and those of Dodson *et al.*'s at 13.250 and 14.505 eV achieved by setting our ion yield to an absolute scale using their two absolute measurements (the procedure for scaling an ion yield using multiple fixed-energy cross section points will be detailed in paragraph 2.3.4). The new value at 13.250 eV is in excellent agreement with our previous work. The value at 14.505 eV however is situated above the two previously published results, but both points are within the error bars of the original study.

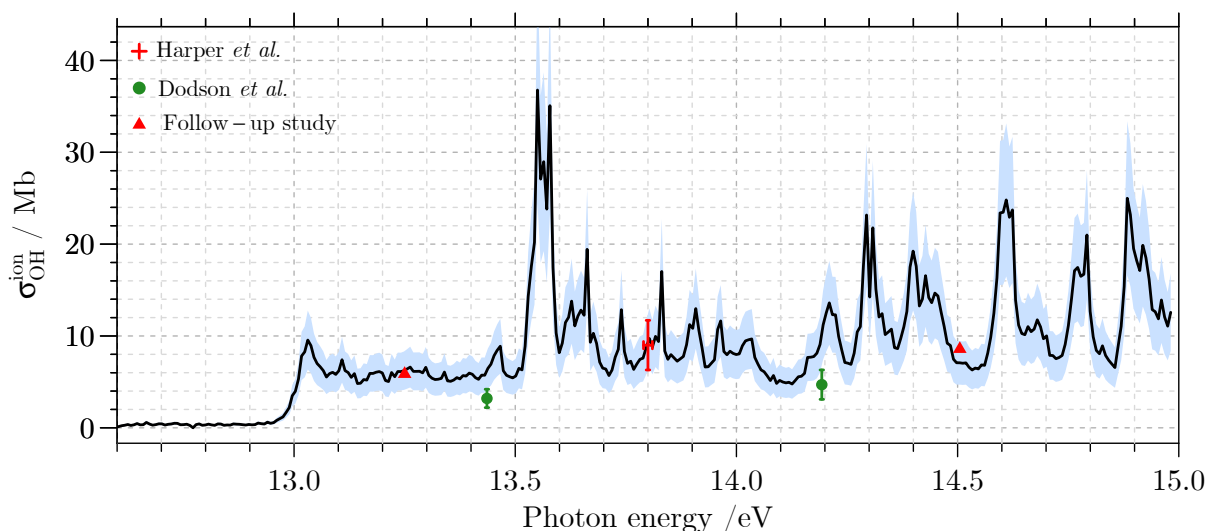


FIGURE 2.10: Absolute photoionisation cross section of OH from this work (black curve) as a function of photon energy from ref. [46, 47]; the blue area represents the error bars presented with a 2σ confidence level. The red cross at 13.800 eV constitutes the absolute fixed energy measurement and associated uncertainties on both x - and y -values from ref. [46, 47]. The green points represent the absolute measurements from Dodson *et al.* [45]. Red triangles represent cross section values determined in this follow-up study at 13.250 and 14.505 eV.

In the light of this follow-up study, it would seem that our previously published results have been verified and reproduced. As Dodson *et al.*'s values do not intercept our error bars, but only narrowly, the question may still not be settled. Once again, more work is needed to be able to decide. In particular, an experiment relying on an OH radical production method not used within this work or that of Dodson *et al.* would be of great interest to independently solve the disagreement. More tests are also required to better understand the behaviour of the shower-head injector and way it modifies kinetics compared to using the single-hole injector.

2.3 The absolute photoionisation cross section of the amino (NH₂) free radical

Another free radical cross section of great astrophysical interest and determined in this work is that of NH₂. No absolute cross section of this free radical has been reported in the literature to our knowledge.

2.3.1 The NH₂ free radical: current state-of-the-art

The amino radical or amidogen (NH₂) is a molecule of great astrophysical interest. In a similar way to ammonia, NH₃, it constitutes a building block from which more complex N-bearing species can derive (polycyclic nitrogen-containing hydrocarbons, amino acids, proteins, *etc.*). Additional reactivity can be expected from neutral NH₂, an open-shell species, and even more from the NH₂⁺ cation which is a double radical, isoelectronic to the methylene radical CH₂. NH₂ is present in many astrophysical media in the gas phase [85–87] and within or in the close vicinity of solids (grains and ices) [88, 89] and is implicated in chemical reactions therein. Sandford *et al.* [88] reported, for example, the formation of pyrimidine in ices containing H₂O, NH₃, CH₃OH, and CH₄ following UV photolysis. They went on to expose the major role that neutral NH₂ then plays in reacting with pyrimidine to form cytosine, a nucleobase.

At the time of writing, no absolute photoionisation cross section of NH₂ has been published to our knowledge. Only a relative NH₂⁺ ion yield from threshold up to 16.6 eV has been measured by Gibson *et al.* [90]. In their study, NH₂ was produced by H-addition onto N₂H₄ which initiated a set of reactions finally producing NH₂.

In addition, NH₂ is one of the major fragments formed in the UV/VUV photolysis of ammonia (see Appendix A). Ammonia is an important constituent of many astrophysical environments, including the comae of comets such as Churyumov-Gerasimenko, recently probed by the ROSINA spectrometer [91]. Understanding the photochemistry of NH₃ is essential to constrain the nitrogen chemistry in these media. In the laboratory, its photodissociation fragments can be probed by photoionisation coupled to mass spectrometry to derive photodissociation branching ratios (see preliminary study of Appendix A). In this context, determining the photoionisation cross section for NH₂ is an important step to gain insight into such photochemical processes.

Implementing the procedure described in section 2.1, the NH₂ radical was produced during this PhD in the flow-tube reactor by H-abstraction initiated by F atoms on NH₃. Commercially sourced NH₃ (> 99.96% purity) was used as the gas sample, seeded in He. This method of producing NH₂ was also employed by Holzmeier *et al.*, also on the DESIRS beamline, in order to study the vibrational structure of NH₂⁺ *via* TPES. They compared this production method to the pyrolysis of methyl hydrazine or diphenylmethylamine.

2.3.2 The NH₂⁺ ion yields

Firstly, an ion yield for $m/q = 16$ a.m.u. was recorded from 10.8 to 15 eV at 4 meV resolution, see Fig. 2.11. The photon energy was calibrated to within 4 meV using Ar absorption lines present in the gas filter. Our ion yield compares well with that of the literature [90] with some slight exceptions for photon energies above 14 eV. Both rise characteristically slowly from the first *IP* to around 12.5 eV, *i.e.* the first excited state ($\tilde{a}^+ \ ^1A_1$) of NH₂⁺. During this increase, resonances punctuate the spectrum attributed to autoionising Rydberg states converging to the $\tilde{a}^+ \ ^1A_1$ state [92]. Above 12.5 eV, the ion yield is practically flat, but rises slightly at higher energies. In our

spectrum, dominant resonances are present at around 14.1 eV, the same resonances as in the O^+ ion yield recorded in the previous OH study. This observation shows that the O^+ signal contaminates our NH_2^+ ion signal, both cations being recorded in the same $m/q = 16$ a.m.u. mass channel. This contamination must be accounted for (see following paragraphs) at photon energies above the *IP* of O (*i.e.* 13.61806 eV [78]).

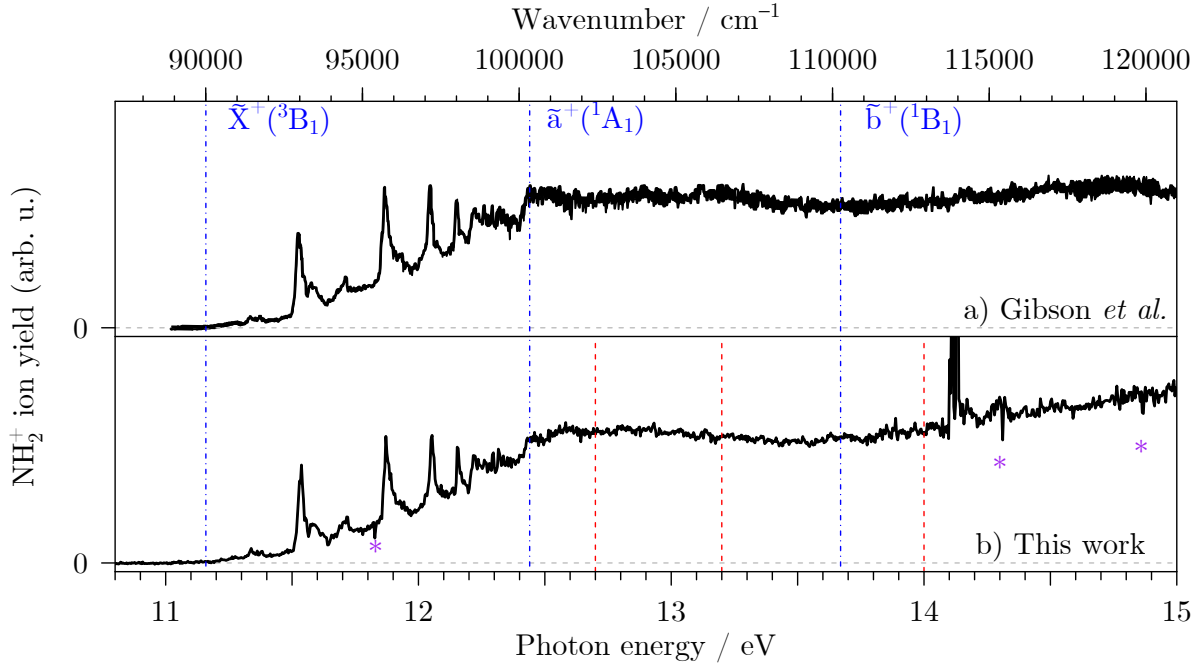


FIGURE 2.11: a) NH_2^+ ion yield from Gibson *et al.* [90]. b) Ion yield measured during this PhD for $m/q = 16$ a.m.u. attributed mainly to NH_2^+ . Sharp and imposing resonances at 14.1 eV are attributed to atomic oxygen autoionisation resonances. Purple asterisks mark Ar absorption lines from the beamline gas filter used to calibrate the photon energy. Both panels feature dot-dashed blue lines pinpointing the three lowest electronic states of NH_2^+ [92]. Panel b) contains dashed red vertical lines pinpointing the energies of the absolute measurements at 12.700, 13.200, and 14.000 eV.

TABLE 2.5: Ionisation potentials of species implicated in the NH_2 photoionisation cross section determination of this work.

Species	<i>IP</i> / eV	<i>m/q</i> (a.m.u.)
NH	13.48 [77]	15
O	13.61806 [78]	16
NH_2	11.1690 [93]	16
NH_3	10.186386 [94]	17
HF	16.03 [95]	20
N_2	15.5809 [96]	28
NO	9.26431 [97]	30
O_2	12.0697 [98]	32

2.3.3 Fixed energy absolute measurements

Three photon energies were selected for absolute photoionisation cross section measurements at 12.700, 13.200, and 14.000 eV. They all belong to the flat plateau region visible in Fig. 2.11 above 12.5 eV. Note that these fixed-energy measurements were recorded at the same spectral resolution as the NH_2^+ ion yield, but with a 10 meV precision imposed by the beamline monochromator.

Conditions in the flow tube reactor are optimised to favour the production of NH_2 , *via* single H abstraction, whilst quenching parasitic reactions: double H abstraction (producing NH) and radical-radical reactions (producing N_xH_y). Small signals of NH^+ can feature in some mass spectra, but are barely observable and are therefore neglected. The origins of signals around $m/q = 30$ a.m.u. are investigated as described in the following paragraphs.

A typical mass spectrum recorded at 13.200 eV is given in Fig. 2.12 b). The left-hand panels (panels a) to c)) show a healthy production of $m/q = 16$ a.m.u. assigned to NH_2^+ when the F-atom-producing discharge is on, *i.e.* when H-abstraction reactions can be initiated. Worryingly, water seems to be present as an impurity, its cation is visible when the discharge is off (panel a)), but no longer present when the discharge is turned on (panel b)). As seen in the previous OH study, H_2O is known to produce OH by F atom induced H-abstraction; OH^+ would contaminate the NH_3^+ signal at $m/q = 17$ a.m.u. In order to determine how water is consumed when the discharge is turned on, mass spectra were recorded in both discharge on and off configurations, but without injecting any ammonia. Typical mass spectra are reported in the right-hand panels of Fig. 2.12 recorded at a high photon energy (17.500 eV) so as to be able to ionise all species (see Table 2.5).

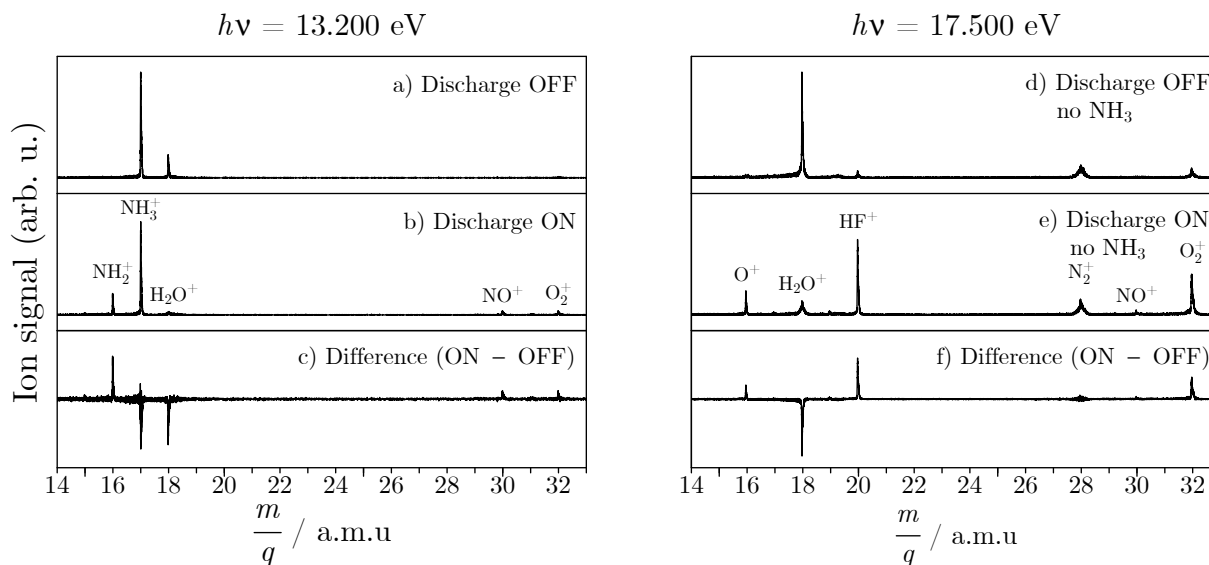


FIGURE 2.12: Left-hand panels a) to c): mass spectra recorded at 13.200 eV in NH_2 study. Spectra recorded with F-atom-producing discharge off (panel a)), on (panel b)) and difference spectrum (panel c)). Right-hand panels d) to f): mass spectra recorded at 17.500 eV in NH_2 study without injecting any NH_3 . Spectra recorded with F-atom-producing discharge off (panel d)), on (panel e)) and difference spectrum (panel f)). Mass peaks are assigned to various ionic fragments as indicated in the middle panel. The bottom panel shows which species are consumed (negative peaks) and which are formed by switching the F producing discharge on.

The ammonia-free spectra of Fig. 2.12 d) to f) show that H_2O is consumed by switching the discharge on, this means that the water contamination is situated upstream from the microwave discharge on the F_2 gas line. Focusing on the difference spectrum of Fig. 2.12 f), species whose peaks are negative are consumed by switching the discharge on and those with positive peaks are produced. It appears that H_2O is consumed producing O and HF ($\text{H}_2\text{O} + 2\text{F} \rightarrow \text{O} + 2\text{HF}$) and that O goes on to self-react producing O_2 ($2\text{O} \rightarrow \text{O}_2$). There also seems to be some reactivity with N_2 producing NO. All other species signals cancel out by performing spectrum differences which means that they are neither consumed nor produced by the discharge. In particular, OH does not exit the reactor (it is possible that OH is consumed by oxygen: $\text{O} + \text{OH} \rightarrow \text{O}_2 + \text{H}$). In the context of the NH_2 study, the main problem is the production of O which in turn contaminates the NH_2^+ signal after ionisation. This contamination was already noted in the $m/q = 16$ a.m.u. ion yield of Fig. 2.11.

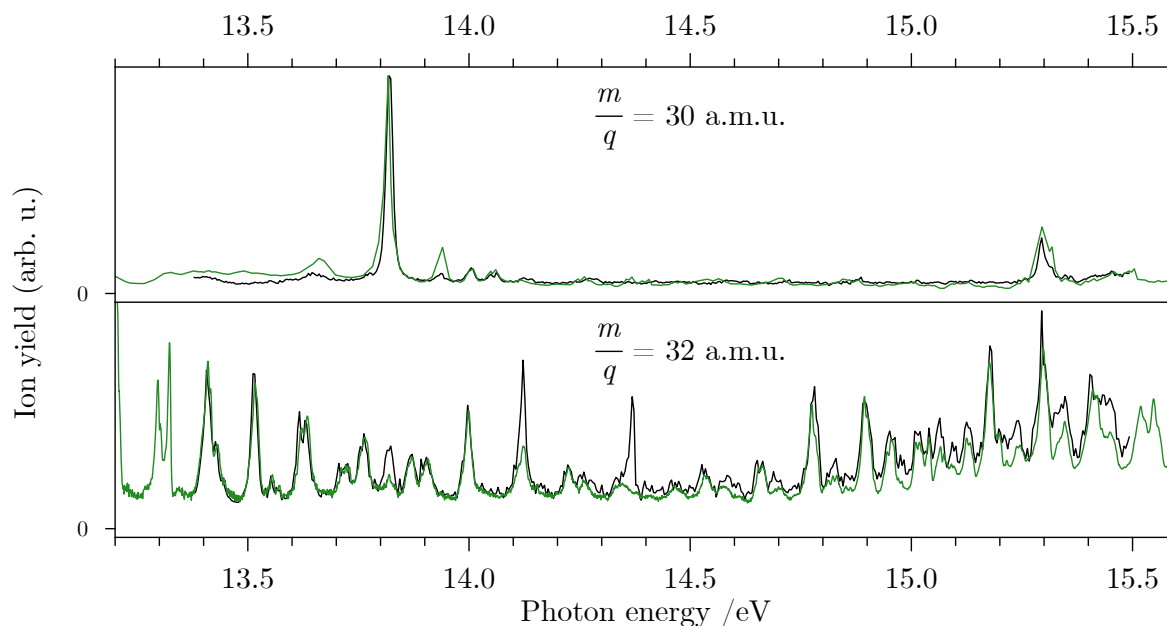


FIGURE 2.13: Top: ion yield of $m/q = 30$ a.m.u. of our study (black line) compared to the NO^+ ion yield of Watanabe *et al.* [44] (green line). Bottom: ion yield of $m/q = 32$ a.m.u. of our study (black line) compared to the O_2^+ ion yield of Holland *et al.* [84] (green line)

Another potential problem is the observation of mass signals at $m/q = 30$ and 32 a.m.u., that could be assigned to N_2H_2^+ and N_2H_4^+ , respectively. This would be a problem as these species would be the result of radical-radical reactions, consuming NH_2 and thus falsifying the matter conservation $\Delta N_{\text{NH}_3} = \Delta N_{\text{NH}_2}$. However, the 17.500 eV mass spectra (of Fig. 2.12 e)) reassuringly also contain $m/q = 30$ and 32 a.m.u. signals despite no NH_3 being injected into the setup. These signals were therefore assigned to NO^+ and O_2^+ , respectively. On top of this, $m/q = 30$ and 32 a.m.u ion yields were recorded and compared to known NO^+ [44] and O_2^+ [84] ion yields (see Fig. 2.13). The excellent agreement between the ion yields, mainly the position and width of autoionisation resonances, confirms $m/q = 30$ and 32 a.m.u as NO^+ and O_2^+ . Comparatively, there is no increased baseline in our ion yields either, which would indicate underlying N_2H_2^+ or N_2H_4^+ signals. Thus, this verification allows us to rule out any NH_2

consumption in forming the N_2H_2 and N_2H_4 species, and to secure our data treatment taking into account the contamination by atomic O only.

2.3.4 NH_2 photoionisation cross section determination

Along with the mass spectra recorded at 17.500 eV, the dominant resonances at 14.1 eV in our $m/q = 16$ a.m.u ion yield (see Fig. 2.11 b)) are proof of O^+ contamination of the channel containing the NH_2^+ signal; the same resonances were observed in the O^+ spectrum recorded in the OH study, see Fig. 2.7. Spectra in both the OH study and this study were recorded at the same 4 meV photon resolution.

Firstly, matter conservation dictates that the consumed quantity of NH_3 corresponds to the produced quantity of NH_2 : $\Delta N_{NH_3} = \Delta N_{NH_2}$. Relating the neutral quantities to ionic signals and remembering the $m/q = 16$ a.m.u signal has contributions from both O^+ and NH_2^+ for photon energies **above** $IP(O)$, the photoionisation cross sections can be expressed as a function of mass signals in equation (2.11):

$$\frac{\Delta S_{NH_3^+}}{\sigma_{NH_3}^{\text{ion}}(h\nu_0)} = \frac{\Delta(S_{\frac{m}{q}=16} - S_{O^+})}{\sigma_{NH_2}^{\text{ion}}(h\nu_0)}. \quad (2.11)$$

The ammonia photoionisation cross section is well known, in this work we used the values of Samson *et al.* [99]. $S_{\frac{m}{q}=16}$ is the total ion yield of $m/q = 16$ a.m.u. **Below** $IP(O)$, this expression is simplified to the usual form:

$$\frac{\Delta S_{NH_3^+}}{\sigma_{NH_3}^{\text{ion}}(h\nu_0)} = \frac{\Delta S_{NH_2^+}}{\sigma_{NH_2}^{\text{ion}}(h\nu_0)}. \quad (2.12)$$

This means that the NH_2 photoionisation cross section can be reliably determined **below** $IP(O)$. This was done using two measurements at 12.700 and 13.200 eV yielding NH_2 photoionisation cross sections (see Table 2.6) using the usual general method (see paragraph 2.1). These absolute measurements allowed the scaling of the NH_2^+ ion yield from threshold to $IP(O)$ following the same scaling procedure and uncertainty determination (on x - and y -values) as with the OH cross section of paragraph 2.2.

TABLE 2.6: NH_2 absolute photoionisation cross section values

Photon energy / eV	$\sigma_{NH_2}^{\text{ion}} / \text{Mb}$
12.700	7.8 ± 2.2
13.200	7.8 ± 2.0
14.000	$7.7^* \pm 2.8$

* given as an indication, see text for details

The scaling **above** $IP(O)$ contains O^+ contributions and can be written as follows:

$$\sigma_{\frac{m}{q}=16} = \sigma_{NH_2}^{\text{ion}} + p \times \sigma_{O^+}^{\text{ion}}. \quad (2.13)$$

The coefficient p represents the fraction of $m/q = 16$ a.m.u. signal stemming from O^+ hits. It can be evaluated by comparing the 14.1 eV resonances in the $m/q = 16$ a.m.u ion yield and those in the O^+ ion yield of the OH study (see Fig. 2.7). In the O^+ photoionisation cross section measured with a 4 meV photon resolution (see Fig. 2.7), the most intense resonance had a maximum height of 275 Mb. Subtracting the underlying continua in both spectra and integrating the resonances, p is simply given as the ratio between the integral of the resonance in the $m/q = 16$ a.m.u ion yield of this study and that in $\sigma_{\text{O}^+}^{\text{ion}}$ of the previous OH study. This procedure yields $p = 13\%$.

Above $IP(\text{O})$, $\sigma_{\text{NH}_2}^{\text{ion}}$ is achieved by subtracting $p \times \sigma_{\text{O}^+}^{\text{ion}}$ to the previously scaled NH_2^+ ion yield (see Fig. 2.13). The O^+ contamination is actually quite low as the continuum values for $\sigma_{\text{O}^+}^{\text{ion}}$ are very low, around 3 Mb [82], compared to typical continuum values for $\sigma_{\text{NH}_2}^{\text{ion}}$, around 8 Mb. This is why no step was observed in the $m/q = 16$ a.m.u. ion yield around $IP(\text{O})$ which would correspond to the appearance of O^+ . The minor O^+ correction can be extended over the whole spectrum at photon energies above $IP(\text{O})$. The cancellation of the 14.1 eV resonance could not be achieved by this subtraction as the resonance was not sampled at the same points, the overall integral is vanishing, but the corrected peak presents positive and negative values. For this reason, the final spectrum is cut at this energy (see Fig. 2.14 a)).

The two fixed-energy values at 12.700 and 13.200 eV are also used to scale the ion yield of Gibson *et al.* [90] over the whole range producing photoionisation cross section values from threshold up to 15.7 eV. Although the ion yield of Gibson *et al.* extends to 16.6 eV, they report that the NH_2^+ signal above 15.7 eV contains contributions from NH_3 dissociative ionisation. We therefore limit the scaling to the region below 15.7 eV (see Fig. 2.14 b)).

A third absolute measurement of the NH_2 photoionisation cross section was performed at 14.000 eV, so above the IP for O (*i.e.* 13.61806 eV [78]): $\sigma_{\text{NH}_2}^{\text{ion}}(14.000 \text{ eV}) = 7.7 \pm 2.8 \text{ Mb}$ (orange cross in Fig. 2.14). At this energy, the $m/q = 16$ a.m.u. mass channel signal contains contributions from O^+ so this cross section value is derived using the same O^+ correction procedure as with the ion yield. Nevertheless, since the ion yield and this absolute measurement were not recorded in exactly the same experimental conditions, especially concerning H_2O or O_2 contamination, the O^+ contribution may not be the same as previously. For this reason, this cross section is just given as an indication and not used to scale the NH_2^+ ion yield. It is still in excellent agreement with the scaled cross section at 14.000 eV, which supports the validity of the two previously determined points. It also indicates that O^+ contributions do not have too big an impact on NH_2 photoionisation cross section values.

It is noteworthy here, as in the OH follow-up study, that the good agreement between absolute measurements recorded at different fixed energies and the resulting scaled ion yield also indicates that the photon flux is successfully corrected, and that uncertainties on the photon flux correction can indeed be neglected.

These newly achieved cross section values can be compared to those available in databases intended to be used in models. The Leiden database [8], for example, proposes NH_2 photoionisation cross section values using the NH_2^+ ion yield of Gibson *et al.* [90] set to an absolute scale using the **arbitrarily** chosen value of 20 Mb at 15.5 eV. These values are compared to our own in Fig. 2.15. The arbitrary scaling factor used in this database overestimates cross section values by around a factor 2 and thus leads to the overestimation of NH_2 photoionisation processes in models relying on this database. This work is therefore an example of the importance of measuring the photoionisation cross sections of molecules of astrophysical interest, especially of free radicals, in order to refine models.

The first experimental determination of the NH_2 photoionisation cross section presents new experimental possibilities for deriving the NH photoionisation cross section, which has never been determined experimentally. Compared to the NH_2 study, flow-tube conditions will

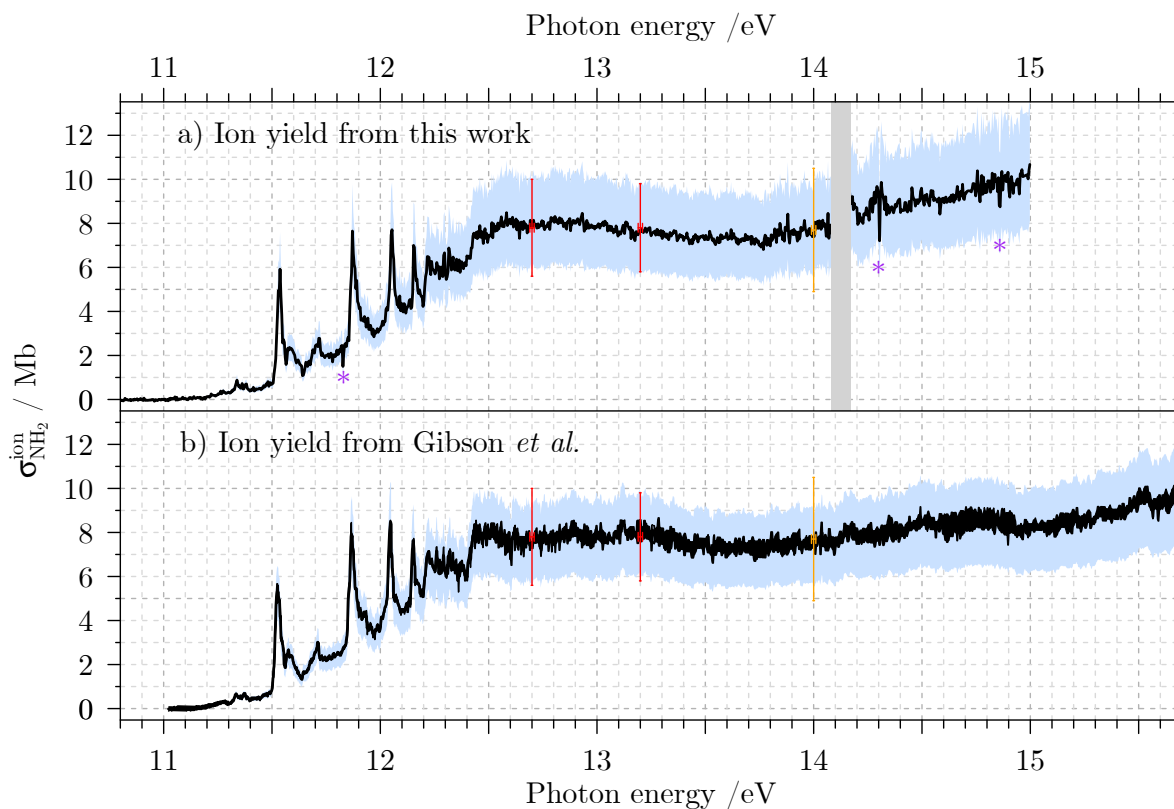


FIGURE 2.14: NH_2 photoionisation cross section as a function of photon energy. Panels a) and b) display our ion yield and the ion yield of Gibson *et al.* [90]), respectively, set to an absolute scale using our fixed-energy values at 12.700 and 13.200 eV, noted in red along with their respective error bars (see Table 2.6). An orange cross marks a fixed-energy cross section value at 14.000 eV, corrected for O^+ contributions, but not used in the scaling of the ion yield. The blue area denotes error bars extended over the whole range. A grey area in the top panel around 14.1 eV masks the O^+ resonance that could not be corrected, cross section values could not be determined in this narrow area. Drops in the spectrum due to gas filter absorption lines also constitute points where cross section values cannot be determined (purple asterisks).

be modified to allow two H-abstraction reactions on NH_3 whilst preventing radical-radical reactions forming N_2H_4 , N_2H_2 , *etc.*, but the method is the same.

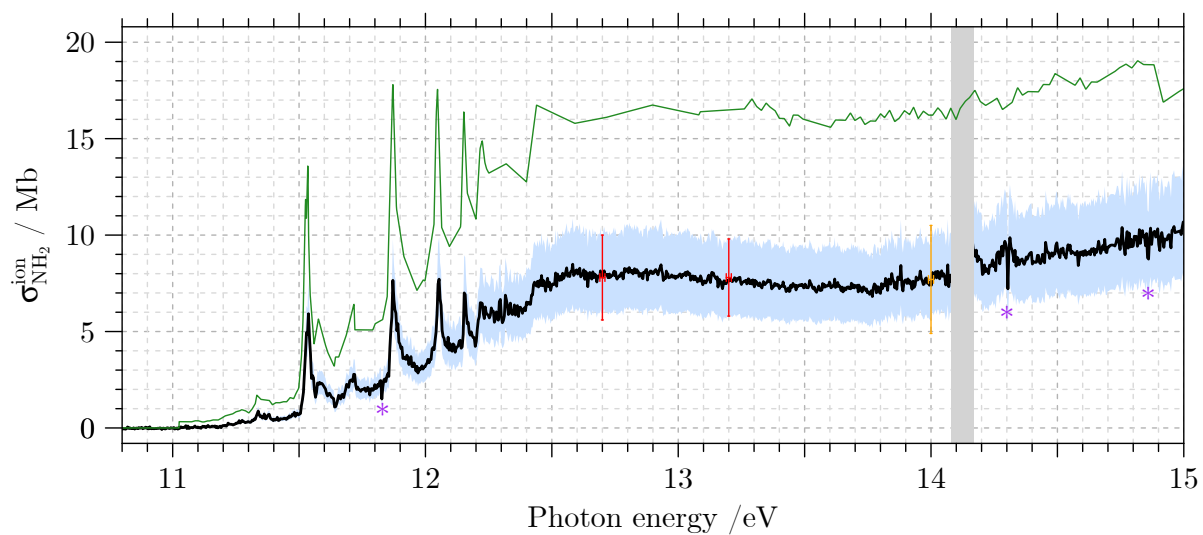


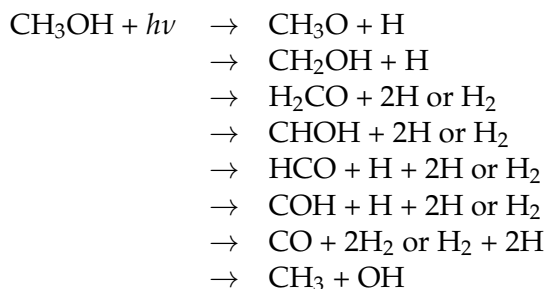
FIGURE 2.15: NH_2 photoionisation cross section as a function of photon energy. All values and notations are the same as in Fig. 2.14 a) with in addition a green line representing NH_2 cross section values from the Leiden database [8].

2.4 Preliminary study on the carbonated fragments of methanol

2.4.1 Context and motivation

The knowledge of photoionisation cross sections is not only important for astrophysical and atmospheric applications, but also for all quantitative experiments when the produced quantity of ions needs to be determined with reference to the initial quantity of neutral species (using equation (2.6) in particular). Within the context of this PhD, the link between neutral and ionic products was needed when studying photodissociation processes probed by single-photon ionisation and mass spectrometry (see Appendix A). As the dissociation products are often free radicals, the corresponding photoionisation cross sections, enabling the quantification of the ionisation process, are generally not known.

In the case of methanol (CH_3OH) photodissociation, at the Lyman- α radiation wavelength (121.6 nm) for instance, the following fragmentation channels are thermodynamically allowed and have to be considered (see also Appendix A):



Except for CH_3 [53–55] and OH [45–47] the photoionisation cross section values for all the other free radical carbonated products are unknown. The HCO photoionisation cross section has only been determined at three discrete energies (not at the Lyman- α photon energy) [51], or using very large energy steps (≈ 0.5 eV) [52]. All photoionisation cross sections of the stable or atomic species featuring in the above channels are known (CH_3OH [100], H_2CO [50], CO [101], H_2 [102] and H [103]). Hence, in connection with the study of photolysis processes undertaken during this PhD, an experimental campaign was conducted at SOLEIL in 2019 to tentatively measure the missing photoionisation cross section values, using a similar procedure to that exposed previously in this chapter. The free radicals were produced by F-induced H-abstraction reactions in the reactor source from the methanol precursor.

In this particular case, there is an increased difficulty with the production of isomer species, *i.e.* $\text{CH}_3\text{O}/\text{CH}_2\text{OH}$, $\text{CH}_2\text{O}/\text{HCOH}$, and HCO/CHO . Indeed, the two isomer products, once ionised, are undistinguishable by their m/q value in a mass spectrum. In photolysis experiments, the isomers can potentially be discriminated by tuning the ionising probe photon energy to in between the IP values of each isomer, thus selectively ionising one of them (if each ion yield (and/or cross section) is well known individually).

To get around this problem for cross section measurements, deuterated isotopologues can be used as the photoionisation cross sections are expected to be the same, at least in a first approximation, and the ionised products fall into different m/q channels. The d3-deuterated isotopologue of methanol, CD_3OH , was thus used in the same way as methanol, as a precursor in the flow-tube reactor to yield free radicals. Indeed, Deuterium (^2H), noted D, reacts in the same way with F atoms as H (^1H), with similar efficiency [104]. Table 2.7 summarises the expected products for the two studied isotopologues and their corresponding m/q values.

2.4.2 Specific experimental details

TABLE 2.7: m/q values and IPs of methanol isotopomers and their flow-tube products

Isotopologue	m/q (a.m.u.)	IP /eV	Isotopologue	m/q (a.m.u.)
CH ₃ OH	32	10.846 [105]	CD ₃ OH	35
CH ₃ O	31	10.72 [106]	CD ₃ O	34
CH ₂ OH	31	7.55 [106]	CD ₂ OH	33
CH ₂ O	30	10.8887 [107]	CD ₂ O	32
CHOH	30	8.86 [108]	CDOH	31
HCO	29	8.14 [109]	DCO	30
COH	29	not reported	COH	29

The means of producing and probing free radicals were exposed in section 1.1.3 of chapter 1. In this study, CD₃OH (purchased from Sigma-Aldrich, 99.8% D purity [110]) was used as precursor in addition to standard methanol. Deuterium rearrangements are possible, but the sample was delivered just before the beamtime and was only opened just before conducting the experiments, which lasted for under 5 hours. Rearrangement is also conceivable once in the experiment with impurities (*e.g.* H₂O), but such processes are more likely with O-bonded H rather than C-bonded H which should not affect CD₃OH [111]. Both samples were carried into the reactor source using a helium flow. The flow tube injector distance was set to 10 mm, and medium F₂ flow rates were used.

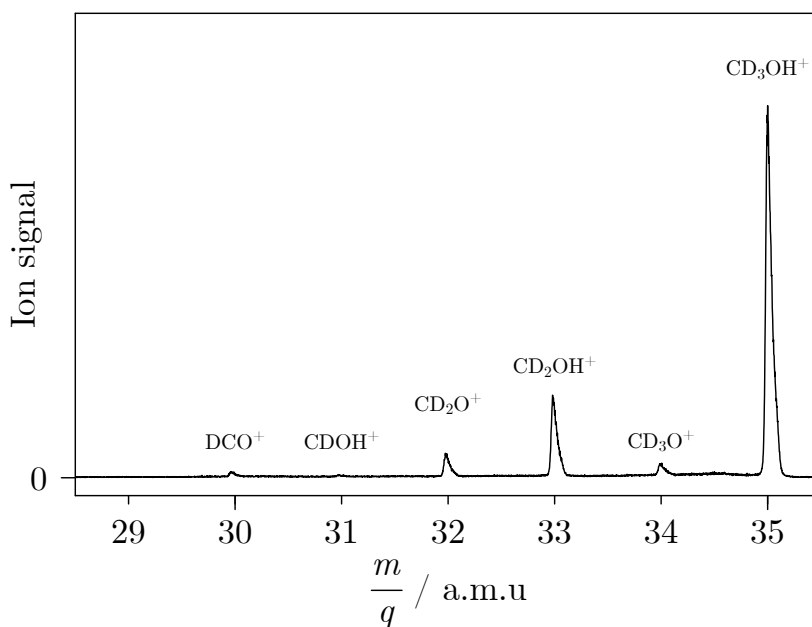


FIGURE 2.16: Typical mass spectrum obtained by summing all mass spectra recorded between 7.4 and 11.4 eV when using CD₃OH as a precursor.

Conditions in the reactor could never be adjusted to favour only one reaction (see mass spectrum of Fig. 2.16). Hence the precursors and their corresponding successive H-abstraction

products were ionised simultaneously, and their ion yields were recorded within the same experimental conditions and similar scan parameters, mainly:

- extraction voltage: 750 V,
- range: 7.4 - 11.4 eV,
- photon resolution: 6 meV,
- step scan: 5 meV for CH₃OH and 100 meV for CD₃OH.

Larger scan steps were used for CD₃OH as a compromise between available quantity (5 g) and scan duration. The photon energy of the CH₃OH scan is calibrated using Kr absorption lines due to the beamline gas filter. This calibration is not possible for the CD₃OH scan as the scan steps are too large. It is worth noting that CO⁺ was never observed as the photon energies in this study were much below its *IP* (*IP*(CO) = 14.01339 eV [112]).

2.4.3 Ion yields

As conditions in the flow-tube reactor could not be adjusted to only allow one reaction, absolute photoionisation cross section values could not be determined as too many unknowns are present in the matter conservation equation. The following results compare the ion yields of the two isotopologues and their flow-tube products.

As shown in Table 2.7, the *IP*s of the precursors and flow-tube products lie between 7.5 and 11 eV. Their ion yields are presented by series in order to compare isotopologue products from the two precursors. The appearance energies of the various fragments in the ion yields are compared to reported *IP* values and to dissociative ionisation thresholds when available in order to determine if the fragment is produced by direct ionisation or dissociative ionisation.

Only the dissociative ionisation of the precursor can be checked. To this end, a mass spectrum was recorded at 11.4 eV using CD₃OH as a precursor and with the microwave discharge off. As shown in Fig. 2.17, no fragment except for the direct ionisation product of the precursor is observed in the mass spectrum. Dissociative ionisation of methanol (or its isotopologue) is thus not present within the scope of this study.

The dissociative ionisation of flow-tube products is more challenging to study because this would imply the recording of mass spectra of each product isolated from the others. Unfortunately, this was not possible with our experiment. Another possibility would be to use the DELICIOUS 3 spectrometer in a dedicated mode which allows the discrimination of ions with excessive kinetic-energy. Indeed, dissociative ionisation often produces ions with extra kinetic energy due to the fragmentation process. In our case, this may still be difficult considering the low mass of the neutral by-products (H and H₂), expected to carry most of the excess kinetic energy.

Precursor ion yields (CH₃OH⁺)

The first ions in the series result from the direct ionisation of the methanol isotopologue precursors: CH₃OH⁺. Their ion yields are presented in Fig. 2.18.

As expected, the ion yields from the two precursor isotopologues are practically identical, with the same apparent *IP*. As an indication, a TPES of CH₃OH is displayed in Fig. 2.18. It was obtained using the SPES technique (see section 1.1.3) from the same scan as the ion yield. The first peak corresponds to the rise in ion yield and the *IP* of CH₃OH, thus confirming the assignment.

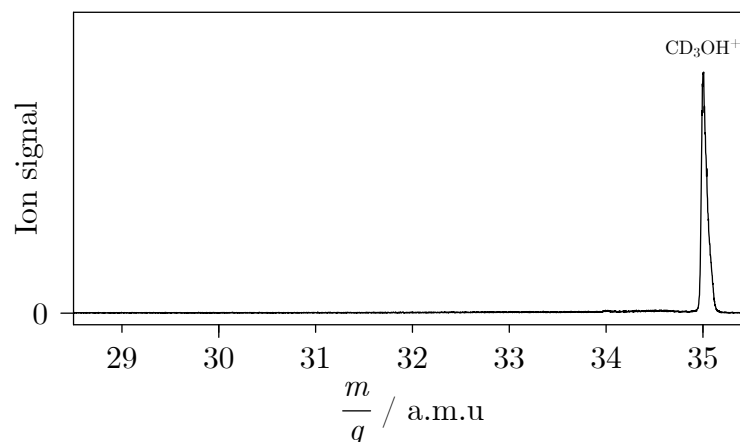


FIGURE 2.17: Typical mass spectrum at 11.4 eV when using CD_3OH as a precursor and the microwave discharge turned off.

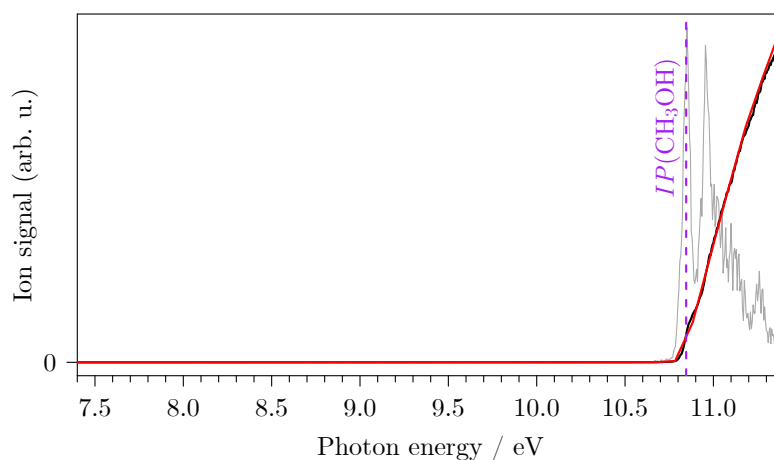


FIGURE 2.18: Ion yields resulting from the direct ionisation of CH_3OH (black line) and CD_3OH (red line). A TPES of CH_3OH is also presented in grey. A purple dashed line at 10.846 eV locates the $IP(\text{CH}_3\text{OH})$ [105].

Single H-abstraction product ion yields

Figure 2.19 displays the products ion yields for single-H abstraction. The $m/q = 31$ a.m.u. ion yield (black line of panel c)) from the CH_3OH study is compared to $m/q = 34$ (panel b)) and 33 a.m.u. (panel a)) ion yields from the CD_3OH study, respectively assigned to CD_3O^+ and CD_2OH^+ . In panel c), the $m/q = 31$ a.m.u. ion yield is compared to a linear combination 40/60 of CD_3O^+ and CD_2OH^+ ion yields.

Figure 2.19 shows that two regions can be distinguished in the $m/q = 31$ a.m.u. ion yield of the CH_3OH study. The first displays a fragment appearing at an energy close to the IP of CH_2OH (7.55 eV [106]). Above this energy, the ion yield varies as the $m/q = 33$ a.m.u. ion yield from the CD_3OH study, assigned to CD_2OH^+ . This trend is broken at around 10.7 eV by a marked increase. This energy is comparable to the IP of CH_3O (10.72 eV [106]). In a similar fashion to the $m/q = 34$ a.m.u. ion yield from the CD_3OH study, assigned to CD_3O^+ , the ion yield continues to increase from 10.7 eV until the end of the scan. Given how well the red line fits the black line in Fig. 2.19 and the appearance energies of CD_3O^+ and CD_2OH^+ correspond

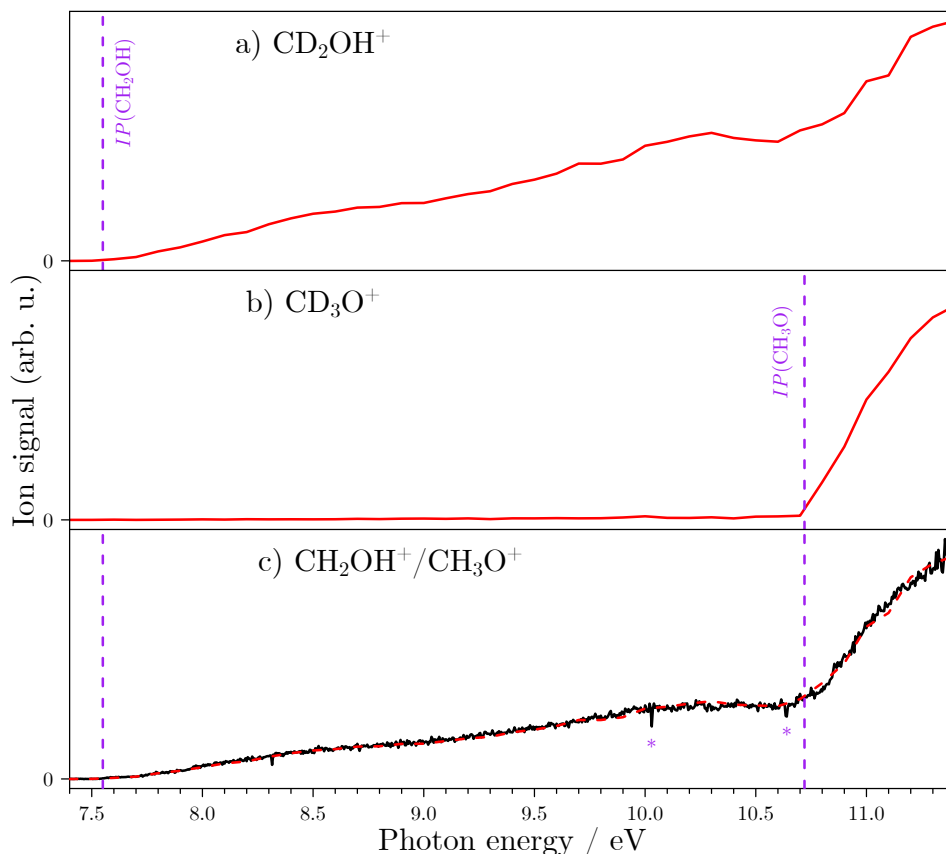


FIGURE 2.19: Single H-abstraction product ion yields. a) The $m/q = 33$ a.m.u. ion yield from the CD_3OH study assigned to CD_2OH^+ with a dashed vertical line at 7.55 eV locating the IP of CH_2OH [106]. b) The $m/q = 34$ a.m.u. ion yield from the CD_3OH study assigned to CD_3O^+ with a dashed vertical line at 10.72 eV locating the IP of CH_3O [106]. c) The $m/q = 31$ a.m.u. ion yield (black line) from the CH_3OH study is compared to a linear combination (red dashed line) of panels a) and b) with a 60/40 ratio. The same y -axis arbitrary unit is used in all panels. Purple asterisks locate Kr absorption lines caused by the beamline gas filter used to calibrate the photon energy for all non-deuterated scans of this section.

to the IP s of the non-deuterated equivalents, it seems clear that the $m/q = 31$ a.m.u. ion yield from the CH_3OH study is composed of both CH_3O^+ and CH_2OH^+ isomer products. This means that the single F-induced H-abstraction reaction on CH_3OH is located on both the methyl and the hydroxyl groups producing CH_2OH and CH_3O , respectively.

We are not able to quantify the relative production ratio of these two isomers as their photoionisation cross sections are not known and because dissociative ionisation of CH_2OH (at 8.61 eV [113]) and CH_3O (at 8.73 eV [114]) is likely to occur, yielding HCO^+ , thus depleting the direct ionisation signals. CH_3O^+ can be produced by dissociative ionisation of CH_3OH , but the reported threshold for this process is 11.67 eV [115] so is not present here.

Although not quantified, the observation of both CH_3O^+ and CH_2OH^+ is however in agreement with the results of a F + CH_3OH reactivity study, which set the $\text{CH}_3\text{O} / \text{CH}_2\text{OH}$ production ratio by F-induced H-abstraction on methanol at 50.3(1.3)/49.7(1.3), *i.e.* in roughly equal proportions [116]. If CH_2OH and CH_3O are produced in equal proportions, the coefficients of the linear combination of CD_3O^+ and CD_2OH^+ ion yields of Fig. 2.19 c) give the ratio of

the respective photoionisation cross sections in very rough terms in this energy region. This is assuming that isotopologues share common photoionisation properties. Using equation (2.5):

$$\frac{\sigma_{\text{CH}_3\text{O}}^{\text{ion}}}{\sigma_{\text{CH}_2\text{OH}}^{\text{ion}}} = \frac{2}{3}. \quad (2.14)$$

Double H-abstraction product ion yields

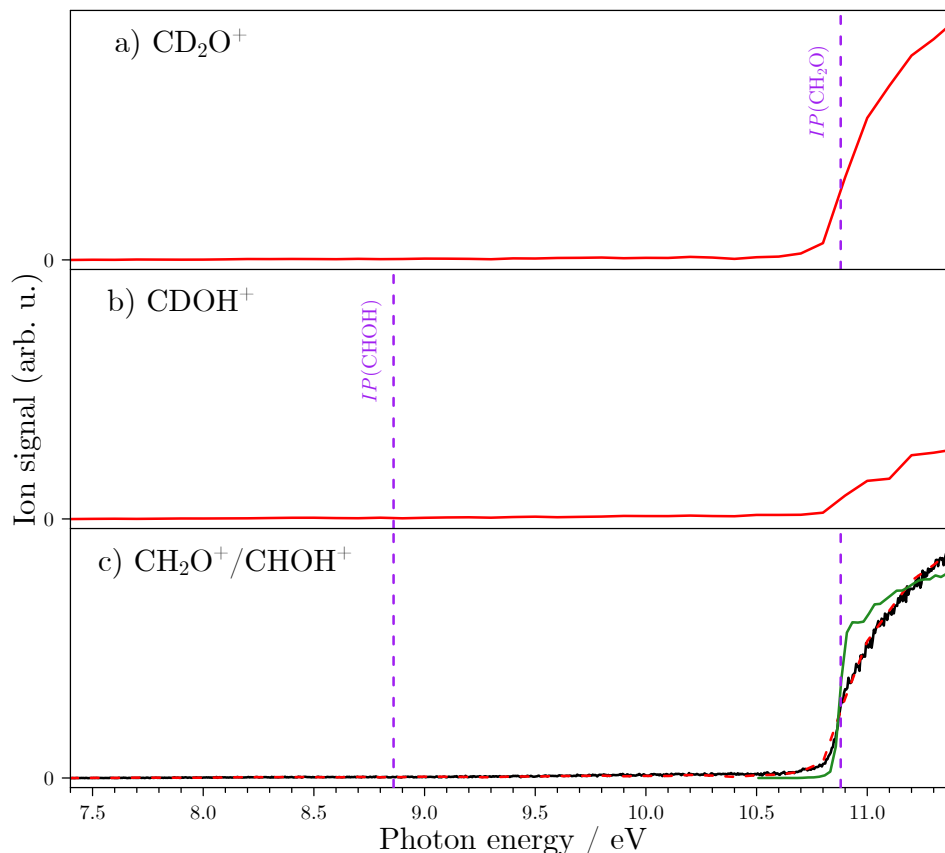


FIGURE 2.20: Double H-abstraction product ion yields. a) The $m/q = 32$ a.m.u. ion yield from the CD_3OH study assigned to CD_2O^+ . b) The $m/q = 31$ a.m.u. ion yield from the CD_3OH study assigned to CDOH^+ . c) The $m/q = 30$ a.m.u. ion yield (black line) from the CH_3OH study is compared to a linear combination (red dashed line) of panels a) and b) with a 95/5 ratio. This panel also features a H_2CO^+ ion yield from Dodson *et al.* [50] in green. Vertical purple dashed lines at 8.86 and 10.72 eV locate the ionisation potentials of CHOH [108] and CH_2O [107], respectively. The same y -axis arbitrary unit is used in all panels.

Reaction products resulting from a double H-abstraction on CD_3OH are also observed in the mass spectrum of Fig. 2.16. Their corresponding ion yields are displayed in the panels a) (CD_2O^+) and b) (CDOH^+) of Fig. 2.20 and compared to the ion yield of $m/q = 30$ a.m.u. of the CH_3OH study in panel c). As with the single H-abstraction products, the comparison relies on a linear combination of the ion yields of panels a) and b) using a 95/5 ratio, but also a H_2CO^+ ion yield from the literature [50] used in a H_2CO photoionisation cross section study (green trace).

The red and black lines of Fig. 2.20 c) are almost identical which would indicate that H_2CO^+ is 95% responsible for the $m/q = 30$ a.m.u. ion yield in the CH_3OH study. In addition, the H_2CO^+ ion yield from the literature is also comparable to our $m/q = 30$ a.m.u. ion yield; some intensity differences can be explained by differences in sample temperatures between the two works. The formation of H_2CO over CHOH is more intuitive in the flow-tube reactor as H_2CO (formaldehyde) is a much more stable species. H_2CO^+ can be produced by dissociative ionisation of CH_3OH , but the reported threshold for this process is 12.05 eV [117] so is not present here. This is confirmed by the mass spectrum of Fig. 2.17.

In the CD_3OH study, the $m/q = 31$ a.m.u. signal assigned to CDOH^+ of Fig. 2.20 b) rises very slowly from around 8.8 eV (it is hardly visible in the figure). This appearance energy is in agreement with the IP of CHOH at 8.86 eV [108]. This ion signal then increases markedly from 10.8 eV, which could be due to dissociative ionisation of a single H-abstraction product. The $m/q = 30$ a.m.u. signal in the CH_3OH study may therefore have contributions from CHOH^+ above 10.8 eV, but these ion signals may not stem from direct ionisation. In any case, these contributions are small given the excellent agreement between the solid lines of Fig. 2.20.

Triple H-abstraction product ion yields

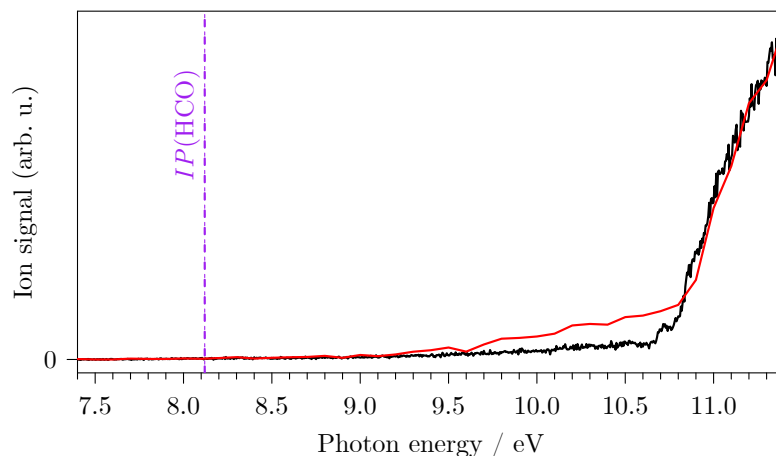


FIGURE 2.21: Triple H-abstraction product ion yields. The $m/q = 29$ a.m.u. ion yield (black line) from the CH_3OH study is compared to the $m/q = 30$ a.m.u. ion yield (red line) from the CD_3OH study. A vertical purple dashed line at 8.14 eV locates the $IP(\text{HCO})$ [109].

In the case of HCO^+ and COH^+ , the isotopologue study is seemingly easier as no $m/q = 29$ a.m.u. signal in the CD_3OH study corresponding to COH^+ is present (see Fig. 2.16), which would mean that the third H-abstraction is always on the hydroxyl rather than the methyl group. The knowledge of $IP(\text{COH})$ is needed to confirm this statement, but it is not reported in the literature. In our experiment, if $IP(\text{COH}) > 11.4$ eV, COH could be formed, but is just not ionised at our photon energies. This IP is not known, but a rough estimate can be given as the difference between formation enthalpies of COH and COH^+ [118]: 7.4 eV. COH is therefore expected to ionise in the energy range of this study.

Fig. 2.21 compares the $m/q = 29$ a.m.u. ion yield from the CH_3OH study to the $m/q = 30$ a.m.u. ion yield (assigned to DCO^+) from the CD_3OH study. The ion yields are very similar especially

for the marked rise from 10.8 eV, which is in agreement with the assignment of the previous paragraph. There is some difference before this increase, which is difficult to explain.

In both experiments, the corresponding ions do not appear at $IP(\text{HCO}) = 8.14$ eV, but around 9.5 eV. There is no step in the ion yield, but rather a gradual rise so this threshold is difficult to evaluate. It has been reported that HCO^+ is produced by dissociative ionisation from CH_2OH and CH_3O at 8.61 [113] and 8.73 eV [114], respectively. It is also conceivable that it stems from the dissociative ionisation of H_2CO . The HCO^+ (or DCO^+) signal may therefore not be produced by direct ionisation of triple H-abstraction products, but by dissociative ionisation of single or double H-abstraction products. We are not able to distinguish both types of processes.

Methanol isotopologue summary

It was assumed, and this was confirmed by strong likeness between ion yields, that methanol isotopologues and their H/D-abstraction products would have similar if not the same photoionisation properties. As conditions in the flow-tube reactor could not be adjusted to selectively favour only single, double or triple H/D-abstraction at any given time, absolute measurements could not be made meaning that photoionisation cross sections could not be deduced.

Following the single F-induced H/D-abstraction reaction, it would seem that both products, CH_2OH and CH_3O , are formed based on the similarities between spectra in Fig. 2.19. This is in agreement with recent findings, which actually report production of each radical at 50/50 [116]. We are not able to measure this ratio in our experiment as the photoionisation cross sections for both radicals are required and these are not yet known.

The species resulting from the double F-induced H-abstraction reaction of methanol would appear to be the most intuitive product H_2CO (formaldehyde). The presence of CHOH^+ cannot be ruled out, but could be explained by dissociative ionisation of single H-abstraction products rather than the direct ionisation of CHOH .

The triple F-induced H-abstraction product is not COH as no $m/q = 29$ a.m.u. signal was observed in the CD_3OH experiment. DCO^+ ions were detected in the CD_3OH experiment and the corresponding ion yield matches that of $m/q = 29$ a.m.u. in the CH_3OH experiment. These observations would indicate that triple H-abstraction reactions on methanol produce HCO . However, these ion signals do not necessarily stem from the direct ionisation of HCO (DCO), but maybe from the dissociative ionisation of single H-abstraction products so there actually may not be any triple H abstractions. We are not able to distinguish direct ionisation from dissociative ionisation in this case.

These experiments constitute important preliminary work on the determination of photoionisation cross sections of carbonated free radicals, which are of important for astrophysical applications and all quantitative experiments using photoionisation to probe neutral species (see Appendix A).

2.5 Photoionisation cross section and ion yield conclusions

The quantitative description of photoionisation processes for free radicals is rarely reported in the literature and given the experimental difficulties exposed in this chapter, it is easy to understand why. The results presented in this chapter do however offer new information on such processes. The new photoionisation cross section values of OH and NH_2 provide reliable parameters for adequately modelling astrophysical and atmospheric phenomena. With

the knowledge of the NH_2 photoionisation cross section and by adapting experimental conditions, we should be able to determine, for the first time experimentally, the NH photoionisation cross section in future experimental campaigns.

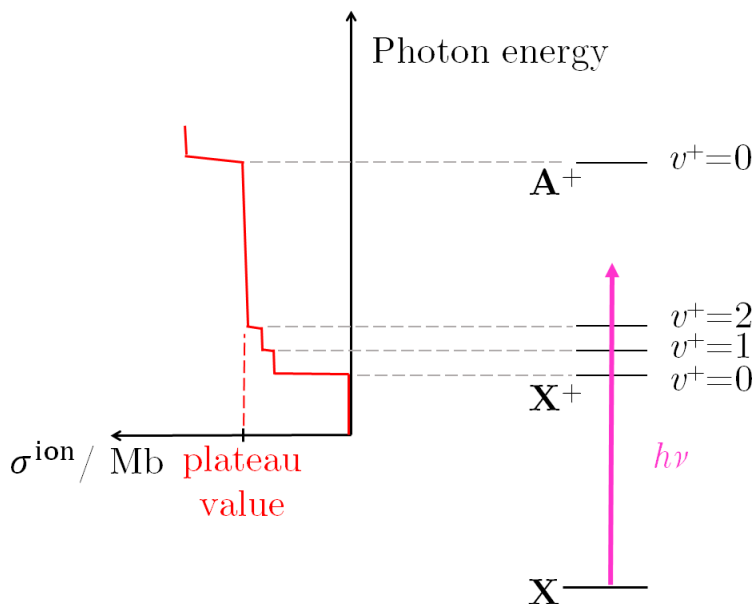


FIGURE 2.22: Schematic representation of a photoionisation cross section as a function of incident photon energy. The plateau value is reached at photon energies above vibrational levels of the cationic electronic ground state with non-vanishing FCF, but below the first excited state.

In the absence of known photoionisation cross sections of free radicals, they can however be evaluated using a simple model as described in more detail in ref. [62] that focuses on the molecular orbital from which is emitted the photoelectron. The main idea behind this model is based on the simplest *molecule*: the hydrogen atom, containing only one electron. Just above threshold, the photoionisation cross section of the H atom is around 6 Mb [103]. The next step is to consider the number of electrons in the molecular orbital that issues the photoelectron in the species of interest. The photoionisation cross section, in the energy region situated above all non-vanishing FCF for the $\text{X}^+ \leftarrow \text{X}$ transition (see Fig. 2.22), is then given, in very rough terms, by the orbital occupancy times 6 Mb. If the orbital is over half full, it is given by the orbital vacancy times 6 Mb. In the case of free radicals, one lone unpaired electron is often the ejected photoelectron, so the photoionisation cross section for most free radicals should be around 6 Mb. Of course, this simple model does not consider autoionisation or more complex aspects of photoionisation, but can be used as a rule of thumb especially when no other data are available. This order of magnitude is verified experimentally as shown in Table 2.8.

The ion yields of the carbonated fragments of methanol are also a first step towards cross section determination. The assignment of masses was facilitated by the use of the CD_3OH isotopologue. Future experiments will aim to clarify these results regarding dissociative ionisation contributions (determine thresholds to be able to distinguish direct ionisation and dissociative ionisation signals) and to favour only one type of reaction to measure photoionisation cross sections. This selectivity could be reached by substituting F_2 with Cl_2 in the discharge for example. Cl atoms can have a different reactivity to F atoms.

TABLE 2.8: Photoionisation cross section evaluation using a simple model.

Species	$\sigma^{\text{ion}} / \text{Mb}$ typical plateau value ^a	Photoelectron molecular orbital	$\sigma^{\text{ion}} / \text{Mb}$ model prediction
OH	6 ± 2	$(1\pi)^3$	6
NH ₂	8 ± 2	$(1b_1)^1$	6
NH	7.5^{b} [119]	$(1\pi_+)^1$ or $(1\pi_-)^1$	6
CH ₃	7 ± 2 [53–55]	$(1a_2'')^1$	6
C ₂ H ₃	12 ± 3 [56, 57]	$(a'')^2$	12

^a Typical photoionisation cross section plateau value just above the Franck-Condon envelope for the $X^+ \leftarrow X$ transition, see Fig. 2.22.

^b Theoretical value, no experimental value has been reported to our knowledge.

Chapter 3

Photoelectron spectroscopy, from medium to high resolution

In this chapter, I will present spectroscopic results on photoelectron spectroscopy. This technique offers both quantitative and qualitative information on cations of molecules, whether they be stable or free radicals.

Quantitatively it constitutes a means of accessing the (ro)vibronic structure of cations without needing to produce them in the first place. The resulting spectroscopic parameters can predict, for example, IR or microwave spectra, which are of great interest to astrophysicists to guide new discoveries. From a fundamental perspective, it also offers information on neutral and cationic state geometries and their changes when undergoing photoionising processes. The use of VUV spectroscopy over UV or visible REMPI spectroscopy offers the advantage of not relying on intermediate neutral states.

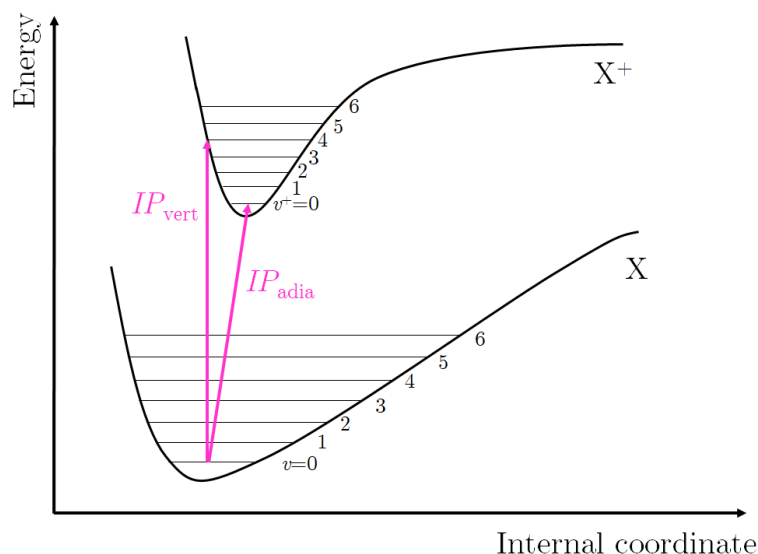


FIGURE 3.1: Scheme illustrating the difference between vertical and adiabatic IPs (pink arrows). Projections of the neutral (X) and cationic (X^+) potential energy surfaces along an internal coordinate are drawn along with vibrational energy levels. The internal coordinate can be a bond length, an angle, or a function of several geometric parameters.

Quantitatively, the vertical and adiabatic ionisation potentials (IP_{vert} and IP_{adia} , respectively) can be determined (see Fig. 3.1), which in turn provide thermodynamic quantities. The

ionization energy of a molecule is a fundamental quantity which is often involved in thermochemical cycles aimed at determining parameters such as heats of formation, bond energies and proton affinities. These quantities are then important to be included in calculations and simulations modelling the environments where such species are present.

Focusing mainly on molecules of astrophysical interest, I will start by presenting the medium high resolution photoionisation spectroscopy of a molecule, CH_3NCO , and then a diradical, C_2 , recorded at SOLEIL on the DESIRS beamline. This will be followed by a section on the first PFI-ZEKE spectroscopy experiments undertaken with VULCAIM at ISMO on rare gases and CO_2 . I will conclude this chapter by describing a new PFI-ZEKE analysis technique inspired by SPES image treatments (see chapter 1).

3.1 Photoelectron spectroscopy with synchrotron radiation

The methods used for performing mass-selective photoelectron spectroscopy on the DESIRS beamline were described in chapter 1: TPES, SPES, *etc.* They were employed on several occasions during my PhD when studying the photoionisation of CH_3NCO and C_2 . A third study, similar to that of C_2 , was conducted on the CH_2NC radical (isocyanomethyl). The results are reported in ref. [120].

3.1.1 Threshold photoelectron spectroscopy of CH_3NCO

Astrophysical context

On Earth, methyl isocyanate, CH_3NCO is widely used in the production of pesticides, rubbers and adhesives. It is an infamous molecule and mainly associated to the Bhopal disaster in India in 1984.

It has attracted a lot of interest recently having being observed in Space. Halfen *et al.* [121], in 2015, were the first to report on the occurrence of CH_3NCO in the interstellar medium, more precisely in the Sgr B2 giant molecular cloud. It was then found to be one of the most abundant molecules after water and formamide on the surface of the comet 67P/Churyumov-Gerasimenko [4]. Cernicharo *et al.* documented the abundance of CH_3NCO in very diverse interstellar media and extensively characterised its rotational spectrum, as rotational spectral lines are the current detection method of CH_3NCO in Space [122].

Spectroscopic context

CH_3NCO is a non-rigid quasi-symmetric top as illustrated in Fig. 3.2. In its ground electronic state, the NCO part is almost linear with an angle of 172.9° and the CNCO structure lies in the same plane, but the methyl group fully breaks linearity with a 44.3° angle from the NCO chain (see Table 3.1). The CH_3 group is almost a free rotor as the corresponding barrier is only 16.2 cm^{-1} [123] and the CNC bending mode presents large amplitude motion [124].

Since its first laboratory observation in 1963 [125], many studies in the microwave and IR regions have characterised its low energy properties [124, 126] and CH_3NCO has often been compared to its isomers (methyl cyanate and methyl fulminate) and thiocyanate substitutes [127, 128].

Higher energy studies are much scarcer. For example, photoelectron studies do exist, but the lack of mass selectivity and low resolution in these works make assignments difficult [129–132].

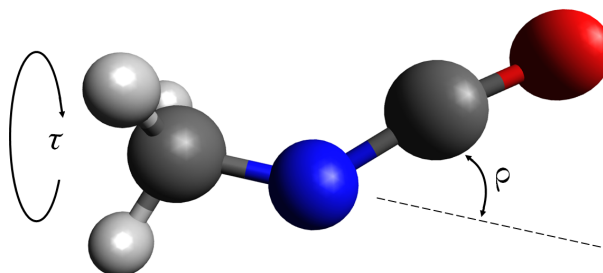


FIGURE 3.2: Sketch of the CH_3NCO molecule (geometry adopted in the neutral ground electronic state \tilde{X}^1A'). White, grey, blue, and red spheres represent hydrogen, carbon, nitrogen, and oxygen atoms, respectively. The coordinates of the two large amplitude motions are marked (angles τ and ρ).

TABLE 3.1: Summary of internal coordinates of CH_3NCO in the three electronic states of interest extracted from the *ab initio* calculations.

Coordinate	X^1A'	$X^+ 2A''$	$A^+ 2A'$
$\tau / ^\circ$	0	0	60
$\rho / ^\circ$	44.3	48.1	1.9
$\angle \text{NCO} / ^\circ$	172.9	170.4	179.8
$d(\text{C-N}) / \text{Å}$	1.206	1.263	1.209
$d(\text{C-O}) / \text{Å}$	1.176	1.145	1.165
$d(\text{C}_\alpha\text{-N})^* / \text{Å}$	1.447	1.436	1.417

* C_α is the carbon atom bound to the H atoms.

This means that very little information is currently available on the cation CH_3NCO^+ , a reactive species which could be involved in photochemical processes in molecular clouds or comet surfaces. The cation could act as a reaction intermediate, being formed by photoionisation from neutral CH_3NCO , that would in turn participate in complex photochemical networks.

Specific experimental details

The experimental work was carried out on the DESIRS beamline at the SOLEIL synchrotron facility using the DELICIOUS 3 spectrometer (see chapter 1).

Specifically to this CH_3NCO study, a few grams of the sample, synthesised by Jean-Claude Guillemin (Rennes University), were placed in a vial attached to the experiment. The relevant physical properties of CH_3NCO are summarised in Table 3.2. Due to high room-temperature vapour-pressure, the vial was plunged into a chiller set at -40°C which lowered the pressure. This step was necessary to avoid too great a build up of the sample in the experiment, which could lead to polymerisation or blockages, but also to limit the consumption of the sample, which is not commercially available. Maintaining the sample at a constant temperature also provided pressure stability.

A high-resolution scan was recorded between 10.3 and 12.5 eV. Photoelectrons were extracted using a 53 V/m DC field, which induces a Stark shift of photoionising transition energies by 5.4 meV. The TPES was obtained using the SPES technique producing a spectrum with a total resolution of 11 meV. A CH_3NCO^+ ion yield was also recorded in a different scan (see

TABLE 3.2: Summary of physical properties of CH₃NCO

Molecular mass	57 a.m.u.
Melting point	- 45°C ^a
Boiling point	38.3°C ^a
vapour pressure at 20°C	540 mbar ^a
vapour pressure at 0°C	280 mbar ^b
vapour pressure at -40°C	≈ 0.1 mbar ^b

^a from chemistry handbook [133],

^a measured during our study.

Appendix B). It does not present any visible autoionisation features, which justifies the SPES treatment. The beamline gas filter was filled with Ar to enable spectral purity. Absorption lines from this gas filter, present in the ion yield, are used to calibrate the photon energy scale.

Theoretical model

The theoretical model used to simulate our experimental spectrum was developed by Laurent Coudert, a theoretician from our team at ISMO, and is discussed in detail in ref. [134]. Using *ab initio* calculations of the neutral \tilde{X}^1A' and cationic \tilde{X}^+2A'' and \tilde{A}^+2A' states provided by Jean-Christophe Loison of Bordeaux University, this model accounts for the two large amplitude motion (internal rotation of the CH₃ group and the CNC bending mode) along with five small amplitude vibrational modes implicating atoms of the NCO group.

The full description of the model is available in ref. [134] so only a brief overview is provided here. The *ab initio* calculations yield equilibrium structures for the 3 electronic states of interest here: \tilde{X}^1A' , \tilde{X}^+2A'' and \tilde{A}^+2A' . Along with the two large amplitude coordinates, 13 small amplitude coordinates describe the geometry of CH₃NCO and CH₃NCO⁺. The first step is to compute harmonic expansions describing the behaviour of the small amplitude coordinates as functions of the large amplitude coordinates (further *ab initio* calculations are used for these out-of-equilibrium geometries). The expansions are used in the FG method [135] to derive normal modes and fundamental vibrational frequencies. Anharmonicity is accounted for in the part of the potential depending on the large amplitude coordinates. Vibration-bending-torsion energy levels are then computed using the harmonic adiabatic approximation [136]. Finally, Franck-Condon factors (FCF) are determined for the $\tilde{X}^+2A'' \leftarrow \tilde{X}^1A'$ and $\tilde{A}^+2A' \leftarrow \tilde{X}^1A'$ transitions in order to simulate the spectra including spectral intensities.

Results and discussion

The experimental TPES of CH₃NCO is compared to the calculated spectrum resulting from the previously described theoretical model in Fig. 3.3. It is made up of $\tilde{X}^+2A'' \leftarrow \tilde{X}^1A'$ and $\tilde{A}^+2A' \leftarrow \tilde{X}^1A'$ photoionising transitions. The 10 visible peaks are labelled in the figure and their corresponding energies are reported, once Stark-shift corrected, in Table 3.3. When possible they are also assigned to vibrational modes of the neutral (ν_i) and cationic (ν_i^+) species, guided by the theoretical model. The peaks at around 10.6 eV and above are mainly vibrational progressions belonging to the cation ground state \tilde{X}^+2A'' since the geometry change between

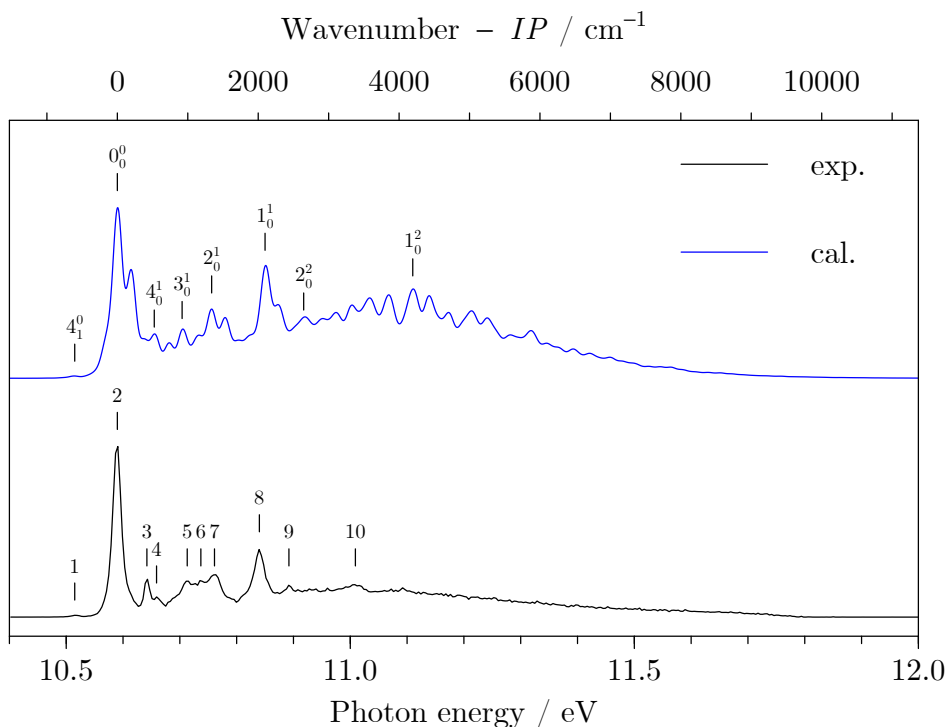


FIGURE 3.3: Experimental TPES (black) of CH_3NCO with the peak labelling referring to Table 3.3 compared to a calculated spectrum (blue) using a vibrational temperature of 300 K. The *ab initio* calculated spectrum is shifted -0.133 eV to fit the experimental spectrum. Assignments in the calculated spectrum refer to vibrational bands of the $\tilde{X}^+ \ ^2A'' \leftarrow \tilde{X} \ ^1A'$ photoionising transition. The labels correspond to vibrational mode numbers (see Table 3.3) followed by cationic (superscript) and neutral (subscript) vibrational quantum numbers.

the neutral and the cation ground states is moderate. On the contrary, the change is much more pronounced for the A^+ cationic state and the broad feature, from 10.6 to 11.8 eV, is assigned to transitions to the $\tilde{A}^+ \ ^2A'$ state. Our *ab initio* calculations found the CNC angle to go from 44.3° for the $\tilde{X} \ ^1A'$ equilibrium geometry to 1.9° , *i.e.* almost linearity, for the $\tilde{A}^+ \ ^2A'$ equilibrium geometry. Such a marked change in geometries produces long FC vibrational progressions in the $\tilde{A}^+ \ ^2A' \leftarrow \tilde{X} \ ^1A'$ transition, which is reproduced theoretically. This long progression results in a broad feature in our experimental spectrum at our spectral resolution. There is a good agreement in general between experimental and calculated results, including the vibrational frequencies.

Pasinszki *et al.* [130] observed a strong main peak in their PES, but at 10.630(15) eV, *i.e.* 34 meV higher than our own 0_0^0 band (peak 2 of Fig. 3.3). They also reported vibrational frequencies for the ν_1^+ , ν_2^+ , and ν_3^+ modes at 2150, 1290, and 800 cm^{-1} , which differ from our values.

Finally, they report excited states above 12 eV, mainly around 14 and 18 eV, but these were never observed in our higher energy experiments (see Appendix B). As Pasinszki *et al.*'s spectra are not mass-selective, this discrepancy can be explained by contamination of the spectra by other species, notably CHNCO^+ . States at higher energies than the $\tilde{A}^+ \ ^2A'$ are therefore suspected to be dissociative.

With these results, it is possible to extract the first adiabatic ionisation potential of CH_3NCO

TABLE 3.3: Peak energies^a and assignments.

Peak	E / eV	ΔE / cm^{-1}	Involved vibrational mode ^b	$\tilde{\nu}_{\text{cal.}}$ / cm^{-1}
1	10.521	-604	ν_4	621 ^c
2	10.596	0	origin band	
3	10.648	420	$\nu_4^{+\text{d}}$?	
4	10.665	555	ν_4^+	541
5	10.719	986	ν_3^+	920
6	10.743	1186		
7	10.767	1374	ν_2^+	1338
8	10.846	2011	ν_1^+	2104
9	10.898	2430	$2\nu_2^+$	2658
10	11.015	3376		

^a The Stark-shift corrected ionization energy is given in the column labelled E ; the energy difference with respect to the main peak, peak 2, is given in the column labelled ΔE .

^b Vibrational mode assignment. The ν_i (ν_i^+) denotes those of the neutral molecule (cation). The mode numbering is consistent with the labelling of the calculated spectrum of Fig. 3.3.

^c Hot band originating from an excited vibrational state of neutral CH_3NCO .

^d Peak 3 could be assigned to the ν_4^+ mode even though peak 4 is closer to the theoretical vibrational energy.

corresponding to the $\tilde{X}^+ \ ^2A'' \leftarrow \tilde{X} \ ^1A'$ transition: 10.596(6) eV. This value is lower than that of Pasinszki *et al.* [130]: 10.630(15) eV. Despite no spectroscopic assignments being made for the $\tilde{A}^+ \ ^2A' \leftarrow \tilde{X} \ ^1A'$ transition, *ab initio* calculations yield an IP of 10.759(50) eV by adjusting the calculated spectrum on the experimental one and computing the energy difference between the two states.

Conclusion

This TPES work on CH_3NCO offers a better understanding of this species and the photoionisation transitions. As it is a complex system, a theoretical model was developed to describe the species and simulate the experimental spectrum. In particular, this model accounts for the two large amplitude motions and some small amplitude vibrational modes. The agreement between the calculated and experimental spectra is satisfactory. The calculated and experimental frequencies are in good agreement also. The first adiabatic IP for CH_3NCO was determined experimentally: 10.596(6) eV. The ionisation potential corresponding to the photoionisation to the first excited electronic state of the cation ($\tilde{A}^+ \ ^2A' \leftarrow \tilde{X} \ ^1A'$) was also extracted from our simulations: 10.759(50) eV. Additional work on the dissociative ionisation channels of methyl isocyanate was also carried out, and the corresponding results are presented in Appendix B.

3.1.2 First single-photon ionisation study of C₂

Although not a free radical, the C₂ carbon dimer has a tendency to polymerise in standard pressure and temperature conditions which is why it is not found in abundance on Earth; its high reactivity therefore means it can be classified as a transient species. This study constitutes the first photoionisation study of C₂ relying on single-photon ionisation to our knowledge.

Astrophysical context

The C₂ molecule is present on Earth in exotic environments such as carbon vapour, flames and plasmas [137, 138]. In Space, it is remarkable at being one of the first reactive species to have been observed in a comet's coma in 1864 [139] and is omnipresent in some types of diffuse interstellar clouds. Absorption features in these clouds, Diffuse Interstellar Bands (DIB's), are even named C₂-DIB's in reference to the high column densities of C₂ observed therein [140].

As for the C₂⁺ cation, it is actually more reactive with H₂ than neutral C₂ [70, 141]. Noting the important UV photon fluxes in such media, it is important to quantify the photoionisation of C₂ as it could constitute a first elementary step in a series of chemical reactions.

Spectroscopic context

Neutral C₂ has been extensively studied using absorption and emission spectroscopy. In particular, a great number of low lying electronic states can be identified by visible and even IR transitions from the ground state ¹Σ_g⁺ [142]. However, studies on the C₂⁺ cation are rarer and in fact photoionisation studies are mostly theoretical [143, 144]. Until recently, reported *IP* values ranged from 10.9 to 13 eV. This was until 2016, when Krechkivska *et al.* reported the first experimental determination of the ionisation energy of C₂ corresponding to the X⁺ ⁴Σ_g⁻ ← a ³Π_u transition [145]. Since the direct transition from the neutral ¹Σ_g⁺ ground state to the cationic ⁴Σ_g⁻ is spin-forbidden within the electric dipole approximation, they produced the C₂ molecule in the metastable a ³Π_u state using an electric discharge and performed resonant two-photon threshold-ionisation spectroscopy to excite C₂ to X⁺ ⁴Σ_g⁻ *via* the neutral a ³Π_u state.

They experimentally determined the X⁺ ← a ionisation energy at 11.788(5) eV. They then combined this value with the X – a energy difference (613.650(3) cm⁻¹, *i.e.* 76 meV) measured by Chen *et al.* [146] to find the ionisation energy of the X ¹Σ_g⁺ ground state. During my PhD, we applied another experimental approach employing VUV single-photon transitions and the production of neutral C₂ in its two lowest electronic states. Indeed, using single-photon transitions, the neutral ground state can give access to excited doublet cationic states of the cation (corresponding to a spin change of Δ*S* = 1/2); the cationic quartet ground state can be accessed from excited triplet neutral states, the a ³Π_u metastable state in particular. Observing transitions between these states of various spin-multiplicities allows the adiabatic *IP* of C₂ to be determined by energy differences from the very same experiment.

Specific experimental details

This work was carried out on the DESIRS beamline at the synchrotron SOLEIL. The main description of the setup and the experimental techniques were described in chapter 1 and only the specificities of the C₂ study are presented here.

As C₂ is a transient molecule, it must be produced *in situ*. This was achieved using the flow tube reactor as described in paragraph 1.1.3 of chapter 1 and using CH₄ as a precursor, high F₂

flow rates (to increase radical production) and medium injector distances (for high reactivity whilst still retaining transient species). These parameters are adjusted by optimising the C_2^+ signal in the mass spectrum. A typical mass spectrum recorded during this study is presented in Fig. 3.4. As this mass spectrum shows, many species are produced in the flow tube reactor, in particular $m/q = 24$ a.m.u. assigned to C_2^+ , the ionised product of C_2 formed in the flow tube reactor, but the complete reaction scheme is not known. The production mechanism of C_2 from CH_4 must involve multiple F-induced H abstractions and radical-radical reactions:

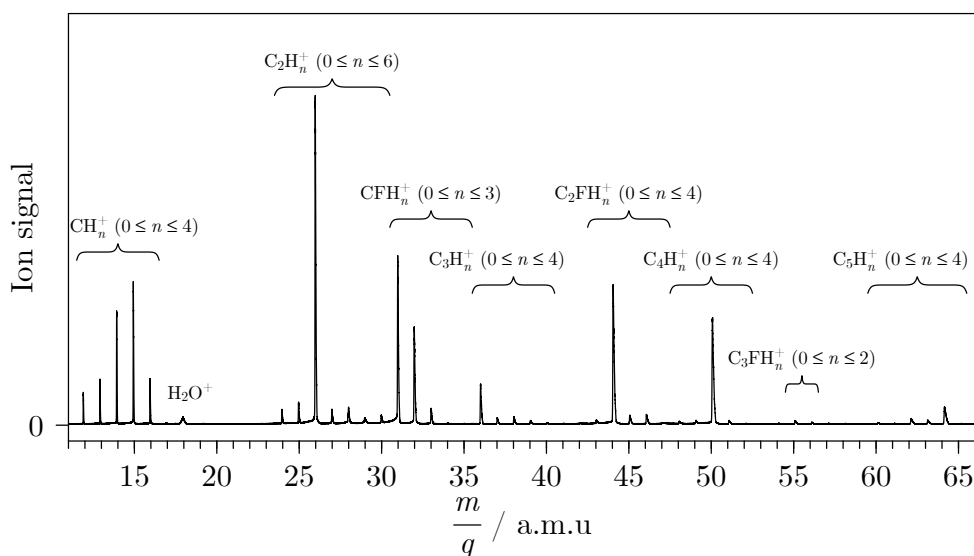
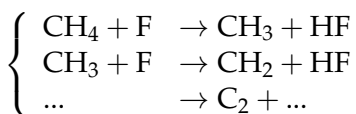


FIGURE 3.4: Typical mass spectrum obtained by summing all mass spectra recorded between 12.4 and 13.6 eV using CH_4 as a precursor.

As H-abstraction reactions are exothermic, the reaction products are often generated with excess energy that can be distributed among internal degrees of freedom, or can lead to electronic excitation. As the $a^3\Pi_u$ metastable neutral state is only 76 meV above the electronic ground state [146], C_2 produced in the flow tube is formed in this triplet state along with the singlet electronic ground state. Excitation of vibrational states in the neutral species is also expected from this production scheme.

Photon energy scans were performed between 11.5 and 14 eV at a photon resolution of 9 meV. After irradiation by the synchrotron radiation, the ensuing photoelectrons were extracted using a 88 V/cm electric field and analysed in order to form a TPES spectrum whose final resolution is 25 meV (see Fig. 3.5). The extraction fields induce a 7 meV Stark red shift which is accounted for in the reported threshold values. The spectrum was obtained using the SPES technique (see section 1.1.3 of chapter 1) and displays many peaks, with the most intense located at around 12.43 eV. At the same time, the $m/q = 24$ a.m.u. photoion yield was recorded and is also represented in Fig. 3.5. Dips in the ion yields of fragments featuring in Fig. 3.4 due to Ar absorption lines from the gas filter can be used to calibrate the photon energy to within 7 meV. The calibration can be undertaken using a more intense ion yield of a different fragment

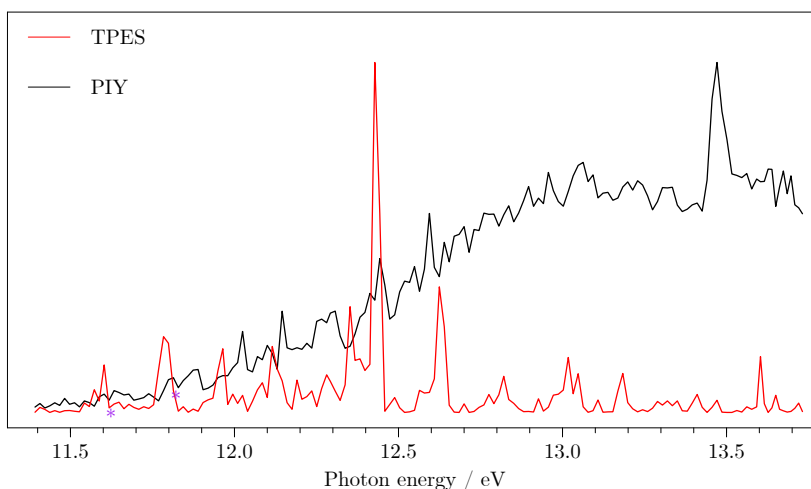


FIGURE 3.5: Experimental TPES (red line) and PIY (black) of C_2 . Purple asterisks locate Ar absorption lines visible in the PIY and used to calibrate the energy scale of the spectrum.

to C_2^+ (e.g. CH_3^+). All in all, the overall accuracy of the energy values given in this section is around 10 meV (2σ confidence level).

Ab initio calculations

In order to support the analysis and assignments of the experimental spectra of Fig 3.5, our collaborator, Jean-Christophe Loison from Bordeaux University, performed *ab initio* calculations on C_2 and C_2^+ . The first step was to produce potential energy surfaces of both species. This was achieved by employing the internally contracted multireference configuration interaction method with Davidson correction (MRCI+ Q) with complete active space self-consistent field (CASSCF) wavefunctions using the MOLPRO 2012 package. As shown in Fig. 3.6, potential energy curves of the two lowest states of neutral C_2 and the seven lowest states of C_2^+ were determined with respect to the bond length $d(C-C)$. The two lowest neutral electronic states lie very close to each other. In the vicinity of the cationic electronic ground state (less than 3 eV from the X^+ state), several electronic states are also present.

Using a series of VnZ ($n=T, Q, 5$ and 6) basis sets, extrapolations were carried out to evaluate complete basis set (CBS) energy values for each equilibrium geometry. More precisely, CASSCF and dynamical correlation ($E_{MRCI+Q} - E_{CASSCF}$) energies were respectively extrapolated using the functions $E_{CASSCF}(CBS) + A \times \exp(-B \times n)$ and $E_{Corr}(CBS) + C \times n^{-3}$. The final theoretical energies given combine the two: $E(CBS) = E_{CASSCF}(CBS) + E_{Corr}(CBS)$.

Harmonic vibrational frequencies were determined using the standard MOLPRO procedure using normal and Hessian modes. The theoretical energy values are summarised in Table 3.4 along with the main configurations for each electronic state.

In addition to the spin-selection rules, only transitions between states whose configurations differ by the ejection (from an orbital) of one electron are possible at the first order. Transitions are possible between states whose configurations change by more than one electron by configuration mixing (also called shake-up processes), but they are expected to be much weaker [144]. In total, between the states listed in Table 3.4, only one direct photoionising transition should be possible from the neutral ground state, i.e. $a^+ 2\Pi_u \leftarrow X 1\Sigma_g^+$. However two more are made

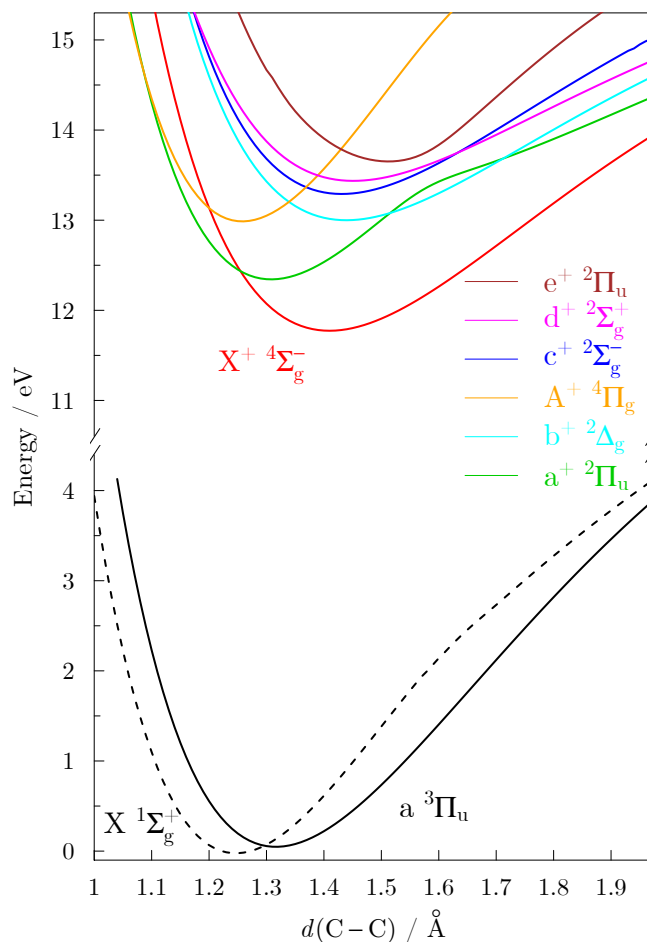


FIGURE 3.6: Theoretical potential energy curves of C_2 and C_2^+ from ref. [147]

possible by shake-up processes [144]: $c^+ 2\Sigma_g^- \leftarrow X 1\Sigma_g^+$ and $d^+ 2\Sigma_g^+ \leftarrow X 1\Sigma_g^+$. All states are accessible from the metastable $a^3\Pi_u$ state except for the $e^+ 2\Pi_u$ state which is not reachable from the ground state either.

Assignment of the Threshold-Photoelectron spectrum of C_2

The previously described *ab initio* calculations were used as input data in the PGOPHER software program to determine Franck-Condon factors (FCF) and to simulate each possible vibronic transition between states listed in Table 3.4. The stick spectra obtained by these means were convoluted by a gaussian line shape profile whose *FWHM* was set to 25 meV to reproduce the experimental spectrum bandwidth (corresponding to the rotational structure convoluted with the instrumental resolution). A vibrational temperature of 1500 K was used to account for the internal energy of the formed C_2 species. These simulations are reported in Fig. 3.7 and compared to the experimental spectrum.

Only the three following transitions were unambiguously assigned and used to reproduce most of the spectral features of the experimental spectrum:

- $X^+ 4\Sigma_g^-(v^+) \leftarrow a^3\Pi_u(v)$, with $0 \leq v \leq 2$ and $0 \leq v^+ \leq 3$,

- $a^+ 2\Pi_u(v^+ = 0) \leftarrow a^3\Pi_u(v = 0)$, and
- $a^+ 2\Pi_u(v^+) \leftarrow X^1\Sigma_g^+(v)$, with $0 \leq v \leq 2$ and $0 \leq v^+ \leq 3$.

The simulated spectra from these three transitions were combined, adjusting manually the relative intensities between the $a^+ 2\Pi_u \leftarrow X^1\Sigma_g^+$, $X^+ 4\Sigma_g^- \leftarrow a^3\Pi_u$, and $a^+ 2\Pi_u \leftarrow a^3\Pi_u$ transitions to 1.00, 0.60 and 0.42, respectively. The *ab initio* origin energy values were slightly shifted in order to better fit the experimental spectrum. The resulting complete simulated spectrum is directly compared to the experimental TPES in Fig. 3.8. The agreement between simulations and experiments is very good, both for the vibrational spacings and for the relative intensities. Some bands around 13 eV and above are missing from the simulation though. They are no doubt due to transitions towards higher excited states in C_2^+ (see panels 3, 4, 7, 8, 9 and 10 of Fig. 3.7), but the number of states and their close vicinity prevents unambiguous assignments.

TABLE 3.4: C_2 and C_2^+ electronic state energies extrapolated to the CBS limit (see text) as presented in ref. [147].

Species	State	Main configurations ^a	$E(\text{CBS}) / \text{Ha}$	$E_{I,\text{calc.}}^b / \text{eV}$
C_2	$X^1\Sigma_g^+$	71% $(2\sigma_u)^2(1\pi_u)^4$ +14% $(2\sigma_u)^0(1\pi_u)^4(3\sigma_g)^2$	-75.811535	0.000
	$a^3\Pi_u$	88% $(2\sigma_u)^2(1\pi_u)^3(3\sigma_g)^1$ +5% $(2\sigma_u)^1(1\pi_u)^2(3\sigma_g)^2(1\pi_g)^1$	-75.809599	0.053
C_2^+	$X^+ 4\Sigma_g^-$	86% $(2\sigma_u)^2(1\pi_u)^2(3\sigma_g)^1$ + 7% $(2\sigma_u)^1(1\pi_u)^1(3\sigma_g)^2(1\pi_g)^1$	-75.377781	11.803
	$a^+ 2\Pi_u$	72% $(2\sigma_u)^2(1\pi_u)^3$ +13% $(2\sigma_u)^0(1\pi_u)^3(3\sigma_g)^2$	-75.356565	12.381
	$A^+ 4\Pi_g$	86% $(2\sigma_u)^1(1\pi_u)^3(3\sigma_g)^1$ +6% $(2\sigma_u)^2(1\pi_u)^2(1\pi_g)^1$	-75.333358	13.012
	$b^+ 2\Delta_g$	88% $(2\sigma_u)^2(1\pi_u)^2(3\sigma_g)^1$	-75.332633	13.032
	$c^+ 2\Sigma_g^-$	88% $(2\sigma_u)^2(1\pi_u)^2(3\sigma_g)^1$	-75.322311	13.313
	$d^+ 2\Sigma_g^+$	82% $(2\sigma_u)^2(1\pi_u)^2(3\sigma_g)^1$	-75.316892	13.460
	$e^+ 2\Pi_u$	85% $(2\sigma_u)^2(1\pi_u)^1(3\sigma_g)^2$	-75.308704	13.683 ^c

^a Main contributing configurations calculated at the optimised geometry of each state. For the sake of clarity, the common part of the configuration, *i.e.* $(1\sigma_g)^2(1\sigma_g)^2(2\sigma_g)^2$, is omitted, and the configurations contributing to less than 5% are ignored.

^b Calculated ionization energy with respect to the $X^1\Sigma_g^+$ neutral ground state.

^c Unreachable state from the two neutral lowest electronic states due to configuration changes.

Confronting the theory and experiment, the adiabatic *IPs* for the three aforementioned transitions can be determined experimentally. These are summarised alongside the theoretical *IP* values of the other transitions in Table 3.5. Notably, the adiabatic *IP* for the $X^+ 4\Sigma_g^- \leftarrow a^3\Pi_u$ transition in our work (11.873(10) eV) agrees well with that reported by Krechkivska *et al.* (11.791(5) eV) [145]. As for the $a^+ 2\Pi_u \leftarrow X^1\Sigma_g^+$ and $a^+ 2\Pi_u \leftarrow a^3\Pi_u$ transitions, this is the first time that the *IP* for these transitions has been reported. As the ionising transitions are vibrationally resolved, the vibrational harmonic frequencies can be determined for the two lowest states $X^+ 4\Sigma_g^-$ and $a^+ 2\Pi_u$, respectively:

- $\tilde{\nu}_0(X^+) = 1460(80) \text{ cm}^{-1}$, and

- $\tilde{\nu}_0(a^+) = 1590(80) \text{ cm}^{-1}$.

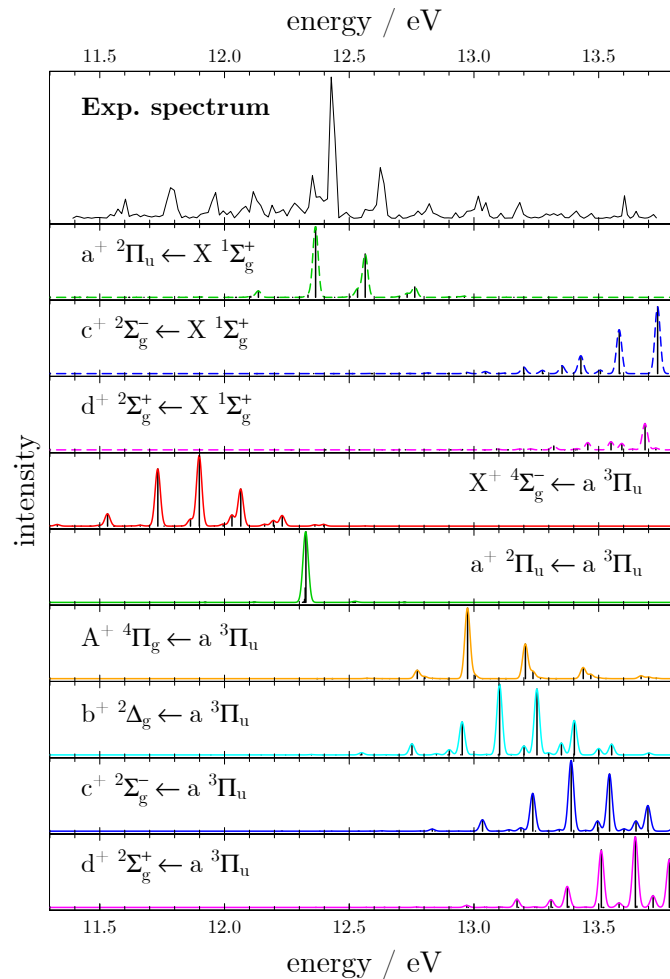


FIGURE 3.7: Experimental TPE spectrum of C_2 (upper panel) compared to FCF simulations of vibronic transitions (other panels) from ref. [147]. The same colour code as in Fig. 3.6 is used for the final state of the transition. Full line spectra correspond to transitions from the neutral metastable $a^3\Pi_u$ state and those with dashed lines correspond to transitions from the neutral ground state $X^1\Sigma_g^+$. Black stick spectra in the simulated spectra correspond to FCF, the resulting spectra result from convoluting the FCF by a gaussian function whose $FWHM = 25 \text{ meV}$.

As the $a^3\Pi_u$ and $a^+2\Pi_u$ states have similar C-C bond lengths at equilibrium and their potential energy surfaces are similar at least at low energy (see Fig. 3.6), it is normal that no vibrational progressions are observed in the $a^+2\Pi_u \leftarrow a^3\Pi_u$ transition of Fig. 3.8, FCF are expected largely to favour $\Delta v = 0$ transitions.

These three main transitions can be combined to determine $\Delta E(a - X)$ and $\Delta E(a^+ - X^+)$ corresponding to the singlet-triplet and quadruplet-doublet energy differences in C_2 and C_2^+ , respectively. Their combination also allows the determination of the adiabatic IP of the spin-forbidden $X^+4\Sigma_g^- \leftarrow X^1\Sigma_g^+$ transition between ground states noted $\Delta E(X^+ - X)$. Note that, unlike in the work of Krechkivska *et al.*, the $\Delta E(X^+ - X)$ is retrieved from ionisation energies measured within the same spectrum and does not use other values determined independently. These energy differences are reported in Table 3.6.

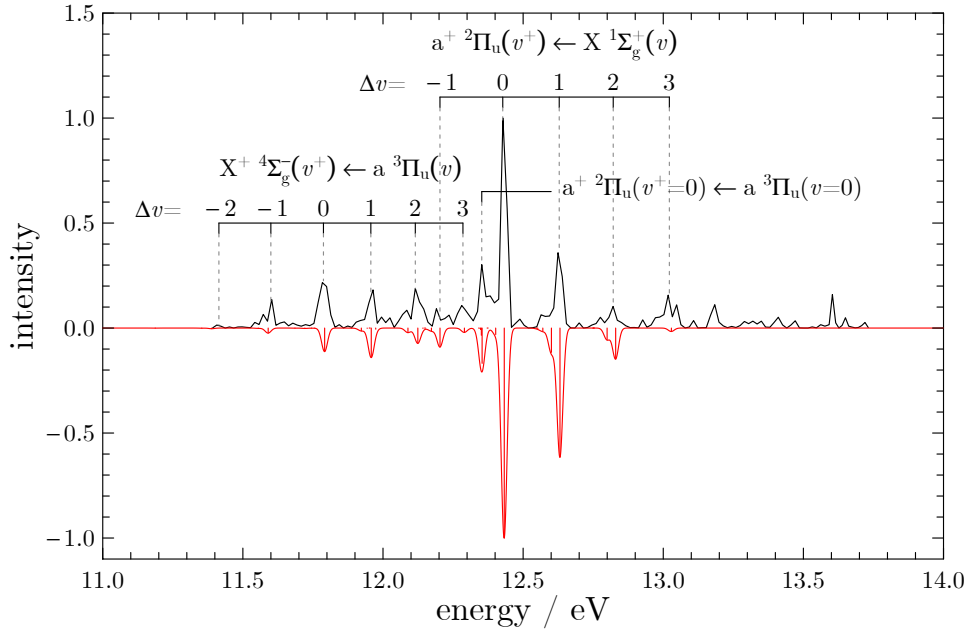


FIGURE 3.8: Experimental TPE spectrum of C_2 (upper black trace) compared to a simulated spectrum (lower red trace) which combines the simulated $a^+ 2\Pi_u \leftarrow X^1\Sigma_g^+$, $X^+ 4\Sigma_g^- \leftarrow a^3\Pi_u$, and $a^+ 2\Pi_u \leftarrow a^3\Pi_u$ vibronic transitions from ref. [147]. The red stick spectrum represents FCF values and the red trace, their convolution by a gaussian function whose $FWHM$ is 25 meV.

TABLE 3.5: Adiabatic ionization energies of C_2 .

Transition	$E_{I,calc.} / eV$		$E_{I,calc.corr.ZPE} / eV$		$E_{I,exp.} / eV$	
	Ref. [143] ^a	this work ^b	this work ^b	Ref. [145] ^c	this work	
$X^+ 4\Sigma_g^- \leftarrow X^1\Sigma_g^{+d}$	-	11.803	11.771	11.866(5)	11.873(10)	
$a^+ 2\Pi_u \leftarrow X^1\Sigma_g^+$	12.40	12.381	12.365	-	12.440(10)	
$c^+ 2\Sigma_g^- \leftarrow X^1\Sigma_g^+$	-	13.313	13.275	-	-	
$d^+ 2\Sigma_g^+ \leftarrow X^1\Sigma_g^+$	-	13.460	13.413	-	-	
$X^+ 4\Sigma_g^- \leftarrow a^3\Pi_u$	11.75	11.750	11.733	11.791(5)	11.795(10)	
$a^+ 2\Pi_u \leftarrow a^3\Pi_u$	12.29	12.328	12.326	-	12.361(10)	
$A^+ 4\Pi_g \leftarrow a^3\Pi_u$	-	12.959	12.974	-	-	
$b^+ 2\Delta_g \leftarrow a^3\Pi_u$	-	12.979	12.953	-	-	
$c^+ 2\Sigma_g^- \leftarrow a^3\Pi_u$	-	13.260	13.236	-	-	
$d^+ 2\Sigma_g^+ \leftarrow a^3\Pi_u$	-	13.404	13.374	-	-	

^a CCSD(T) values.

^b Derived from the complete basis set (CBS) limit extrapolations.

^c Resonant two-photon threshold ionization spectroscopy.

^d Forbidden transition.

As evoked in the introduction to this chapter, the final quantity that can be extracted from the measurement of such ionisation energies is the enthalpy of formation of C_2^+ in its doublet

TABLE 3.6: Energy differences between C_2 and C_2^+ states.

Energy difference	Value from this work	Literature value	Literature technique
$\Delta E(a - X)$	79(10) meV	76.0829(4) meV [146]	Rotational analysis [146]
$\Delta E(a^+ - X^+)$	567(10) meV	/ *	/ *
$\Delta E(X^+ - X)$	11.873(10) eV	11.866(5) eV [145]**	REMPI [145]

* No value is available in the literature,

** Value derived from a combination of two values determined by two different groups.

ground state ($a^+ \ ^2\Pi_u$). This is achieved by adding the $\Delta E(a^+ - X^+)$ energy difference to the 0 K gas-phase enthalpy of formation of C_2^+ (*i.e.* $\Delta_f H^0(0K)(C_2^+(^4\Sigma_g^+)) = 1965.2 \text{ kJ.mol}^{-1}$) [118]. This summation yields $\Delta_f H^0(0K)(C_2^+(^2\Pi_u)) = 2019.9(10) \text{ kJ.mol}^{-1}$

Ion yield

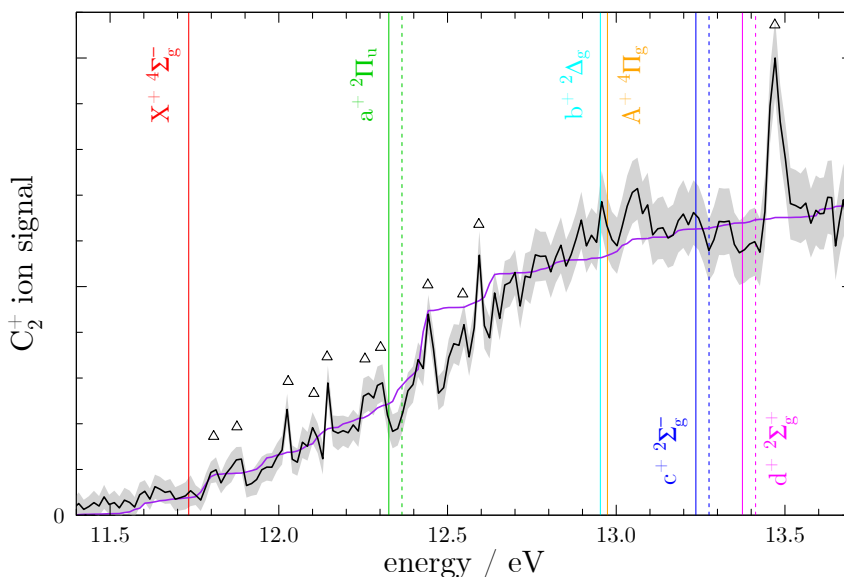


FIGURE 3.9: C_2^+ ion yield adapted from ref. [147]. The vertical lines mark the transition energies ($E_{I,calc,corr,ZPE}$) from the $a \ ^3\Pi_u$ state (full line) or $X \ ^1\Sigma_g^+$ state (dashed line). Triangles locate the position of autoionising features. The grey area represents the statistical error on the C_2^+ ion signal. A purple line represents the integrated experimental TPES.

In addition to the TPE analysis presented above, the experimental scan allowed the production of a C_2^+ ion yield as featured in Fig. 3.9. The ion yield is gradually increasing with photon energy from threshold. As more and more excited electronic states become accessible, there are no marked steps in the curve at the corresponding transition energies.

On top of this general trend, several features are identifiable (marked by triangles in Fig. 3.9) and are attributed to autoionising Rydberg states. Such states have been identified before, but only above 13 eV [144]. Due to the dense electronic landscape, there must be a multitude of

Rydberg series in this energy region which means it is not straightforward to assign the Rydberg states to a given series. It is not trivial to state which states the Rydberg states are reached from, nor if the autoionising processes are electronic or vibrational. More work is needed to make the assignments unambiguously. For example, similar experiments could be carried out with state-selected C_2 (in either the $X^1\Sigma_g^+$ or a $^3\Pi_u$ state) which would facilitate assignments.

It is interesting how the integrated experimental TPES of C_2 (purple line in Fig. 3.9) reproduces the C_2^+ photoion yield with the exception of the autoionisation resonances. This comparison can be generalised for any species undergoing photoionisation and is found to be often verified.

Conclusion on the C_2 study

From this C_2 study, we identified a high density of electronic states in both the neutral and cationic species. Single-photon ionisation explored transitions between these states, some of which could be identified with the help of *ab initio* calculations. From a single TPE spectrum, $a^+{}^2\Pi_u \leftarrow X^1\Sigma_g^+$, $X^+{}^4\Sigma_g^- \leftarrow a^3\Pi_u$, and $a^+{}^2\Pi_u \leftarrow a^3\Pi_u$ were vibronically analysed. Using energy differences, the adiabatic *IP* for the spin-forbidden $X^+{}^4\Sigma_g^- \leftarrow X^1\Sigma_g^+$ transition between ground states was determined and the enthalpy of formation of the C_2^+ cation in its lowest doublet electronic state was retrieved. All of these results are compared to, and are in good agreement with, literature values when available. Hence, this study illustrates how much qualitative and quantitative information can be gained from photoelectron spectroscopy measurements, even from one spectrum.

It is interesting to note at the end of this section how much information could be extracted out of a single scan on C_2 . Coming back to the mass spectrum of Fig. 3.4, a great number of other species are present. Some of these have already been studied, not necessarily from this scan, such as CH [148], CH_2 [149], CH_3 [55], C_2H [150], and C_3H_n ($1 \leq n \leq 3$) [151]. Others have yet to be studied. This goes to show the power and the multiplex character of the DELICIOUS 3 spectrometer coupled with the DESIRS beamline of SOLEIL and the flow tube reactor.

3.2 High-resolution photoelectron spectroscopy

The synchrotron-based photoelectron studies presented so far in this chapter have focused on ionising transitions which could be vibrationally resolved. In order to produce rotationally-resolved spectra in the VUV range, the laboratory laser-based setup VULCAIM was used. As the setup was developed over the course of my PhD, the work presented in this section was intended to better understand and characterise the new setup. The main technique used to produce these rotationally-resolved spectra is Pulsed-Field-Ionisation - ZERO Kinetic Energy (PFI-ZEKE) spectroscopy. I will start by describing this technique, before presenting an example of its use when studying the photoionisation of CO_2 . Finally, the last part of this chapter is dedicated to a new approach for performing Pulsed-Field-Ionisation inspired by the treatment procedure of SPES described in chapter 1.

3.2.1 Pulsed Field Ionisation - ZERO Kinetic Energy (PFI-ZEKE) spectroscopy

Introduction

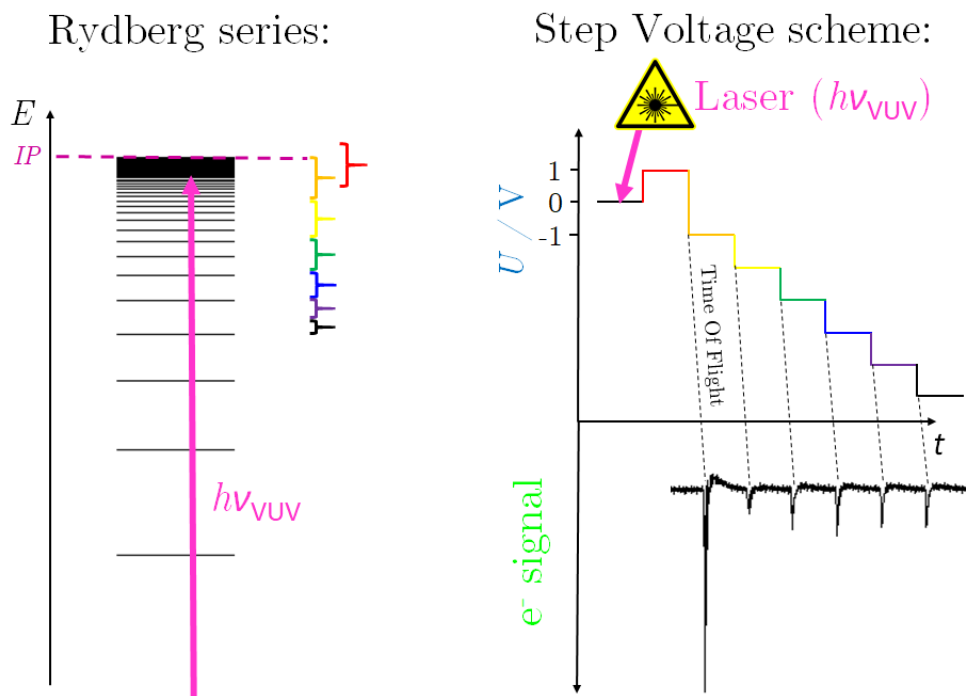


FIGURE 3.10: Illustration of PFI-ZEKE scheme. Left: Rydberg states, reached using a VUV photon (pink), converging to IP . Right: voltage scheme applied to electrons in interaction zone after laser excitation; an electron signal on the MCP is detected for each voltage step after a time-of-flight. Each section of Rydberg states (colour code) is ionised at each successive voltage step (same colour code).

The basic idea behind PFI-ZEKE spectroscopy is the VUV excitation to neutral Rydberg states just below an ionisation threshold (see left panel of Fig 3.10). Once in the excited states, pulsed voltages are carefully applied, to induce the Stark effect, as illustrated in Fig. 1.26 of chapter 1, in order to allow the selective ionisation of given Rydberg states. Indeed, application of a static electric field F results in a drop in ionisation potential (ΔIP), following the quadratic law of equation (1.9) ($\Delta IP \propto \sqrt{|F|}$).

Application of sequences of voltage steps to electrodes in the interaction zone with the VUV laser where the excited electronic states have been created allows a deeper probing of Rydberg states (colour code) at each voltage step (same colour code), as illustrated in the right panel of Fig 3.10. This high-resolution photoelectron spectroscopy was employed using the laboratory-based setup VULCAIM. The ensuing electrons are detected after a time-of-flight. Unlike the synchrotron setup which uses electron-ion coincidences to produce mass-selected photoelectron spectra or the VULCAIM setup when detecting ions, the detection of electrons with VULCAIM is not mass-selective. In general only one species is injected into the experiment, but impurities do exist. Nevertheless, if the IP s of the impurities are not in the same energy range, the measurement is not affected. Mass selectivity can be achieved using a similar technique, but by detecting ions instead of electrons. This is known as MATI (Mass Analysed Threshold Ionisation) spectroscopy [152], but this was not investigated in this PhD. High-resolution MATI spectroscopy does exist, but it is not clear if this technique is capable of the same high resolution as PFI-ZEKE.

Ionisation rates of Rydberg states

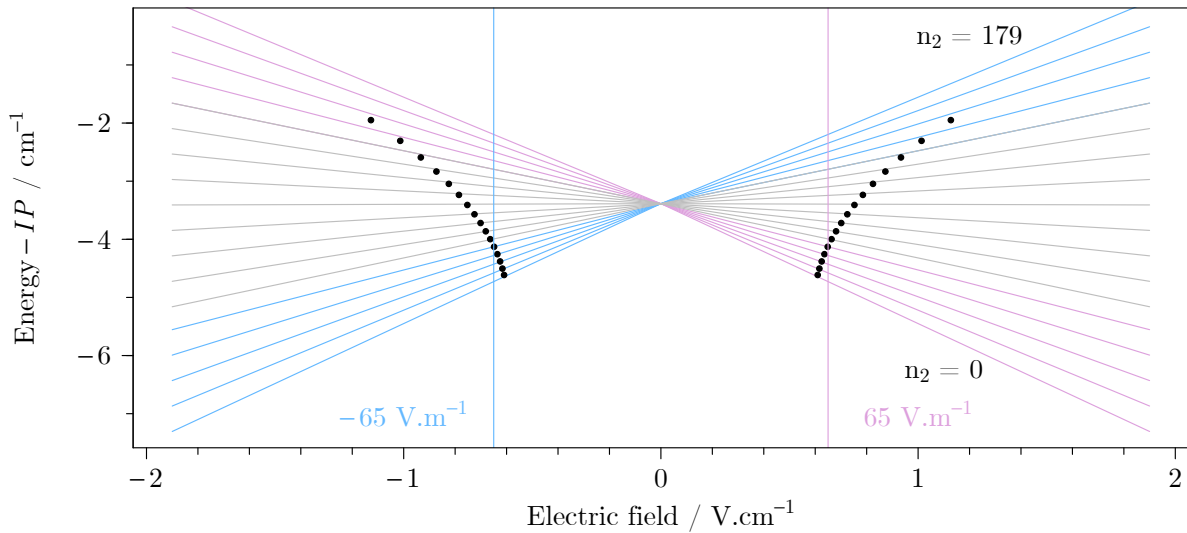


FIGURE 3.11: Simulated degeneracy lifting of a $n = 180$ ($m = 0$) Rydberg state with electric field F , only states with n_2 a multiple of 10 are represented for clarity (except for $n_2 = 179$) adapted from ref. [18]. Black dots locate field thresholds for which the ionisation rate is high enough for detection. States represented by light pink lines are ionised under a 65 V.m^{-1} field. States represented by green lines are ionised under a -65 V.m^{-1} field. In grey are states ionised by neither voltage.

Before presenting the experimental implementation of ZEKE spectroscopy, a final theoretical aspect of Rydberg states must be considered, that is ionisation rates (noted Γ), *i.e.* the number of ionisation events per unit-time. This dynamical aspect must be considered in PFI experiments as only ionisation processes occurring fast enough with respect to the experimental time scale can be detected [18]. Experimentally, a given voltage is applied for up to $1 \mu\text{s}$ and ionisation processes can be detected for our setup if they occur at a rate greater than around 10^7 s^{-1} . Using the same notations as in equation (1.8) of chapter 1, noting $R' = (-2(E - IP))^{3/2}/F$ and

according to Damburg and Kolosov [153], Γ can be written

$$\Gamma = \frac{(4R')^{2n_2+m+1}}{n^3 n_2! (n_2 + m)!} \exp\left\{-\frac{2}{3}R' - \frac{1}{4}n^3 F(34n_2^2 + 34n_2m + 46n_2 + 7m^2 + 23m + \frac{53}{3})\right\}, \quad (3.1)$$

which was achieved using fourth order perturbation theory. This equation can be solved numerically to determine the experimental ionisation threshold field. The threshold field for each state of the $n = 180$ manifold is represented as black dots in Fig. 3.11 and was determined numerically from equation (3.1). Values could not be determined for the most blue-shifted states within the context of equation (3.1), problems within this theory for the description of blue-shifted states have already been reported [18]. The notion of blue or red-shifted states is relative to the sign of the applied field: if the field changes sign, blue-shifted states become red and *vice versa*. This is apparent in Fig. 3.11.

If the applied electric field F intensity is greater than the threshold field, ionisation can occur on a detectable scale. For $F = 65 \text{ V.m}^{-1}$ this is true for states with parabolic number $n_2 \lesssim 50$ (light pink lines in Fig. 3.11). For $F = -65 \text{ V.m}^{-1}$ this is true for states with parabolic number $n_2 \gtrsim 130$ (green lines in Fig. 3.11). For the other states (grey lines in Fig. 3.11), their ionisation is not detected for either voltage step.

Figure 3.11 demonstrates how the application of a first positive voltage followed by a second voltage still ionises Rydberg states on a detectable scale. This is true even if the second voltage is no more intense (in terms of absolute amplitude) than the first.

Experimental implementation

When implementing the PFI-ZEKE scheme of Fig. 3.10, the first voltage step (red) is positive (typically +1V). It is used to get rid of the prompt electrons directly produced by the laser and to pulse ionise the higher Rydberg states. Prompt electrons contain kinetic energy and are not of interest here as this technique focuses on electrons whose kinetic energy is vanishing.

The second voltage step (orange) is negative and generally of the same absolute amplitude as the first. Based on equation (1.9) of chapter 1, no extra products are ionised compared to the first step, but with the knowledge of paragraph 3.2.1, ionised products will be detected if the first voltage step induced detectable ionisation. Pushing the theory of paragraph 3.2.1 further, it is possible to detect ionised products by applying a negative voltage step less intense than the first. This comes at a cost in signal, but an increase in resolution as fewer states are selectively ionised.

As shown in Fig. 3.10, at each negative voltage step, a thin slice of lower energy Rydberg states is ionised. These subsequent voltage steps can be a lot smaller than the two first in order to ionise fewer states and thus achieve greater photoelectron resolution. The only limitation is the decrease in electron signal as fewer states are probed, which in the extreme results in a loss of detection. Scanning the VUV laser photon energy and recording the number of electron hits at each energy step enables the construction of a spectrum presented in Fig. 3.12.

So far, the highest photoelectron resolution using this technique with VULCAIM of 0.14 cm^{-1} was achieved using 0.83 V/m steps when probing the first *IP* of Kr ($\text{Kr}^+ (4s^2 4p^5)^2 P_{3/2} \leftarrow \text{Kr} (4s^2 4p^6)^1 S$). The resolution is measured in the same way as in chapter 1 in the I_2 study or the rare gas Rydberg series study. The resolution may actually be even higher than this as there are several transitions within this band corresponding to the five most abundant Kr isotopes [34].

Note that the peak in Fig. 3.12 is not centered at the Kr ionisation potential, which is reported at $112\,914.441(0.016) \text{ cm}^{-1}$ [41]. The observed shift to lower energy is due to the Stark effect,

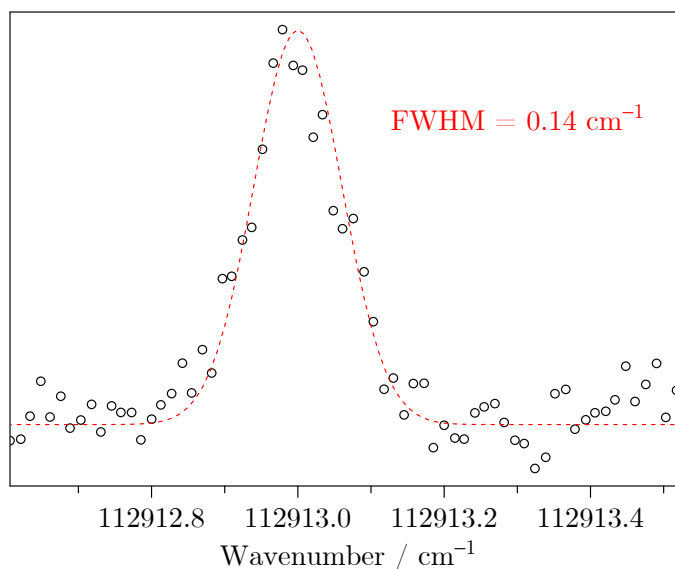


FIGURE 3.12: PFI-ZEKE spectrum (points) around the first IP of Kr. Superimposed on this experimental spectrum is a red-dashed gaussian line shape whose $FWHM$ is 0.14 cm^{-1} .

which can be rationalised using equation (1.9) of chapter 1 ($\Delta IP \propto \sqrt{U}$). Correcting the Stark shift ($-1.7(3) \text{ cm}^{-1}$), we can determine $IP(\text{Kr}) = 112\,914.7(3) \text{ cm}^{-1}$. This correction procedure is detailed in paragraph 3.2.2.

Another way of determining the Stark shift is to use the H atom model described in ref. [18] to compute the Stark shift. This yields a shift of -1.43 cm^{-1} . Our recorded PFI-ZEKE spectrum is centred around $112\,913.00(0.14) \text{ cm}^{-1}$. Adding the calculated shift, this value sets the Kr IP at $112\,914.43(0.14) \text{ cm}^{-1}$, which is even closer to the reported value [41].

3.2.2 CO₂ PFI-ZEKE spectroscopy

Motivations

Carbon dioxide, or CO₂, is a molecule of great atmospheric and astrophysical importance. On Earth, it is well known as a green house gas in Earth's atmosphere and is also well known to be an important player in other planetary atmospheres: it makes up over 95% of the Martian atmosphere for example. It has furthermore been detected in the ISM, in the vicinity of comets and within ice dust grains in molecular clouds.

Its choice as the first molecule for a PFI-ZEKE study with VULCAIM, however, is mainly motivated by spectroscopic arguments. CO₂ was chosen as a test species following the recently published paper by Hollenstein *et al.* [154] in 2019 reporting the adiabatic ionisation energy of CO₂ using PFI-ZEKE spectroscopy. Hence the goal of my PhD study was to reproduce their results, determine the performances of the new VULCAIM setup, and thus verify that it was performing properly.

Neutral CO₂ has been extensively studied along with its cation. CO₂⁺ is usually produced and studied in a discharge or by electron-bombardment ionisation. Focusing on studies of the cation, its complex emission spectrum was first observed in 1927 by Fox *et al.* [155], although the lines at the time were assigned to neutral CO₂ emission. Subsequent papers confirmed the

cationic emission in assigning spectral features between 280 nm to 450 nm to the $B^+ \ ^2\Sigma_u^+ \rightarrow X^+ \ ^2\Pi_g$ and $A^+ \ ^2\Pi_u \rightarrow X^+ \ ^2\Pi_g$ transitions in CO_2^+ .

As the symmetry of the cationic ground electronic state is $X^+ \ ^2\Pi_g$, it is apparent that spin-orbit effects will complicate the observed spectra. In addition, CO_2^+ is linear, which means that the Renner-Teller effect will further complicate spectra in the levels associated to the ν_2 bending mode. Such an effect is the result of a vibronic coupling present in degenerate electronic states of linear species and due to the coupling between electronic orbital and vibrational angular momenta [156]. It manifests itself, in particular, in vibrationally excited states and the rotational states therein. Following this elucidation, rovibronic transitions within CO_2^+ have been observed and assigned, which enabled the determination of spin-orbit constants, vibrational frequencies, rotational constants, *etc.* [157–159].

TABLE 3.7: Vibrational modes of $\text{CO}_2(X)$ and $\text{CO}_2^+(X^+)$

ν_i	Assignment	$\tilde{\nu}_i(\text{CO}_2(X)) / \text{cm}^{-1}$	$\tilde{\nu}_i(\text{CO}_2^+(X^+)) / \text{cm}^{-1}$
ν_1	symmetric stretch	1332.9 [160]	1255 [161]
ν_2	bend*	667.4 [160]	516.332 [159]
ν_3	asymmetric stretch	2349.2 [160]	1423.08 [162]

* Twice degenerate mode

A final level of complexity is observed in vibronic states of the $(\nu_1, \nu_2, \nu_3) = (1, 0, 0)$ and $(0, 2, 0)$ bands due to a Fermi resonance (see Table 3.7). A Fermi resonance is a coupling between vibronic states of same symmetry and close energies. It results in the shifting of levels in addition to the Renner-Teller and spin-orbit effects. This has been studied in CO_2^+ produced in a discharge in a number of works [161, 163].

The first PFI-ZEKE study of $X^+ \ ^2\Pi_g$ was that of Merkt *et al.* [164], who presented spectra with a resolution of 1.5 cm^{-1} and described the various vibronic states of the $(0, 0, 0)$ and $(0, 1, 0)$ levels. A subsequent study presented rotationally-resolved (resolution 0.6 cm^{-1}) PFI-ZEKE spectra, which confirmed the previous findings [165]. Later, a medium-high-resolution (7 cm^{-1}) PFI-PE study investigated the vibronic structure of CO_2^+ over a broader energy range (13.6 to 14.7 eV) [166]. The study at higher resolution (0.2 cm^{-1}) by Hollenstein *et al.* [154] in 2019 offered yet improved precision and accuracy, of the adiabatic ionisation energy in particular. As previously mentioned, this study will provide a benchmark for our findings. The results of Merkt *et al.* [164] will guide the study of the $(0, 1, 0)$ states. To our knowledge, the $(1, 0, 0)$ and $(0, 2, 0)$ bands have never been studied by PFI-ZEKE spectroscopy, but we will rely on IR results directly obtained in the cation [161, 163].

Overview of the $X^+ \ ^2\Pi_g \ \text{CO}_2^+$ ground state

As depicted in Fig. 3.13, the lowest vibrational levels of the $\text{CO}_2^+ \ X^+ \ ^2\Pi_g$ ground state were recorded using the PFI-ZEKE technique. Commercially available CO_2 gas seeded in Ar at a concentration of around 1/6 was fed into the experiment as described in section 1.2.7. The molecules were irradiated by VUV laser radiation whose photon energy was scanned around the first *IP* of CO_2 . This VUV radiation was achieved by tuning the high-resolution UV laser to around the Kr(1) resonance of Table 1.7 (chapter 1) and by scanning the high resolution visible laser around 600 nm. Both laser sources were combined in by four-wave (summed) frequency

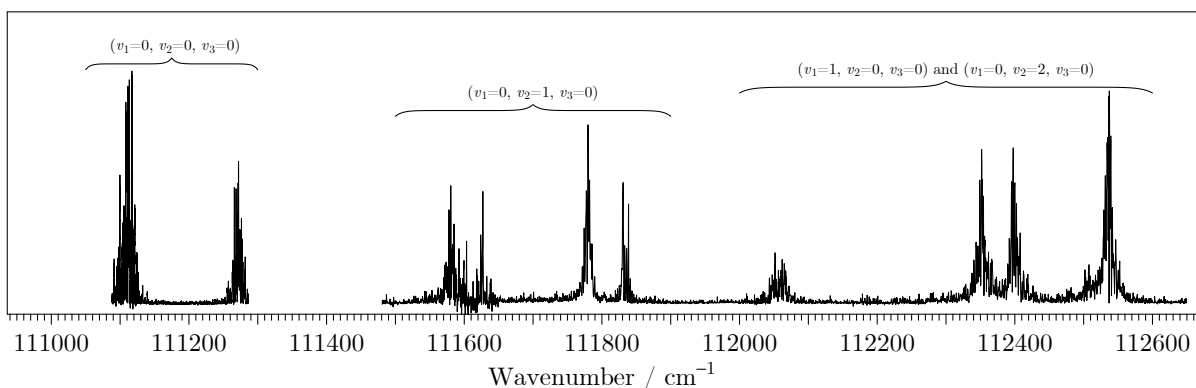


FIGURE 3.13: Raw PFI-ZEKE spectrum of the lowest vibrational levels of the CO_2^+ $X^+ \ ^2\Pi_g$ ground state.

mixing to provide the corresponding VUV radiation (see Figs. 1.13 and 1.14 of chapter 1). Following irradiation, voltages were applied to electrodes and resulting electrons were detected, as illustrated in Fig. 3.10.

The first overview scans used the following parameters:

- $\approx 3.10^{-1} \text{ cm}^{-1}$ photon energy steps,
- 2 V voltage steps,
- $\approx 0.6 \text{ cm}^{-1}$ photoelectron resolution.
- statistics 50 (counts per point)

These scans are used to produce PFI-ZEKE spectra of the excited vibrational levels of CO_2^+ $X^+ \ ^2\Pi_g$ as a first step before exploring the pertinent zones at yet higher spectral resolution. Higher resolution scans have been recorded and will be detailed in the following paragraphs.

Note that the spectra are corrected by the VUV photon flux (see section 1.2.6 of chapter 1). However, the relative intensities between bands are arbitrary as we were not able to record spectra encompassing multiple vibronic states. The vibrational bands of this spectrum are assigned following the vibronic energy diagram adapted from ref. [157] and pictured in Fig. 3.14.

In the following sections, three regions of interest in the CO_2^+ $X^+ \ ^2\Pi_g$ ground state will be detailed:

- the complete study of the vibrationless spin-orbit components of the (0, 0, 0) level at 0.2 cm^{-1} resolution,
- the partial study of the (0, 1, 0) level combining the Renner-Teller effect with the spin-orbit coupling at 0.6 cm^{-1} resolution, and
- the partial study of the (0, 2, 0) and (1, 0, 0) levels combining the Renner-Teller and spin-orbit effects with the Fermi resonance at 0.6 cm^{-1} resolution.

We have not yet recorded very high-resolution spectra for the vibrationally excited states, but the simulations offer insight into the complex couplings.

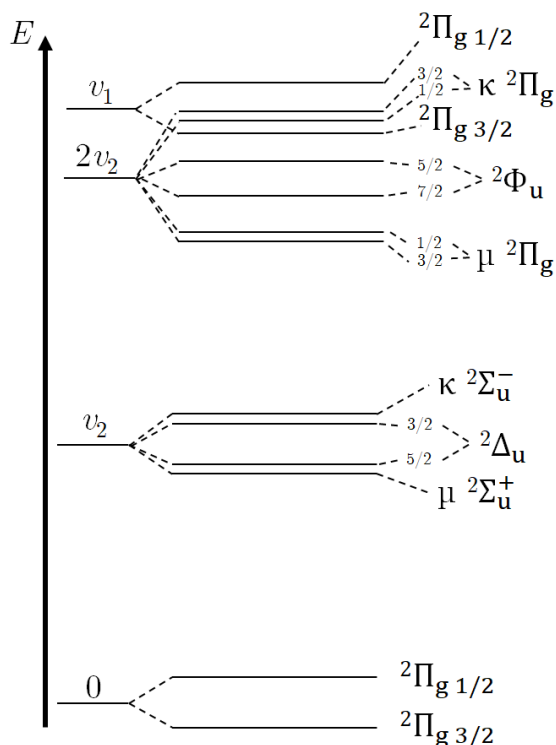


FIGURE 3.14: Energy diagram of the lowest vibrational levels of the $\text{CO}_2^+ X^+ 2\Pi_g$ ground state accounting for the Renner-Teller and spin-orbit effects adapted from ref. [157].

Spin-orbit components of $X^+ 2\Pi_g(v_1 = 0, v_2 = 0, v_3 = 0)$

A first scan was recorded spanning the two spin-orbit components of $X^+ 2\Pi_g(0, 0, 0)$ using the following parameters:

- $\approx 7.10^{-2} \text{ cm}^{-1}$ photon energy steps,
- 500 mV voltage steps, and
- $\approx 0.4 \text{ cm}^{-1}$ photoelectron resolution.

The resulting rotationally-resolved PFI-ZEKE spectrum is presented in Fig. 3.15.

Since the spin-orbit parameter in CO_2^+ is negative, the $\Omega^+ = 3/2$ component is at lower energy compared to the $\Omega^+ = 1/2$ [157]. As this scan expands over both spin-orbit components, the relative spin-orbit intensities can be determined. This is done by integrating the signal of each component in the spectrum of Fig. 3.15 and comparing integrals as a ratio. The result is that the $\Omega^+ = 3/2$ ($\Omega^+ = 1/2$) component makes up around 70% (30%) of the spectrum intensity. This is in excellent agreement with Merkt *et al.*, who also performed PFI-ZEKE spectroscopy and found a ratio of 68:32. However, this ratio disagrees with that found by other works employing different techniques (PES, theory...), which found a more equal share between components [164]. Different physical aspects of the employed experimental techniques can explain the differences between PES and ZEKE intensities, but these are not discussed in detail here (see ref. [167] for instance).

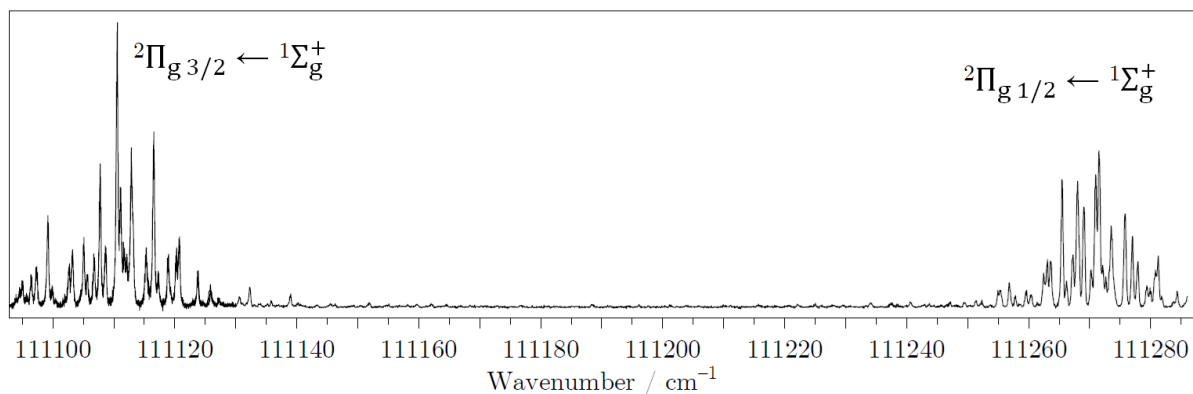


FIGURE 3.15: PFI-ZEKE spectrum of both spin-orbit components of the CO_2^+ $X^+ \ ^2\Pi_g(v_1 = 0, v_2 = 0, v_3 = 0)$.

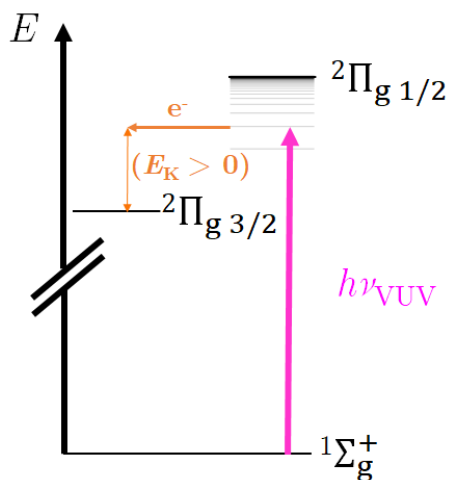


FIGURE 3.16: Illustration of an autoionisation process from a Rydberg state converging to the $^2\Pi_{1/2}$ to the $^2\Pi_{3/2}$ ground state in CO_2^+ (X^+). This process yields an electron with non-zero kinetic energy ($E_K > 0$).

This discrepancy can be explained by the presence of autoionisation processes from Rydberg states converging to the $^2\Pi_{1/2}$ state, autoionising to the $^2\Pi_{3/2}$ state below, as illustrated in Fig. 3.16. Autoionisation intervenes after the VUV excitation to a Rydberg state, as there is a slight pause (around a few μs) before applying pulsed voltages. During this time, the occupied Rydberg state, being situated above the cationic ground state ($^2\Pi_{3/2}$), can autoionise. In doing so, an electron whose kinetic energy is non-zero is produced and is thus not detected using PFI-ZEKE spectroscopy. The effect on the PFI-ZEKE spectrum of CO_2^+ (X^+) is a loss of signal from the $^2\Pi_{1/2}$ component. The $^2\Pi_{3/2}$ component is not affected as it is already the lowest cationic state, it would have no other state to ionise to. As other techniques do not use the pulsed ionisation of Rydberg states, autoionisation does not affect the spectra in this way, which can explain the 1:1 intensity ratio between multiplets found in other studies.

In the following paragraphs, the rotational structure of each component will be investigated further.

Rotational energy levels of a linear triatomic molecule in a ${}^2\Pi$ electronic state - simulations

In the aim of simulating experimental spectra, and assigning features therein, the rotational energy levels of the neutral and cationic states must be determined. These simulations are implemented using a home-made code relying on models described in the following paragraphs.

The rotational structure of a ${}^2\Pi$ electronic state in the case of a linear triatomic molecule was determined in 1962 by Hougen [168]. His work builds on the vibronic work of Pople, who had already developed a Hamiltonian that accounted for the spin-orbit and the vibronic (Renner-Teller) couplings [169]. Hougen proposed a rotational Hamiltonian to be used in addition to that of Pople's and analytically derived rotational energy levels for each vibronic state.

Hougen identified an important quantum number for describing rotation in such vibronic states: $K = |\Lambda + l|$; with Λ , the projection of total orbital angular momentum of the electrons along the linear axis and l , the bending vibrational angular momentum along this axis. In a ${}^2\Pi$ electronic state, $\Lambda = \pm 1$ and for a given bending vibrational quantum v_2 , $-v_2 \leq l \leq v_2$ by steps of 2. In his paper, Hougen details rotational energy values for each K value.

In the case of the $(0, 0, 0)$ ground state of CO_2^+ , the vibronic states fall into the $K = v_2 + 1$ category described by Hougen [168]. Rotational energy level values are then given by

$$\begin{aligned} E^+(J^+ = \frac{1}{2}) &= E_0 + C + v_2\omega_2 + B^+K - \frac{1}{2}A_{\text{eff}} + g_K\Lambda K \\ E^+(J^+ > \frac{1}{2}) &= E_0 + C + v_2\omega_2 + B^+\{(J + \frac{1}{2})^2 - K^2\} + g_K\Lambda K \\ &\quad \pm \frac{1}{2}\sqrt{4B^{+2}(J + \frac{1}{2})^2 + A_{\text{eff}}(A_{\text{eff}} - 4B^+K)}, \end{aligned} \quad (3.2)$$

with:

- the $E^+(J^+ = \frac{1}{2})$ level only present in the ${}^2\Pi_{1/2}$ state,
- E_0 , the energy offset of the cationic ground state. E_0 will be adjusted manually to fit the experimental data with the simulations,
- J^+ , the rotational quantum number in CO_2^+ ($X^+ {}^2\Pi$), a positive half-integer,
- $\epsilon = -0.189$, the Renner parameter for the CO_2^+ ($X^+ {}^2\Pi$) state [159],
- $\omega_2 = 516.332 \text{ cm}^{-1}$, the harmonic vibrational frequency for the bending mode of CO_2^+ ($X^+ {}^2\Pi$) [159],
- $B^+ = 0.380511 \text{ cm}^{-1}$, the rotational constant for the vibrationless CO_2^+ ($X^+ {}^2\Pi$) state [159],
- $C = -(v_2 + 1)(v_2 + 2)\epsilon\omega_2/8$,
- $A_{\text{SO}} = -162.34 \text{ cm}^{-1}$, the spin-orbit parameter for CO_2^+ ($X^+ {}^2\Pi$) [159],
- $A_{\text{eff}} = A(1 - (\epsilon^2/8)K(K + 1))$, the effective spin-orbit parameter for CO_2^+ ($X^+ {}^2\Pi$) [168],
- the $g_K\Lambda K$ term was introduced by Brown [170] to account for second order vibronic couplings with orbital momentum. Sears *et al.* derived $g_K = 2.914 \text{ cm}^{-1}$ for CO_2^+ , by fitting experimental data with a model relying on the harmonic approximation, and
- the \pm sign refers to each spin-orbit component. '+' is for the upper ${}^2\Pi_{1/2}$ state and '-' is for the lower ${}^2\Pi_{3/2}$ state.

The above parameters provide good starting values to describe our spectra. Using equation (3.2), the rotational states in CO_2^+ ($X^+ \ ^2\Pi$) can be adequately described. In the $^1\Sigma_g^+$ state of the neutral CO_2 ground state, rotational energy level values are simply written

$$E(J) = BJ(J + 1), \quad (3.3)$$

with:

- J , the rotational quantum number in CO_2 ($X \ ^1\Sigma_g^+$), an even integer due to spin statistics (^{16}O nuclear spin is 0) [38],
- $B = 0.39021894 \text{ cm}^{-1}$, the rotational constant for the vibrationless CO_2 ($X \ ^1\Sigma_g^+$) state [171].

For both neutral and cationic species, the simulations do not take centrifugal distortion into account. Indeed, as the sample in our jet experiment is cold ($\approx 10 \text{ K}$) and as the centrifugal distortion affects significantly only high J values, there is no need to introduce it in our calculations. The reference energy is set as the lowest rotational level of the neutral ground state, *i.e.* $E(J = 0) = 0$. The photoionisation transition energies between these rotational states are noted $\Delta E = E^+(J^+) - E(J)$. Note that there is no selection rule for $\Delta J = J^+ - J$.

To determine spectral intensities, the population of each rotational state of the electronic ground state must be determined as a function of temperature T . This is achieved using a Boltzmann distribution which gives the population of energy level, $\text{pop}(E(J))$, as:

$$\frac{\text{pop}(E(J))}{\text{pop}(E(0))} = (2J + 1)\exp\left(\frac{-E(J)}{k_B T}\right). \quad (3.4)$$

In addition to the Boltzmann factor of equation (3.4), the spectral intensities can be computed using the methods reported in refs. [172, 173]. This method is simplified here by introducing an additional term $W(\Delta J)$ to the simulations in order to properly fit the experimental relative intensities as done in ref. [164]. This term acts as a weight for each ΔJ branch and is adjusted manually to best fit the experimental spectrum.

The Boltzmann factors and ΔJ branch weights are used as a relative intensities in the simulations. These simulations yield a line spectrum which is convoluted by a gaussian function, whose *FWHM* is adjusted to fit the photoelectron resolution.

Stark-shift corrections

When applying the voltage step scheme of Fig. 3.10, each step generates electrons stemming from transitions whose energies are shifted due to the Stark effect (see equation (1.9) of chapter 1). The resulting PFI-ZEKE spectrum is thus also Stark-shifted, proportionately to \sqrt{F} . This shift can be computed theoretically in a model that treats the Rydberg atom or molecule as a hydrogen atom [18]. This model was used to compute the Kr *IP* in paragraph 3.2.1.

Experimentally, the shift can be corrected by recording PFI-ZEKE spectra using successive voltage steps. The energy of a given transition is noted for each voltage and extrapolations can be undertaken to determine the transition energy in the absence of electric field $F = 0$.

This procedure is illustrated in Fig. 3.17 presenting raw PFI-ZEKE spectra. This figure displays a zoom on a rotational transition of the vibrationless $X^+ \ ^2\Pi_{3/2} \leftarrow X \ ^1\Sigma_g^+$ transition, recorded using the step voltage scheme of Fig. 3.10. The consecutive voltage steps are +1 V, -1 V, -1.1 V, -1.2 V, -1.3 V, -1.4 V and -1.5 V. The energy of a given transition is pinpointed using a gaussian function fit whose central value is represented by a red dot in Fig. 3.17. A linear regression between each energy value and $\sqrt{-U}$, with U the corresponding voltage step value, yields

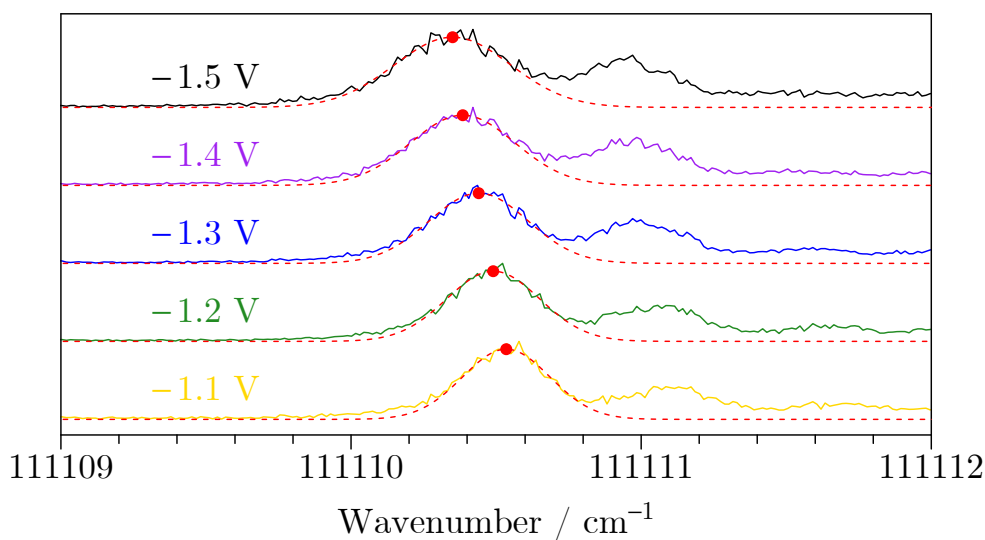


FIGURE 3.17: Zoom on PFI-ZEKE experimental spectra of the vibrationless $X^+ \ ^2\Pi_{3/2} \leftarrow X \ ^1\Sigma_g^+$ transition recorded at different voltage steps. Using colour coding, the spectrum for each voltage step is represented, shifted vertically for clarity. Red dots locate maxima for a given transition which move to lower energies, the lower the voltage.

the zero-field transition energy as the intercept according to equation (1.9) of chapter 1. Stark shifts are deduced as the difference between the raw transition energy for the given voltage step and the zero-field transition energy.

The $\text{CO}_2^+ X^+ \ ^2\Pi_{3/2}$ vibronic state

The experimental PFI-ZEKE spectrum (black) of the vibrationless $X^+ \ ^2\Pi_{3/2} \leftarrow X \ ^1\Sigma_g^+$ transition is presented alongside the simulated spectrum (blue) in Fig. 3.18. The parameters used in this scan are:

- $\approx 6.10^{-3} \text{ cm}^{-1}$ photon energy steps,
- 100 mV voltage steps,
- averaging 100 (counts per point),
- $\approx 0.2 \text{ cm}^{-1}$ photoelectron resolution.

It is interesting to note here, given these scan parameters, that the spectrum of Fig. 3.18 took over 4 hours to record.

The rotational temperature used in the simulations is $T = 10 \text{ K}$. The E_0 energy shift is adjusted to fit the experimental spectrum with the simulation. The values of all other constants are left unchanged from the previous section. The simulated spectrum is produced from a line spectrum convoluted by a gaussian function whose $FWHM = 0.2 \text{ cm}^{-1}$, which gives the experimental photoelectron resolution.

The resulting simulation is in very good agreement with the experimental findings, in both the line positions and relative intensities. Thanks to the simulation, ΔJ branches are identified

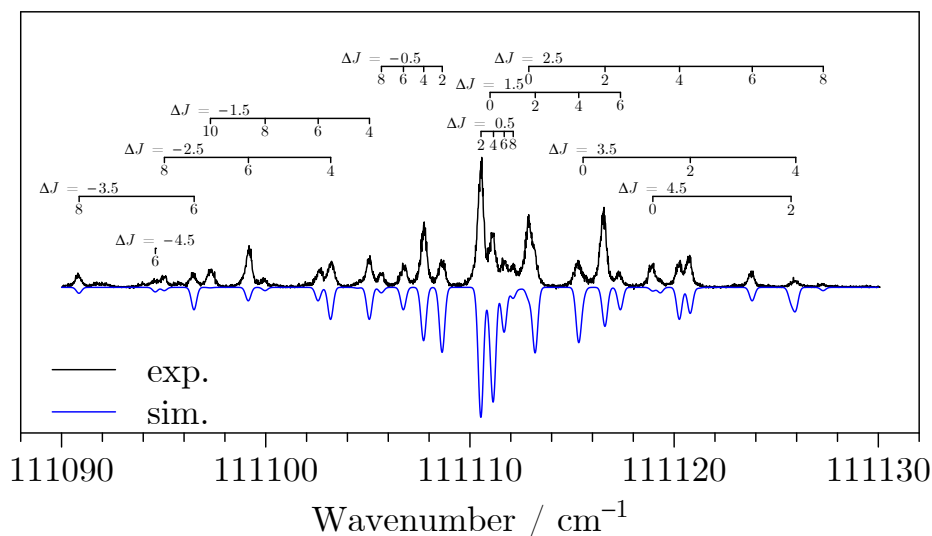


FIGURE 3.18: PFI-ZEKE experimental (black) and simulated (blue) spectra of the vibrationless $X^+ \ ^2\Pi_{3/2} \leftarrow X \ ^1\Sigma_g^+$ transition. Note the simulated spectrum used $T = 10$ K and is inverted with respect to the experimental spectrum to facilitate comparisons. Assignments to ΔJ branches are noted with the ground state rotational quantum J underneath.

TABLE 3.8: ΔJ branch weightings for the vibrationless $X^+ \ ^2\Pi_{3/2} \leftarrow X \ ^1\Sigma_g^+$ transition

ΔJ	-9/2	-7/2	-5/2	-3/2	-1/2	1/2	3/2	5/2	7/2	9/2
W	0.1	0.5	0.3	0.3	0.5	1	0.3	0.4	0.2	0.1

ranging from $-9/2$ to $9/2$. In each branch, the neutral ground state J value is marked for each transition and the rotational autoionisation weights are summarised in Table 3.8.

Merket *et al.* [164] suggested that electronic, spin-orbit or rotational autoionisation (similar to the scheme depicted in Fig. 3.16) could also have an impact on relative intensities [164]. These autoionisation processes affect spectral intensities in PFI-ZEKE spectroscopy. It could also be possible that the neutral state population distribution is more complicated than a single Boltzmannian distribution, which would also affect the relative intensities.

It is possible to extract the first adiabatic IP of CO_2 from the spectrum in Fig. 3.18. In this case it corresponds to the energy difference between the $X^+ \ ^2\Pi_{3/2} (J^+ = 3/2)$ and $X \ ^1\Sigma_g^+ (J = 0)$ states. As $E(J = 0) = 0$, $IP = E^+(X^+ \ ^2\Pi_{3/2} (J^+ = 3/2))$, a value that can be extracted from the simulations and their fit to the experimental spectrum. The value is corrected for the Stark shift following the method described in paragraph 3.2.2. The result is compared to Hollenstein *et al.*'s value in Table 3.9; there is an excellent agreement between both results. This result confirms the energy scale is correctly calibrated and shows that the VULCAIM is very capable of undertaking PFI-ZEKE spectroscopic studies.

The error bar on our IP_{adia} value is given by the error on the intercept of the Stark-shift correction procedure (see paragraph 3.2.2). The laser calibration error (0.02 cm^{-1} [33]) is neglected.

TABLE 3.9: Adiabatic IP of CO_2

	This work	Hollenstein <i>et al.</i> [154]
$IP_{\text{adia}} / \text{cm}^{-1}$	111 112.24(21)	111 112.29(18)

The $\text{CO}_2^+ X^+ 2\Pi_{1/2}$ vibronic state

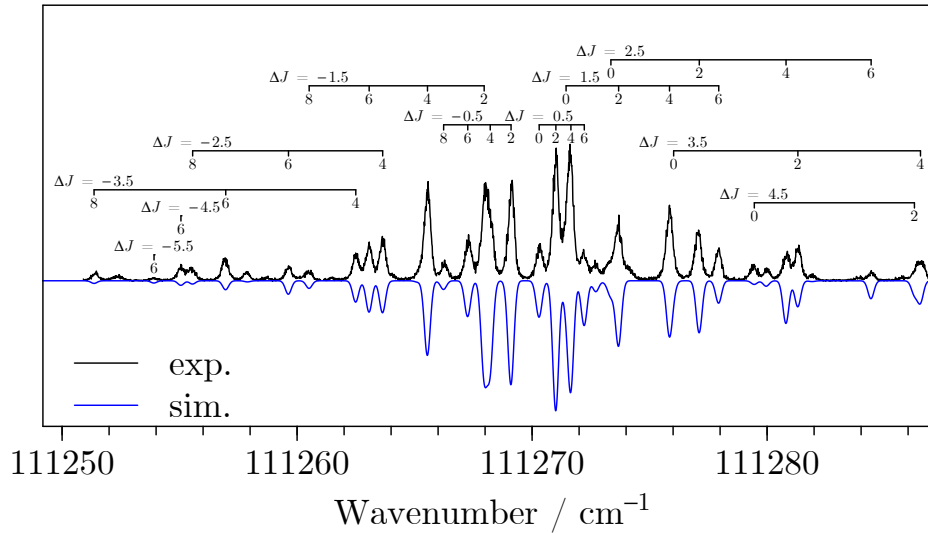


FIGURE 3.19: PFI-ZEKE experimental (black) and simulated (blue) spectra of the vibrationless $X^+ 2\Pi_{1/2} \leftarrow X 1\Sigma_g^+$ transition. Note the simulated spectrum uses $T = 10$ K and is inverted with respect to the experimental spectrum to facilitate comparisons. Assignments to ΔJ branches are noted with the ground state rotational quantum J underneath.

Using the same method as described previously on the lower spin-orbit component, the experimental PFI-ZEKE spectrum (black) of the vibrationless $X^+ 2\Pi_{1/2} \leftarrow X 1\Sigma_g^+$ transition is presented alongside the simulated spectrum (blue) in Fig. 3.19. The energy shifts, constants and bandwidth (0.2 cm^{-1}) are the same as previously. ΔJ branches are once again identified and their weights are summarised in Table 3.10.

TABLE 3.10: ΔJ branch weightings for the vibrationless $X^+ 2\Pi_{1/2} \leftarrow X 1\Sigma_g^+$ transition

ΔJ	-11/2	-9/2	-7/2	-5/2	-3/2	-1/2	1/2	3/2	5/2	7/2	9/2
W	0.05	0.1	0.2	0.3	0.7	0.8	1	0.5	0.4	0.2	0.1

The important spectroscopic parameter that can now be determined is the effective spin-orbit parameter, A_{eff} , responsible for the splitting of the two spin-orbit components of $X^+ 2\Pi$. Equation (3.2) is implemented to simulate both spin-orbit components simultaneously which allows the isolation of A_{eff} as summarised in Table 3.11.

TABLE 3.11: Spin-orbit parameter of CO_2^+

	This work	Sears <i>et al.</i> [159]
$A_{\text{eff}} / \text{cm}^{-1}$	-159.70(5)	-159.7202(92)

The determination of A_{eff} does not need a Stark-shift correction as it is deduced from the relative positions of each spin-orbit component. The A_{eff} error is therefore lower than that of IP_{adia} and only accounts for the fit parameter adjustment and the relative calibration of the photon energy. The literature value was obtained using IR-absorption spectroscopy performed directly on CO_2^+ produced in a discharge at 200 K. Given this experimental technique and higher sample temperature (offering more rotational lines for the fit), a higher precision is expected in their case. Both results are in very good agreement.

Vibronic states of the $(v_1 = 0, v_2 = 1, v_3 = 0)$ band.

The $(0, 1, 0)$ level of the CO_2^+ electronic ground state splits into three components due to the Renner-Teller effect: a ${}^2\Delta$ state with $K = 1 + 1 = 2$ and a μ and a κ ${}^2\Sigma$ states with $K = 1 - 1 = 0$. Due to spin-orbit coupling, the ${}^2\Delta$ state is further split into two components for spin up and spin down. As illustrated in Fig. 3.14, there are therefore four vibronic levels in the $(0, 1, 0)$ vibrational level.

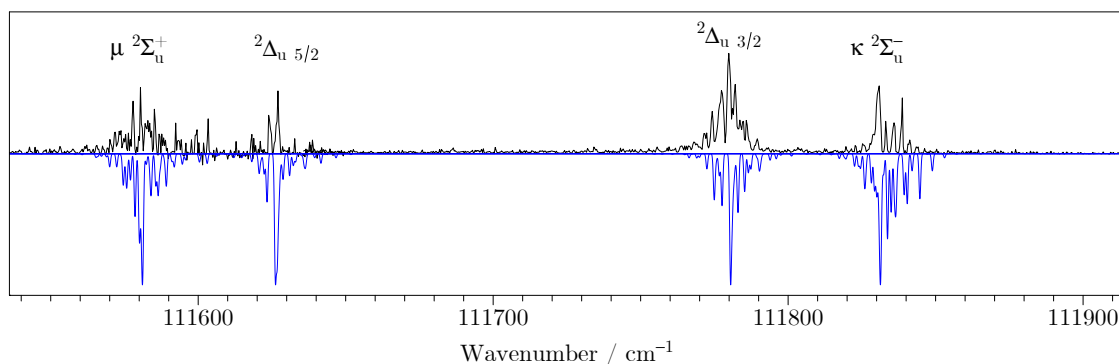


FIGURE 3.20: Raw PFI-ZEKE experimental (black) and simulated (blue) spectra of the $X^+ {}^2\Pi(0, 1, 0) \leftarrow X {}^1\Sigma_g^+(0, 0, 0)$ transition. Note the simulated spectrum uses $T = 10$ K and is inverted with respect to the experimental spectrum to facilitate comparisons. Assignments to vibronic states are noted.

A zoom on these components from Fig. 3.13 is presented in Fig. 3.20 along with simulations. The four aforementioned vibronic states are observed experimentally and are well reproduced by the simulated spectra. The simulations are produced in a similar way to those presented in the vibrationless ground state, but rely on different expressions for the excited energy levels.

The ${}^2\Delta$ states fall into the same category of states $K = v_2 + 1$ as described by equation (3.2). The same constants from Sears *et al.* [159] are used to produce the ${}^2\Delta$ state simulations of Fig. 3.20.

Hund's case (a) can be applied to these ${}^2\Delta$ states and the ${}^2\Pi$ states of the $(0, 0, 0)$ band. This is not the case for the ${}^2\Sigma$ states ($\Lambda = 0$) for which Hund's case (b) is applied. In this case, a new quantum number N is introduced representing total angular momentum excluding electron

spin: $J = N \pm 1/2$. Due to spin statistics, only odd (even) N values exist for Σ^+ (Σ^-) states in CO_2^+ . An important parameter in the description of the ${}^2\Sigma$ states is

$$r = \frac{1}{2} \sqrt{A_{\text{SO}}^2 + ((v_2 + 1)^2 - K^2) \epsilon^2 \omega_2^2}. \quad (3.5)$$

Using the same constants as in equation (3.2), but with $K = 0$ and $v_2 = 1$, we compute $r = 125 \text{ cm}^{-1}$. In this context, neglecting centrifugal distortion and being as $r \gg BJ$, the energy levels of the ${}^2\Sigma$ states can be written [157, 159, 168]:

$$\begin{aligned} E_1(\kappa {}^2\Sigma_u^-, N) &= E_0 + C' + v_2 \omega_2 + r + B_{\text{eff}}^+ N(N+1) + \frac{1}{2} \gamma_{\text{RT}}^+ (N+1) \\ E_2(\kappa {}^2\Sigma_u^-, N) &= E_0 + C' + v_2 \omega_2 + r + B_{\text{eff}}^+ N(N+1) - \frac{1}{2} \gamma_{\text{RT}}^+ N \\ E_1(\mu {}^2\Sigma_u^+, N) &= E_0 + C' + v_2 \omega_2 - r + B_{\text{eff}}^+ N(N+1) + \frac{1}{2} \gamma_{\text{RT}}^+ (N+1) \\ E_2(\mu {}^2\Sigma_u^+, N) &= E_0 + C' + v_2 \omega_2 - r + B_{\text{eff}}^+ N(N+1) - \frac{1}{2} \gamma_{\text{RT}}^+ N \end{aligned} \quad (3.6)$$

with the same notations as in equation (3.2) and in addition:

- $C' = -(v_2 + 1) \epsilon^2 \omega_2 / 8$,
- $B_{\text{eff}}^+ = B^+ (1 \pm \frac{A_{\text{SO}}^2 B^+}{8r^3})$, with a '+' for $\kappa {}^2\Sigma$ states and a '-' for $\mu {}^2\Sigma$ states,
- $\gamma_{\text{RT}}^+ = 2B^+ (1 - |\frac{(v_2+1)\epsilon\omega_2}{2r}| \pm \frac{A_{\text{SO}}^2 B^+}{8r^3})$, with a '+' for $\kappa {}^2\Sigma$ states and a '-' for $\mu {}^2\Sigma$ states. Note $0 \leq \gamma_{\text{RT}}^+ \leq 2B_{\text{eff}}^+$, so the two N -dependent terms of the above equations are of similar magnitude.

The newly introduced constants used in the simulations of the ${}^2\Sigma$ spectra are reported in Table 3.12 and are the same as in ref. [159], all other constants remain the same as in the vibrationless ground state.

The rotational energy expressions of each κ and $\mu {}^2\Sigma_u^\pm$ state in equation (3.6) are reminiscent of rotational energy values of ${}^2\Sigma$ states of a diatomic molecule [38] also featuring a splitting constant γ . In that case however, the spin-uncoupling constant γ is very small compared to the rotational constant, whereas the splitting and rotational constants in these κ and $\mu {}^2\Sigma_u^\pm$ states are of the same order of magnitude (see Table 3.12). For example, in the ${}^2\Sigma^+$ ground state of CN, $\gamma = 0.007254979 \text{ cm}^{-1}$ while $B_0 = 1.89109061 \text{ cm}^{-1}$ [174].

TABLE 3.12: Fit parameters for ${}^2\Sigma$ states of $(0, 1, 0)$ states of CO_2^+ from ref. [159].

	$\mu {}^2\Sigma_u^+$	$\kappa {}^2\Sigma_u^-$
$B_{\text{eff}}^+ / \text{cm}^{-1}$	0.381703	0.381414
$\gamma_{\text{RT}}^+ / \text{cm}^{-1}$	0.166714	0.16782

As there is no overlap between vibronic states in the experimental spectra, relative band intensities cannot be deduced. For this reason, the intensity of each simulated band is renormalised for each state. It is however of interest that, like Merkt *et al.* [164], all $X {}^2\Pi_g(0, 1, 0)$ ($\mu {}^2\Sigma_u^+, {}^2\Delta_{u,5/2}, {}^2\Delta_{u,3/2}, \kappa {}^2\Sigma_u^-$) $\leftarrow X {}^1\Sigma_g^+(0, 0, 0)$ transitions are observed, despite their forbidden nature by symmetry [172]. The photoelectron most likely stems from the HOMO π_g

of CO_2 , the photoelectron wavefunction is thus of *ungerade* symmetry. The final $(0, 1, 0)$ vibronic states being also *ungerade*, the final total wavefunction is the product of two *ungerade* wavefunctions so is of *gerade* symmetry, as the $X^1\Sigma_g^+$ ground state. Merkt *et al.* explained the possible transition by configuration mixing, made possible by the Renner-Teller effect.

Higher resolution spectra are needed to be able to fully resolve the ΔJ branches as in the $(0, 0, 0)$ states and deduce precise branch weights. Nevertheless, there is already an excellent agreement between the experimental and simulated spectra of Fig. 3.20. Once the higher resolution spectra has been recorded, the simulations will be refined if needed to assign the rovibronic transitions and determine branch weights intrinsic to PFI-ZEKE spectroscopy.

Vibronic states of the $(v_1 = 0, v_2 = 2, v_3 = 0)$ and $(v_1 = 1, v_2 = 0, v_3 = 0)$ bands.

As in the $(0, 1, 0)$ level, the $(0, 2, 0)$ level of the CO_2^+ electronic ground state splits into 6 components due to the Renner-Teller effect and spin-orbit coupling producing two ${}^2\Phi_u$ ($K = 1 + 2$), two κ and two μ ${}^2\Pi_g$ ($K = -1 + 2 = 1$) states. The Renner-Teller effect does not affect the $(1, 0, 0)$ level, which has 2 spin-orbit components as the origin. The various level splittings are illustrated in Fig. 3.14. They are observed experimentally *via* PFI-ZEKE spectroscopy (using the same parameters as in the $(0, 1, 0)$ spectra) and simulated accordingly as displayed in Fig. 3.21.

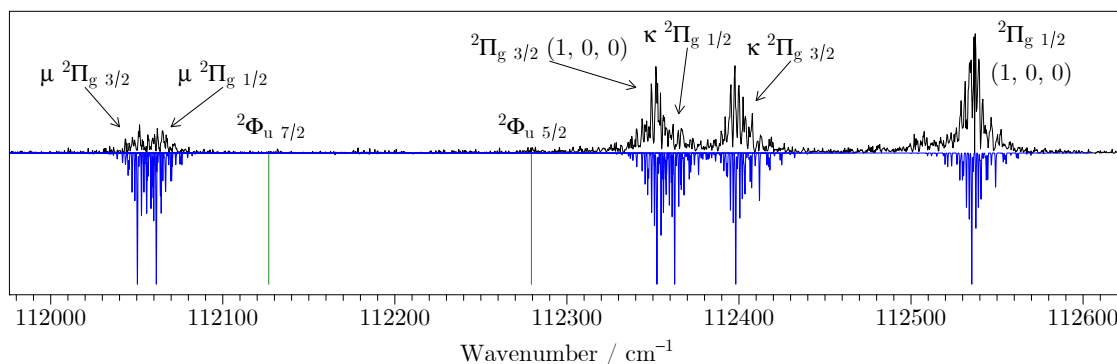


FIGURE 3.21: Raw PFI-ZEKE experimental (black) and simulated (blue) spectra of the $X^+ {}^2\Pi(0,2,0) \leftarrow X^1\Sigma_g^+$ and $X^+ {}^2\Pi(1,0,0) \leftarrow X^1\Sigma_g^+$ transitions. Note the simulated spectrum uses $T = 10\text{ K}$ and is inverted with respect to the experimental spectrum to facilitate comparisons. Assignments to vibronic states are noted. The positions of the ${}^2\Phi$ states are noted with green vertical lines according to the model, but are not observed experimentally.

The $(1, 0, 0)$ and $(0, 2, 0)$ levels are however very close in energy. There is therefore a Fermi resonance between the vibronic states of same symmetry of these levels, that is the four ${}^2\Pi$ states of the $(0, 2, 0)$ level and the two ${}^2\Pi$ states of the $(1, 0, 0)$ level. This resonance has been the subject of several works, in particular that of Larcher *et al.* [161]. Their work used the same experimental setup as Gauyacq *et al.* [157] based around a hollow-cathode lamp coupled to an electron bombardment source. The experimental observations are understood by the means of an effective Hamiltonian H_{eff} accounting for the Renner-Teller effect, spin-orbit coupling and the Fermi resonance simultaneously, which we heavily rely on to model our own PFI-ZEKE spectra.

This Hamiltonian can be represented in the $|v_1 v_2 v_3, \Lambda l \Sigma, J^+ P\rangle$ basis (P being the total angular momentum) by the following matrix [161]:

$$H_{\text{eff}} = E_0 + Bx^2 + g_K \Lambda K +$$

$$\begin{pmatrix} E_{100} - \frac{1}{2}A_{100} & -B^+ \sqrt{x^2 - 1} & 2F_1 & 0 & \sqrt{8}F_2 & 0 \\ -B^+ \sqrt{x^2 - 1} & E_{100} + \frac{1}{2}A_{100} & 0 & 2F_1 & 0 & \sqrt{8}F_2 \\ 2F_1 & 0 & E_{02^0 0} - \frac{1}{2}A_{02^0 0} & -B^+ \sqrt{x^2 - 1} & \sqrt{2}(\epsilon\omega_2)_{020} & 0 \\ 0 & 2F_1 & -B^+ \sqrt{x^2 - 1} & E_{02^0 0} + \frac{1}{2}A_{02^0 0} & 0 & \sqrt{2}(\epsilon\omega_2)_{020} \\ \sqrt{8}F_2 & 0 & \sqrt{2}(\epsilon\omega_2)_{020} & 0 & E_{02^2 0} + \frac{1}{2}A_{02^2 0} & -B^+ \sqrt{x^2 - 1} \\ 0 & \sqrt{8}F_2 & 0 & \sqrt{2}(\epsilon\omega_2)_{020} & -B^+ \sqrt{x^2 - 1} & E_{02^2 0} - \frac{1}{2}A_{02^2 0} \end{pmatrix} \quad (3.7)$$

with:

- $E_{v_1 v_2' v_3'}$, the effective energy origin for each vibronic state (I recall that l is the quantum number for bending vibration, with $l = K \pm 1$)
- $A_{v_1 v_2' v_3'}$, the effective spin-orbit parameter for each vibronic state,
- $x = J^+ + 1/2$,
- $F_1 = W_1 - \epsilon W_2$ and $F_2 = W_2 - \epsilon W_1/2$, Fermi parameters depending on W_i constants defined by Hougen [175] and quantifying the coupling through the Fermi resonance,
- $(\epsilon\omega_2)_{020}$, the effective Renner-Teller constant.

All of these effective constants are functions of the aforementioned parameters (A_{SO} , ϵ , ω_1 , ω_2 , l , v_1 , v_2 , and g_K) and two additional parameters g_{22} and g'_{22} , which have the same origin as g_K , but account for anharmonic corrections [161, 176]. The effective parameter values used in the simulations are those of Larcher *et al.* [161] and summarised in Table 3.13. All other parameters are the same as in the previous sections.

TABLE 3.13: Effective parameters (in cm^{-1}) for $^2\Pi$ states of $(0, 2, 0)$ and $(1, 0, 0)$ states of CO_2^+ from ref. [161].

E_{100}	1254.0
$E_{02^0 0}$	1019.4
$E_{02^2 0}$	1035.1
$A_{100} = A_{\text{SO}}$	159.9
$A_{02^0 0}$	156.0
$A_{02^2 0}$	157.5
W_1	23.6
W_2	-2.2
$(\epsilon\omega_2)_{020}$	-97.4

The eigenvalues of H_{eff} constitute the rotational energy levels of the six $^2\Pi$ states of the $(1, 0, 0)$ and $(0, 2, 0)$ levels in reference to the vibrationless ground state. In order to simulate the spectrum, transition energies are computed along with spectral intensities as in section 3.2.2. As there is no overlap between vibronic states in the experimental spectra, relative band intensities

cannot be deduced. For this reason, the intensity of each simulated band is renormalised for each state. Higher resolution spectra are needed to be able to fully resolve the ΔJ branches and deduce branch weights. Nevertheless, there is already an excellent agreement between the experimental and simulated spectra of Fig. 3.21. Once the higher resolution spectrum has been recorded, the simulations will be refined if needed to assign the rovibronic transitions and determine branch weights intrinsic to PFI-ZEKE spectroscopy.

The ${}^2\Phi_u$ states of (0, 2, 0) fall into the $K = v_2 + 1$ category as the (0, 0, 0) states and the ${}^2\Delta$ states of (0, 1, 0). They can therefore be simulated in the same way following equation (3.2) by adjusting the parameters accordingly. These states however are not observed experimentally (see Fig. 3.21), the simulated spectra are thus not presented. Only green vertical lines locate the origins of these states if they were reachable. This is expected as $\Phi \leftarrow \Sigma$ transitions are not allowed.

CO₂ photoionisation summary

This CO₂ PFI-ZEKE study, the first such study with VULCAIM, displays the capabilities of the new laboratory-based setup. The results yielded so far are in excellent agreement with those in the literature and the experimental spectra are finely reproduced using simulated spectra based on a theoretical model.

The next step in this study is to refine the study of the excited vibronic levels in CO₂⁺ using the same PFI-ZEKE technique. Adapting the model parameters if need be, it will be of interest to observe using PFI-ZEKE spectroscopy the relative spectral intensities of the various vibronic states. Such results have never been published at the resolution we are now able to achieve.

3.2.3 Pulsed-Ramped-Field-Ionisation ZERo-Kinetic-Energy

Parallel to the PFI-ZEKE study of the vibrationless $X^+ {}^2\Pi \leftarrow X {}^1\Sigma_g^+$ transition of the previous section, an imaging technique was developed also using the ionisation of CO₂ as a test system. Where traditional PFI-ZEKE employs step voltages, this technique uses ramped voltages and will thus be referred to as Pulsed-Ramped-Field-Ionisation ZERo-Kinetic-Energy (PRFI-ZEKE). It is built on the work of Reiser *et al.* [97] who also investigated the use of voltage ramps or slopes, and it is inspired by the SPES image analysis technique that we are accustomed to with the SOLEIL experiments (see chapter 1).

Technique description

The ramp voltage scheme of PRFI-ZEKE can be thought of as a step voltage scheme using an infinite number of voltage steps, each infinitesimally close to the next. This means that rather than having electrons arriving at discrete time intervals like in PFI-ZEKE, electrons continuously hit the detector (see Fig. 3.22 a)). At each energy step in the scan, such a pulsed-ramped-voltage is applied producing electron signal traces, which are then gathered in a PRFI-ZEKE matrix which has three dimensions. The x -axis is the photon energy or wavenumber of the point in the scan. The y -axis is the time coordinate for the pulsed-ramped-voltage; as the voltage is proportionate to time during the voltage ramp, the y -axis can also be thought of as the applied voltage. The conversion is slightly more complicated than it seems, but this is discussed below. The z -axis is electron signal intensity.

Given the Stark effect due to static electric fields, spectral features are expected to be shifted quadratically with the applied electric field (see equation (1.9) of chapter 1). The PRFI-ZEKE

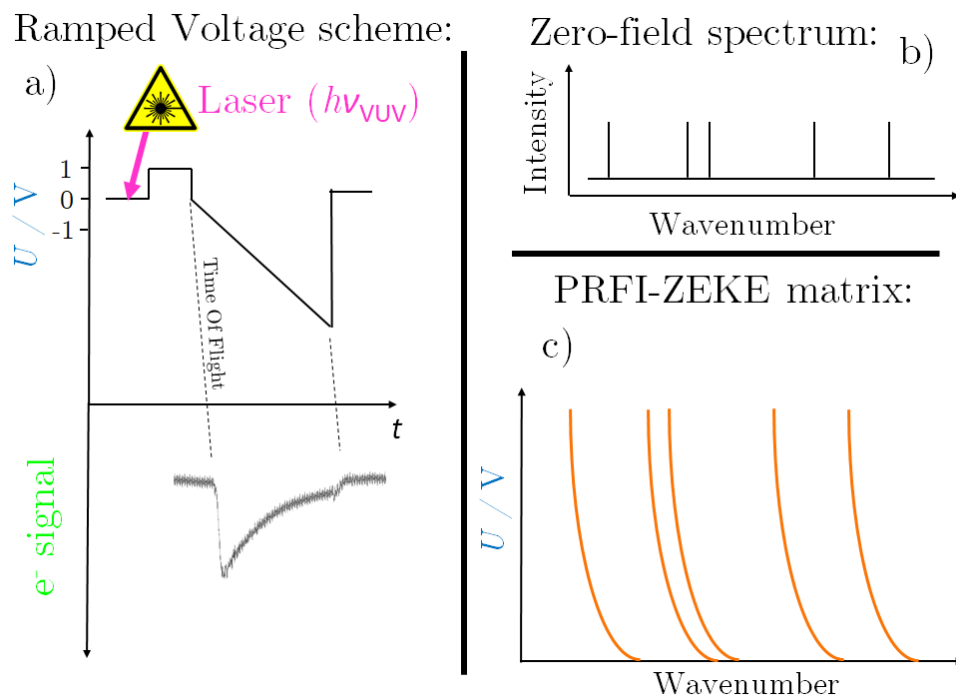


FIGURE 3.22: Illustration of the PRFI-ZEKE spectroscopy technique. a) Fixed photon energy ramped voltage scheme analogous to the step voltage scheme of Fig. 3.10. b) Zero-field stick spectrum. c) PRFI-ZEKE matrix gathering electron signals from ramped voltage schemes (a) for every photon energy step of the scan, note the shift of spectral maxima (b) with voltage follows a quadratic law (orange curves).

matrix is therefore expected to display quadratic curves (see Fig. 3.22 c)) as spectral features shift from their zero-field values under electric fields (see Fig. 3.22 b)).

This imaging technique would appear to be very similar to SPES as used at SOLEIL. It is true that both techniques can be used to study photoionisation and the image treatment may be similar in both cases, but the matrices of each technique are not obtained in the same way. The SPES technique records electrons of all velocities although only *slow* electrons are used in the end to produce spectra. PRFI-ZEKE, however, only records electrons produced with zero kinetic energy at each point of the voltage step. The main difference in the matrices is the y -axis: in SPES, electron kinetic energy is represented on this axis, whereas applied voltage is the y -axis variable in a PRFI-ZEKE matrix.

Having established SPES and PRFI-ZEKE as different experimental techniques, the image treatment involved in each case is similar and will be illustrated on the previously described vibrationless $X^+ \ ^2\Pi_{1/2} \leftarrow X \ ^1\Sigma_g^+$ photoionising transition in CO_2 .

Image treatment

Using the technique described in Fig. 3.22, a PRFI-ZEKE matrix is recorded around the vibrationless $X^+ \ ^2\Pi_{1/2} \leftarrow X \ ^1\Sigma_g^+$ photoionising transition in CO_2 . Experimentally, the conditions were the same (including the statistics) as in the classical PFI-ZEKE study of CO_2 as presented

in the previous section. The only difference is the voltage applied to the electrodes, which now follows a ramp scheme rather than steps (see Figs. 3.22 a) and 3.23).

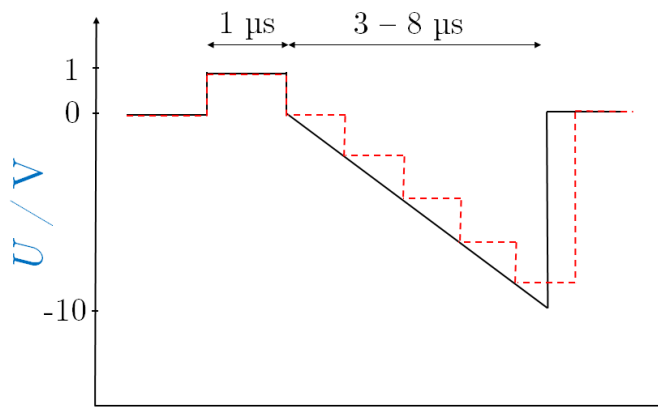


FIGURE 3.23: PRFI-ZEKE ramped voltage scheme (black line). A traditional PFI-ZEKE scheme (red dashed line) is used to relate electron arrival times to voltage values.

More precisely and around 5 μs after the laser irradiation, the initial positive +1 V prepulse of 1 μs of is applied to expel all directly charged species from the extraction zone. After this, the voltage is taken back to zero before starting the -1 to -3 V/ μs voltage ramp to -10 V. The voltage then goes back to zero in preparation for the next laser pulse.

A difficulty is to relate the arrival time of an electron and the corresponding voltage that caused its pulsed-field-ionisation. Another unknown is the ramp start time, that is when the voltage starts to decrease on the electrodes. This time is slightly different to the voltage application time, which is controlled *via* the electronic interface, as the various components have temporal response functions and the length of cables induces delays (≈ 5 ns/m). For this reason, each ramped voltage scheme is accompanied by a calibration step voltage scheme, which is applied before or after the PRFI-ZEKE scan in order to relate the electron arrival time to the ionising voltage. As shown in Fig. 3.23, voltage steps correspond to points in the ramped voltage. As in classical PFI-ZEKE, electron arrival times are recorded for each voltage step value. Electron arrival times are then converted to ramp voltage values.

An example of the PRFI-ZEKE image treatment is presented in Fig. 3.24 along with PRFI-ZEKE matrices at different steps in the image treatment and the transformational procedures between them. A raw PRFI-ZEKE image is presented first of all. The ramp time y -axis is already converted to a voltage scale using the calibration method of the previous paragraph. This matrix displays the aforementioned quadratic *curves* as predicted in Fig.3.22 c). These curves are linearised by taking the square root which yields a PRFI-matrix containing straight diagonals instead of curves. Similarly to the SPES image treatment, these images are rotated and portions of the rotated, now-vertical lines are integrated to yield the final PRFI-ZEKE spectrum.

Discussion

The corresponding experimental spectrum is compared to simulations, obtained as in the classical PFI-ZEKE study. Simulated line spectra are convoluted by a gaussian line shape, whose *FWHM* is 0.3 cm^{-1} , to replicate the experimental spectral resolution. Beyond the excellent

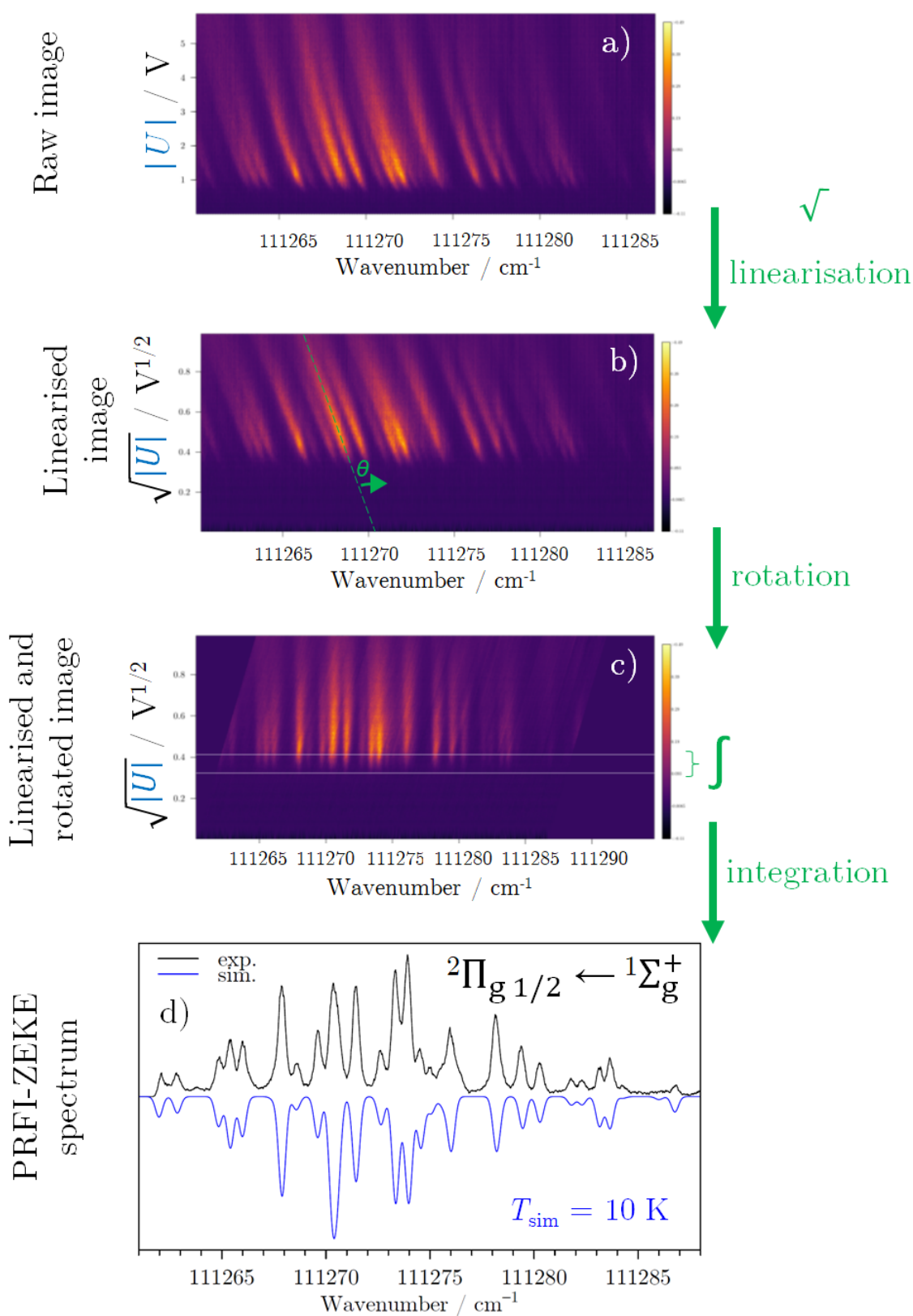


FIGURE 3.24: PRFI-ZEKE image treatment on the $X^+ 2\Pi_{1/2} \leftarrow X^+ 1\Sigma_g^+$ photoionising transition in CO_2 . a) Raw PRFI-ZEKE matrix. b) Linearised PRFI-ZEKE matrix. c) Linearised and rotated PRFI-ZEKE matrix. d) PRFI-ZEKE spectrum (black) obtained by summing all electron signals in dashed box in c), compared to a simulated spectrum.

agreement between experimental and simulated spectra, the signal-to-noise ratio of the experimental spectrum is remarkable. This stems from the integration procedure featured in Fig. 3.24, which amounts to the consideration and averaging of more spectra.

The resolution, although still high, is slightly lower than in the case of classical PFI-ZEKE spectroscopy. Different ramped voltage schemes were tried, *e.g.* the voltage was taken directly to -1 V instead of 0 V between the positive prepulse and the ramp, but no improvement could be made on the resolution. An explanation of this resolution limitation can be put forward starting by the observation of the diagonals of Fig. 3.22 b). In this image, the diagonals widen for greater applied voltages. Once again, this widening is reminiscent of the widening of diagonals in PES matrices in the SPES image treatment. The cause cannot be the same however: SPES deals with slow electrons and the widening of diagonals was explained by spherical aberrations in electrostatic lenses which manifest themselves in off-axis or fast electrons; PRFI-ZEKE, on the other hand, only deals with electrons whose kinetic energy is vanishing so such aberrations are not present. In the case of the PRFI-ZEKE widening, it can be rationalised using equation (1.9) and mainly the fact that the constant A varies (between 2 and 6) depending on the character of the Rydberg state in the Stark manifold. A is generally lower for blue-shifted states and higher for those red-shifted. As the energies of Rydberg states are shifted in different ways depending on their character, the overall effect on all states in the Stark manifold is a broadening which leads to the resolution limit which we measured empirically to be around 0.3 cm^{-1} . The different ionisation mechanisms were explored theoretically by Chupka, who set this resolution limit at around 0.4 cm^{-1} for a $n = 200$ Rydberg state in such a voltage scheme [167].

Tests are ongoing to surpass this limit, in particular with different ramped voltage schemes, different slew rates and prepulse values. According to the high-resolution PFI-ZEKE work of Hollenstein *et al.* [18], this limit should be possible to beat if the negative ramped voltage does not exceed the positive prepulse value (in terms of absolute value). The idea is to selectively ionise red- (with the positive pulse) and blue-shifted (with the negative pulse) Rydberg states and never the whole Stark manifold, which induces the loss in resolution due to differences in ionisation rates.

Even if the 0.3 cm^{-1} is found to be insurmountable, the PRFI-ZEKE technique already offers several advantages over traditional PFI-ZEKE. Due to the superior signal-to-noise ratio for spectra recorded in the same conditions, PRFI-ZEKE spectra could be recorded using fewer scans (less averaging) at the same signal-to-noise ratio as a PFI-ZEKE spectrum. This would greatly decrease scan times. For example, if spectra were recorded with 16 times fewer statistics (therefore 16 times faster), this would result in a signal-to-noise ratio degraded by a factor of $\sqrt{16} = 4$. Given the clarity of Fig. 3.24 d), this would be perfectly acceptable. Of course PRFI-ZEKE comes with increased complexity in terms of image treatment, but the procedure depicted in Fig. 3.24 can be automated for any scan so this is no hardship! As the spectrum of Fig. 3.24 d) took around 4 hours to record, recording it 16 times faster would mean it would only take 15 min. Producing a high-resolution rotationally-resolved photoionising transition this fast would be unprecedented.

Conclusions & perspectives

In this manuscript, I investigated one of the major gas-phase relaxation channels following a VUV excitation, the photoionisation process, exploring both its qualitative and quantitative aspects. This work was mainly focused on molecules of astrophysical or planetary relevance, with an emphasis on free radical species. Two experimental setups have been used to gain insight into photoionisation processes, employing complementary VUV photon sources in terms of resolution and spectral tunability:

- The synchrotron-based setup used the DELICIOUS 3 spectrometer coupled to the DESIRS beamline of SOLEIL. The double imaging photoelectron/photoion coincidence detection technique and the corresponding data analysis and image treatments were used to extract spectra (photoion yields and TPES), and in particular mass-selected photoelectron spectra.
- The laboratory-based high-resolution laser setup, VULCAIM, is a new instrument, entirely developed during my PhD. A thorough determination of its main characteristics was conducted to prepare for future high-resolution VUV spectroscopic studies, in particular using PFI-ZEKE photoelectron spectroscopy.

Quantitative information on photoionisation process has been obtained at SOLEIL synchrotron, with the determination of absolute photoionisation cross sections for two free radicals (OH and NH₂). These species were produced using a flow tube reactor inducing H-abstraction from a chosen precursor, and the cross sections were determined by applying a meticulous method. It has to be stressed that only a handful of absolute photoionisation cross sections of free radicals are currently known, thus the present work represents an important contribution in this field of research. The OH cross section has been determined from 12.8 to 15 eV. These results are somewhat in disagreement with recently published results by the group of Okumura at ALS, Berkeley. This discrepancy was investigated and possible explanations were given, illustrating the difficulties of such quantitative measurements to yield reliable values. The NH₂ cross section had never been determined prior to this work, and is now available from 11 to 15 eV. It therefore constitutes a new important parameter to be included in models in the near-future to better describe the photochemistry of cometary or planetary atmospheres. Indeed, some models that do include NH₂ photoionisation rely on arbitrarily chosen cross section values that differ by over a factor 2 to those determined in this manuscript. The new quantitative results reported in this manuscript will be included in the Leiden database update (<https://home.strw.leidenuniv.nl/moldata/>).

In addition to these two case studies, relative ion yields of the fragmentation products of methanol and its d₃-isotopologue have been reported. They constitute preliminary work for quantitative experiments. These are essential for future methanol photodissociation studies that we plan to perform using photoionisation to probe all the produced species before detecting them *via* mass spectrometry.

The photoionisation process has also been investigated in this thesis work from a fundamental point of view, leading to new VUV spectroscopic results. With medium high-resolution

experiments at SOLEIL, photoionising transitions of methylisocyanate, CH_3NCO , and the di-carbon molecule, C_2 , have been studied at vibrational resolution. These experimental results were supported by theoretical calculations performed by colleagues, in order to assign vibrational modes and determine corresponding frequencies and electronic ionisation energies. The importance of this fundamental spectroscopic work for applications is highlighted through the determination of thermodynamic parameters, in particular enthalpies of formation and ionisation potentials. The adiabatic ionisation potential of the forbidden $X^+ (^4\Sigma_g^-) \leftarrow X (^1\Sigma_g^+)$ single-photon transition in C_2 has been measured for the first time using energy differences retrieved from a single experimental spectrum, thus ensuring a self-coherent determination.

Exploring the cation spectroscopy further at rotational resolution, the first high-resolution spectra, obtained with VULCAIM using PFI-ZEKE spectroscopy, have been recorded at the end of this PhD. The excellent performances of VULCAIM have been highlighted with the case of CO_2 photoionisation. The rovibrational structure of the electronic ground state and its excited vibrational levels have been studied in detail, simultaneously exhibiting spin-orbit coupling, Renner-Teller effect and a Fermi resonance between (1, 0, 0) and (0, 2, 0) states. The vibrationless ground state was completely analysed and assignments were made, supported by simulations. Excited vibronic levels are not yet fully resolved, but the spectra obtained so far, whose analysis is also supported by simulations, are very promising.

Finally, an imaging technique, inspired by the SPES treatment of the SOLEIL experiments, was developed during this work. Instead of using step voltages, as in traditional PFI-ZEKE spectroscopy, it relies on ramped voltages. This technique, baptised PRFI (Pulsed-Ramped-Field Ionisation)-ZEKE, enables the production of high-resolution spectra with very impressive signal-to-noise ratios. It therefore opens exciting possibilities for recording high-resolution VUV photoelectron spectra in a fraction of the time typically needed as less averaging is required to obtain spectra with very acceptable signal-to-noise ratios.

Although a major part of my work was dedicated to photoionisation, other relaxation processes following VUV photoexcitation have been addressed in the appendices of this manuscript.

Photodissociation studies have been conducted during my PhD using the laboratory-based setup available prior to VULCAIM. This setup was used to perform UV/VUV pump- VUV probe experiments in order to initiate photodissociation (with the pump laser) and then ionise the products (with the probe laser) before being detected *via* mass spectrometry. The photodissociation of NH_3 at 213 nm was explored this way, in the aim of measuring branching ratios. An interesting finding was that the $\text{NH}_2 + \text{H}$ fragmentation channel is the only one observed, despite the $\text{NH} + \text{H}_2$ channel being thermodynamically accessible. This work also highlighted the possibility of determining free radical photoionisation cross sections in a different way to that carried out at SOLEIL, provided that multiphoton processes can be quenched. An important preliminary work on the photodissociation of CH_3OH at 118.2 nm was also undertaken, paving the way for future photodissociation studies at the Lyman- α photon energy.

In addition, dissociative ionisation has been investigated whilst extending the CH_3NCO study to higher energies. With the help of *ab initio* calculations and thermodynamic tables, the recording of ion yields of the various fragments were used to assign fragments and determine the corresponding appearance energies. This work completes our CH_3NCO photoionisation study by reconciling our findings with literature results thanks to the identification of the dissociative character of excited electronic states of the cation.

Future studies

The results of this manuscript underline the importance of VUV photoionisation studies from both a fundamental perspective and the many applications to which they are related. The work on photoionisation cross sections, which is now a recognised expertise of our group among the physical-chemistry community, should be continued as the absolute values for many free radicals are still unknown. Now that the NH_2 photoionisation cross section has been determined, that of NH should definitely be within our reach, adapting the radical source conditions in order to induce single- and double-H abstraction from NH_3 in a controlled way.

In terms of astrophysical applications, it would be interesting to determine the VUV photoionisation cross sections of the 50 plus free radicals observed in the InterStellar Medium in order to properly model the photophysics and photochemistry of the associated environments. Most are C- and/or N-bearing species, but recent observations have also detected Si-bearing molecules, for which there is very little quantitative data to describe the ensuing photochemistry. Using silane, SiH_4 , as a precursor in the flow tube radical source should allow the production of SiH_3 , SiH_2 , *etc.* The study of their photoionisation has never been investigated to our knowledge.

Photoionisation cross sections are also needed by other fields which rely on ionisation and mass spectrometry as a means of quantifying neutral products in their experiments. In particular, for our photodissociation experiments, the studies on methanol-derived isotopologues should be continued replacing fluorine with chlorine to induce a different H-abstraction reactivity. Once the photoionisation of CH_3O , CH_2OH , CHOH and HCO / COH has been quantified, we will be able to determine branching ratios for methanol photodissociation in pertinent VUV regions for cometary or planetary atmospheres. Methanol is a complex organic molecule (COM) that is abundant in a wide variety of astrophysical media, but there are many more whose photodissociation has not been quantified (HCONH_2 , CH_3NCO , HC_3N ,...) and should be investigated. Ammonia photolysis studies should also be performed at higher photon energies than that explored in the present work, especially at Lyman- α photon energy.

The medium-high-resolution spectroscopy conducted at SOLEIL shows the capability of this experiment to reliably produce VUV threshold-photoelectron spectra of astrophysical molecules, even of free radicals, which are normally more challenging to work with. There is a great number of species whose photoionisation spectra has yet to be reported, but could be achieved using this setup. In order to guide future experiments and the choice of species of study, it is important to remember their quantitative aspect through the determination of ionisation energies. These are important quantities in themselves, but can also be related to other quantitative parameters (bond energies, enthalpies of formation,...). Finally, the DELICIOUS 3 setup is able to perform medium-high-resolution studies over a wide spectral range and should therefore be used in the future to locate spectral regions of interest to be explored further with the higher-resolution setup developed at ISMO. An example would be to study the differences in ionisation potential between cyclic and linear N_3 . The *IP* of the cyclic species is not known, but is calculated to be around 0.9 eV above the *IP* of the linear species. This has yet to be determined experimentally.

A lot of energy was spent on the development of the new laboratory-based setup: VULCAIM. I am pleased to have been able to develop this instrument to the point where it is now able to conduct high-resolution VUV spectroscopy as characterised in this manuscript. The next step will be to finalise the $\text{CO}_2^+(X^+)$ study by recording the transitions to excited vibronic states using the same scan parameters as those used to investigate the vibrationless electronic ground state. It will be interesting to fine-tune the parameters of the simulations in order to extract

the spectroscopic constants, determine spectral intensities, and compare them to rotationally-resolved IR spectroscopy conducted directly in the cation. The aim of future work will then be to move to more reactive species, which are less well characterised. Reactive species will be produced *in situ* by adapting the flow tube reactor from SOLEIL to VULCAIM. Such a reactor has been designed and tested; it is still based around F-induced H-abstractions, but is more compact than the SOLEIL reactor, uses an electric discharge instead of a microwave discharge, and is pulsed in accordance with the light source. Mass spectra have shown it was able to initiate H-abstractions, but it has not yet been used in a spectroscopic study. The aim will be to explore (ro)vibronic couplings as in the CO₂ study, but on reactive species (*e.g.* the Renner-Teller effect in C₃N⁺ A⁺ ³Π). High-resolution studies will also aim to produce important quantitative information. An example could be a precise determination of the first *IP* of HCO (X⁺ ¹Σ⁺ ← X̃ ²A'), which is otherwise difficult given the large geometry changes between the neutral (bent) and cationic (linear) species in their ground electronic states; this difficulty is reflected in the number of different reported values. After having determined the *IPs* of cyclic and linear N₃ at medium high resolution, it will be interesting to study their thresholds at high resolution with VULCAIM.

Finally, the development of the impressive PRFI-ZEKE technique should be pursued. It shows the promise of being able to produce high-resolution photoelectron spectra in a fraction of the time normally needed to produce such spectra. The image treatment procedure needs to be finalised, but it should be possible to automate. Once perfected, this technique will enable photoionisation high-resolution studies that are fast and effective in order to explore all the species now available to study with VULCAIM. This will be particularly interesting when using synthesised samples only available in a limited amount, or when probing free radicals formed in various sources, which may be functional only for a limited time (electric discharge, pyrolysis,...).

Appendix A

Exploratory studies of the photodissociation process

In all the studies presented so far, molecules of study were irradiated by photons whose energies were in the vicinity of or above their first ionisation potential. Photoionisation was then a major means of relaxation following light-induced excitation. Below the first *IP* and in the absence of an electric field, molecules cannot ionise; in this case, a primary relaxation mechanism in the UV and VUV spectral domains is photodissociation. It consists in the fragmentation of the excited molecule producing neutral fragments.

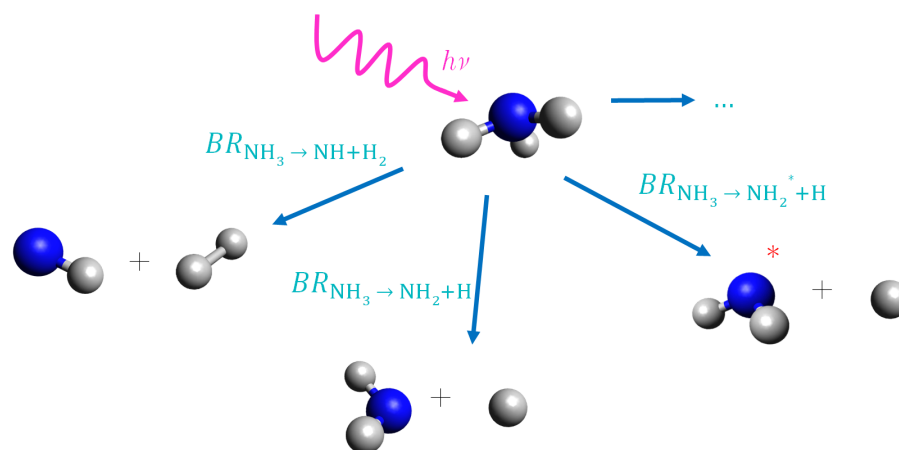


FIGURE A.1: NH₃ photodissociation scheme. Following photoexcitation, excited NH₃ can relax *via* a number of different photodissociation channels. Branching ratios (*BR*) are noted for each.

The example of NH₃ photodissociation is given in Fig. A.1. Following photoexcitation, NH₃* can relax *via* a number of different fragmentation pathways; only three are reported as examples, but others are imaginable. Asterisks in this section denote electronically excited species, and will be distinguished from electronic ground state species. Each relaxation pathway is quantified by its energy-dependent branching ratio, noted BR_{\dots} , which gives the fraction of excited molecules that relaxes *via* that given pathway.

Determining branching ratios is of particular atmospheric and astrophysical interest, as these parameters should be included in models in order to properly describe the photochemistry therein. As with photoionisation cross sections, they are difficult quantities to measure. The start of this appendix will be dedicated to the general method of determining photodissociation branching ratios, before presenting two case studies explored during this PhD: NH₃ and CH₃OH.

A.1 Experimental setup

A.1.1 General principle of the measurement: pump-probe scheme

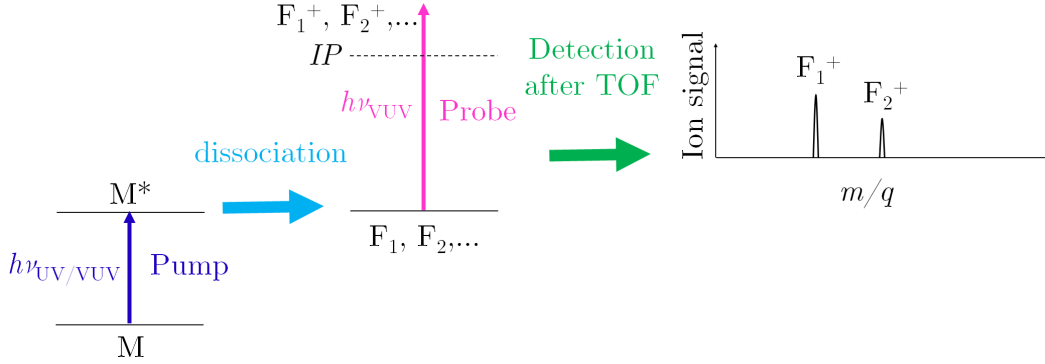


FIGURE A.2: General pump-probe scheme dissociating a generic molecule M producing neutral fragments (F_1, F_2, \dots). The neutral fragments are then ionised to form cations which are detected after a time-of-flight (TOF) and recorded in a mass spectrum. Note that if $h\nu_{\text{probe}} > IP(M)$, M^+ also appears in the mass spectrum.

In photodissociation studies, a first laser, denoted pump laser, is used to irradiate molecules initiating photodissociation at the laser photon energy ($h\nu_{\text{pump}}$). The number of excited molecules, n_{M^*} , is related to the initial number of irradiated molecules, N_M , using the photoabsorption cross section for species M at the pump laser photon energy ($\sigma_M^{\text{abs}}(h\nu_{\text{pump}})$) and the photon flux (ϕ_{pump}):

$$N_{M^*} = N_M \times \sigma_M^{\text{abs}}(h\nu_{\text{pump}}) \times \phi_{\text{pump}}. \quad (\text{A.1})$$

Once excited, the molecules then photodissociate producing fragments F_i along various relaxation channels. The produced quantities are related to the number of excited molecules with the help of branching ratios ($BR_i(h\nu_{\text{pump}})$), which also depend on the pump laser photon energy:

$$N_{F_i} = N_{M^*} \times BR_i(h\nu_{\text{pump}}). \quad (\text{A.2})$$

Note that the sum of the branching ratios of all the photodissociation channels equals 1 due to matter conservation:

$$\sum_i BR_i(h\nu_{\text{pump}}) = 1. \quad (\text{A.3})$$

In order to detect the neutral fragments, a second laser, denoted probe laser (photon energy: $h\nu_{\text{probe}}$), irradiates the neutral species to produce cations. For a given fragment F_i , the charged and neutral quantities are related using the photoionisation cross section for species F_i at the probe laser photon energy ($\sigma_M^{\text{ion}}(h\nu_{\text{probe}})$) and the photon flux (ϕ_{probe}):

$$N_{F_i^+} = N_{F_i} \times \sigma_{F_i}^{\text{ion}}(h\nu_{\text{probe}}) \times \phi_{\text{probe}}. \quad (\text{A.4})$$

As in chapter 2, the ion signal of each fragment ($S_{F_i^+}$) is proportionate to the number of ions and the instrument response function $f(m_{F_i}/q)$:

$$S_{F_i^+} = N_{F_i^+} \times f(m_{F_i}/q). \quad (\text{A.5})$$

The instrument response function can be determined using a gas mixture containing known proportions of H₂, N₂, Ar, Kr, and Xe. The photoionisation cross sections are known for these species. Hence, the instrument response function can be deduced from equations (A.4) and (A.5) and by measuring ion signals. This will be done for more refined experiments, but the $f(m_{F_i}/q)$ function is assumed constant for the preliminary work of this appendix. This method is similar to that used by Savee *et al.* [61].

Combining equations (A.2) and (A.4), equation (A.5) can be expressed as:

$$S_{F_i^+} = N_{M^*} \times BR_i(h\nu_{\text{pump}}) \times \sigma_{F_i}^{\text{ion}}(h\nu_{\text{probe}}) \times \phi_{\text{probe}} \times f(m_{F_i}/q). \quad (\text{A.6})$$

Thus, the branching ratio $BR_i(h\nu_{\text{pump}})$ for the given photodissociation channel is given by the proportionality law:

$$BR_i(h\nu_{\text{pump}}) \propto \frac{S_{F_i^+}}{\sigma_{F_i}^{\text{ion}}(h\nu_{\text{probe}})}, \quad (\text{A.7})$$

where the proportionality factor contains the pump and probe photon fluxes, the absorption cross section of M, which are all independent of the relaxation channel, and the instrument response function, which can be determined as previously stated, but was assumed constant here. The proportionality factor is then fixed using the normalisation of the BR_i given by equation (A.3).

Experimentally, the branching ratios are determined by measuring ion signals of the corresponding fragments and by the knowledge of the relevant photoionisation cross sections. Since the photodissociation products are often free radicals, the photoionisation cross sections are not known. This is why an effort was made during this PhD to separately determine these unknown quantities (see chapter 2).

A.1.2 Modified Icare setup

Photodissociation studies were undertaken with a slightly different setup to that presented in section 1.2. Before VULCAIM was built, Icare was adapted to be able to perform pump-probe experiments.

Compared to the previously described setup, the VUV detector is removed to allow the pump laser into the setup in order to dissociate molecules.

The difficulties in spatial and temporal optimisation, already mentioned in section 1.2 of chapter 1, are further increased in pump-probe studies with the addition of another laser. Spatially, the pump and the probe lasers must irradiate the same sample zone; temporally, the pump must irradiate the molecules before the probe. The setup optimisation is the same as in section 1.2.7. The exception is for the VUV generation, which is directly optimised on ion signals, as there is no longer a VUV detector. The characteristics of the pump and probe lasers will be presented for each case study.

A.1.3 VUV production via four-wave mixing in a rare gas cell

In the pump-probe studies carried out during my PhD, both the pump and probe lasers function at fixed energy. For this reason, a non-resonant four-wave mixing scheme can be used to generate VUV radiation by tripling the frequency of a UV laser (see Fig. 1.13). This process can also be referred to as third harmonic generation. It is implemented experimentally in a rare gas cell (typically Xe, but Kr could also be used), as shown in Fig. A.4. Ar is added to the rare gas to

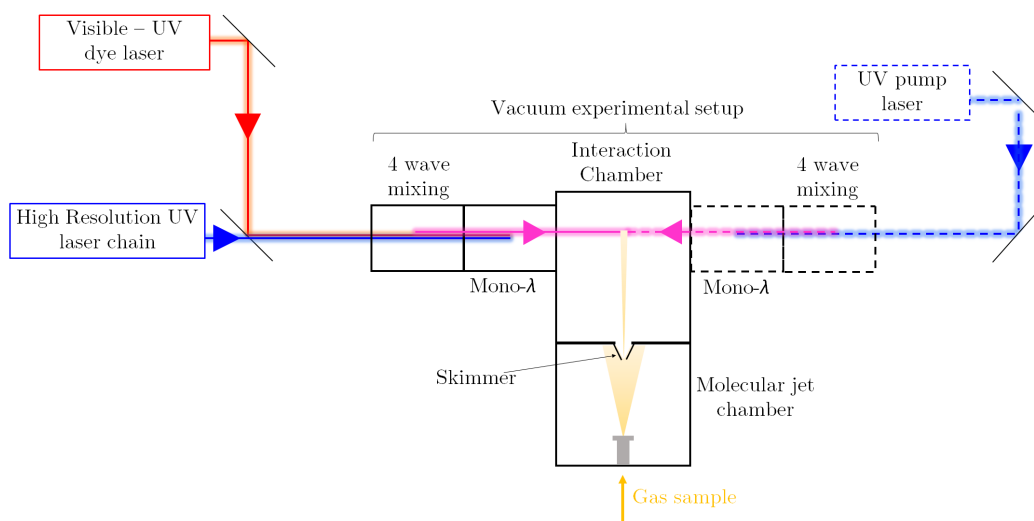


FIGURE A.3: Icare adaptation scheme for pump-probe setup. Each UV laser can be used directly or frequency tripled (*via* four-wave mixing) to provide VUV radiation if needed.

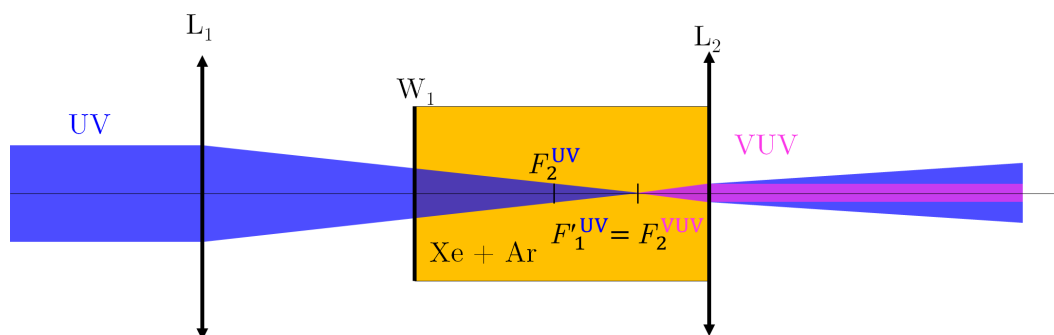


FIGURE A.4: Implementation of four-wave mixing to generate VUV laser radiation in a rare gas cell.

optimise the phase-matching of the non-linear process, thus improving the VUV production efficiency; optimal partial pressures (ranging from 1 to 500 mbar) depend greatly on the intended VUV wavelength. Gas pressures are optimised on the resulting ion signals or directly using the VUV signal if a detector can be placed in the setup.

Experimentally (see Fig. A.5), a commercially available UV laser is focused using lens L_1 in the rare gas through the entry window W_1 . The exit window, consisting in lens L_2 , collimates the VUV radiation generated in the cell. L_1 and W_1 are made out of CaF_2 , whereas L_2 is made out of MgF_2 or LiF , which can transmit lower wavelengths in the VUV (110 and 105 nm respectively) [177]. Focal distances are around 20 cm, but depend on the wavelength. L_1 and L_2 form an afocal system for the VUV radiation, but not for the UV radiation which continues to diverge after the cell due to the focal distance wavelength-dependency of the lens.

As in Fig. 1.12 of chapter 1, a monochromator is used as a dispersion system to separate the VUV and UV beams. Due to availability, a MgF_2 prism is used instead of a VUV grating to disperse the radiation exiting the rare gas cell. An iris selects the VUV radiation for the experiment, whilst blocking the UV radiation. The deviation is typically a few degrees, the iris

diameter is therefore 1 or 2 mm.

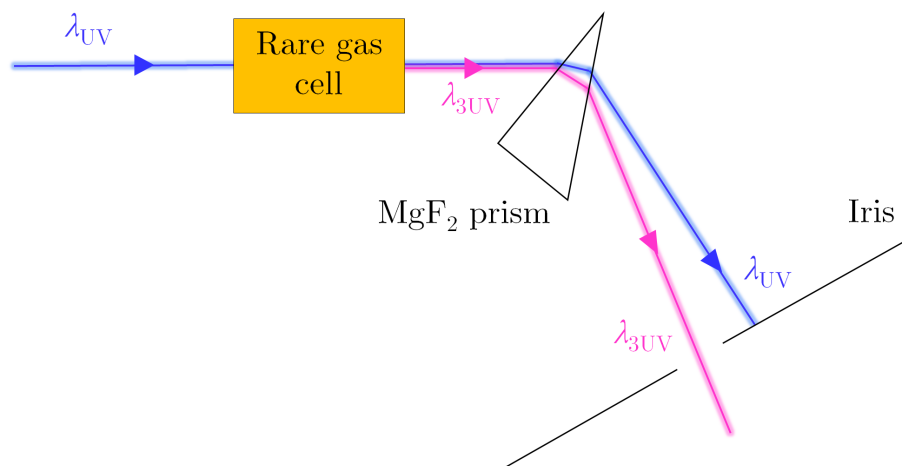


FIGURE A.5: Illustration of the role of the MgF_2 prism to disperse the radiation exiting the rare gas cell. An iris selects the VUV radiation for the experiment.

A.2 NH_3 photodissociation at 213 nm

A.2.1 Context and motivations

Astrophysical interest

Ammonia, NH_3 , is the first polyatomic molecule (more than 3 atoms) to have been observed in the interstellar medium in 1968 [178]. Since then it has become a ubiquitous molecule to a wide variety of astrophysical media, such as gas giants [179], telluric planets [180], cold stars [181], external galaxies [182] and comets. Indeed, Rubin *et al.* [91], for example, observed the presence of NH_3 in the coma of comet 67P/Churyumov-Gerasimenko, along with many other nitrogenous compounds, using the ROSINA spectrometer.

As one of the simplest N-bearing molecules, it is of great interest to astrophysicists and astrochemists and is extensively studied in order to better understand the N-based photochemistry of astrophysical environments.

NH_3 photodissociation, state-of-the-art

NH_3 photodissociation has been studied at least since the 1980s [183, 184]. It constitutes an ideal test system for probing photodissociation dynamics, in particular the effect of the initial NH_3 state (electronic and vibrational) on the photodissociation products [185, 186] and the anisotropy of ejected fragments [187–189]. The dynamics of ultra-fast dissociation from the first excited electronic state has also been explored [190]. Theoretical works support the experimental results reported in the literature and computed the different geometries the molecule takes during dissociation, potential energy surfaces and dissociation pathways on these surfaces.

Despite the number of works on NH_3 photodissociation dynamics, none have reported, to our knowledge, photodissociation branching ratios.

Choice of photodissociation photon energy

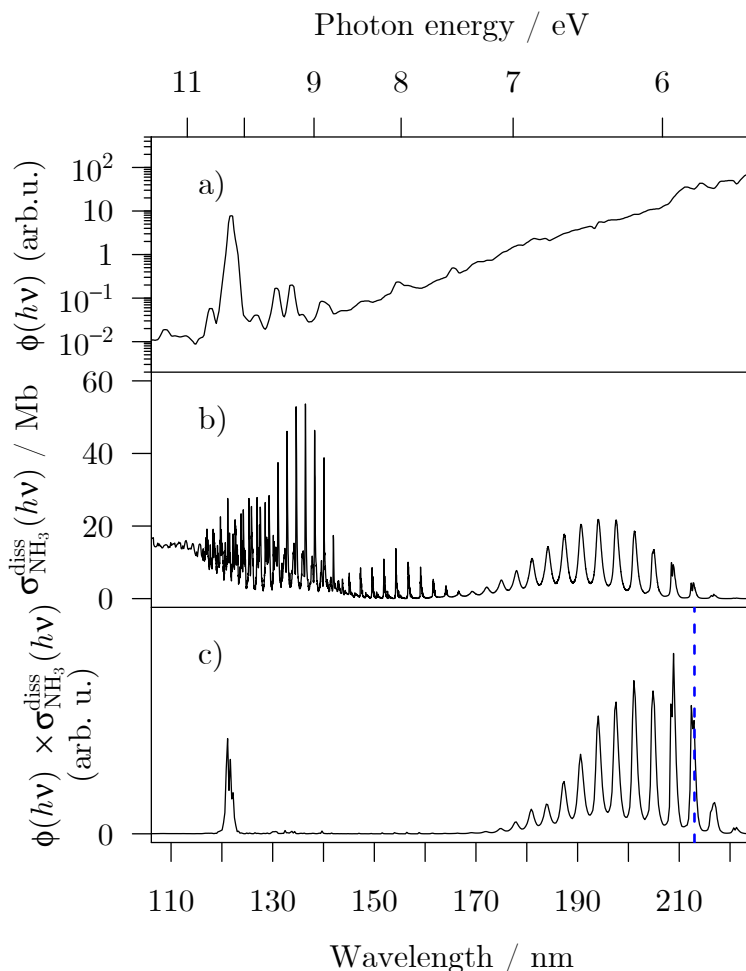


FIGURE A.6: a) Typical VUV solar flux taken from ref. [191]. b) NH_3 VUV photodissociation cross section [8]. c) Product of the solar flux with the photodissociation cross section (c) = a) \times b)), a blue vertical line at 213 nm (5.82 eV) locates the photodissociation energy of this work.

In the aim of providing branching ratios for astrophysical applications, it is important to firstly determine photon energies or wavelengths that NH_3 molecules in astrophysical media are susceptible of being irradiated by. At this end, a typical solar flux (noted $\phi(h\nu)$) is considered (see Fig. A.6 a)). This quantity gives the wavelength-dependency of the emitted light of the Sun or any other similar star. It represents a black-body emission spectrum containing emission lines of elements present in the Sun. In the VUV spectral domain, an important feature is the Lyman- α emission line of hydrogen at 121.567 nm. Note that Fig. A.6 a) uses a logarithmic scale, which artificially reduces the intensity of this line compared to the surrounding spectral intensities.

The solar flux represents the typical photon flux that irradiates any molecule in the solar system. To determine which spectral components of this flux incur NH_3 photodissociation, the NH_3 photodissociation cross section is used: $\sigma_{\text{NH}_3}^{\text{diss}}$. If photoionisation and photodissociation

are considered to be the only relaxation mechanisms following photoabsorption, the photodissociation cross section is defined as the difference between the absorption and photoionisation cross sections ($\sigma_{\text{NH}_3}^{\text{diss}} = \sigma_{\text{NH}_3}^{\text{abs}} - \sigma_{\text{NH}_3}^{\text{ion}}$) and is presented in Fig. A.6 b).

The components of the solar flux most probable of inducing the photodissociation of NH_3 are given by the product of the solar flux by the photodissociation cross section (see Fig. A.6 c)). The two main photodissociating spectral regions can be identified: around the Lyman- α emission line and then between 220 and 180 nm (5.6 - 6.9 eV). The lower energy region corresponds to the excitation of the $\tilde{\text{A}}$ electronic state and its vibrationally active mode ν_2 (umbrella mode). The Lyman- α region corresponds to transitions to higher energy Rydberg states ($\tilde{\text{C}}$ to $\tilde{\text{G}}$).

It is in these two regions of astrophysical interest that photodissociation branching ratios should be determined. For each photodissociation channel, it is possible to determine a thermodynamic threshold, *i.e.* the minimum energy required to access that given channel based on the energy difference between final and initial states. In photodissociation, that energy is to be brought by the photon. The thresholds are obtained using Hess' law of Constant Heat Summation by combining known formation enthalpies at 0 K [118] and, for excited states, excited electronic state energies [21, 190]. The first NH_3 photodissociation channels and their corresponding thermodynamic thresholds are summarised in Table A.1. Despite it being energetically the most accessible, the $\text{NH}_3(\tilde{\text{X}}^1\text{A}_1) + h\nu \rightarrow \text{NH}(\text{X}^3\Sigma^-) + \text{H}_2(^1\Sigma_g^+)$ channel is spin-forbidden and therefore not considered here.

TABLE A.1: $\text{NH}_3(\tilde{\text{X}}^1\text{A}_1)$ photodissociation relaxation channels and their calculated thermodynamic thresholds (assuming there is no potential energy barrier) at 0 K [118]. Accessible channels whose thresholds are below 5.82 eV are separated from the others with a dashed line.

Photodissociation products	Threshold / $\text{kJ}\cdot\text{mol}^{-1}$	Threshold / nm	Threshold / eV
$\text{NH}(\text{X}^3\Sigma^-) + \text{H}_2(^1\Sigma_g^+)$ *	422	283	4.38
$\text{NH}_2(\tilde{\text{X}}^2\text{B}_1) + \text{H}(^2\text{S})$	444	269	4.60
$\text{NH}(\text{a}^1\Delta) + \text{H}_2(^1\Sigma_g^+)$	548	218	5.68
-----	-----	-----	-----
$\text{NH}_2(\tilde{\text{A}}^2\text{A}_1) + \text{H}(^2\text{S})$	567	211	5.87
$\text{NH}(\text{b}^1\Sigma^+) + \text{H}_2(^1\Sigma_g^+)$	651	184	6.75
$\text{NH}(\text{A}^3\Pi) + \text{H}_2(^1\Sigma_g^+)$ *	754	159	7.81
$\text{NH}(\text{X}^3\Sigma^-) + 2\text{H}(^2\text{S})$	829	144	8.59
$\text{NH}(\text{c}^1\Pi) + \text{H}_2(^1\Sigma_g^+)$	915	131	9.49
$\text{NH}(\text{a}^1\Delta) + 2\text{H}(^2\text{S})$	980	122	10.20

* Spin-forbidden photodissociation channel using one photon

Given the spectral regions of interest of Fig. A.6 c) and experimental constraints (see next section), a photodissociation energy of 5.82 eV (213 nm) was selected (blue dashed line in Fig. A.6 c)).

As seen in Table A.1, where this energy limit is materialised by a dashed horizontal line, two photodissociation channels are thermodynamically accessible and spin-allowed at this photon energy producing both NH and NH_2 :

- $\text{NH}_2(\tilde{\text{X}}^2\text{B}_1) + \text{H}(^2\text{S})$, and
- $\text{NH}(\text{a}^1\Delta) + \text{H}_2(^1\Sigma_g^+)$.

A.2.2 Experimental specificities

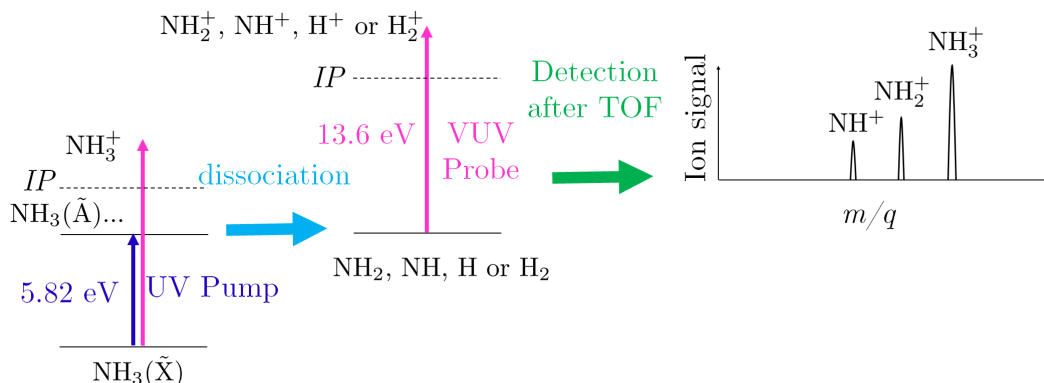


FIGURE A.7: Pump-probe scheme of Fig. A.2 adapted to this specific NH_3 study.

The pump-probe setup of section A.1 was used to determine NH_3 photodissociation branching ratios. A more specific scheme is presented in Fig. A.7. The 213 nm (5.82 eV) radiation was obtained using a Surelite Nd:YAG laser equipped with a doubler, quadrupler and mixer to generate the 5th harmonic at 213 nm. The laser beam was fed directly into the setup.

In order to ionise species supposedly present in the experiment, particularly NH and NH_2 (see *IP*s of Table A.2), the probe laser photon energy was set to 13.6 eV (91 nm) using the high-resolution VUV laser chain of section 1.2 coupled to the modified Icare setup. This particular energy was achieved *via* summed-frequency mixing (see Fig. 1.13) using the Kr two-photon transition at $94\,092.86\text{ cm}^{-1}$ (see Table 1.4).

TABLE A.2: Ionisation Potentials of species implicated in the NH_3 photodissociation study of this work.

Species	<i>IP</i> / eV	<i>m/q</i> (a.m.u.)
NH	13.48 [77]	15
NH_2	11.1690 [93]	16
NH_3	10.186386 [94]	17
OH	13.0170 [79]	17
H_2O	12.62656 [80]	18

Commercially available NH_3 gas, seeded in Ar at 1/6 concentration, was fed into the experiment using a General Valve pulsed gas nozzle.

A.2.3 Results

Mass spectra from this work are presented in Fig. A.8. Fragments at $m/q = 15, 16, 17$, and 18 a.m.u. are detected, assigned to NH^+ , NH_2^+ , NH_3^+ and H_2O^+ , respectively. Water is present in the experimental setup as an impurity. Its cation is not an issue as the resolution in the mass spectrum is below 1 a.m.u. H_2O could however lead to the contamination of the $m/q = 17$ a.m.u. channel caused by photodissociation producing OH ($\text{H}_2\text{O} + h\nu_{\text{pump}} \rightarrow \text{OH} + \text{H}$), followed by ionisation yielding OH^+ . This was checked by recording a mass spectrum without

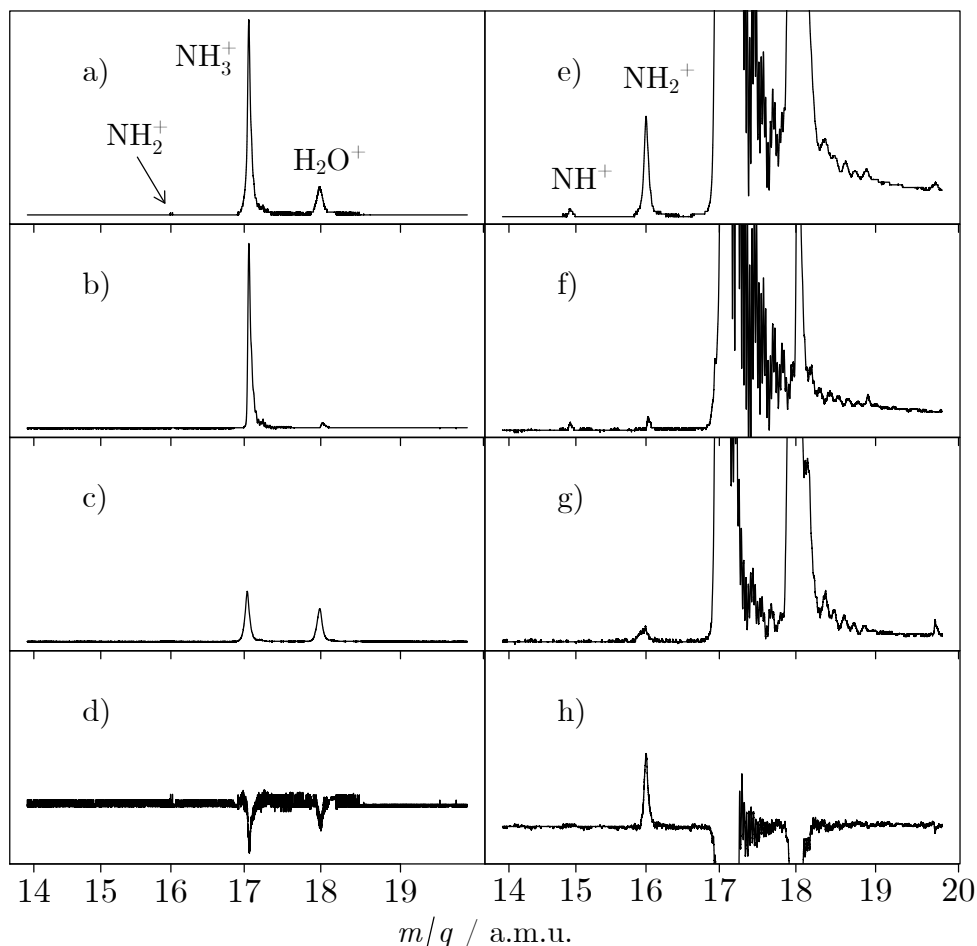


FIGURE A.8: Mass spectra obtained during the NH_3 photodissociation study using a photodissociating pump at 5.82 eV (213 nm) and a photoionising probe at 13.6 eV (91 nm) in different laser configurations:

- a) Pump + probe (see e) for zoom)
- b) Pump only (see f) for zoom)
- c) Probe only (see g) for zoom)
- d) difference spectrum (= a) - b) - c)) (see h) = e) - f) - g) for zoom)

injecting NH_3 , in which no $m/q = 17$ a.m.u. signal was present, so no OH. This can be understood by observing that the H_2O photoabsorption cross section is very low in this energy range (below 0.01 Mb) [192]. ^{15}N species are not responsible for the $(m + 1)/q$ signals here as the terrestrial abundance for these isotopes is around 0.4%.

In order to verify if the NH_2^+ and NH^+ peaks rely on photodissociation, mass spectra were recorded using various laser configurations as shown in the panels of Fig. A.8. In this figure, the right-hand panels display zoomed spectra obtained in the same way as in the left-hand panels. The zoomed spectra intentionally saturate the NH_3^+ and H_2O^+ peaks in order to clearly observe the weaker signals. It is therefore not possible to relate intensities between the zoomed and non-zoomed spectra. However, the same relative intensities are conserved for panels a), b), and c) on one hand, and for panels e), f), and g) on the other, to allow comparisons.

When only the UV pump laser is turned on (panels b) and f) of Fig. A.8), small amounts

of NH^+ and NH_2^+ are still present in the mass spectrum alongside NH_3^+ and H_2O^+ . The UV photon energy is too small to ionise these species using one photon, these panels therefore indicate the presence of multiphoton processes dissociating and ionising fragments.

When only the VUV probe laser is turned on (panels c) and g) of Fig. A.8), a small NH_2^+ signal can be observed in the mass spectrum alongside NH_3^+ and H_2O^+ . Again, this signal does not result from processes of interest here. It is not expected to result from the dissociative ionisation of NH_3 as the threshold for this process is above 15 eV [21]. It most probably stems from the VUV dissociation of NH_3 , followed by the direct ionisation of NH_2 .

As the processes identified when only one of the lasers is operating are not of interest here (they do not result from the UV pump - VUV probe scheme), the pump - probe spectra (panels a) and e) of Fig. A.8) are corrected by subtracting the two lower panels producing the difference spectra of panels d) and h). In order to verify that the corrected NH_2^+ signal is produced by two distinct single-photon steps (UV photodissociation, then VUV photoionisation), the corrected NH_2^+ signal is recorded by varying UV laser intensities. As the ion signal (S^+) resulting from the fragment formation varies proportionately to the incident light intensity (I_1^p), with p the number of implicated photons:

$$S^+ \propto I_1^p, \quad (\text{A.8})$$

the variation of laser intensity allows the determination of the number of implicated photons. Experimentally, the UV laser intensity was varied by placing a gas cell containing bromoform (CHBr_3) on the beam's path before entering the experiment. As bromoform absorbs at 213 nm, varying the pressure in the gas cell allowed control over the laser intensity on exiting the cell. UV laser intensity was measured using a photodiode.

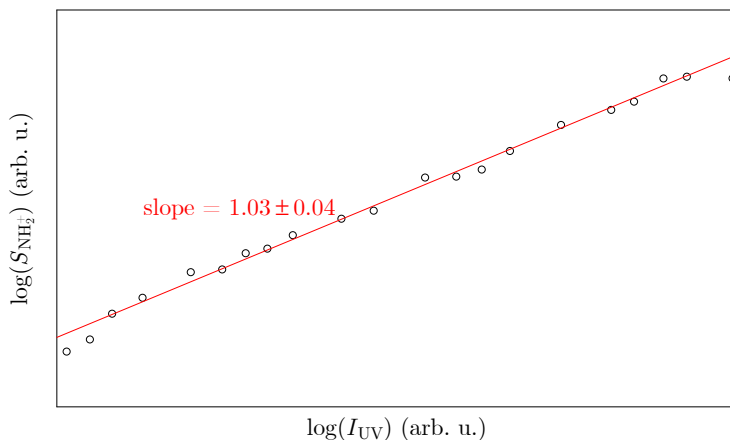


FIGURE A.9: The NH_2^+ signal as a function of incident UV laser intensity on a log-log scale. Circles represent experimental points, the linear fit, whose slope is 1.03 ± 0.04 , is represented as a red line.

NH_2^+ signal as a function of incident UV intensity is presented in Fig. A.9, which uses a log-log scale in order to isolate p as the slope. The result of a slope of 1.03(4) confirms the formation of NH_2 using only one UV photon in the UV pump - VUV probe scheme. A similar study could be conducted on the VUV ionising process, but as VUV lasers are far less intense (see section 1.2.1), if a multiphoton process is not present in the UV, it is highly unlikely that it occurs in the VUV.

The corrected spectra of panels d) and h) of Fig. A.8 show depleted species by action of the UV pump - VUV probe as having negative peaks, and produced species as having positive peaks. Importantly, **only** NH₂⁺ (not NH⁺) is present, which means that **only** NH₂ is produced by photodissociation. For energetic reasons, NH₂ is in its ground state so the only relaxation channel for NH₃ following UV irradiation at 213 nm is forming NH₂(\tilde{X}^2B_1) + H(²S).

At 5.82 eV (213 nm), as no NH is produced, the NH₃(\tilde{X}^1A_1) + $h\nu \rightarrow$ NH₂(\tilde{X}^2B_1) + H(²S) branching ratio is therefore 100%. The absence of NH can be explained by a potential energy barrier, which sets the threshold for NH production higher than simply the thermodynamic threshold of 5.68 eV (see Table A.1). This result is in agreement with the work of Woodbridge *et al.* [193], who studied NH₃ photodissociation at 193 nm (even higher energy) and still did not observe any NH production.

Many studies (*e.g.* refs. [194–196]) relying on electron impact to induce dissociation identify NH rather than NH₂ as the main neutral product, but the interest here is more on photon-induced fragmentation processes.

A.2.4 Conclusions and perspectives

Towards free radical photoionisation cross section measurements

As only NH₂ is produced by photodissociation, matter conservation would appear to dictate that the consumed quantity of NH₃ is equal to the produced quantity of NH₂

$$\Delta N_{\text{NH}_2}(h\nu_{\text{pump}}) = \Delta N_{\text{NH}_3}(h\nu_{\text{pump}}). \quad (\text{A.9})$$

This reasoning is reminiscent of the photoionisation cross section determination procedure of chapter 2. It is true that in these conditions, neglecting the mass apparatus response function $f(m/q)$, and using similar notations to those used in chapter 2, the NH₂ photoionisation cross section can be expressed:

$$\sigma_{\text{NH}_2}^{\text{ion}}(h\nu_{\text{probe}}) = \frac{\Delta S_{\text{NH}_2^+}}{\Delta S_{\text{NH}_3^+}} \times \sigma_{\text{NH}_3}^{\text{ion}}(h\nu_{\text{probe}}), \quad (\text{A.10})$$

However, as highlighted in Fig. A.8 b), a large proportion of NH₃ is directly ionised by the pump laser, *via* a multiphoton process, before being probed. The matter conservation law therefore does not hold as NH₃ is consumed by other processes than single-photon fragmentation. Following the pump laser pulse, the probe laser therefore does not irradiate a quantity of NH₂ equal to the consumed quantity of NH₃. For this reason, the NH₂ photoionisation cross section cannot be extracted as yet.

This study does however shed light on free radical photoionisation measurement possibilities, by forming them through photolysis of a stable precursor. This strategy should become possible once multiphoton processes can be suppressed. In order to quench these processes, the UV pump laser intensity should be reduced. This can be achieved by reducing the Q-switch delay of the laser or, whilst maintaining laser output power, defocusing the UV laser to lower the intensity irradiating the sample. The second option also has the benefit of irradiating more molecules so potentially improving the signal-to-noise ratio.

Summary

The important information from this study is that only NH_2 is produced by photodissociation of NH_3 at 213 nm. NH is not detected despite it being thermodynamically accessible at this photon energy. This can be explained by a potential energy barrier. Bearing Fig. A.6 in mind, it would be interesting to determine NH_3 photodissociation ratios at higher energies (between 180 and 220 nm and the Lyman- α transition energy at 121.6 nm) in order to determine thresholds for new fragmentation channels and their corresponding branching ratios.

This experimental setup shows another means of measuring the NH_2 photoionisation cross section and potentially those of other free radicals. The next step in this study is to adjust experimental conditions so as to suppress multiphoton processes.

A.3 CH_3OH photodissociation studies

A.3.1 Context and motivations

Astrophysical interest

Methanol, or CH_3OH , is another species of astrophysical interest, having been identified in a great number of different media. In the gas phase, it has been observed in molecular interstellar clouds (*e.g.* Sgr B2) [197], planetary atmospheres (*e.g.* Titan) [198] and proto solar systems (*e.g.* IRAS 16293-2422) [199]. It has also been detected in the solid phase: in interstellar ice grains [200], icy grains or dust in the vicinity of proto solar systems [201] and in the comae or on the surfaces of comets. In fact, CH_3OH was found to be one of the most abundant molecules in the ices of comet Hale-Bopp [202].

As well as being observed in a wide variety of astrophysical environments, methanol is thought of as a link in astrophysical chemistry between simple diatomic interstellar molecules and Complex Organic Molecules (COM) [203]. From this point of view, methanol itself can be considered a COM, being the simplest alcohol, and at the same time an elementary building block leading to even more complexity.

CH_3OH photodissociation, state-of-the-art

Photodissociation could be a pathway for producing more complex molecules from stable CH_3OH , as once again, reactive species, such as free radicals, are expected to be produced (see Table A.3 for thermodynamic thresholds). All possible fragments are thermodynamically accessible in the VUV range, at least in their electronic ground state.

Owing to its astrophysical application value, but also from a fundamental point of view, methanol has been extensively studied, including its photodissociation. The first photodissociation study by Hagege *et al.* [204] at 123.6 and 184.9 nm was in 1965 and many more have followed since. In this section, CH_3OH photodissociation results from the literature will be summarised by wavelength (*i.e.* photon energy) with a focus on branching ratios when available (see Table A.4).

At 193 nm, Satyapal *et al.* [205] detected photodissociation products by Laser Induced Fluorescence (LIF) of H atoms; their setup was therefore only sensitive to relaxation channels producing H atoms. They identified $\text{CH}_3\text{O} + \text{H}$ as a major channel, and suggested $\text{CH}_2\text{O} + \text{H}_2$ and $\text{CH}_3 + \text{OH}$ as minor channels. The theoretical works of Marston *et al.* [206] support $\text{CH}_3\text{O} + \text{H}$ as the major channel at 193 nm. They also identified a barrier to $\text{CH}_3 + \text{OH}$. Wen *et al.* [207],

TABLE A.3: CH₃OH(\tilde{X}^1A') photodissociation relaxation channels (forming fragments in their ground electronic states) and their calculated thermodynamic thresholds (assuming there is no potential energy barrier) at 0 K [118]. All products are thermodynamically accessible at 121.6 nm (10.20 eV).

Photodissociation products	Threshold / kJ.mol ⁻¹	Threshold / nm	Threshold / eV
CO($^1\Sigma^+$) + 2 H ₂ ($^1\Sigma_g^+$)	94	1262	0.98
CH ₂ O(1A_1) + H ₂ ($^1\Sigma_g^+$)	96	1237	1.00
HCOH($^1A'$) + H ₂ ($^1\Sigma_g^+$)	318	375	3.30
CH ₂ OH($^2A''$) + H(2S)	414	288	4.31
CH ₃ ($^2A''_2$) + OH($^2\Pi$)	418	285	4.34
CH ₃ O(2E) + H(2S)	440	271	4.58
HCO($^2A'$) + H ₂ ($^1\Sigma_g^+$) + H	465	256	4.84
COH($^2A'$) + H ₂ ($^1\Sigma_g^+$) + H	640	186	6.66
CH ₂ O(1A_1) + 2 H(2S)	641	186	6.67

using high- n Rydberg Time-Of-Flight (HRTOF) with H atoms, offered insights into bond energies, internal energies, anisotropy, but were also only able to characterise relaxation channels producing H atoms. Finally, Weaver *et al.* [208] reported the production of CH₂OH and CH₃O in almost equal proportions (using mm-spectroscopy), which opposes previously mentioned works identifying CH₃O + H as the major channel.

At 185 nm, Hagege *et al.* [204, 213], using gas-phase chromatography, found the formation of CH₃O + H as the major pathway, whilst identifying CH₂O + H₂ and CH₃ + OH as minor channels. The *ab initio* calculations of Buenker *et al.* [209] support these results.

At 157 nm, Yuan *et al.* [210] identified CH₂O + 2H and CH₃O + H as major channels, CH₂OH + H as a minor channel, but were not able to detect other pathways as fragments were probed using HRTOF. Lee *et al.* [214] observed many fragmentation channels using mass spectrometry (CH₃O + H, CH₂O + 2H, HCOH + H₂, CO + 2H₂ and CH₃ + OH), but did not provide branching ratios. Rather than directly from methanol photodissociation, they suggested that some species are produced indirectly by chemical reactivity between photodissociation products. Harich *et al.* [211] reported CH₃O + H and CH₂OH + H as major channels and HCOH as a minor channel. Once more, their detection technique PTS (Photofragment Translational Spectroscopy) prevented detection of CH₃ and OH as it can only detect light fragments (H and H₂).

Hagege *et al.* [204] also studied photodissociation at 123.6 nm and found similar results to those at 185 nm. Lucas *et al.* [212] however found the formation of CH₂O + 2H to be the major relaxation channel, whilst identifying single loss of H forming CH₃O + H and CH₂OH + H as minor channels. In their case, fragment detection relied on HRTOF so only pathways producing H atoms were observed.

All of these studies show the great interest in methanol photodissociation. There is however a great dispersion of BR values in the literature, especially for lower wavelengths. Also, most works only present relative branching ratios as the detection techniques are not capable of probing all suspected fragments.

TABLE A.4: CH₃OH branching ratios at different photolysis wavelengths (photon energies) from the literature.

Wavelength / nm	Photon energy / eV	Ref.	Method	Products	BR
193	6.42	[205]	LIF	CH ₃ O + H	86 ± 10 %
				CH ₂ O + H ₂	minor
				CH ₃ + OH	minor
		[206]	<i>ab initio</i>	CH ₃ O + H	major*
		[207]	HRTOF	CH ₃ O + H	major*
[208]	mm-spectroscopy	CH ₃ O + H	40 %*		
				CH ₂ OH + H	50 %*
185	6.70	[204]	gas chromatography	CH ₃ O + H	75 %
				CH ₂ O + H ₂	20 %
				CH ₃ + OH	5 %
[209]	<i>ab initio</i>	CH ₃ O + H	major		
157	7.90	[210]	HRTOF	CH ₃ O + H	50 %*
				CH ₂ O + 2H	47 %*
				CH ₂ OH + H	3 %*
				[211]	PTS
				CH ₂ OH + H	47.6 %*
				HCOH + H ₂	13.8 %*
				CH ₂ O + H ₂	0.2 %*
123.6	10.03	[204]	gas chromatography	CH ₃ O + H	75 %
				CH ₂ O + H ₂	20 %
				CH ₃ + OH	5 %
121.6	10.20	[212]	HRTOF	CH ₂ O + 2H	71 %*
				CH ₃ O + H	18 %*
				CH ₂ OH + H	11 %*

* Relative BR only, as detection technique does not account for all possible fragments.

Choice of photodissociation photon energy

By selectively tuning the probe laser photon energy, our experimental setup is capable of detecting all possibly formed photodissociation fragments. The first step is to select the photodissociation photon energy or wavelength for the experiments. In the context of solar photodissociation of methanol, the reasoning is the same as in the NH₃ case: determine spectral components of the solar flux that induce photodissociation (see Fig. A.10).

Fig. A.10 c) shows that only spectral components of the solar flux around the Lyman- α transition energy induce CH₃OH photodissociation. This wavelength was therefore chosen as the intended pump laser wavelength for the photodissociation studies.

A.3.2 Experimental specificities

The pump-probe setup of section A.1 was used to determine CH₃OH photodissociation branching ratios. Before using a pump laser emitting at 121.6 nm (obtainable by third harmonic generation of a frequency-doubled pulsed dye-laser emitting at 364.8 nm), a pump laser emitting

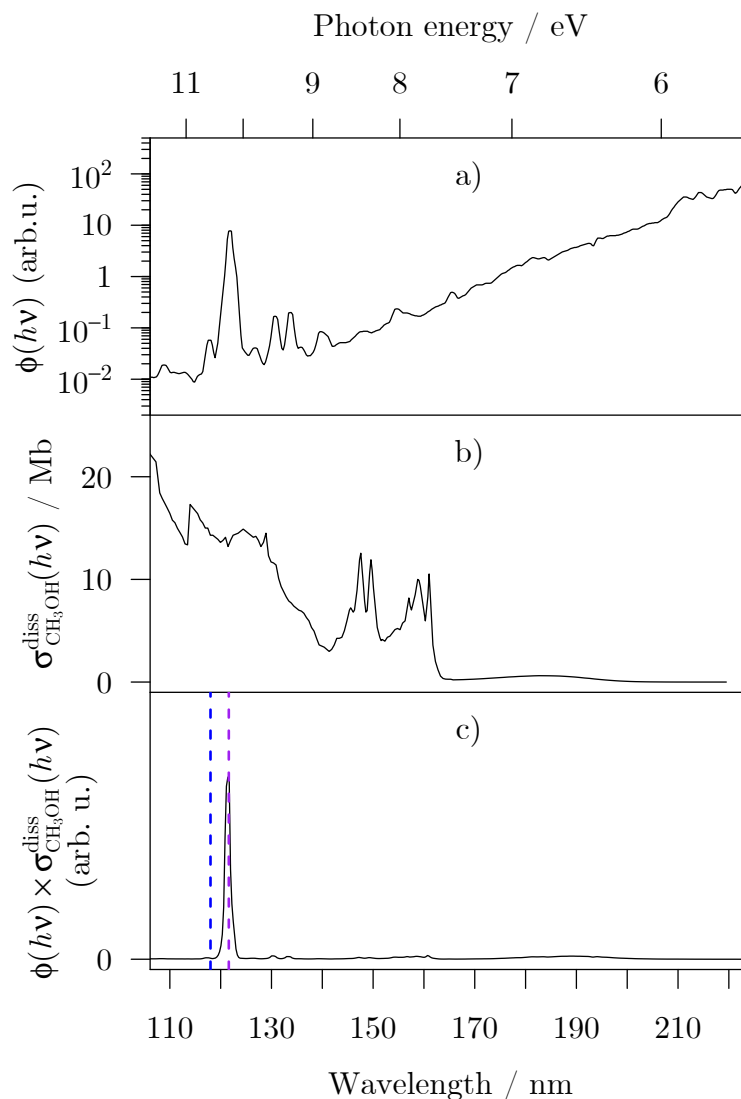


FIGURE A.10: a) Typical VUV solar flux taken from [191]. b) CH_3OH VUV photodissociation cross section [8]. c) Product of the solar flux with the photodissociation cross section ($c = a \times b$), a dashed blue vertical line at 118.2 nm (10.49 eV) locates the photodissociation energy of this work. A dashed purple vertical line at 121.6 nm (10.20 eV) locates the relevant wavelength for astrophysical applications.

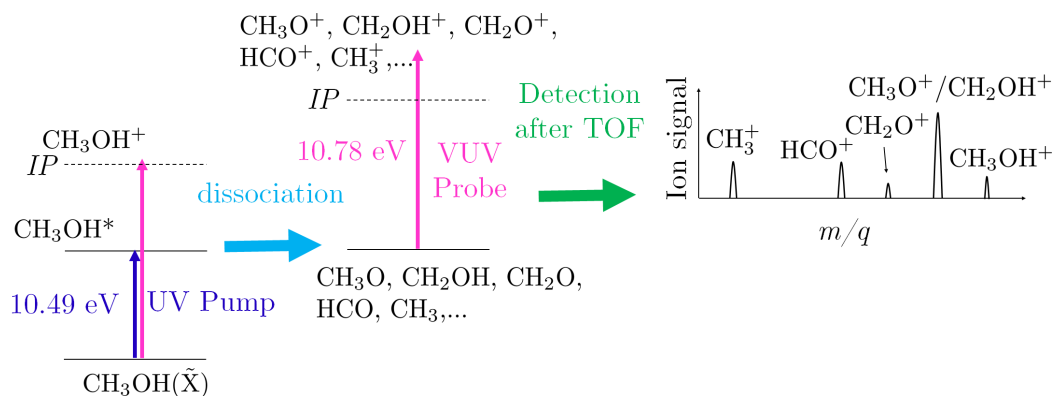
at 118.2 nm was used first of all. This neighbouring wavelength is easier to obtain by third harmonic generation of the 3rd harmonic of a Nd:YAG laser (at 354.7 nm). As well as being easier to implement, this radiation can be produced at higher intensities, which is useful when optimising the pump-probe setup. The pump-probe scheme specific to this CH_3OH study is presented in Fig. A.11.

In order to ionise at least one product from each possible relaxation channel (see *IPs* of Table A.5), the probe laser photon energy was set to 10.78 eV (115 nm). It is true that this energy is below *IP*(CH_2O), but unlike with NH_3 , it is interesting to be able to set the probe laser photon energy below the precursor *IP* so that the CH_3OH^+ signal does not saturate the detector. Depending on the temperature of the sample, a CH_3OH^+ signal may still be observed

TABLE A.5: Ionisation potentials of species implicated in the CH₃OH photodissociation study of this work.

Species	IP / eV	<i>m/q</i> (a.m.u.)
CH ₃ OH	10.846 [105]	32
CH ₃ O	10.72 [106]	31
CH ₂ OH	7.55 [106]	31
CH ₂ O	10.8887 [107]	30
HCOH	8.86 [108]	30
HCO	8.14 [109]	29
OH	13.0170 [79]	17
CH ₃	9.8380 [215]	15
CH ₂	10.3864 [216]	14

(likewise for CH₂O), but it will be much weaker than if it was above the IP. This photon energy is also insufficient for ionising OH, but its by-product CH₃ is ionised at 10.78 eV.

FIGURE A.11: Pump-probe scheme of Fig. A.2 adapted to this specific CH₃OH study.

The probe laser radiation was obtained using the Cobra-Stretch pulsed dye laser emitting at 345 nm (with a BBO crystal inserted on the output of the laser for frequency doubling) and focusing the laser beam in a Xe cell as with the pump laser enabling third harmonic generation. The VUV laser chain of section 1.2 is modified to replace to the rare gas nozzle with a rare gas cell and the high-resolution UV laser chain is not required.

Commercially available CH₃OH is placed in a bubbler. Ar is passed through the bubbler to carry CH₃OH towards the setup.

Before using the setup to study CH₃OH, CH₄ (seeded in Ar) was used as an intermediate test sample. This preliminary study was conducted as CH₄ is already known to photodissociate at 118.2 nm producing CH₂ and CH₃ [68], it therefore enables the optimisation of part of the experimental setup before using CH₃OH.

A.3.3 CH₄ photodissociation

Unlike all other experiments of this appendix, the goal in this paragraph is to photodissociate at 118.2 nm CH₄ and then ionise the neutral fragments with the **same** laser pulse. It can therefore

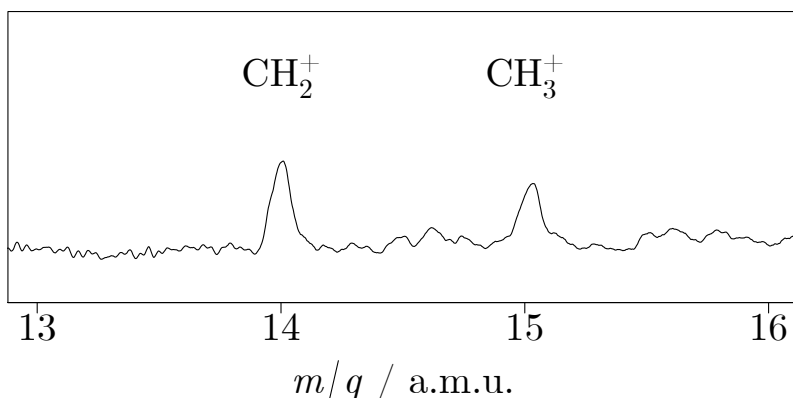


FIGURE A.12: Mass spectra obtained during the CH₄ photodissociation at 10.49 eV (118.2 nm) probed at the same energy.

be thought of as a two-photon one-colour scheme. The 118.2 nm radiation is reached using the pump laser of the CH₃OH study (the probe laser is not used here). This scheme acts as a step in optimising the pump laser and its irradiation of the molecular beam.

As displayed in Fig. A.12, the non-negligible detection of CH₂⁺ and CH₃⁺ confirms that the pump laser is optimised. The ratio of the CH₂⁺ and CH₃⁺ integrated peaks is 1.19. This is in agreement with ref. [68], who also observed the production of CH₂ and CH₃ at 118.2 nm.

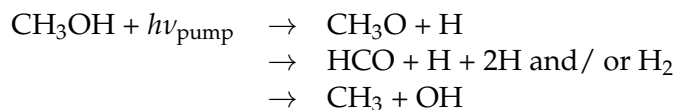
A.3.4 CH₃OH photodissociation at 118.2 nm: results

Coming back to methanol, CH₄ was replaced by CH₃OH and the probe laser was switched on, whilst retaining the same setup parameters from the CH₄ study. As in the NH₃ study, mass spectra are recorded in various experimental configurations (see Fig. A.13).

Ionised fragments are assigned in panel a) of Fig. A.13. Isomers sharing the same m/q value (at our mass spectrum resolution) are not distinguishable: *e.g.* CH₃O and CH₂OH or CH₂O and CHOH. The chemical formulas of Fig. A.13 are not structural for this reason. The small $m/q = 17$ a.m.u. signal is assigned to NH₃⁺, but is caused no doubt from ammonia contamination of the setup following the previous NH₃ photodissociation study. By subtracting the pump-probe spectrum by the spectra of each individual laser, the resulting spectrum (Fig. A.13 d)) shows that only signals at $m/q = 29$ and 31 a.m.u. depend on both the pump and the probe; we also cannot rule out, due to the low signal-to-noise ratio of the spectra, the presence of CH₃⁺ in the difference spectrum.

Noises at times corresponding to masses ≈ 16.5 and 19 a.m.u. are most probably due to electronic signals in the setup, *e.g.* opening or closing of time gates.

Observing fragments depending on both the pump and the probe lasers, it is possible to determine the photodissociation relaxation channels at 118.2 nm (10.49 eV):



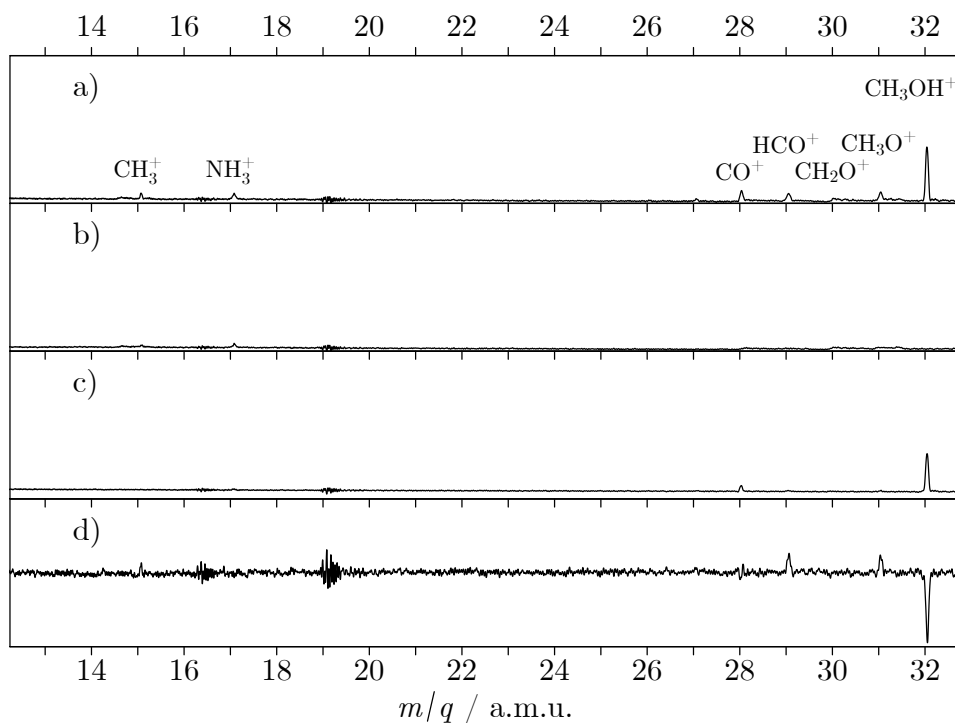


FIGURE A.13: Mass spectra obtained during the CH_3OH photodissociation at 10.49 eV (118.2 nm) probed at 10.78 eV (115 nm) in different laser configurations:
 a) Pump + probe
 b) Pump only
 c) Probe only
 d) difference spectrum (= a) - b) - c))

The next step in determining branching ratios would be to relate ion signals to produced neutral quantities. This requires the knowledge of photoionisation cross sections at the photon energy of the probe laser, for all detected fragments. Measuring these essential parameters was an objective of an experimental campaign at SOLEIL, as detailed in section 2.4 of chapter 2. However it was not possible to determine these absolute photoionisation cross sections for HCO, CH_2OH , and CH_3O . In addition, there is ambiguity in the present photodissociation experiment using solely the CH_3OH isotopologue, concerning isomers and also whether the by-product is 2H or H_2 .

Based on the signals of Fig. A.13 d), it would however appear that the production of HCO and CH_3O and/or CH_2OH are the main photodissociation channels at 118.2 nm, if photoionisation cross sections are considered the same for all species. The relaxation towards HCO is in disagreement with other works in this energy range [204, 212], but CH_3O and/or CH_2OH are often reported as being major photodissociation products. Literature results also identified the production of CH_2O as a major relaxation pathway, but we cannot rule this out as the photon energy of the probe laser was just below $IP(\text{CH}_2\text{O})$. In our case, the HCO^+ signal of the $m/q = 29$ a.m.u. channel may actually stem, not from the direct ionisation of HCO, but rather from the dissociative ionisation of CH_3O or CH_2OH . Such a process was suggested in section 2.4 of chapter 2, but this has not yet been verified.

A.3.5 CH_3OH photodissociation summary

More work is needed to confirm these preliminary results. In particular, the aforementioned relaxation pathways identified for photodissociation at 118.2 nm must be verified. Performing the study with various deuterated isotopologues of methanol should help greatly the isomer fragment identification (*e.g.* $\text{CH}_3\text{O}/\text{CH}_2\text{OH}$). It can be noted that all results presented in this appendix employed the Icare setup, so it will be interesting in the future to see how these pump-probe studies can be improved with the VULCAIM setup. As the new vacuum chambers were designed from scratch with high precision, it is expected to be easier to achieve pump-probe ion signals, the laser alignment and optimisation being easier.

Furthermore, photoionisation cross sections of the relevant free radicals must be determined in order to deduce branching ratios. We already have the means and the know-how to undertake such measurements, but photoionisation cross section studies are always challenging (see chapter 2).

Once this study at 118.2 nm has been finalised, it will be of most interest to be able to provide methanol photodissociation branching ratios at 121.6 nm for astrophysicists. We have the equipment to reach this wavelength, but it is achieved with a lower photon flux, which will represent an additional difficulty.

Appendix B

Dissociative ionisation of CH₃NCO

At higher and higher energies in the CH₃NCO study (see section 3.1.1 of chapter 2), direct ionisation is not the only means of relaxation upon VUV irradiation. Dissociative ionisation, *i.e.* the formation of charged products by dissociation, becomes another means of relaxing at higher energies. Typically, this denotes the formation of a cation, an electron, and a neutral by-product. Schematically, dissociative ionisation follows the general reaction:



In this appendix, we present the additional information obtained on this relaxation channel, from the photoionisation study of CH₃NCO performed at SOLEIL. We will identify the various dissociative ionisation channels, locate the appearance energies of the corresponding fragments and compare these appearance energies to thermodynamic thresholds and calculated values.

Dissociative ionisation can also lead to ion-pair formation. Schematically,



This process is different to the formation of a cation, an electron, and a neutral by-product; it is mostly studied separately. In our experiment, it is not possible to detect ion-pair formation because the positive charged particles must be detected in coincidence with an electron. The time-of-flight of the anion being much longer than that of an electron, this process could not be investigated in this work.

B.1 Experimental details

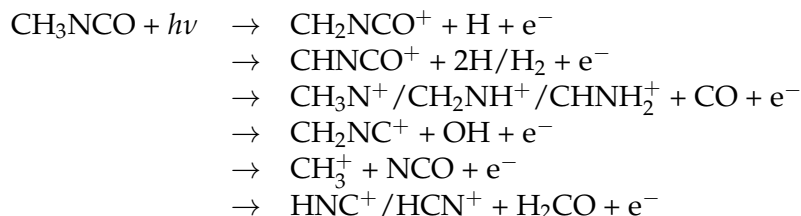
The specificities of the experimental setup are the same as those described in the spectroscopic study of CH₃NCO of section 3.1.1 of chapter 2. In order to extend the study to higher energies, a longer scan was recorded at a photon resolution of 15 meV from 10.3 to 15.7 eV with 10 meV steps. A 1000 V repeller voltage was used in order to collect all ionised species up to 6 eV above their *IPs*.

B.2 Context

The context for CH₃NCO photoionisation was recalled at the beginning of section 3.1.1 chapter 2. Photoionisation studies of CH₃NCO do exist, but are scarce and focus on the first *IP*. Very few works deal with higher energy relaxation mechanisms. In particular, we could find no literature references on dissociative ionisation induced by photons. Haney and Franklin [217]

determined the relaxation towards $\text{CH}_3^+ + \text{NCO} + \text{e}^-$ to have a threshold of 14.6 eV, but this was measured using the electron impact ionisation technique.

A number of dissociative ionisation relaxation pathways are nevertheless imaginable, producing a wide variety of neutral and charged species. Interestingly for astrophysical applications, most are reactive species:



B.3 Ion yields and assignments of the products of CH_3NCO dissociative ionisation

In order to identify the ions produced by dissociative ionisation of CH_3NCO , mass spectra recorded over the whole scan range were summed to produce the mass spectrum of Fig. B.1.

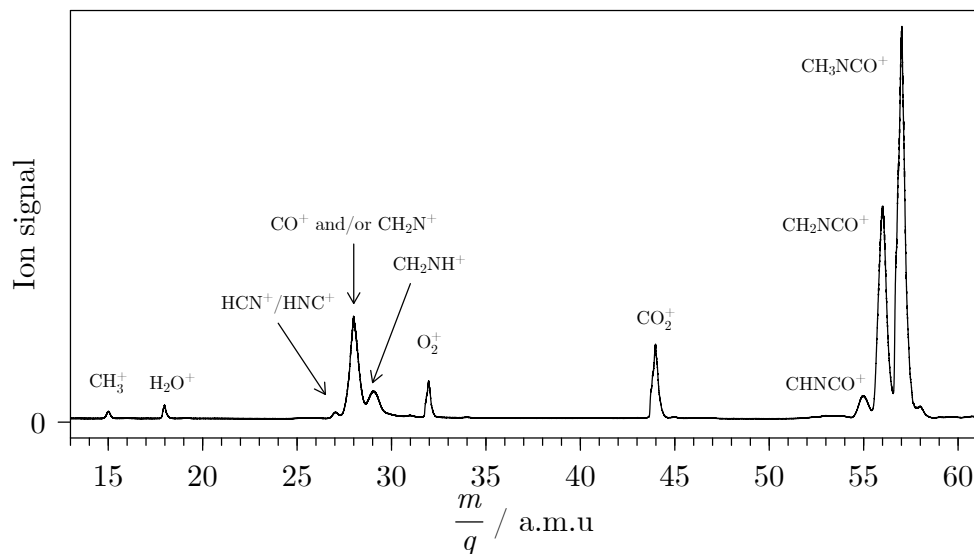


FIGURE B.1: Summed mass spectrum over the whole scan (10.3 to 15.7 eV). CH_3NCO dissociative ionisation products are identified.

All fragments identified in Fig. B.1 are products of CH_3NCO dissociative ionisation, except for the $m/q = 57$ a.m.u. fragment corresponding to the direct ionisation of the parent molecule and $m/q = 18, 32,$ and 44 associated with impurities, respectively $\text{H}_2\text{O}^+, \text{O}_2^+,$ and CO_2^+ . In mass spectra, ion signals issuing from dissociative ionisation have wider peaks than those from direct ionisation; this is due to an excess of kinetic energy carried by the products of dissociative ionisation. The assignment of dissociative ionisation products is not unambiguous in the mass spectrum of Fig. B.1, isomers are notably not distinguishable at this point. Most ambiguities can be lifted through the study of ion yields.

For all the cations produced *via* CH_3NCO dissociative ionisation, ion yields are recorded using the techniques described in section 1.1.3 of chapter 1. These ion yields are reported in Fig. B.2. Note that not all ion yields are issued from the same scan and do not therefore cover the same photon energy range. Despite this, the x -axes of all panels of Fig. B.2 are the same to facilitate comparing spectra.

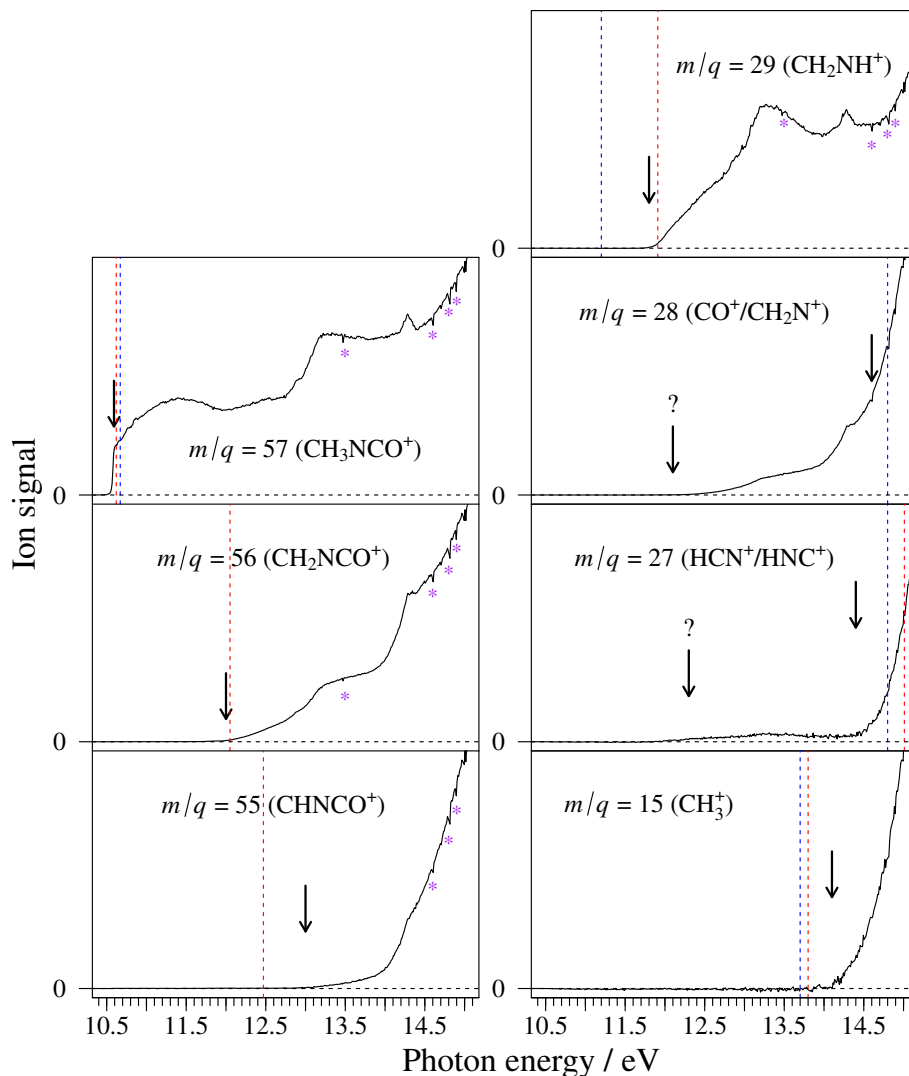


FIGURE B.2: Ion yields of the products of CH_3NCO dissociative ionisation. Blue- and red-dashed lines correspond to the thermodynamic thresholds (E_T) and the theoretical thresholds (E_{th}) of Table B.1, respectively. Black arrows pinpoint appearance energies (E_a) of the corresponding fragments, also summarised in Table B.1. Purple asterisks locate Ar absorption lines from the beamline gas filter used to calibrate the energy scale.

The analysis of these ion yields enables the determination of appearance energies (E_a) for each fragment. These are defined as threshold energies above which the corresponding ion signal is no longer vanishing. Their localisation is usually not easy since the rising slope is often very smooth. The corresponding uncertainty is thus often large (around 0.1 eV) and dependent on the ion yield trend around the appearance threshold. These appearance energies

are compared to thermodynamic thresholds (E_T), as in appendix A, determined using Hess' law of Constant Heat Summation by combining known formation enthalpies at 0 K [118] when available.

TABLE B.1: Observed cationic fragments following the dissociative ionisation of CH₃NCO and corresponding measured appearance energies (E_a). These energies are compared to the thermodynamic (E_T) and theoretical thresholds (E_{th}) that sometimes account for transition states (TS).

m/q (a.m.u.)	Cationic fragment	Dissociative ionisation channel	E_a / eV	E_T / eV	E_{th}^* / eV
57	CH ₃ NCO ⁺	CH ₃ NCO ⁺ + e ⁻ **	10.59(1)	-	10.592
56	CH ₂ NCO ⁺	CH ₂ NCO ⁺ + e ⁻ + H	12.0(1)	?	12.05 (no TS)
55	CHNCO ⁺	CHNCO ⁺ + e ⁻ + H ₂	13.0(2)	?	12.47 (TS)
29	CH ₂ NH ⁺	CH ₂ NH ⁺ + e ⁻ + CO	11.8(1)	11.2	11.91 (TS)
28	CO ⁺	CO ⁺ + e ⁻ + CH ₂ NH	14.5(2) ?	14.8	15.15 (TS ?)
27	HCN ⁺	HCN ⁺ + e ⁻ + CH ₂ O	14.4(1)	14.8	15.0 (TS ?)
27	HNC ⁺	HNC ⁺ + e ⁻ + CH ₂ O	12.3(1) ?	13.9	14.1 (TS ?)
15	CH ₃ ⁺	CH ₃ ⁺ + e ⁻ + NCO	14.1(1)	13.7	13.8 (no TS)

*These theoretical energies account for potential energy barriers of transition states (TS) when identified. Sometimes a transition state could not be verified (TS ?) or was found to not exist (no TS).

** The fragment at $m/q = 57$ a.m.u. is the direct ionisation product of CH₃NCO. The appearance energy is just compared to the *IP* determined in section 3.1.1 of chapter 2.

They are also compared to the *ab initio* calculations (E_{th}) performed by Jean-Christophe Loison, of Bordeaux University. For some cases, transition states and potential energy barriers have also been predicted in these calculations, which can sometimes explain the energy difference between appearance and thermodynamic threshold energies. The theoretical energy for direct ionisation is taken from the spectroscopic study of section 3.1.1 of chapter 2. All these energies are summarised in Table B.1. Their comparison enables a more reliable identification of produced charged fragments and dissociative ionisation relaxation channels.

The main information retrieved from these ion yields are summarized below:

- The ion yield of the direct ionisation product of $m/q = 57$ a.m.u. (CH₃NCO⁺) is reminiscent of the schematic ion yield of Fig. 1.7 of chapter 1. The inflection point in the ion yield, at 10.59 eV, corresponds to the origin in the $\tilde{X}^+ \leftarrow \tilde{X}$ photoionising transition in CH₃NCO. This energy is directly compared to the first *IP* of CH₃NCO (10.592 eV) obtained in the spectroscopic study of section 3.1.1 of chapter 2, with which the agreement is excellent. It does not make sense to compare the appearance energy to a thermodynamic tabulated value as the energy difference between the cation and neutral CH₃NCO is again the ionisation potential.
- The $m/q = 56$ a.m.u. signal is unambiguously assigned to CH₂NCO⁺, H is the neutral by-product. In this only possible dissociative ionisation channel forming a cation at $m/q = 56$ a.m.u., no thermodynamic information is available, but there is an excellent agreement between the appearance energy (12.0 eV) and the theoretical threshold (12.05 eV). *Ab initio* calculations show that this channel does not implicate a transition state.

- The $m/q = 55$ a.m.u. signal is assigned to CHNCO^+ , H_2 is the neutral by-product. Thermodynamic information on CHNCO is not available, nor on its cation. The theoretical threshold (12.47 eV), accounting for a TS, is in agreement with the appearance energy (13.0 eV), especially given the low signal at threshold making the determination of E_a uncertain. The calculations help to identify H_2 as a by-product rather than 2H , whose threshold would be 16.64 eV (without TS).
- The $m/q = 29$ a.m.u. signal is assigned to CH_2NH^+ , CO is the neutral by-product. The thermodynamic threshold (11.2 eV) is situated below the appearance energy (11.8 eV), but its delayed appearance in the scan is explained by a potential energy barrier (11.91 eV) predicted by the *ab initio* calculations. The calculations for CH_3N^+ and CHNH_2^+ do not converge, which indicates that these fragments, also at $m/q = 29$ a.m.u., are probably unstable, which supports the assignment.
- The $m/q = 28$ a.m.u. signal is also problematic, appearing at around 12.1 eV. One dissociative ionisation channel producing a charged fragment at $m/q = 28$ a.m.u. yields $\text{CH}_2\text{N}^+ + \text{e}^- + \text{HCO}$, but its thermodynamic threshold is at 16.5 eV, so is not likely responsible for the observed signal. CO^+ is actually the easiest formed (lowest energy) fragment from CH_3NCO at $m/q = 28$ a.m.u. with CH_2NH as its neutral by-product (the formation of CH_3N requires more energy), but the thermodynamic (14.8 eV) and theoretical (15.15 eV) thresholds are still much higher than the appearance energy. HCNH^+ or CNH_2^+ could also correspond to $m/q = 28$ a.m.u., but their formation requires substantial geometric rearrangement compared to the parent molecule so a high potential energy barrier is expected. A final possibility would be N_2^+ issued, not from dissociative ionisation, but direct ionisation of impurities within the setup. However, $IP(\text{N}_2) = 15.5809$ eV [96], which is again above the appearance energy, so not likely the cause. The appearance energy of $m/q = 28$ a.m.u. at 12.1 eV is not explained, but the ion signal increases markedly from around 14.5 eV, which is in agreement with the thermodynamic and theoretical thresholds for $\text{CO}^+ + \text{e}^- + \text{CH}_2\text{NH}$. The ion yield above ≈ 14.5 eV is therefore likely due to CO^+ . Note that *ab initio* calculations were not able to identify the presence or absence of a TS.
- There is however ambiguity concerning the $m/q = 27$ a.m.u. signal which can be assigned to HCN^+ or its isomer HNC^+ , the neutral by-product in either case is CH_2O . The problem is that thermodynamic thresholds (14.8 and 13.9 eV, respectively) and theoretical appearance energies (15.0 and 14.1 eV, respectively) are within 1 eV for both fragments. *Ab initio* calculations were not able to locate or rule out a possible transition state. Finally the $m/q = 27$ a.m.u. ion yield increases markedly above 14.4 eV, which is not easily comparable with the thermodynamic or theoretical results. The discrepancy between isomers at $m/q = 27$ a.m.u. cannot be lifted for these reasons, but the experimental appearance energy does seem closer to that calculated for the channel leading to HNC^+ . The formation pathway of either isomer is complex and ambiguous; studies of the dynamics are needed to clarify this point.
- The $m/q = 15$ a.m.u. signal is assigned unambiguously to CH_3^+ . The thermodynamic threshold (13.7 eV) and *ab initio* calculations ($E_{\text{th}} = 13.8$ eV) are in agreement with the appearance energy (14.1 eV) of the fragment. Our value is 0.5 eV below the reported value measured by electron impact [217]. The *ab initio* calculations show that the formation of CH_3^+ does not implicate a potential energy barrier. The neutral by-product is NCO .

Note that there may be some slight cross-contamination between neighbouring fragments ($m/q = 27, 28$, and 29 a.m.u.) given the forms of the peaks of the mass spectra of Fig. B.1. There can also be contributions from ^{13}C isotopologues at $(m + 1)/q$. These two effects, if present at all, are expected to be small and probably only affect the overall tendency of the ion yield, not the determination of appearance energies.

B.4 TPES of dissociative states

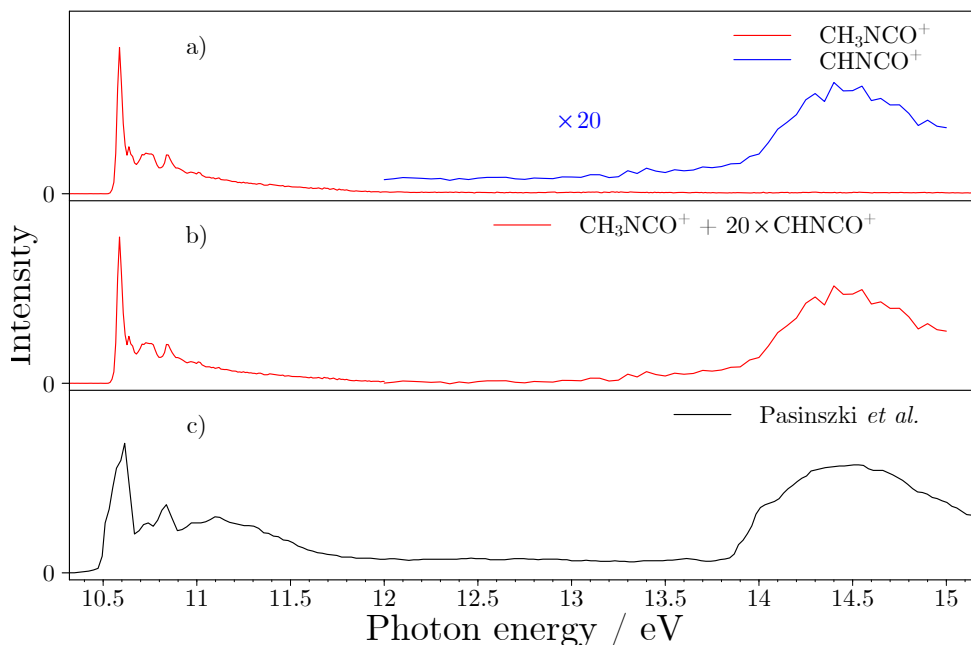


FIGURE B.3: a) TPES of $m/q = 55$ (red) and 57 a.m.u. (blue) spectra from this work, assigned to CHCNO^+ and CH_3NCO^+ , respectively; $m/q = 55$ a.m.u. has a $\times 20$ zoom. b) TPES combining the two spectra from panel a). c) Digitalised He I PES of CH_3NCO from ref. [130].

As mentioned in the spectroscopic study of section 3.1.1 of chapter 2, our TPES of CH_3NCO does not reveal any higher excited states in the cation than the $\text{A}^+ \ ^2\text{A}'$ state. This is in disagreement with Pasinszki *et al.* [130] who observed four extra bands, notably one between 14 and 15 eV and peaking at 14.55 eV. The study of this appendix has shown that dissociative ionisation starts to compete with direct ionisation from around 12 eV. It is therefore possible that the bands identified by Pasinszki *et al.* correspond to dissociative states. In our case, the electrons produced by dissociative ionisation hit the detector in coincidence with ions of a different mass than the parent (as long as the dissociation dynamics are faster than the time-of-flight) and are thus not recorded in the channel of the parent molecule. The setup of Pasinszki *et al.* was not mass-selective so the electrons are all collected indiscriminately.

Concerning the $14 - 15$ eV band, we are able to reconstruct this spectral feature using the TPES of $m/q = 55$ a.m.u., assigned to CHNCO^+ (see Fig. B.3). As found in section B.3 (see Table B.1), the $\text{CHNCO} + \text{H}_2 + \text{e}^-$ dissociative ionisation channel starts to appear at $13.0(2)$ eV, and the corresponding ejected electrons contribute to the electron signal observed in the PES of Pasinszki *et al.* above 13.8 eV. A similar intensity to the spectrum of Pasinszki *et al.* is reproduced

by multiplying our spectrum by a factor 20. Intensity differences can be explained as the two spectra are recorded using different techniques and different experimental setups. In particular, our spectrum is produced only using threshold electrons, so faster electrons do not contribute. This can explain why our signal is much lower than that of Pasinszki *et al.*. In addition to this band, Pasinszki *et al.* identified three others, at 16.0, 16.75, and 18.0 eV, but these are also expected to be dissociative.

B.5 CH₃NCO dissociative ionisation summary

The dissociative ionisation of CH₃NCO has been studied from 10.4 to 15.7 eV. All cationic fragments, except for $m/q = 27$ and 28 a.m.u., were assigned leading to the identification of the corresponding dissociative ionisation relaxation channels:

- CH₂NCO⁺ + H + e⁻,
- CHNCO⁺ + H₂ + e⁻,
- CHNH₂⁺ + CO + e⁻, and
- CH₃⁺ + NCO + e⁻.

The assignments were facilitated by comparing fragment appearance energies in the ion yield to thermodynamic and theoretical thresholds. The theoretical thresholds were determined using *ab initio* calculations that were able to identify, when possible, the absence or presence of transition states resulting in potential energy barriers. There is also an excellent agreement between the energy of the inflexion point of the CH₃NCO⁺ ion yield and the first adiabatic *IP* of CH₃NCO determined in section 3.1.1 of chapter 2.

The appearance energies are not measured with great accuracy due to the temperature-dependency of the dissociative ionisation thresholds (measured at around 300 K here). Not only is the internal energy of the parent molecule a factor, but also the internal energies of the formed fragments. The thresholds are also difficult to identify because the slopes are sometimes very small, which makes them all the more sensitive to the temperature. Despite not being defined with great accuracy, the thresholds are still useful. The study of dissociative ionisation reconciles discrepancies between our spectroscopic results of section 3.1.1 of chapter 2 and those of Pasinszki *et al.* [130]: the high energy bands of Pasinszki *et al.* correspond to dissociative states, which are detected in different channels in our mass-selective experiment to direct ionisation.

As seen in chapter 2, it is important to know dissociative ionisation thresholds in photoionisation experiments, especially quantitative experiments, in order to distinguish ion signals issued from direct ionisation from those issued from dissociative ionisation. The DELICIOUS 3 spectrometer is equipped with a mode allowing this discrimination by comparing the differences in kinetic energy of the produced cationic fragments. However, this mode must be selected before performing the experiments and cannot be used *a posteriori* in data analysis.

Appendix C

List of publications as co-author

Published:

- **"Quantifying the photoionization cross section of the hydroxyl radical".** O. J. Harper, M. Hassenfratz, J.-C. Loison, G. A. Garcia, N. de Oliveira, H. R. Hrodmarsson, S. T. Pratt, S. Boyé-Péronne, and B. Gans. In: *The Journal of Chemical Physics* 150.14 (2019), p. 141103. DOI 10.1063/1.5091966
- **Erratum: "Quantifying the photoionization cross section of the hydroxyl radical" [J. Chem. Phys. 150, 141103 (2019)].** O. J. Harper, M. Hassenfratz, J.-C. Loison, G. A. Garcia, N. de Oliveira, H. R. Hrodmarsson, S. T. Pratt, S. Boyé-Péronne, and B. Gans. In: *The Journal of Chemical Physics* 152.18 (2020), p. 189903. DOI 10.1063/5.0010934
- **"To see C₂: Single-photon ionization of the dicarbon molecule".** O. J. Harper, S. Boyé-Péronne, G. A. Garcia, H. R. Hrodmarsson, J.-C. Loison, and B. Gans. In: *The Journal of Chemical Physics* 152.4 (2020), p. 041105. DOI: 10.1063/1.5139309
- **"VUV photoionization of the CH₂NC radical: adiabatic ionization energy and cationic vibrational mode wavenumber determinations."** B. Gans, S. Hartweg, G. A. Garcia, S. Boyé-Péronne, O. J. Harper, J.-C. Guillemin, and J.-C. Loison. In: *Physical Chemistry Chemical Physics* 22 (2020), p. 12496-12501. DOI: 10.1039/d0cp01901
- **"Quasi-symmetry effects in the threshold photoelectron spectrum of methyl isocyanate".** O. J. Harper, L. H. Coudert, J.-C. Loison, B. Gans, S. Douin, G. A. Garcia, J.-C. Guillemin, and S. Boyé-Péronne. In: *The Journal of Chemical Physics* 153.7 (2020), p. 074308. DOI: 10.1063/5.0017753

In preparation:

- **"Photoionization cross-section measurement of the NH₂ radical".** O. J. Harper, B. Gans, J.-C. Loison, G. A. Garcia, H. R. Hrodmarsson, and S. Boyé-Péronne.

Bibliography

- [1] A. S. Eddington. "The deviation of stellar material from a perfect gas". In: *Monthly Notices of the Royal Astronomical Society* 88 (1928), p. 352.
- [2] B. T. Draine. "Photoelectric heating of interstellar gas". In: *The Astrophysical Journal Supplement Series* 36 (1978), pp. 595–619. DOI: [10.1086/190513](https://doi.org/10.1086/190513).
- [3] *Cologne Database for Molecular Spectroscopy (CDMS)*. URL: <https://cdms.astro.uni-koeln.de>.
- [4] F. Goesmann et al. "Organic compounds on comet 67P/Churyumov-Gerasimenko revealed by COSAC mass spectrometry." In: *Science* 349.6247 (2015), aab0689. DOI: [10.1126/science.aab0689](https://doi.org/10.1126/science.aab0689).
- [5] M. J. Mumma, M. A. DiSanti, N. D. Russo, M. Fomenkova, K. Magee-Sauer, C. D. Kaminiski, and D. X. Xie. "Detection of abundant ethane and methane, along with carbon monoxide and water, in comet C/1996 B2 Hyakutake: evidence for interstellar origin". In: *Science* 272.5266 (1996), pp. 1310–1314. DOI: [10.1126/science.272.5266.1310](https://doi.org/10.1126/science.272.5266.1310).
- [6] J. M. Dyke. "Photoionization studies of reactive intermediates using synchrotron radiation". In: *Physical Chemistry Chemical Physics* 21.18 (2019), pp. 9106–9136. DOI: [10.1039/c9cp00623k](https://doi.org/10.1039/c9cp00623k).
- [7] *Kinetic Database for AstroChemistry (KIDA)*. URL: <http://kida.astrophy.u-bordeaux.fr/>.
- [8] A. N. Heays, A. D. Bosman, and E. F. van Dishoeck. "Photodissociation and photoionisation of atoms and molecules of astrophysical interest". In: *Astronomy & Astrophysics* 602 (2017), A105. DOI: [10.1051/0004-6361/201628742](https://doi.org/10.1051/0004-6361/201628742).
- [9] D. W. Turner and M. A. Jobory. "Determination of ionization potentials by photoelectron energy measurement". In: *The Journal of Chemical Physics* 37.12 (1962), pp. 3007–3008. DOI: [10.1063/1.1733134](https://doi.org/10.1063/1.1733134).
- [10] D. W. Turner. "Limits to Resolving Power in Photoelectron Spectroscopy". In: *Nature* 213.5078 (1967), pp. 795–796. DOI: [10.1038/213795a0](https://doi.org/10.1038/213795a0).
- [11] D. Villarejo, R. R. Herm, and M. G. Inghram. "Measurement of threshold electrons in the photoionization of Ar, Kr, and Xe". In: *The Journal of Chemical Physics* 46.12 (1967), pp. 4995–4996. DOI: [10.1063/1.1840677](https://doi.org/10.1063/1.1840677).
- [12] T. Baer, W. B. Peatman, and E. W. Schlag. "Photoionization resonance studies with a steradiancy analyzer. II. The photoionization of CH₃I". In: *Chemical Physics Letters* 4.5 (1969), pp. 243–247. DOI: [10.1016/0009-2614\(69\)80174-0](https://doi.org/10.1016/0009-2614(69)80174-0).
- [13] T. Baer and R. P. Tuckett. "Advances in threshold photoelectron spectroscopy (TPES) and threshold photoelectron photoion coincidence (TPEPICO)". In: *Physical Chemistry Chemical Physics* 19.15 (2017), pp. 9698–9723. DOI: [10.1039/C7CP00144D](https://doi.org/10.1039/C7CP00144D).

- [14] P. A. Hatherly, M. Stankiewicz, K. Codling, J. C. Creasey, H. M. Jones, and R. P. Tuckett. "A threshold electron analyser for use in coincidence experiments". In: *Measurement Science and Technology* 3.9 (1992), pp. 891–896. DOI: [10.1088/0957-0233/3/9/015](https://doi.org/10.1088/0957-0233/3/9/015).
- [15] G. A. Garcia, H. Soldi-Lose, and L. Nahon. "A versatile electron-ion coincidence spectrometer for photoelectron momentum imaging and threshold spectroscopy on mass selected ions using synchrotron radiation". In: *Review of Scientific Instruments* 80.2 (2009), p. 023102. DOI: [10.1063/1.3079331](https://doi.org/10.1063/1.3079331).
- [16] K. Mueller-Dethlefs, M. Sander, and E. W. Schlag. "Two-colour photoionization resonance spectroscopy of NO: Complete separation of rotational levels of NO⁺ at the ionization threshold". In: *Chemical Physics Letters* 112.4 (1984), pp. 291–294. DOI: [10.1016/0009-2614\(84\)85743-7](https://doi.org/10.1016/0009-2614(84)85743-7).
- [17] U. Hollenstein, H. Palm, and F. Merkt. "A broadly tunable extreme ultraviolet laser source with a 0.008 cm⁻¹ bandwidth". In: *Review of Scientific Instruments* 71.11 (2000), p. 4023. DOI: [10.1063/1.1310344](https://doi.org/10.1063/1.1310344).
- [18] U. Hollenstein, R. Seiler, H. Schmutz, M. Andrist, and F. Merkt. "Selective field ionization of high Rydberg states: Application to zero-kinetic-energy photoelectron spectroscopy". In: *The Journal of Chemical Physics* 115.12 (2001), pp. 5461–5469. DOI: [10.1063/1.1396856](https://doi.org/10.1063/1.1396856).
- [19] SOLEIL website. URL: <http://www.synchrotron-soleil.fr/SourceAccelerateur>.
- [20] L. Nahon, N. de Oliveira, G. A. Garcia, J.-F. Gil, B. Pilette, O. Marcouillé, B. Lagarde, and F. Polack. "DESIRS: a state-of-the-art VUV beamline featuring high resolution and variable polarization for spectroscopy and dichroism at SOLEIL". In: *Journal of Synchrotron Radiation* 19.4 (2012), pp. 508–520. DOI: [10.1107/S0909049512010588](https://doi.org/10.1107/S0909049512010588).
- [21] NIST website. URL: <https://webbook.nist.gov/chemistry/form-ser/>.
- [22] N. de Oliveira, M. Roudjane, D. Joyeux, D. Phalippou, J.-C. Rodier, and L. Nahon. "High-resolution broad-bandwidth Fourier-transform absorption spectroscopy in the VUV range down to 40 nm". In: *Nature Photonics* 5.3 (2011), pp. 149–153. DOI: [10.1038/nphoton.2010.314](https://doi.org/10.1038/nphoton.2010.314).
- [23] G. A. Garcia, X. Tang, J.-F. Gil, L. Nahon, M. Ward, S. Batut, C. Fittschen, C. A. Taatjes, D. L. Osborn, and J.-C. Loison. "Synchrotron-based double imaging photoelectron/photoion coincidence spectroscopy of radicals produced in a flow tube: OH and OD". In: *The Journal of Chemical Physics* 142.16 (2015), p. 164201. DOI: [10.1063/1.4918634](https://doi.org/10.1063/1.4918634).
- [24] G. A. Garcia, B. K. Cunha de Miranda, M. Tia, S. Daly, and L. Nahon. "DELICIOUS III: A multipurpose double imaging particle coincidence spectrometer for gas phase vacuum ultraviolet photodynamics studies". In: *Review of Scientific Instruments* 84.5 (2013), p. 53112. DOI: [10.1063/1.4807751](https://doi.org/10.1063/1.4807751).
- [25] X. Tang, G. A. Garcia, J.-F. Gil, and L. Nahon. "Vacuum upgrade and enhanced performances of the double imaging electron/ion coincidence end-station at the vacuum ultraviolet beamline DESIRS". In: *Review of Scientific Instruments* 86.12 (2015), p. 123108. DOI: [10.1063/1.4937624](https://doi.org/10.1063/1.4937624).
- [26] J. C. Pouilly et al. "Photoionization of 2-pyridone and 2-hydroxypyridine". In: *Physical Chemistry Chemical Physics* 12.14 (2010), pp. 3566–3572. DOI: [10.1039/B923630A](https://doi.org/10.1039/B923630A).

- [27] A. T. J. B. Eppink and D. H. Parker. "Velocity map imaging of ions and electrons using electrostatic lenses: Application in photoelectron and photofragment ion imaging of molecular oxygen". In: *Review of Scientific Instruments* 68.9 (1997), pp. 3477–3484. DOI: [10.1063/1.1148310](https://doi.org/10.1063/1.1148310).
- [28] P. Rupper and F. Merkt. "Intense narrow-bandwidth extreme ultraviolet laser system tunable up to 20 eV". In: *Review of Scientific Instruments* 75.3 (2004), pp. 613–622. DOI: [10.1063/1.1646744](https://doi.org/10.1063/1.1646744).
- [29] J. Sugar and A. Musgrove. "Energy levels of krypton, Kr I through Kr XXXVI". In: *Journal of Physical and Chemical Reference Data* 20.5 (1991), pp. 859–915. DOI: [10.1063/1.555896](https://doi.org/10.1063/1.555896).
- [30] C. J. Humphreys and E. Paul. "Interferometric wavelength determinations in the first spectrum of ^{136}Xe ". In: *Journal of the Optical Society of America* 60.10 (1970), p. 1302. DOI: [10.1364/JOSA.60.001302](https://doi.org/10.1364/JOSA.60.001302).
- [31] *Horiba website*. URL: <https://www.horiba.com>.
- [32] *Sirah website*. URL: <https://www.sirah.com>.
- [33] *High Finesse website*. URL: <https://www.highfinesse.com/>.
- [34] U. Hollenstein. "Erzeugung und spektroskopische Anwendungen von schmalbandiger kohaerenter, vakuum-ultravioletter Strahlung." In: *Dissertation ETH No. 15237* (2003).
- [35] H. Salami and A. J. Ross. "A molecular iodine atlas in ascii format". In: *Journal of Molecular Spectroscopy* 233.1 (2005), pp. 157–159. DOI: [10.1016/J.JMS.2005.06.002](https://doi.org/10.1016/J.JMS.2005.06.002).
- [36] *Hamamatsu website*. URL: <https://www.hamamatsu.com>.
- [37] *Amsterdam piezo valve website*. URL: <http://www.amsterdampiezovalve.com>.
- [38] G. Herzberg. *Spectra of Diatomic Molecules*. Vol. 1. 1950.
- [39] M. L. Zimmerman, M. G. Littman, M. M. Kash, and D. Kleppner. "Stark structure of the Rydberg states of alkali-metal atoms". In: *Physical Review A* 20.6 (1979), pp. 2251–2275. DOI: [10.1103/PhysRevA.20.2251](https://doi.org/10.1103/PhysRevA.20.2251).
- [40] F. Merkt, A. Osterwalder, R. Seiler, R. Signorell, H. Palm, H. Schmutz, and R. Gunzinger. "High Rydberg states of argon: Stark effect and field-ionization properties". In: *Journal of Physics B: Atomic, Molecular and Optical Physics* 31.8 (1998), pp. 1705–1724. DOI: [10.1088/0953-4075/31/8/020](https://doi.org/10.1088/0953-4075/31/8/020).
- [41] U. Hollenstein, R. Seiler, and F. Merkt. "Determination of the ionization energy of krypton by Rydberg-state-resolved threshold-ionization spectroscopy". In: *Journal of Physics B: Atomic, Molecular and Optical Physics* 36.5 (2003), pp. 893–903. DOI: [10.1088/0953-4075/36/5/309](https://doi.org/10.1088/0953-4075/36/5/309).
- [42] N. Lamarre, B. Gans, C. Alcaraz, B. Cunha de Miranda, J.-C. Guillemin, M. Broquier, J. Liévin, and S. Boyé-Péronne. "Vibronic structure of the $^2\Pi_u$ ground electronic state of dicyanoacetylene cation revisited by PFI-ZEKE photoelectron spectroscopy and ab initio calculations". In: *Molecular Physics* 113.24 (2015), pp. 3946–3954. DOI: [10.1080/00268976.2015.1075074](https://doi.org/10.1080/00268976.2015.1075074).
- [43] B. K. Cunha de Miranda. *Études de la photoionisation de radicaux et de réactions ion-molécule d'intérêt planétaire avec du rayonnement VUV synchrotron et laser*. Cotutelle PhD thesis of Paris-Sud University and Fluminense Federal University, 2011.

- [44] K. Watanabe, F. M. Matsunaga, and H. Sakai. "Absorption coefficient and photoionization yield of NO in the region 580-1350 Å". In: *Applied Optics* 6.3 (1967), p. 391. DOI: [10.1364/AO.6.000391](https://doi.org/10.1364/AO.6.000391).
- [45] L. G. Dodson, J. D. Savee, S. Gozem, L. Shen, A. I. Krylov, C. A. Taatjes, D. L. Osborn, and M. Okumura. "Vacuum ultraviolet photoionization cross section of the hydroxyl radical". In: *The Journal of Chemical Physics* 148.18 (2018), p. 184302. DOI: [10.1063/1.5024249](https://doi.org/10.1063/1.5024249).
- [46] O. J. Harper, M. Hassenfratz, J.-C. Loison, G. A. Garcia, N. de Oliveira, H. R. Hrodmarsson, S. T. Pratt, S. Boyé-Péronne, and B. Gans. "Quantifying the photoionization cross section of the hydroxyl radical". In: *The Journal of Chemical Physics* 150.14 (2019), p. 141103. DOI: [10.1063/1.5091966](https://doi.org/10.1063/1.5091966).
- [47] O. J. Harper, M. Hassenfratz, J.-C. Loison, G. A. Garcia, N. de Oliveira, H. R. Hrodmarsson, S. T. Pratt, S. Boyé-Péronne, and B. Gans. "Erratum: "Quantifying the photoionization cross section of the hydroxyl radical" [*J. Chem. Phys.* 150, 141103 (2019)]". In: *The Journal of Chemical Physics* 152.18 (2020), p. 189903. DOI: [10.1063/5.0010934](https://doi.org/10.1063/5.0010934).
- [48] H. R. Hrodmarsson, G. A. Garcia, L. Nahon, J.-C. Loison, and B. Gans. "The absolute photoionization cross section of the mercapto radical (SH) from threshold up to 15.0 eV". In: *Physical Chemistry Chemical Physics* (2019), pp. 25907–25915. DOI: [10.1039/C9CP05809E](https://doi.org/10.1039/C9CP05809E).
- [49] R. Flesch, M. C. Schürmann, J. Plenge, M. Hunnekuhl, H. Meiss, M. Bischof, and E. Rühl. "Absolute photoionization cross sections of the primary photofragments of chlorine dioxide and dichlorine monoxide". In: *Physical Chemistry Chemical Physics* 1.24 (1999), pp. 5423–5428. DOI: [10.1039/A905259C](https://doi.org/10.1039/A905259C).
- [50] L. G. Dodson, L. Shen, J. D. Savee, N. C. Eddingsaas, O. Welz, C. A. Taatjes, D. L. Osborn, S. P. Sander, and M. Okumura. "VUV photoionization cross sections of HO₂, H₂O₂, and H₂CO". In: *The Journal of Physical Chemistry A* 119.8 (2015), pp. 1279–1291. DOI: [10.1021/jp508942a](https://doi.org/10.1021/jp508942a).
- [51] V. A. Shubert and S. T. Pratt. "Photodissociation of Acetaldehyde and the Absolute Photoionization Cross Section of HCO". In: *The Journal of Physical Chemistry A* 114.42 (2010), pp. 11238–11243. DOI: [10.1021/jp102992b](https://doi.org/10.1021/jp102992b).
- [52] B. L. FitzPatrick, B. W. Alligood, L. J. Butler, S.-H. Lee, and J. J.-M. Lin. "Primary photodissociation pathways of epichlorohydrin and analysis of the C-C bond fission channels from an O(³P)+allyl radical intermediate". In: *The Journal of Chemical Physics* 133.9 (2010), p. 094306. DOI: [10.1063/1.3475001](https://doi.org/10.1063/1.3475001).
- [53] C. A. Taatjes, D. L. Osborn, T. M. Selby, G. Meloni, H. Fan, and S. T. Pratt. "Absolute photoionization cross-section of the methyl radical". In: *The Journal of Physical Chemistry A* 112.39 (2008), pp. 9336–9343. DOI: [10.1021/jp8022937](https://doi.org/10.1021/jp8022937).
- [54] J.-C. Loison. "Absolute Photoionization Cross Section of the Methyl Radical". In: *The Journal of Physical Chemistry A* 114.23 (2010), pp. 6515–6520. DOI: [10.1021/jp1024312](https://doi.org/10.1021/jp1024312).
- [55] B. Gans et al. "Determination of the absolute photoionization cross sections of CH₃ and I produced from a pyrolysis source, by combined synchrotron and vacuum ultraviolet laser studies". In: *The Journal of Physical Chemistry A* 114.9 (2010), pp. 3237–3246. DOI: [10.1021/jp909414d](https://doi.org/10.1021/jp909414d).

- [56] J. C. Robinson, N. E. Sveum, and D. M. Neumark. "Determination of absolute photoionization cross sections for vinyl and propargyl radicals". In: *The Journal of Chemical Physics* 119.11 (2003), pp. 5311–5314. DOI: [10.1063/1.1606440](https://doi.org/10.1063/1.1606440).
- [57] J. D. Savee, J. F. Lockyear, S. Borkar, A. J. Eskola, O. Welz, C. A. Taatjes, and D. L. Osborn. "Note: Absolute photoionization cross-section of the vinyl radical". In: *The Journal of Chemical Physics* 139.5 (2013), p. 056101. DOI: [10.1063/1.4817320](https://doi.org/10.1063/1.4817320).
- [58] B. L. FitzPatrick, M. Maienschein-Cline, L. J. Butler, S.-H. Lee, and J. J. Lin. "Determining the partial photoionization cross-sections of ethyl radicals". In: *The Journal of Physical Chemistry A* 111.49 (2007), pp. 12417–12422. DOI: [10.1021/jp073828h](https://doi.org/10.1021/jp073828h).
- [59] B. Gans, G. A. Garcia, S. Boyé-Péronne, J.-C. Loison, S. Douin, F. Gaie-Levrel, and D. Gauyacq. "Absolute photoionization cross section of the ethyl radical in the range 8 - 11.5 eV: Synchrotron and vacuum ultraviolet laser measurements". In: *The Journal of Physical Chemistry A* 115.21 (2011), pp. 5387–5396. DOI: [10.1021/jp202648m](https://doi.org/10.1021/jp202648m).
- [60] F. Holzmeier, I. Fischer, B. Kiendl, A. Krueger, A. Bodi, and P. Hemberger. "On the absolute photoionization cross section and dissociative photoionization of cyclopropenyli-dene". In: *Physical Chemistry Chemical Physics* 18 (13 2016), pp. 9240–9247. DOI: [10.1039/C6CP01068G](https://doi.org/10.1039/C6CP01068G).
- [61] J. D. Savee, S. Soorkia, O. Welz, T. M. Selby, C. A. Taatjes, and D. L. Osborn. "Absolute photoionization cross-section of the propargyl radical". In: *The Journal of Chemical Physics* 136.13 (2012), p. 134307. DOI: [10.1063/1.3698282](https://doi.org/10.1063/1.3698282).
- [62] H. Xu and S. T. Pratt. "Photoionization cross section of the propargyl radical and some general ideas for estimating radical cross sections". In: *The Journal of Physical Chemistry A* 117.39 (2013), pp. 9331–9342. DOI: [10.1021/jp309874q](https://doi.org/10.1021/jp309874q).
- [63] J. C. Robinson, N. E. Sveum, and D. M. Neumark. "Determination of absolute photoionization cross sections for isomers of C₃H₅: allyl and 2-propenyl radicals". In: *Chemical Physics Letters* 383.5 (2004), pp. 601–605. DOI: [10.1016/j.cplett.2003.11.075](https://doi.org/10.1016/j.cplett.2003.11.075).
- [64] H. R. Hrodmarsson, J.-C. Loison, U. Jacovella, D. M. P. Holland, S. Boyé-Péronne, B. Gans, G. A. Garcia, L. Nahon, and S. T. Pratt. "Valence-shell photoionization of C₄H₅: The 2-Butyn-1-yl Radical". In: *The Journal of Physical Chemistry A* 123.8 (2019), pp. 1521–1528. DOI: [10.1021/acs.jpca.8b11809](https://doi.org/10.1021/acs.jpca.8b11809).
- [65] N. E. Sveum, S. J. Goncher, and D. M. Neumark. "Determination of absolute photoionization cross sections of the phenyl radical". In: *Physical Chemistry Chemical Physics* 8.5 (2006), pp. 592–598. DOI: [10.1039/b513960k](https://doi.org/10.1039/b513960k).
- [66] H. Xu and S. T. Pratt. "Photodissociation of anisole and absolute photoionization cross-section of the phenoxy radical". In: *The Journal of Physical Chemistry A* 117.46 (2013), pp. 12075–12081. DOI: [10.1021/jp4047177](https://doi.org/10.1021/jp4047177).
- [67] J. M. Dyke, M. V. Ghosh, M. Goubet, E. P. F. Lee, G. Levita, K. Miqueu, and D. E. Shallcross. "A study of the atmospherically relevant reaction between molecular chlorine and dimethylsulfide (DMS): Establishing the reaction intermediate and measurement of absolute photoionization cross-sections". In: *Chemical Physics* (2006). DOI: [10.1016/j.chemphys.2005.11.045](https://doi.org/10.1016/j.chemphys.2005.11.045).
- [68] B. Gans. *Photolyse du méthane, application à l'atmosphère de Titan*. PhD thesis of Paris-Sud University, 2010.

- [69] F. J. Comes. "Recycling in the Earth's atmosphere: the OH radical - its importance for the chemistry of the atmosphere and the determination of its concentration". In: *Angewandte Chemie International Edition in English* 33.18 (1994), pp. 1816–1826. DOI: [10.1002/anie.199418161](https://doi.org/10.1002/anie.199418161).
- [70] V. G. Anicich. "An index of the literature for bimolecular gas phase cation-molecule reaction kinetics". In: *Jet Propulsion Laboratory Publication* 19 (2003).
- [71] M. Agúndez, E. Roueff, F. Le Petit, and J. Le Bourlot. "The chemistry of disks around T Tauri and Herbig Ae/Be stars". In: *Astronomy & Astrophysics* 616 (2018), A19. DOI: [10.1051/0004-6361/201732518](https://doi.org/10.1051/0004-6361/201732518).
- [72] P. M. Dehmer. "Photoionization of OH in the region 750 - 950 Å". In: *Chemical Physics Letters* 110.1 (1984), pp. 79–84. DOI: [10.1016/0009-2614\(84\)80150-5](https://doi.org/10.1016/0009-2614(84)80150-5).
- [73] J. N. Cutler, Z. X. He, and J. A. R. Samson. "Relative photoionization cross section study of OH and OD from 68 nm to 95 nm". In: *Journal of Physics B: Atomic, Molecular and Optical Physics* 28.21 (1995), p. 4577. DOI: [10.1088/0953-4075/28/21/007](https://doi.org/10.1088/0953-4075/28/21/007).
- [74] J. A. Stephens and V. McKoy. "Photoionization of the valence orbitals of OH". In: *The Journal of Chemical Physics* 88.3 (1988), pp. 1737–1742. DOI: [10.1063/1.454097](https://doi.org/10.1063/1.454097).
- [75] L. Veseth and H. P. Kelly. "Polarizabilities and photoionization cross sections of OH and HF". In: *Physical Review A* 45.7 (1992), pp. 4621–4630. DOI: [10.1103/PhysRevA.45.4621](https://doi.org/10.1103/PhysRevA.45.4621).
- [76] F. le Petit, C. Nehmé, J. Le Bourlot, and E. Roueff. "A model for atomic and molecular interstellar gas: The Meudon PDR code". In: *The Astrophysical Journal Supplement Series* 164.2 (2006), p. 506. DOI: [10.1086/503252](https://doi.org/10.1086/503252).
- [77] G. A. Garcia, B. Gans, X. Tang, M. Ward, S. Batut, L. Nahon, C. Fittschen, and J.-C. Loison. "Threshold photoelectron spectroscopy of the imidogen radical". In: *Journal of Electron Spectroscopy and Related Phenomena* 203 (2015), pp. 25–30. DOI: [10.1016/J.ELSPEC.2015.05.010](https://doi.org/10.1016/J.ELSPEC.2015.05.010).
- [78] C. E. Moore. *Tables of spectra of hydrogen, carbon, nitrogen, and oxygen atoms and ions*. CRC Press, 1993. ISBN: 0849374200.
- [79] R. T. Wiedmann, R. G. Tonkyn, M. G. White, K. Wang, and V. McKoy. "Rotationally resolved threshold photoelectron spectra of OH and OD". In: *The Journal of Chemical Physics* 97.2 (1992), pp. 768–772. DOI: [10.1063/1.463179](https://doi.org/10.1063/1.463179).
- [80] C. Lauzin, U. Jacovella, and F. Merkt. "Threshold ionization spectroscopy of H₂O, HDO and D₂O and low-lying vibrational levels of HDO⁺ and D₂O⁺". In: *Molecular physics* 113.24 (2015), pp. 3918–3924. DOI: [10.1080/00268976.2015.1049971](https://doi.org/10.1080/00268976.2015.1049971).
- [81] J.-H. Fillion, F. Dulieu, S. Baouche, J.-L. Lemaire, H. W. Jochims, and S. Leach. "Ionization yield and absorption spectra reveal superexcited Rydberg state relaxation processes in H₂O and D₂O". In: *Journal of Physics B: Atomic, Molecular and Optical Physics* 36.13 (2003), pp. 2767–2776. DOI: [10.1088/0953-4075/36/13/308](https://doi.org/10.1088/0953-4075/36/13/308).
- [82] G. C. Angel and J. A. R. Samson. "Total photoionization cross sections of atomic oxygen from threshold to 44.3 Å". In: *Physical Review A* 38.11 (1988), pp. 5578–5585. DOI: [10.1103/PhysRevA.38.5578](https://doi.org/10.1103/PhysRevA.38.5578).
- [83] J. Berkowitz. "Absolute photoionization cross sections of atomic oxygen". In: *Journal of Physics B: Atomic, Molecular and Optical Physics* 30.3 (1997), p. 583. DOI: [10.1088/0953-4075/30/3/014](https://doi.org/10.1088/0953-4075/30/3/014).

- [84] D. M. P. Holland, D. A. Shaw, S. M. McSweeney, M. A. MacDonald, A. Hopkirk, and M. A. Hayes. "A study of the absolute photoabsorption, photoionization and photodissociation cross sections and the photoionization quantum efficiency of oxygen from the ionization threshold to 490 Å". In: *Chemical Physics* 173.2 (1993), pp. 315–331. DOI: [10.1016/0301-0104\(93\)80148-3](https://doi.org/10.1016/0301-0104(93)80148-3).
- [85] C. M. Persson et al. "Nitrogen hydrides in interstellar gas". In: *Astronomy & Astrophysics* 521 (2010), p. L45. DOI: [10.1051/0004-6361/201015105](https://doi.org/10.1051/0004-6361/201015105).
- [86] E. F. van Dishoeck, D. J. Jansen, P. Schilke, and T. G. Phillips. "Detection of the interstellar NH₂ radical". In: *The Astrophysical Journal* 416 (1993), pp. L83–L86.
- [87] P. Swings, A. McKellar, and R. Minkowski. "Cometary emission spectra in the visual region." In: *Astrophysical Journal* 98 (1943), p. 142. DOI: [10.1086/144556](https://doi.org/10.1086/144556).
- [88] S. A. Sandford, P. P. Bera, T. J. Lee, C. K. Materese, and M. Nuevo. "Photosynthesis and photo-stability of nucleic acids in prebiotic extraterrestrial environments". In: *Photoinduced phenomena in nucleic acids II: DNA fragments and phenomenological aspects*. Ed. by Mario Barbatti, Antonio Carlos Borin, and Susanne Ullrich. Springer International Publishing, 2015, pp. 123–164. ISBN: 978-3-319-13272-3. DOI: [10.1007/128_2013_499](https://doi.org/10.1007/128_2013_499).
- [89] P. Ehrenfreund and S. B. Charnley. "Organic molecules in the interstellar medium, comets, and meteorites: A voyage from dark clouds to the early Earth". In: *Annual Review of Astronomy & Astrophysics* 38.1 (2000), pp. 427–483. DOI: [10.1146/annurev.astro.38.1.427](https://doi.org/10.1146/annurev.astro.38.1.427).
- [90] S. T. Gibson, J. P. Greene, and J. Berkowitz. "Photoionization of the amidogen radical". In: *The Journal of Chemical Physics* 83.9 (1985), pp. 4319–4328. DOI: [10.1063/1.449045](https://doi.org/10.1063/1.449045).
- [91] M. Rubin et al. "Molecular nitrogen in comet 67P/Churyumov-Gerasimenko indicates a low formation temperature". In: *Science* 348.6231 (2015), pp. 232–235. DOI: [10.1126/science.aaa6100](https://doi.org/10.1126/science.aaa6100).
- [92] S. J. Dunlavey, J. M. Dyke, N. Jonathan, and A. Morris. "Vacuum ultraviolet photoelectron spectroscopy of transient species". In: *Molecular Physics* 39.5 (1980), pp. 1121–1135. DOI: [10.1080/00268978000100931](https://doi.org/10.1080/00268978000100931).
- [93] S. Willitsch, C. Jungen, and F. Merkt. "Bending energy level structure and quasilinearity of the $\tilde{X}^+ \ ^3B_1$ ground electronic state of NH₂⁺". In: *The Journal of Chemical Physics* 124.20 (2006), p. 204312. DOI: [10.1063/1.2193519](https://doi.org/10.1063/1.2193519).
- [94] R. Seiler, U. Hollenstein, T. P. Softley, and F. Merkt. "High-resolution threshold-ionization spectroscopy of NH₃". In: *The Journal of Chemical Physics* 118.22 (2003), pp. 10024–10033. DOI: [10.1063/1.1571528](https://doi.org/10.1063/1.1571528).
- [95] J. Berkowitz. "Experimental potential energy curves for X ²Π and ²Σ⁺ states of HF⁺". In: *Chemical Physics Letters* 11.1 (1971), pp. 21–26. DOI: [10.1016/0009-2614\(71\)80522-5](https://doi.org/10.1016/0009-2614(71)80522-5).
- [96] F. Merkt and T. P. Softley. "Rotationally resolved zero-kinetic-energy photoelectron spectrum of nitrogen". In: *Physical Review A* 46.1 (1992), pp. 302–314. DOI: [10.1103/PhysRevA.46.302](https://doi.org/10.1103/PhysRevA.46.302).
- [97] G. Reiser, W. Habenicht, K. Müller-Dethlefs, and E. W. Schlag. "The ionization energy of nitric oxide". In: *Chemical Physics Letters* 152.2 (1988), pp. 119–123. DOI: [10.1016/0009-2614\(88\)87340-8](https://doi.org/10.1016/0009-2614(88)87340-8).
- [98] R. G. Tonkyn, J. W. Winniczek, and M. G. White. "Rotationally resolved photoionization of O₂⁺ near threshold". In: *Chemical Physics Letters* 164.2 (1989), pp. 137–142. DOI: [10.1016/0009-2614\(89\)85005-5](https://doi.org/10.1016/0009-2614(89)85005-5).

- [99] J. A. R. Samson, G. N. Haddad, and L. D. Kilcoyne. "Absorption and dissociative photoionization cross sections of NH_3 from 80 to 1120 Å". In: *The Journal of Chemical Physics* 87.11 (1987), pp. 6416–6422. DOI: [10.1063/1.453472](https://doi.org/10.1063/1.453472).
- [100] G. R. Burton, W. F. Chan, G. Cooper, and C. E. Brion. "Absolute oscillator strengths for photoabsorption (6-360 eV) and ionic photofragmentation (10-80 eV) of methanol". In: *Chemical Physics* 167.3 (1992), pp. 349–367. DOI: [10.1016/0301-0104\(92\)80208-D](https://doi.org/10.1016/0301-0104(92)80208-D).
- [101] W. F. Chan, G. Cooper, and C. E. Brion. "Absolute optical oscillator strengths for discrete and continuum photoabsorption of carbon monoxide (7-200 eV) and transition moments for the $X^1\Sigma^+ \rightarrow A^1\Pi$ system". In: *Chemical Physics* 170.1 (1993), pp. 123–138. DOI: [10.1016/0301-0104\(93\)80098-T](https://doi.org/10.1016/0301-0104(93)80098-T).
- [102] W. F. Chan, G. Cooper, and C. E. Brion. "Absolute optical oscillator strengths (11–20 eV) and transition moments for the photoabsorption of molecular hydrogen in the Lyman and Werner bands". In: *Chemical physics* 168.2-3 (1992), pp. 375–388. DOI: [10.1016/0301-0104\(92\)87171-5](https://doi.org/10.1016/0301-0104(92)87171-5).
- [103] C. Mendoza. "Results from the opacity project and TOP base". In: *Physica Scripta* T65 (1996), pp. 198–206. DOI: [10.1088/0031-8949/1996/t65/030](https://doi.org/10.1088/0031-8949/1996/t65/030).
- [104] B. Dill, B. Hildebrandt, H. Vanni, and H. Heydtmann. "Infrared chemiluminescence in the reactions of atomic fluorine with ethanol, propanol-(2) and some deuterated analogs". In: *Chemical Physics* 58.2 (1981), pp. 163–174. DOI: [10.1016/0301-0104\(81\)80053-5](https://doi.org/10.1016/0301-0104(81)80053-5).
- [105] K. A. G. Macneil and R. N. Dixon. "High-resolution photoelectron spectroscopy of methanol and its deuterated derivatives: Internal rotation in the ground ionic state". In: *Journal of Electron Spectroscopy and Related Phenomena* 11.3 (1977), pp. 315–331. DOI: [10.1016/0368-2048\(77\)80007-8](https://doi.org/10.1016/0368-2048(77)80007-8).
- [106] B. Ruscic and J. Berkowitz. "Photoionization mass spectrometric studies of the isomeric transient species CD_2OH and CD_3O ". In: *The Journal of Chemical Physics* 95.6 (1991), pp. 4033–4039. DOI: [10.1063/1.460758](https://doi.org/10.1063/1.460758).
- [107] B. Niu, D. A. Shirley, and Y. Bai. "High resolution photoelectron spectroscopy and femtosecond intramolecular dynamics of H_2CO^+ and D_2CO^+ ". In: *The Journal of Chemical Physics* 98.6 (1993), pp. 4377–4390. DOI: [10.1063/1.464999](https://doi.org/10.1063/1.464999).
- [108] L. Koziol, V. A. Mozhayskiy, B. J. Braams, J. M. Bowman, and A. I. Krylov. "Ab initio calculation of the photoelectron spectra of the hydroxycarbene diradicals". In: *The Journal of Physical Chemistry A* 113.27 (2009), pp. 7802–7809. DOI: [10.1021/jp903476w](https://doi.org/10.1021/jp903476w).
- [109] J. M. Dyke. "Properties of gas-phase ions. Information to be obtained from photoelectron spectroscopy of unstable molecules". In: *Journal of the Chemical Society, Faraday Transactions 2* 83.1 (1987), pp. 69–87. DOI: [10.1039/F29878300069](https://doi.org/10.1039/F29878300069).
- [110] *Sigma-Aldrich website*. URL: <https://www.sigmaaldrich.com/>.
- [111] J. Berkowitz. "Photoionization of CH_3OH , CD_3OH , and CH_3OD : Dissociative ionization mechanisms and ionic structures". In: *The Journal of Chemical Physics* 69.7 (1978), pp. 3044–3054. DOI: [10.1063/1.436995](https://doi.org/10.1063/1.436995).
- [112] W. Kong, D. Rodgers, J. W. Hepburn, K. Wang, and V. McKoy. "Pulsed-field ionization threshold photoelectron spectroscopy with coherent extreme ultraviolet radiation: A comparison of CO and N_2 ". In: *The Journal of Chemical Physics* 99.5 (1993), pp. 3159–3165. DOI: [10.1063/1.465176](https://doi.org/10.1063/1.465176).

- [113] W. Tao, R. B. Klemm, F. L. Nesbitt, and L. J. Stief. "A discharge flow-photoionization mass spectrometric study of hydroxymethyl radicals (H_2COH and H_2COD): photoionization spectrum and ionization energy". In: *The Journal of Physical Chemistry* 96.1 (1992), pp. 104–107. DOI: [10.1021/j100180a023](https://doi.org/10.1021/j100180a023).
- [114] S.-C. Kuo, Z. Zhang, R. B. Klemm, J. F. Liebman, L. J. Stief, and F. L. Nesbitt. "Photoionization of hydroxymethyl (CD_2OH and CD_2OD) and methoxy (CD_3O) radicals: Photoion efficiency spectra, ionization energies, and thermochemistry". In: *The Journal of Physical Chemistry* 98.15 (1994), pp. 4026–4033. DOI: [10.1021/j100066a021](https://doi.org/10.1021/j100066a021).
- [115] R. D. Bowen and A. Maccoll. "Low energy, low temperature mass spectra of some small saturated alcohols and ethers". In: *Organic Mass Spectrometry* 19.8 (1984), pp. 379–384. DOI: [10.1002/oms.1210190806](https://doi.org/10.1002/oms.1210190806).
- [116] E. Assaf, C. Schoemaeker, L. Vereecken, and C. Fittschen. "The reaction of fluorine atoms with methanol: yield of $\text{CH}_3\text{O}/\text{CH}_2\text{OH}$ and rate constant of the reactions CH_3O^+ CH_3O and CH_3O^+ HO_2 ". In: *Physical Chemistry Chemical Physics* 20.16 (2018), pp. 10660–10670. DOI: [10.1002/kin.21191](https://doi.org/10.1002/kin.21191).
- [117] P. Warneck. "Photoionisation von Methanol und Formaldehyd / Photoionisation of Methanol and Formaldehyd". In: *Zeitschrift für Naturforschung A* 26.12 (1971), pp. 2047–2057. DOI: [10.1515/zna-1971-1214](https://doi.org/10.1515/zna-1971-1214).
- [118] B. Ruscic and D. H. Bross. *Active Thermochemical Tables (ATcT) values based on ver. 1.122g of the Thermochemical Network, Argonne National Laboratory (2019); available at ATcT.anl.gov*. 2019. URL: <https://atct.anl.gov/>.
- [119] K. Wang, J. A. Stephens, and V. McKoy. "Non-F-Condon effects in photoionization of the $3^3\Pi$ Rydberg state of NH ". In: *The Journal of Chemical Physics* 93.11 (1990), pp. 7874–7882. DOI: [10.1063/1.459369](https://doi.org/10.1063/1.459369).
- [120] B. Gans, S. Hartweg, G. A. Garcia, S. Boyé-Péronne, O. J. Harper, J.-C. Guillemin, and J.-C. Loison. "VUV photoionization of the CH_2NC radical: adiabatic ionization energy and cationic vibrational mode wavenumber determinations". In: *Physical Chemistry Chemical Physics* 20 (2020), pp. 12496–12501. DOI: [10.1039/D0CP01901A](https://doi.org/10.1039/D0CP01901A).
- [121] D. T. Halfen, V. V. Ilyushin, and L. M. Ziurys. "Interstellar detection of methyl isocyanate CH_3NCO in Sgr B2(N): A link from molecular clouds to comets". In: *The Astrophysical Journal Letters* 812.1 (2015), p. L5. DOI: [10.1088/2041-8205/812/1/L5](https://doi.org/10.1088/2041-8205/812/1/L5).
- [122] J. Cernicharo et al. "A rigorous detection of interstellar CH_3NCO : An important missing species in astrochemical networks". In: *Astronomy & Astrophysics* 587 (2016), p. L4. DOI: [10.1051/0004-6361/201527531](https://doi.org/10.1051/0004-6361/201527531).
- [123] S. Dalbouha, M. L. Senent, N. Komaha, and R. Domínguez-Gómez. "Structural and spectroscopic characterization of methyl isocyanate, methyl cyanate, methyl fulminate, and acetonitrile N-oxide using highly correlated *ab initio* methods". In: *The Journal of Chemical Physics* 145.12 (2016), p. 124309. DOI: [10.1063/1.4963186](https://doi.org/10.1063/1.4963186).
- [124] J. Koput. "Methyl isocyanate: An analysis of the low- J rotational spectrum using the quasi-symmetric top molecule approach". In: *Journal of Molecular Spectroscopy* 106.1 (1984), pp. 12–21. DOI: [10.1016/0022-2852\(84\)90078-X](https://doi.org/10.1016/0022-2852(84)90078-X).
- [125] R. F. Curl Jr., V. M. Rao, K. V. L. N. Sastry, and J. A. Hodgeson. "Microwave spectrum of methyl isocyanate". In: *The Journal of Chemical Physics* 39.12 (1963), pp. 3335–3340. DOI: [10.1063/1.1734198](https://doi.org/10.1063/1.1734198).

- [126] J. Koput. "Characteristic patterns in microwave spectra of quasi-symmetric top molecules of the WH_3XYZ type". In: *Journal of Molecular Spectroscopy* 118.2 (1986), pp. 448–458. DOI: [10.1016/0022-2852\(86\)90181-5](https://doi.org/10.1016/0022-2852(86)90181-5).
- [127] D. W. W. Anderson, D. W. H. Rankin, and A. Robertson. "Electron diffraction determination of the molecular structures of methylazide, methylisocyanate and methylisothiocyanate in the gas phase". In: *Journal of Molecular Structure* 14.3 (1972), pp. 385–396. DOI: [10.1016/0022-2860\(72\)85186-X](https://doi.org/10.1016/0022-2860(72)85186-X).
- [128] M. Kręglewski. "Methyl isothiocyanate as a quasi-symmetric top. A reinterpretation of the microwave spectrum". In: *Chemical Physics Letters* 112.3 (1984), pp. 275–278. DOI: [10.1016/0009-2614\(84\)80549-7](https://doi.org/10.1016/0009-2614(84)80549-7).
- [129] T. Pasinszki and N. P. C. Westwood. "He I photoelectron, photoionization mass spectroscopy, mid-infrared, and *ab Initio* study of the unstable CH_3OCN Molecule". In: *The Journal of Physical Chemistry* 99.6 (1995), pp. 1649–1654. DOI: [10.1021/j100006a005](https://doi.org/10.1021/j100006a005).
- [130] T. Pasinszki, T. Veszprèmi, M. Fehèr, B. Kovac, L. Klasinc, and S. P. Mcglynn. "The photoelectron spectra of methyl pseudohalides". In: *International Journal of Quantum Chemistry* 44.S26 (1992), pp. 443–453. DOI: [10.1002/qua.560440840](https://doi.org/10.1002/qua.560440840).
- [131] J. H. D. Eland. "The photoelectron spectra of isocyanic acid and related compounds". In: *Philosophical Transactions of the Royal Society A: Mathematical, Physical and Engineering Sciences* 268.1184 (1970), pp. 87–96. DOI: [10.1098/rsta.1970.0063](https://doi.org/10.1098/rsta.1970.0063).
- [132] S. Cradock, E. A. V. Ebsworth, and J. D. Murdoch. "Photoelectron spectra of some group 4 pseudohalides and related compounds". In: *Journal of the Chemical Society, Faraday Transactions 2* 68.0 (1972), pp. 86–100. DOI: [10.1039/F29726800086](https://doi.org/10.1039/F29726800086).
- [133] D. Lide. *Handbook of Chemistry and Physics*. 1992.
- [134] O. J. Harper, L. H. Coudert, J.-C. Loison, B. Gans, S. Douin, G. A. Garcia, J.-C. Guillemin, and S. Boyé-Péronne. "Quasi-symmetry effects in the threshold photoelectron spectrum of methyl isocyanate". In: *The Journal of Chemical Physics* 153.7 (2020), p. 074308. DOI: [10.1063/5.0017753](https://doi.org/10.1063/5.0017753).
- [135] W. E. Bright. *Molecular Vibrations*. New York: McGraw-Hill, 1955.
- [136] D. Lauvergnat, A. Nauts, Y. Justum, and X. Chapuisat. "A harmonic adiabatic approximation to calculate highly excited vibrational levels of 'floppy molecules'". In: *The Journal of Chemical Physics* 114.15 (2001), pp. 6592–6604. DOI: [10.1063/1.1350904](https://doi.org/10.1063/1.1350904).
- [137] W. H. Wollaston. "XII. A method of examining refractive and dispersive powers, by prismatic reflection". In: *Philosophical Transactions of the Royal Society of London* 92 (1802), pp. 365–380. DOI: [10.1098/rstl.1802.0014](https://doi.org/10.1098/rstl.1802.0014).
- [138] A. G. Gaydon. *The Spectroscopy of Flames*. Ed. by T & A Constable Ltd. second edi. Springer, Dordrecht, 1974. DOI: [10.1007/978-94-009-5720-6](https://doi.org/10.1007/978-94-009-5720-6).
- [139] G. B. Donati. "Schreiben des Herrn Prof. Donati an den Herausgeber". In: *Astronomische Nachrichten* 62 (1864), p. 375.
- [140] M. Elyajouri, R. Lallement, N. L. J. Cox, J. Cami, M. A. Cordiner, J. V. Smoker, A. Fahrang, P. J. Sarre, and H. Linnartz. "The EDIBLES survey - III. C_2 -DIBs and their profiles". In: *Astronomy & Astrophysics* 616 (2018), A143. DOI: [10.1051/0004-6361/201833105](https://doi.org/10.1051/0004-6361/201833105).
- [141] M. Nakajima, A. Matsugi, and A. Miyoshi. "Mechanism and kinetic isotope effect of the reaction of $\text{C}_2(\text{X}^1\Sigma_g^+)$ radicals with H_2 and D_2 ". In: *The Journal of Physical Chemistry A* 113.31 (2009), pp. 8963–8970. DOI: [10.1021/jp904165s](https://doi.org/10.1021/jp904165s).

- [142] R. Hoffmann. "Marginalia: C₂ in all its guises". In: *American Scientist* 83.4 (1995), pp. 309–311.
- [143] J. D. Watts and R. J. Bartlett. "Coupled-cluster calculations on the C₂ molecule and the C₂⁺ and C₂⁻ molecular ions". In: *The Journal of Chemical Physics* 96.8 (1992), pp. 6073–6084. DOI: [10.1063/1.462649](https://doi.org/10.1063/1.462649).
- [144] D. Toffoli and R. R. Lchese. "Near threshold photoionization of the ground and first excited states of C₂". In: *The Journal of Chemical Physics* 120.13 (2004), pp. 6010–6018. DOI: [10.1063/1.1651477](https://doi.org/10.1063/1.1651477).
- [145] O. Krechkivska, G. B. Bacskay, B. A. Welsh, K. Nauta, S. H. Kable, J. F. Stanton, and T. W. Schmidt. "The ionization energy of C₂". In: *The Journal of Chemical Physics* 144.14 (2016), p. 144305. DOI: [10.1063/1.4944932](https://doi.org/10.1063/1.4944932).
- [146] W. Chen, K. Kawaguchi, P. F. Bernath, and J. Tang. "Simultaneous analysis of the Ballik-Ramsay and Phillips systems of C₂ and observation of forbidden transitions between singlet and triplet states". In: *The Journal of Chemical Physics* 142.6 (2015), p. 064317. DOI: [10.1063/1.4907530](https://doi.org/10.1063/1.4907530).
- [147] O. J. Harper, S. Boyé-Péronne, G. A. Garcia, H. R. Hrodmarsson, J.-C. Loison, and B. Gans. "To see C₂: Single-photon ionization of the dicarbon molecule". In: *The Journal of Chemical Physics* 152.4 (2020), p. 041105. DOI: [10.1063/1.5139309](https://doi.org/10.1063/1.5139309).
- [148] B. Gans, F. Holzmeier, J. Krueger, C. Falvo, A. Roeder, A. Lopes, G. A. Garcia, C. Fittschen, J.-C. Loison, and C. Alcaraz. "Synchrotron-based valence shell photoionization of CH radical". In: *The Journal of Chemical Physics* 144 (May 2016), p. 204307. DOI: [10.1063/1.4950880](https://doi.org/10.1063/1.4950880).
- [149] L. Coudert, B. Gans, F. Holzmeier, J.-C. Loison, G. Garcia, C. Alcaraz, A. Lopes, and A. Roeder. "Experimental and theoretical threshold photoelectron spectra of methylene". In: *The Journal of Chemical Physics* 149 (Dec. 2018), p. 224304. DOI: [10.1063/1.5062834](https://doi.org/10.1063/1.5062834).
- [150] B. Gans, G. Garcia, F. Holzmeier, J. Krueger, A. Roeder, A. Lopes, C. Fittschen, J.-C. Loison, and C. Alcaraz. "Communication: On the first ionization threshold of the C₂H radical". In: *The Journal of Chemical Physics* 146 (Jan. 2017), p. 011101. DOI: [10.1063/1.4973383](https://doi.org/10.1063/1.4973383).
- [151] G. Garcia, B. Gans, J. Krueger, F. Holzmeier, A. Roeder, A. Lopes, C. Fittschen, C. Alcaraz, and J.-C. Loison. "Valence shell threshold photoelectron spectroscopy of the C₃H_x (x=0-3)". In: *Physical Chemistry Chemical Physics* 20 (Feb. 2018), pp. 8707–8718. DOI: [10.1039/C8CP00510A](https://doi.org/10.1039/C8CP00510A).
- [152] C. E. H. Dessent, S. R. Haines, and K. Mueller-Dethlefs. "A new detection scheme for synchronous, high resolution ZEKE and MATI spectroscopy demonstrated on the Phenol-Ar complex". In: *Chemical Physics Letters* 315.1 (1999), pp. 103–108. DOI: [10.1016/S0009-2614\(99\)01193-8](https://doi.org/10.1016/S0009-2614(99)01193-8).
- [153] R. J. Damburg and V. V. Kolosov. "A hydrogen atom in a uniform electric field. III". In: *Journal of Physics B: Atomic and Molecular Physics* 12.16 (1979), pp. 2637–2643. DOI: [10.1088/0022-3700/12/16/011](https://doi.org/10.1088/0022-3700/12/16/011).
- [154] U. Hollenstein, K. Dulitz, and F. Merkt. "The adiabatic ionisation energy of CO₂". In: *Molecular Physics* 117.21 (2019), pp. 2956–2960. DOI: [10.1080/00268976.2019.1600061](https://doi.org/10.1080/00268976.2019.1600061).

- [155] G. W. Fox, O. S. Duffendack, and E. F. Barker. "The spectrum of CO_2 ". In: *Proceedings of the National Academy of Sciences of the United States of America* 13.5 (1927), p. 302. DOI: [10.1073/pnas.13.5.302](https://doi.org/10.1073/pnas.13.5.302).
- [156] R. Renner. "Zur Theorie der Wechselwirkung zwischen Elektronen- und Kernbewegung bei dreiatomigen, stabförmigen Molekülen". In: *Zeitschrift für Physik* 92.3-4 (1934), pp. 172–193. DOI: [10.1007/BF01350054](https://doi.org/10.1007/BF01350054).
- [157] D. Gauyacq, M. Horani, S. Leach, and J. Rostas. "The emission spectrum of the CO_2^+ ion: band system". In: *Canadian Journal of Physics* 53.19 (1975), pp. 2040–2059. DOI: [10.1139/p75-255](https://doi.org/10.1139/p75-255).
- [158] D. Gauyacq, C. Larcher, and J. Rostas. "The emission spectrum of the CO_2^+ ion: Rovibronic analysis of the band system". In: *Canadian Journal of Physics* 57.10 (1979), pp. 1634–1649. DOI: [10.1139/p79-227](https://doi.org/10.1139/p79-227).
- [159] T. J. Sears. "Observation of the ν_2 band of CO_2^+ by diode laser absorption". In: *Molecular Physics* 59.2 (1986), pp. 259–274. DOI: [10.1080/00268978600102061](https://doi.org/10.1080/00268978600102061).
- [160] I. Suzuki. "General anharmonic force constants of carbon dioxide". In: *Journal of Molecular Spectroscopy* 25.4 (1968), pp. 479–500. DOI: [10.1016/S0022-2852\(68\)80018-9](https://doi.org/10.1016/S0022-2852(68)80018-9).
- [161] C. Larcher, D. Gauyacq, and J. Rostas. "The emission spectrum of the CO_2^+ ion: fermi resonance between the 100 and 020 levels of the $\tilde{X}^2\Pi_g$ ground state of $^{12}\text{CO}_2^+$ and $^{13}\text{CO}_2^+$ ions". In: *Journal de Chimie Physique* 77 (1980), pp. 661–665. DOI: [10.1051/jcp/1980770655](https://doi.org/10.1051/jcp/1980770655).
- [162] K. Kawaguchi, C. Yamada, and E. Hirota. "Diode laser spectroscopy of the CO_2^+ ν_3 band using magnetic field modulation of the discharge plasma". In: *The Journal of Chemical Physics* 82.3 (1985), pp. 1174–1177. DOI: [10.1063/1.448489](https://doi.org/10.1063/1.448489).
- [163] J. M. Frye and T. J. Sears. "Measurement of the Renner-Teller effect in $X^2\Pi$ CO_2^+ by diode laser absorption". In: *Molecular Physics* 62.4 (1987), pp. 919–937. DOI: [10.1080/00268978700102671](https://doi.org/10.1080/00268978700102671).
- [164] F. Merkt, S. R. Mackenzie, R. J. Rednall, and T. P. Softley. "Zero-kinetic-energy photoelectron spectrum of carbon dioxide". In: *The Journal of Chemical Physics* 99.11 (1993), pp. 8430–8439. DOI: [10.1063/1.466212](https://doi.org/10.1063/1.466212).
- [165] R. T. Wiedmann, M. G. White, H. Lefebvre-Brion, and C. Cossart-Magos. "Rotational analysis of the threshold photoelectron spectra of room temperature and jet-cooled CO_2 ". In: *The Journal of Chemical Physics* 103.24 (1995), pp. 10417–10423. DOI: [10.1063/1.469890](https://doi.org/10.1063/1.469890).
- [166] J. Liu, W. Chen, C.-W. Hsu, M. Hochlaf, M. Evans, S. Stimson, and C. Y. Ng. "High resolution pulsed field ionization-photoelectron study of $\text{CO}_2^+(X^2\Pi_g)$ in the energy range of 13.6–14.7 eV". In: *The Journal of Chemical Physics* 112.24 (2000), pp. 10767–10777. DOI: [10.1063/1.481721](https://doi.org/10.1063/1.481721).
- [167] W. A. Chupka. "Factors affecting lifetimes and resolution of Rydberg states observed in zero-electron-kinetic-energy spectroscopy". In: *The Journal of Chemical Physics* 98.6 (1993), pp. 4520–4530. DOI: [10.1063/1.465011](https://doi.org/10.1063/1.465011).
- [168] J. T. Hougen. "Rotational energy levels of a linear triatomic molecule in a $^2\Pi$ electronic state". In: *The Journal of Chemical Physics* 36.2 (1962), pp. 519–534. DOI: [10.1063/1.1732544](https://doi.org/10.1063/1.1732544).
- [169] J. A. Pople. "The Renner effect and spin-orbit coupling". In: *Molecular Physics* 3.1 (1960), pp. 16–22. DOI: [10.1080/00268976000100021](https://doi.org/10.1080/00268976000100021).

- [170] J. M. Brown. "The effective Hamiltonian for the Renner-Teller effect". In: *Journal of Molecular Spectroscopy* 68.3 (1977), pp. 412–422. DOI: [10.1016/0022-2852\(77\)90245-4](https://doi.org/10.1016/0022-2852(77)90245-4).
- [171] G. Guelachvili. "High-resolution Fourier spectra of carbon dioxide and three of its isotopic species near 4.3 μm ". In: *Journal of Molecular Spectroscopy* 79.1 (1980), pp. 72–83. DOI: [10.1016/0022-2852\(80\)90293-3](https://doi.org/10.1016/0022-2852(80)90293-3).
- [172] J. Xie and R. N. Zare. "Selection rules for the photoionization of diatomic molecules". In: *The Journal of Chemical Physics* 93.5 (1990), pp. 3033–3038. DOI: [10.1063/1.458837](https://doi.org/10.1063/1.458837).
- [173] S. Willitsch and F. Merkt. "Rovibronic photoionization dynamics of asymmetric-top molecules". In: *International Journal of Mass Spectrometry* 245.1 (2005), pp. 14–25. DOI: [10.1016/j.ijms.2005.06.004](https://doi.org/10.1016/j.ijms.2005.06.004).
- [174] E. Klisch, T. Klaus, S. P. Belov, G. Winnewisser, and E. Herbst. "Laboratory rotational spectrum of CN in the 1 THz region." In: *Astronomy & Astrophysics* 304 (1995), p. L5.
- [175] J. T. Hougen. "Fermi resonance in linear triatomic molecules in Π electronic states". In: *The Journal of Chemical Physics* 37.2 (1962), pp. 403–408. DOI: [10.1063/1.1701334](https://doi.org/10.1063/1.1701334).
- [176] D. Gauyacq and C. Jungen. "Orbital angular momentum in triatomic molecules". In: *Molecular Physics* 41.2 (1980), pp. 383–407. DOI: [10.1080/00268978000102841](https://doi.org/10.1080/00268978000102841).
- [177] *Korth website*. URL: <https://www.korth.de>.
- [178] A. C. Cheung, D. M. Rank, C. H. Townes, D. D. Thornton, and W. J. Welch. "Detection of NH_3 Molecules in the Interstellar Medium by Their Microwave Emission". In: *Physical Review Letters* 21 (25 1968), pp. 1701–1705. DOI: [10.1103/PhysRevLett.21.1701](https://doi.org/10.1103/PhysRevLett.21.1701).
- [179] J. A. Kaye and D. F. Strobel. "Formation and photochemistry of methylamine in Jupiter's atmosphere". In: *Icarus* 55.3 (1983), pp. 399–419. DOI: [10.1016/0019-1035\(83\)90111-2](https://doi.org/10.1016/0019-1035(83)90111-2).
- [180] V. Krasnopolsky. "Observation of DCI and upper limit to NH_3 on Venus". In: *Icarus* 219.1 (2012), pp. 244–249. DOI: [10.1016/j.icarus.2012.02.036](https://doi.org/10.1016/j.icarus.2012.02.036).
- [181] Delorme, P. et al. "CFBDS J005910.90-011401.3: reaching the T-Y brown dwarf transition?" In: *Astronomy & Astrophysics* 482.3 (2008), pp. 961–971. DOI: [10.1051/0004-6361/20079317](https://doi.org/10.1051/0004-6361/20079317).
- [182] Y. Ao, C. Henkel, J. A. Braatz, A. Weiß, K. M. Menten, and S. Mühle. "Ammonia (J, K)=(1, 1) to (4, 4) and (6, 6) inversion lines detected in the Seyfert 2 galaxy NGC 1068". In: *Astronomy & Astrophysics* 529 (2011), A154. DOI: [10.1051/0004-6361/201116595](https://doi.org/10.1051/0004-6361/201116595).
- [183] M. N. R. Ashfold, C. L. Bennett, and R. N. Dixon. "Predissociation dynamics of \tilde{A} -state ammonia probed by two-photon excitation spectroscopy". In: *Chemical Physics* 93.2 (1985), pp. 293–306. DOI: [10.1016/0301-0104\(85\)80026-4](https://doi.org/10.1016/0301-0104(85)80026-4).
- [184] M. N. R. Ashfold, R. N. Dixon, S. J. Irving, H.-M. Koeppe, W. Meier, J. R. Nightingale, L. Schnieder, and K. H. Welge. "Stereochemical and Angular Momentum Constraints in the Photodissociation of Ammonia". In: *Philosophical Transactions of the Royal Society of London A: Mathematical, Physical and Engineering Sciences* 332.1625 (1990), pp. 375–386. DOI: [10.1098/rsta.1990.0121](https://doi.org/10.1098/rsta.1990.0121).
- [185] K. L. Wells, G. Perriam, and V. G. Stavros. "Time-resolved velocity map ion imaging study of NH_3 photodissociation". In: *The Journal of Chemical Physics* 130.7 (2009), p. 74308. DOI: [10.1063/1.3072763](https://doi.org/10.1063/1.3072763).

- [186] A. Bach, J. M. Hutchison, R. J. Holiday, and F. F. Crim. "Competition between adiabatic and nonadiabatic pathways in the photodissociation of vibrationally excited ammonia". In: *The Journal of Physical Chemistry A* 107.49 (2003), pp. 10490–10496. DOI: [10.1021/jp027396g](https://doi.org/10.1021/jp027396g).
- [187] N. Walsh, A. Sankari, J. Laksman, T. Andersson, S. Oghbaie, F. Afaneh, E. P. Mansson, M. Gisselbrecht, and S. L. Sorensen. "Molecular dynamics of NH₃ induced by core-electron excitation". In: *Physical Chemistry Chemical Physics* 17.29 (2015), pp. 18944–18952. DOI: [10.1039/C5CP02959G](https://doi.org/10.1039/C5CP02959G).
- [188] D. H. Mordaunt, M. N. R. Ashfold, and R. N. Dixon. "Photodissociation dynamics of \tilde{A} state ammonia molecules. I. State dependent μ -v correlations in the NH₂(ND₂) products". In: *The Journal of Chemical Physics* 104.17 (1996), pp. 6460–6471. DOI: [10.1063/1.471367](https://doi.org/10.1063/1.471367).
- [189] M. L. Hause, Y. H. Yoon, and F. F. Crim. "Vibrationally mediated photodissociation of ammonia: product angular distributions from adiabatic and nonadiabatic dissociation". In: *Molecular Physics* 106.9-10 (2008), pp. 1127–1133. DOI: [10.1080/00268970802245192](https://doi.org/10.1080/00268970802245192).
- [190] N. L. Evans, H. Yu, G. M. Roberts, V. G. Stavros, and S. Ullrich. "Observation of ultrafast NH₃ (\tilde{A}) state relaxation dynamics using a combination of time-resolved photoelectron spectroscopy and photoproduct detection". In: *Physical Chemistry Chemical Physics* 14.30 (2012), pp. 10401–10409. DOI: [10.1039/C2CP40178A](https://doi.org/10.1039/C2CP40178A).
- [191] G. J. Rottman, T. N. Woods, and T. P. Sparn. "Solar-stellar irradiance comparison experiment 1: 1. Instrument design and operation". In: *Journal of Geophysical Research: Atmospheres* 98.D6 (1993), pp. 10667–10677. DOI: [10.1029/93JD00462](https://doi.org/10.1029/93JD00462).
- [192] W. F. Chan, G. Cooper, and C. E. Brion. "The electronic spectrum of water in the discrete and continuum regions. Absolute optical oscillator strengths for photoabsorption (6–200 eV)". In: *Chemical Physics* 178.1 (1993), pp. 387–400. DOI: [10.1016/0301-0104\(93\)85078-M](https://doi.org/10.1016/0301-0104(93)85078-M).
- [193] E. L. Woodbridge, M. N. R. Ashfold, and S. R. Leone. "Photodissociation of ammonia at 193.3 nm: Rovibrational state distribution of the NH₂(\tilde{A} ²A₁) fragment". In: *The Journal of Chemical Physics* 94.6 (1991), pp. 4195–4204. DOI: [10.1063/1.460653](https://doi.org/10.1063/1.460653).
- [194] M. M. Mann, A. Hustrulid, and J. T. Tate. "The Ionization and Dissociation of Water Vapor and Ammonia by Electron Impact". In: *Phys. Rev.* 58 (4 1940), pp. 340–347. DOI: [10.1103/PhysRev.58.340](https://doi.org/10.1103/PhysRev.58.340).
- [195] I. Tokue and M. Iwai. "Formation of NH(A ³Π, c ¹Π) by the electron impact dissociation of ammonia". In: *Chemical Physics* 52.1 (1980), pp. 47–53. DOI: [10.1016/0301-0104\(80\)85184-6](https://doi.org/10.1016/0301-0104(80)85184-6).
- [196] U. Mueller and G. Schulz. "Formation of NH fragments by electron impact dissociation of ammonia". In: *Chemical Physics Letters* 138.5 (1987), pp. 385–390. DOI: [10.1016/0009-2614\(87\)80526-2](https://doi.org/10.1016/0009-2614(87)80526-2).
- [197] A. H. Barrett, R. N. Martin, P. C. Myers, and P. R. Schwartz. "Observations of methanol in Sagittarius b2 at 48 GHz". In: *The Astrophysical Journal* 178 (1972), p. L23. DOI: [10.1086/181077](https://doi.org/10.1086/181077).
- [198] D. Toubanc, J. P. Parisot, J. Brillet, D. Gautier, F. Raulin, and C. P. McKay. "Photochemical modeling of Titan's atmosphere". In: *Icarus* 113.1 (1995), pp. 2–26. DOI: [10.1006/icar.1995.1002](https://doi.org/10.1006/icar.1995.1002).

- [199] C. J. Chandler, C. L. Brogan, Y. L. Shirley, and L. Loinard. “IRAS 16293–2422: Proper motions, jet precession, the hot core, and the unambiguous detection of infall”. In: *The Astrophysical Journal* 632.1 (2005), p. 371. DOI: [10.1086/432828](https://doi.org/10.1086/432828).
- [200] P. Ehrenfreund, L. D’Hendecourt, E. Dartois, M. J. de Muizon, M. Breittellner, J. L. Puget, and H. J. Habing. “ISO observations of interstellar ices and implications for comets”. In: *Icarus* 130.1 (1997), pp. 1–15. DOI: [10.1006/icar.1997.5895](https://doi.org/10.1006/icar.1997.5895).
- [201] C. J. Skinner, A. G. G. M. Tielens, M. J. Barlow, and K. Justtanont. “Methanol ice in the protostar GL 2136”. In: *The Astrophysical Journal* 399 (1992), pp. L79–L82. DOI: [10.1086/186611](https://doi.org/10.1086/186611).
- [202] J. Crovisier, D. Bockelée-Morvan, P. Colom, N. Biver, D. Despois, and D. C. Lis. “The composition of ices in comet C/1995 O1 (Hale-Bopp) from radio spectroscopy”. In: *Astronomy & Astrophysics* 418.3 (2004), pp. 1141–1157. DOI: [10.1051/0004-6361:20035688](https://doi.org/10.1051/0004-6361:20035688).
- [203] D. C. B. Whittet, A. M. Cook, E. Herbst, J. E. Chiar, and S. S. Shenoy. “Observational constraints on methanol production in interstellar and preplanetary ices”. In: *The Astrophysical Journal* 742.1 (2011), p. 28. DOI: [10.1088/0004-637X/742/1/28](https://doi.org/10.1088/0004-637X/742/1/28).
- [204] J. Hagege, S. Leach, and C. Vermeil. “Photochimie du méthanol en phase vapeur à 1236 et à 1849 Å”. In: *Journal de Chimie Physique* 62 (1965), pp. 736–746. DOI: [10.1051/jcp/1965620736](https://doi.org/10.1051/jcp/1965620736).
- [205] S. Satyapal, J. Park, R. Bersohn, and B. Katz. “Dissociation of methanol and ethanol activated by a chemical reaction or by light”. In: *The Journal of Chemical Physics* 91.11 (1989), pp. 6873–6879. DOI: [10.1063/1.457356](https://doi.org/10.1063/1.457356).
- [206] C. C. Marston, K. Weide, R. Schinke, and H. U. Suter. “Product selectivity of vibrationally mediated photofragmentation of methanol”. In: *The Journal of Chemical Physics* 98.6 (1993), pp. 4718–4727. DOI: [10.1063/1.464976](https://doi.org/10.1063/1.464976).
- [207] Y. Wen, J. Segall, M. Dulligan, and C. Wittig. “Photodissociation of methanol at 193.3 nm: Translational energy release spectra”. In: *The Journal of Chemical Physics* 101.7 (1994), pp. 5665–5671. DOI: [10.1063/1.467352](https://doi.org/10.1063/1.467352).
- [208] S. W. Weaver, C. R. Powers, M. N. McCabe, and S. Zinga. “Laboratory measurements of methanol photolysis branching ratios to guide astrochemical models”. In: *Proceedings of the International Astronomical Union* 13.S332 (2017), pp. 305–311. DOI: [10.1017/S1743921317006408](https://doi.org/10.1017/S1743921317006408).
- [209] R. J. Buenker, G. Olbrich, H. P. Schuchmann, B. L. Schuermann, and C. Von Sonntag. “Photolysis of methanol at 185 nm. Quantum-mechanical calculations and product study”. In: *Journal of the American Chemical Society* 106.16 (1984), pp. 4362–4368. DOI: [10.1021/ja00328a011](https://doi.org/10.1021/ja00328a011).
- [210] K.-J. Yuan, Y. Cheng, F.-Y. Wang, and X.-M. Yang. “Photodissociation dynamics of methanol and ethanol at 157 nm”. In: *Chinese Journal of Chemical Physics* 21.4 (2008), pp. 301–307. DOI: [10.1088/1674-0068/21/04/301-307](https://doi.org/10.1088/1674-0068/21/04/301-307).
- [211] S. Harich, J. J. Lin, Y. T. Lee, and X. Yang. “Competing atomic and molecular hydrogen pathways in the photodissociation of methanol at 157 nm”. In: *The Journal of Chemical Physics* 111.1 (1999), pp. 5–9. DOI: [10.1063/1.479249](https://doi.org/10.1063/1.479249).
- [212] M. Lucas, Y. Liu, R. Bryant, J. Minor, and J. Zhang. “Vacuum ultraviolet photodissociation dynamics of methanol at 121.6 nm”. In: *Chemical Physics Letters* 619 (2015), pp. 18–22. DOI: [10.1016/j.cplett.2014.11.022](https://doi.org/10.1016/j.cplett.2014.11.022).

- [213] J. Hagege, P. C. Roberge, and C. Vermeil. "Collision-induced predissociation in the gas phase. Photolysis of methanol at 1849 Å". In: *Transactions of the Faraday Society* 64 (1968), pp. 3288–3299. DOI: [10.1039/TF9686403288](https://doi.org/10.1039/TF9686403288).
- [214] S.-H. Lee, H.-I. Lee, and Y. T. Lee. "Distributions of angular anisotropy and kinetic energy of products from the photodissociation of methanol at 157 nm". In: *The Journal of Chemical Physics* 121.22 (2004), pp. 11053–11059. DOI: [10.1063/1.1814099](https://doi.org/10.1063/1.1814099).
- [215] J. A. Blush, P. Chen, R. T. Wiedmann, and M. G. White. "Rotationally resolved threshold photoelectron spectrum of the methyl radical". In: *The Journal of Chemical Physics* 98.4 (1993), pp. 3557–3559. DOI: [10.1063/1.464077](https://doi.org/10.1063/1.464077).
- [216] S. Willitsch, L. L. Imbach, and F. Merkt. "The ionization energy of methylene (CH₂) from a rotationally resolved photoelectron spectrum and its thermochemical implications". In: *The Journal of Chemical Physics* 117.5 (2002), pp. 1939–1940. DOI: [10.1063/1.1496468](https://doi.org/10.1063/1.1496468).
- [217] M. A. Haney and J. L. Franklin. "Correlation of excess energies of electron-impact dissociations with the translational energies of the products". In: *The Journal of Chemical Physics* 48.9 (1968), pp. 4093–4097. DOI: [10.1063/1.1669743](https://doi.org/10.1063/1.1669743).

Titre: Photoionisation VUV de molécules d'intérêt astrophysique : aspects fondamentaux et quantitatifs

Mots clés: VUV, photoionisation, molécule, radical, laser, synchrotron, spectroscopie

Résumé: L'évolution de la matière diluée dans les milieux astrophysiques tels que le milieu interstellaire, les atmosphères planétaires ou la coma des comètes, résulte d'une photochimie très complexe faisant intervenir en particulier un grand nombre d'espèces stables et réactives en phase gazeuse. Cette photochimie est induite par le rayonnement galactique ou par le rayonnement solaire dans le domaine spectral de l'ultra-violet du vide (VUV, longueur d'onde < 200 nm). Une bonne compréhension de cette évolution nécessite une modélisation précise de la photochimie de ces milieux, en prenant en compte l'ensemble des réactions chimiques et des processus photo-induits. Dans ce contexte, le travail principal de cette thèse porte sur le processus de photoionisation ($M + h\nu \rightarrow M^+ + e^-$).

Un des buts de cette thèse était de déterminer des paramètres quantitatifs, souvent jamais mesurés, pour décrire le processus de photoionisation de composés d'intérêt astrophysique, en particulier d'espèces réactives. Pour ce faire, le montage moyenne – haute résolution (SAPHIRS) de la ligne DESIRS du synchrotron SOLEIL et le nouveau montage laser haute résolution (VULCAIM) de l'ISMO basé sur un spectromètre de photoélectrons à énergie cinétique nulle (ZEKE) ont été utilisés pour mener diverses études expérimentales. Cette thèse présente aussi le développement de cette nouvelle expérience, unique en France, et la caractérisation de ses principales performances.

Un paramètre quantitatif important est la section efficace de photoionisation, reliant le nombre d'ions

produits au nombre initial d'espèces neutres. Pour les espèces réactives, ce paramètre est rarement connu à cause des difficultés inhérentes à ce type de mesures. Ce travail présente deux mesures de sections efficaces de photoionisation (pour les radicaux NH_2 et OH) et quelques résultats préliminaires sur d'autres sections efficaces de radicaux. D'un point de vue pratique, ces sections efficaces permettent indirectement de quantifier d'autres processus de relaxation (*i.e.* la photodissociation) en utilisant des expériences pompe VUV – sonde VUV, qui sont aussi décrites dans le manuscrit.

En plus de l'importance de ces expériences pour les applications, ces études permettent d'obtenir des informations fondamentales et détaillées sur le processus de photoionisation, surtout *via* la spectroscopie de photoélectrons. Au synchrotron SOLEIL, les structures vibroniques de différentes molécules astrophysiques ont été étudiées au voisinage de leurs premiers potentiels d'ionisation adiabatiques. Au laboratoire, le nouveau laser VUV s'est montré très performant pour des expériences de spectroscopie VUV à des résolutions rarement atteintes dans ce domaine spectral (jusqu'à 0.06 cm^{-1}). L'utilisation de ce laser pour la spectroscopie de photoélectron couplée à une technique d'analyse d'images révèle la possibilité d'entreprendre des études de photoionisation à haute résolution avec un meilleur rapport signal sur bruit, ce qui permettra la détermination de nouvelles informations spectroscopiques concernant la structure rovibronique d'un grand nombre de cations, et en particulier d'espèces radicalaires.



Title: VUV photoionisation of astrophysical molecules: fundamental and quantitative aspects

Keywords: VUV, photoionisation, molecules, radicals, laser, synchrotron, spectroscopy

Abstract: The evolution of diluted matter in various astrophysical media (interstellar space medium, planetary atmospheres, comets) results from complex photochemistry involving many stable and reactive species in the gas phase. This photochemistry is induced by galactic fluxes or by solar radiation in the vacuum ultra-violet spectral domain (VUV, wavelength below 200 nm). An accurate model of the photochemistry of these media is required to understand this evolution. This model must account for all photo-induced processes through pertinent quantitative parameters measured in laboratory experiments. One of these processes is photoionisation ($M + h\nu \rightarrow M^+ + e^-$), which is the focus of this thesis. Other such processes, featuring in this work, are photodissociation and dissociative ionisation.

One of the aims of this PhD work was to determine quantitative and often unprecedented parameters to describe photoionisation processes of compounds of astrophysical interest, in particular of reactive species. These were determined experimentally using the medium high-resolution SAPHIRS setup of the DESIRS beamline of the SOLEIL synchrotron and using the new high-resolution laser setup (VULCAIM) of ISMO based on a Zero Electron Kinetic Energy (ZEKE) photoelectron spectrometer. This thesis also presents details on the development of this new setup, unique to France and one of only three in the world, and on the determination of its main characteristics. Particular care is taken to evaluate the resolution of the VUV laser and of the ensuing photoelectrons.

An important quantifying parameter is the photoionisation cross section, relating the number of produced ions to an initial quantity of neutral species. This parameter is not always available in the literature due to experimental challenges, especially for unstable species. This work presents two photoionisation cross section measurements (NH_2 and OH free radicals) and some preliminary work on other free radical cross sections. From a practical point of view, these cross sections also allow the indirect quantification of processes implicating neutral species (e.g. photodissociation). This aspect also features in the manuscript when studying photodissociation with a VUV pump – VUV probe setup.

On top of their application value, these studies offer fundamental insights, mainly *via* photoelectron spectroscopy, into the fine details of photoionisation processes. At the SOLEIL facility, the vibronic structure of various astrophysical molecules been investigated in the vicinity of their first adiabatic ionisation potentials. At the ISMO laboratory, the new VUV laser has shown to have the capabilities of undertaking spectroscopic studies at a resolution (down to 0.06 cm^{-1}) rarely seen in the VUV range. The use of this laser for photoelectron spectroscopy combined with an imaging technique promises to be able to perform high-resolution photoionisation studies with improved signal-to-noise ratio. It will lead to unprecedented spectroscopic information on the rovibronic structure of a number of cations, in particular for radical species.

